THÈSE

Pour l'obtention du grade de
DOCTEUR DE L'UNIVERSITÉ DE POITIERS
UFR des sciences fondamentales et appliquées
Institut de chimie des milieux et matériaux de Poitiers - IC2MP
(Diplôme National - Arrêté du 25 mai 2016)

École doctorale : Chimie, Écologie, Géosciences et AgroSciences Théodore Monod (Poitiers)
Secteur de recherche : Structure et évolution de la terre et autres planètes

Cotutelle : Université Fédérale d'Ouro Preto

Présentée par :
Ana Carolina Campos Mateus

Sistemas de alteração e gênese de solos em piroclastos da ilha de Trindade, Atlântico sul

Directeur(s) de Thèse :
Sabine Petit, Angélica F. Drummond Chicarino Varajao

Soutenue le 19 février 2020 devant le jury

Jury :

Président	**Edgar Batista Medeiros Jr**	Professor, Universidade de Ouro Preto, Brasil
Rapporteur	**Emmanuel Joussein**	Maître de conférences, GRESE, Université de Limoges
Rapporteur	**Jérémie Garnier**	Professeur, Université de Brasilia, Brésil
Membre	**Sabine Petit**	Directrice de recherche CNRS, IC2MP, Université de Poitiers
Membre	**Angélica F. D. Chicarino Varajao**	Professor, Universidade de Ouro Preto, Brasil
Membre	**Patricia Patrier**	Professeur, IC2MP, Université de Poitiers

Pour citer cette thèse :
Ana Carolina Campos Mateus. *Sistemas de alteração e gênese de solos em piroclastos da ilha de Trindade, Atlântico sul* [En ligne]. Thèse Structure et évolution de la terre et autres planètes. Poitiers : Université de Poitiers, 2020. Disponible sur Internet <http://theses.univ-poitiers.fr>

UNIVERSIDADE FEDERAL DE OURO PRETO
ESCOLA DE MINAS
DEPARTAMENTO DE GEOLOGIA

PROGRAMA DE PÓS-GRADUAÇÃO EM EVOLUÇÃO CRUSTAL
E RECURSOS NATURAIS

Geologia Ambiental e Conservação de Recursos Naturais

TESE DE DOUTORADO

Sistemas de alteração e gênese de solos em piroclastos da Ilha de Trindade, Atlântico Sul

por

Ana Carolina Campos Mateus

Orientadora Brasileira: Profa. Dra. Angélica Fortes Drummond Chicarino Varajão (DEGEO/UFOP)
Orientadora Francesa: Profa. Dra. Sabine Petit (IC2MP/Universidade de Poitiers)

Co-Orientador: Prof. Dr. Fábio Soares de Oliveira (IGC/UFMG)

Ouro Preto – Fevereiro de 2020

THESE

Pour l'obtention du Grade de

DOCTEUR DE L'UNIVERSITE DE POITIERS

(Faculté des Sciences Fondamentales et Appliquées)
(Diplôme National - Arrêté du 25 mai 2016)

Ecole Doctorale : Chimie Ecologie Géosciences Agrosciences « *Théodore Monod* »

Secteur de Recherche : Structure et évolution de la terre et autres planètes

Présentée par :

Ana Carolina Campos Mateus

****

Les systèmes d'altération et la genèse des sols dans les pyroclastes de l'Île de Trindade, Atlantique Sud

****

Co-directrice de Thèse : Sabine Petit (Université de Poitiers)
Co-directrice de Thèse : Angélica Fortes Drummond Chicarino Varajão (Université Federale d'Ouro Preto)

****

Soutenance le 19 février 2020

devant la Commission d'Examen

****

JURY

....

Jéremie Garnier	Professeur, Université de Brasília
Emmanuel Joussein	Maître de Conférences HDR, Université de Limoges
Patricia Patrier	Professeur, Université de Poitiers
Edgar Batista de Medeiros Junior	Professeur, Université Fédérale d'Ouro Preto
Angélica Fortes Drummond Chicarino Varajão	Professeur, Université Fédérale d'Ouro Preto
Sabine Petit	Directrice de Recherche CNRS, Université de Poitiers

FUNDAÇÃO UNIVERSIDADE FEDERAL DE OURO PRETO

Reitora

Cláudia Aparecida Marliére de Lima

Vice-Reitor

Hermínio Arias Nalini Júnior

Pró-Reitor de Pesquisa e Pós-Graduação

Sérgio Francisco de Aquino

ESCOLA DE MINAS

Diretor

Issamu Endo

Vice-Diretor

Hernani Mota de Lima

DEPARTAMENTO DE GEOLOGIA

Chefe

Marco Antônio Fonseca

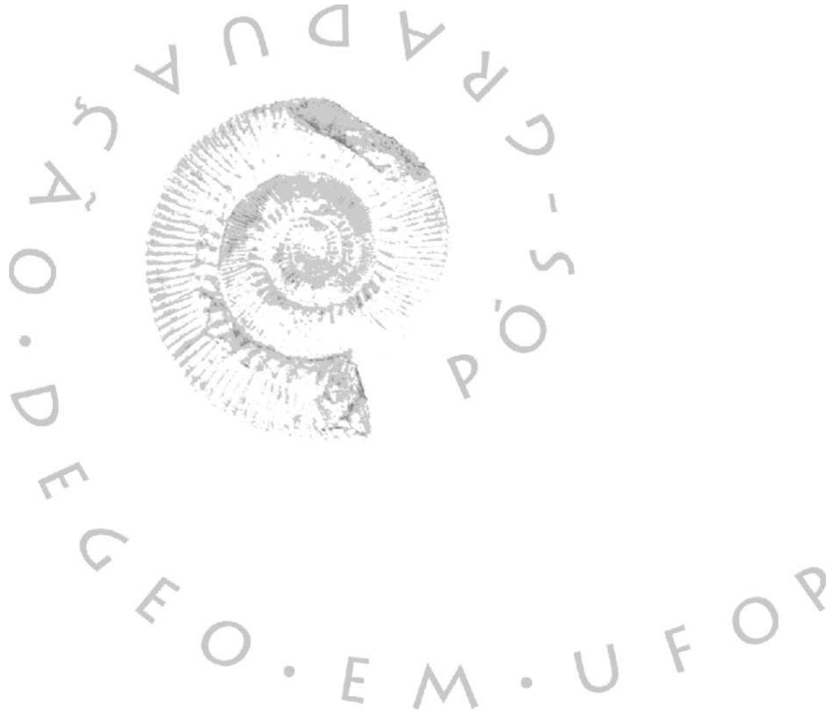

EVOLUÇÃO CRUSTAL E RECURSOS NATURAIS

CONTRIBUIÇÕES ÀS CIÊNCIAS DA TERRA – VOL.78

TESE DE DOUTORAMENTO

Nº 96

SISTEMAS DE ALTERAÇÃO E GÊNESE DE SOLOS EM PIROCLASTOS DA ILHA DE TRINDADE, ATLÂNTICO SUL

Ana Carolina Campos Mateus

Orientadora brasileira- DEGEO/UFOP
Angélica Fortes Drummond Chicarino Varajão

Orientadora francesa- IC2MP - Universidade de Poitiers
Sabine Petit

Co-orientador
Fábio Soares de Oliveira

Tese apresentada ao Programa de Pós-Graduação em Evolução Crustal e Recursos Naturais do Departamento de Geologia da Escola de Minas da Universidade Federal de Ouro Preto como requisito parcial à obtenção do Título de Doutor Ciência Naturais, Área de Concentração: Geologia Ambiental e Conservação de Recursos Naturais

OURO PRETO

2020

Universidade Federal de Ouro Preto – http://www.ufop.br

Escola de Minas - http://www.em.ufop.br
Departamento de Geologia - http://www.degeo.ufop.br/
Programa de Pós-Graduação em Evolução Crustal e Recursos Naturais
Campus Morro do Cruzeiro s/n - Bauxita
35.400-000 Ouro Preto, Minas Gerais
Tel. (31) 3559-1600, Fax: (31) 3559-1606 e-mail: pgrad@degeo.ufop.br

ISSN 85-230-0108-6

Depósito Legal na Biblioteca Nacional

Edição 1ª

Catalogação elaborada pela Biblioteca Prof. Luciano Jacques de Moraes do

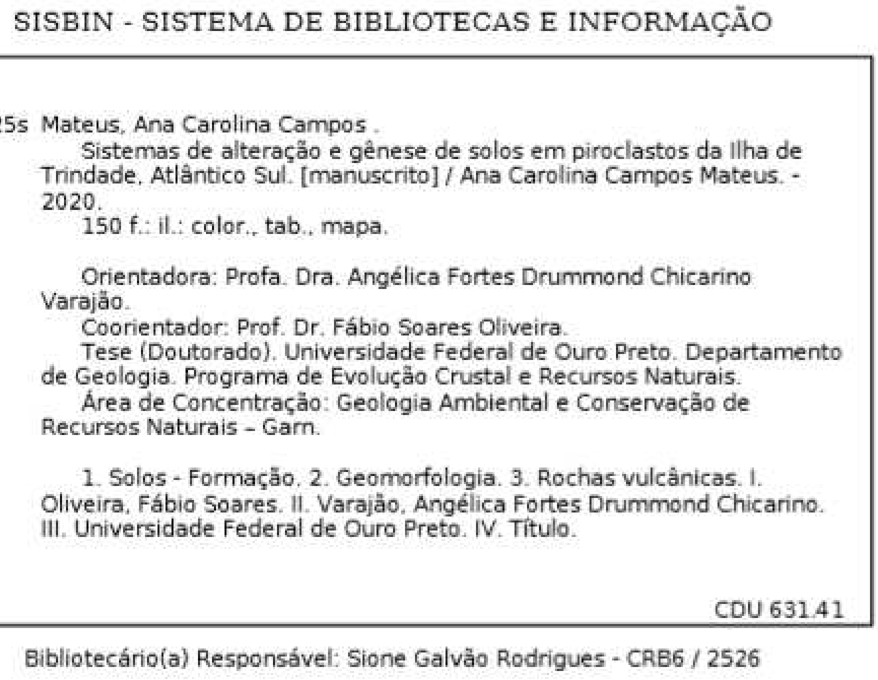

SISBIN - SISTEMA DE BIBLIOTECAS E INFORMAÇÃO

M425s Mateus, Ana Carolina Campos .
Sistemas de alteração e gênese de solos em piroclastos da Ilha de Trindade, Atlântico Sul. [manuscrito] / Ana Carolina Campos Mateus. - 2020.
150 f.: il.: color., tab., mapa.

Orientadora: Profa. Dra. Angélica Fortes Drummond Chicarino Varajão.
Coorientador: Prof. Dr. Fábio Soares Oliveira.
Tese (Doutorado). Universidade Federal de Ouro Preto. Departamento de Geologia. Programa de Evolução Crustal e Recursos Naturais.
Área de Concentração: Geologia Ambiental e Conservação de Recursos Naturais – Garn.

1. Solos - Formação. 2. Geomorfologia. 3. Rochas vulcânicas. I. Oliveira, Fábio Soares. II. Varajão, Angélica Fortes Drummond Chicarino. III. Universidade Federal de Ouro Preto. IV. Título.

CDU 631.41

Bibliotecário(a) Responsável: Sione Galvão Rodrigues - CRB6 / 2526

http://www.sisbin.ufop.br

MINISTÉRIO DA EDUCAÇÃO
Universidade Federal De Ouro Preto
Escola de Minas – Departamento de Geologia
Programa de Pós-Graduação em Evolução Crustal e Recursos Naturais

UFOP
Universidade Federal de Ouro Preto

FICHA DE APROVAÇÃO

TESE DE DOUTORADO EM REGIME DE COTUTELA ENTRE A UNIVERSIDADE FEDERAL DE OURO PRETO E A UNIVERSIDADE DE POITIERS

TÍTULO: *SISTEMAS DE ALTERAÇÃO E GÊNESE DE SOLOS EM PIROCLASTOS DA ILHA DE TRINDADE, ATLÂNTICO SUL.*

AUTOR: Ana Carolina Campos Mateus

ORIENTADORES:

PROF.ª DR.ª ANGÉLICA FORTES DRUMMOND CHICARINO VARAJÃO (UFOP)
PROF.ª DR.ª SABINE PETIT (UNIVERSIDADE DE POITIERS)

DATA DA DEFESA: 19/02/2020

PRESIDENTE: PROF. DR. EDGAR BATISTA DE MEDEIROS JÚNIOR (UFOP)

BANCA EXAMINADORA:

Edgar Batista de Medeiros Júnior
PROF. DR. EDGAR BATISTA DE MEDEIROS JÚNIOR (Presidente UFOP)

PROF.ª DR.ª ANGÉLICA FORTES D. C. VARAJAO (UFOP)

(Participação por Videoconferência)
PROF.ª DR.ª SABINE PETIT(UNIVERSIDADE DE POITIERS)

(Participação por Videoconferência)
PROF. DR. EMMANUEL JOUSSEIN (UNIVERSITÉ LIMOGES)

(Participação por Videoconferência)
PROF.ª DR.ª PATRÍCIA PATRIER (UNIVERSIDADE DE POITIERS)

(Participação por Videoconferência)
PROF. DR. JEREMIE GARNIER (UNB)

Campus Universitário Morro do Cruzeiro - S/N - CEP: 35400-000 - Ouro Preto - MG - Brasil
Tel.: (0..31) 559.1600 - Fax: (0..31) 559.1606 – e-mail: pgrad@degeo.ufop.br

Dedicatória

À minha família e a todos
que me incentivaram nessa longa jornada

Agradecimentos

Ao professor Carlos, coordenador do Projeto das Ilhas Oceânicas Brasileiras, que me concedeu a grande oportunidade de trabalhar em um projeto de extrema importância científica para o Brasil.

À Capes por conceder a bolsa de estudos no Brasil e na França. À FAPEMIG, CNPq, Nouvelle Aquitaine e União Européia pelo auxílio financeiro às análises laboratoriais.

Agradeço à Marinha Brasileira pelo transporte à Ilha de Trindade e principalmente à equipe de marinheiros que foram muito prestativos durante a etapa de coleta em campo.

Meus sinceros agradecimentos aos técnicos Wanderlei, Adriana e Celso do Departamento de Geologia/ Universidade Federal de Ouro Preto, ao técnico Julien e ao professor Claude do Institut de Chimie des Milieux et Matériaux de Poitiers da Université de Poitiers/França, e ao professor Olivier do CINam/CNRS da Universidade Aix Marseille pela ajuda nas análises laboratoriais e pela amizade.

Aos Laboratórios da Universidade Federal de Ouro Preto (UFOP) e Universidade Federal de Minas Gerais pelas análises na Microssonda e no MEV; aos Laboratórios do DEGEO/UFOP e IC2MP/Universidade de Poitiers pelas análises de Difração de Raios-X, e ao CINam-CNRS/Universidade de Aix Marseille pelas análises no MET.

Meus principais agradecimentos aos orientadores Angélica, Fábio e Sabine pelo incentivo, confiança e extrema dedicação à minha pesquisa.

À Mariana pela amizade e ajuda durante a etapa de campo na Ilha de Trindade.

Às minhas amigas Natália e Raissa por estarem sempre comigo nas horas difíceis durante o estágio na França.

Aos meus pais Walter e Rosângela, ao meu irmão Tiago e à minha Tia Wélita que foram exemplos de vida e sempre incentivaram a minha longa jornada de estudos e ao meu companheiro Kevin, sempre muito paciente e cuidadoso.

Table des matiéres

Table de figures

Table des tableaux

Resumo

Este estudo objetivou caracterizar as feições de alteração e a gênese de solos sobre piroclastos da Ilha de Trindade (IT), Atlântico Sul, através de estudos macromorfológicos, micromorfológicos, mineralógicos e geoquímicos. As coletas das amostras foram realizadas no Vulcão do Paredão de idade Holocênica (perfil P1) e a Formação Quartenária Morro Vermelho (perfis P2, P3 e P4). Os piroclastos de P1 e P2 são interpretados como depósito de brecha vulcânica, enquanto o piroclasto de P3 é um depósito de lápili. P4 apresenta fragmentos de rochas com composição mineralógica diferente dos outros perfis sugerindo outro evento de deposição de bombas piroclásticas. As erupções associadas podem ser consideradas como estrombolianas. Os piroclastos são de cor cinza escuro com algumas regiões avermelhadas alteradas. Análises ao microscópio óptico suportada por difração de raios-X revelaram uma mistura de biotita, goethita, ilmenita, anatásio, magnetita, hematita, piroxênios, zeólitas e olivina como seus principais componentes minerais. A análise petrológica mostra estruturas vesiculares e amigdaloides, com uma textura hipocristalina e uma massa vítrea de sideromelano que muda para palagonita, indicando claramente uma erupção freatomagmática. Análises de infravermelho nas regiões palagonitizadas revelaram a presença de haloisita, sugerindo alteração do sideromelano para minerais de argila tubular. Amígdalas e microfraturas estão parcial ou totalmente preenchidas de zeólitas, que são formados pela percolação de água que reage com a palagonita e precipitação de elementos químicos do fluido hidrotermal. Iddingsitas e Ti-magnetitas ocorrem nas fraturas e bordas das olivinas. O avanço da alteração em direção ao perfil do solo, deixando apenas relíquias de cristais de olivinas ou atingindo sua transformação total nos horizontes superiores, mostra que o intemperismo é o principal processo de formação das iddingsitas. Algumas Ti-magnetitas são zonadas com núcleo rico e borda pobre em Cr, sugerindo uma origem mantélica do magma. O diopsídeo explica o alto conteúdo de elementos traços. Dados geoquímicos mostram que os piroclastos estão subsaturados em sílica e encontram-se nos campos dos ultrabásicos e dos foiditos no diagrama de classificação TAS. Os solos de P1 e P2 apresentam, respectivamente, horizontes A-Bi-C e A-C decapitado; e os solos de P3 e P4 apresentam horizontes A-C. Os solos mostram uma matriz argilosa avermelhada e acastanhada e são friáveis com uma consistência plástica. Suas microestruturas são granulares, grãos simples e microagregados intergrãos e, os agregados mostram b-fábrica indiferenciada. Os constituintes mineralógicos da fração pó total são biotita, hematita, magnetita, ilmenita, piroxênio, olivina, haloisita, goethita, anatásio e rutilo. A fração argila é marcada pela presença de haloisita, ferrihidrita e pequenas quantidades de alofana. Todos os solos apresentaram propriedades ândicas e podem ser classificados como Andossolos não alofânicos. Além disso, as características micromorfológicas se assemelham aos Andossolos de outras ilhas vulcânicas descritas na literatura (Pico, Faial, Terceira, Canarias, Santa Fé). A predominância da haloisita na fração argila formada pela alteração do sideromelano, sugere que a alofana seria uma fase intermediária dessa rápida transformação favorecida pelas condições climáticas da IT. A geoquímica total mostrou que em todos os perfis o Al, Fe e Ti se acumulam devido a suas baixas mobilidades e o Ca, Na, K e Mg são os mais intensamente lixiviados. Os perfis localizados nas cotas mais baixas tendem a ter valores de K e Mg mais elevados no horizonte A devido a influência dos *sprays* salinos e a deposição de elementos químicos provenientes das regiões mais elevadas. Ti, Mn, Fe, Co, Cr, Ni, V, Zr, S foram enriquecidos nos solos de P1 e P3 devido à perda de elementos mais móveis durante o processo de formação do solo. Zn e Cu se concentram no horizonte A dos perfis P3 e P4 que apresentaram maior concentração de matéria orgânica e fragmentos de piroclastos inalterados. A lixiviação das ETRs do alto para a encosta inferior levou ao enriquecimento desses elementos, especialmente ETRs leves, no solo de baixa altitude (258 m). O perfil de alta altitude mostrou anomalias positivas de Ce devido a maior exposição ao intemperismo.

Palavras-chave: Ilha de Trindade, Andossolos, rochas vulcânicas, piroclastos

Abstract

This study aimed to characterize the alteration features comprising the genesis and formation of soils on pyroclasts of Trindade Island (TI), South Atlantic, Brazil, through of macromorphological, micromorphological, mineralogical and geochemical studies. Collections of samples were made at the Holocene Paredão volcano (Profile P1) and the Late Quartenary Morro Vermelho Formation (profiles P2, P3 and P4). The pyroclasts of P1 and P2 are interpreted as volcanic breccia deposit, whereas of P3 is a lapilli deposit. P4 presents fragments of rocks with mineralogical composition different from other profiles suggesting another event of deposition of pyroclastic bombs. The eruptions associated can be regarded as strombolians. The pyroclasts are dark gray in color with some altered reddish regions. Optical microscope supported by X-ray diffraction analysis revealed a mixture of biotite, goethite, ilmenite, anatase, magnetite, hematite, pyroxene, zeolites, and olivine as their main mineral components. Petrologic analysis shows sideromelane that changes to palagonite, clearly indicating a phreatomagmatic eruption. Infrared analyses in the palagonitized regions revealed the presence of halloysite, suggesting alteration of sideromelane to tubular clay minerals. Amygdales and microfractures are partially or totally filled with zeolites, which are formed by the percolation of water that reacts with the palagonite and precipitation of chemical elements of hydrothermal fluid. Iddingsite and Ti-magnetites occur in the fractures and edges of the olivine. The advance of the alteration towards the soil profile, leaving only relicts of olivine crystals or reaching their total transformation in the upper horizons, shows that weathering is the main process of iddingsite formation. Some Ti-magnetites are zoned with Cr-rich core and Cr-poor edge, suggesting a deep mantle origin of the magma. The diopside explain the high trace elements contents. Geochemical data show that the pyroclasts are plotting in the ultrabasic and foidites fields on the TAS classification diagram. The soils of P1 and P2 show, respectively, A-Bi-C and decapitated A-C horizons; and P3 and P4 show A-C horizons. The soil profiles show a reddish and brownish clayey matrix and are friable with a plastic consistency. Their microstructures are granular, simple grain and intergrain microaggregate and, the aggregates show undifferentiated b-fabric. The mineralogical constituents of the bulk fraction are biotite, hematite, magnetite, ilmenite, pyroxene, olivine, halloysite, goethite, anatase and rutile. The clay fraction is marked by presence of halloysite, ferrihydrite and little amounts of allophane. All soils can to be classified as non-allophanic Andosols. In addition, the micromorphological characteristics resemble to Andosols from other volcanic islands (Pico, Faial, Terceira, Canarias, Santa Fé). The predominance of halloysite in the clay fraction formed by alteration of sideromelane, suggests that allophane would be an intermediate phase of this rapid transformation favored by climate conditions of the TI. Total geochemistry showed that in all profiles Al, Fe and Ti accumulate due to their low mobility and Ca, Na, K and Mg are the most intensely leached. The profiles located at the lower quotas tend to have higher K and Mg values in A horizon due to the influence of salt sprays and the deposition of chemical elements from the higher regions. Ti, Mn, Fe, Co, Cr, Ni, V, Zr, S were enriched in soil profiles P1 and P3 due to loss of mobile elements during the soil formation process. Zn and Cu concentrate on A horizon of profiles P3 and P4 with higher concentration of organic matter and fragments of unaltered pyroclasts. Leaching of the REEs from higher to the lower slope led to the enrichment of these elements, especially the light REEs, in the low lying (258 m) soil. The high altitude profile showed Ce positive anomaly due to longer exposure to weathering.

Keywords: Trindade island, Andosols, volcanic rocks, pyroclasts

Résumé

Cette étude visait à déterminer les caractéristiques d'altération comprenant la genèse et la formation de sols sur les pyroclastes de l'Île de Trindade (IT), Atlantique Sud, Brésil, à travers des études macromorphologiques, micromorphologiques, minéralogiques et géochimiques. Les échantillons ont été prélevés au Vulcão do Paredão de l'Holocène (profil P1) et dans la Formation Morro Vermelho du Quaternaire ancien (profils P2, P3 et P4). Les pyroclastes de P1 et P2 sont interprétés comme étant des dépôts de brèches volcaniques, tandis que P3 est un dépôt de lapilli. P4 présente des fragments de roches avec une composition minéralogique différente des autres profils suggérant un autre événement de dépôt de bombes pyroclastiques. Les éruptions associées peuvent être considérées comme stromboliennes. Les pyroclastes sont de couleur gris foncé avec quelques zones rougeâtres altérées. Analyse au microscope optique soutenue par la diffraction des rayons X indiquent un mélange de biotite, de goethite, d'ilménite, d'anatase, de magnétite, d'hématite, de pyroxènes, de zéolites et d'olivine comme minéraux principaux. La microscopie optique montre un sidéromélane qui se transforme en palagonite, indiquant clairement une éruption phréato-magmatique. Les spectres obtenus par microscopie infrarouge dans les zones palagonitisées permettent d'identifier la présence d'halloysite, probablement issue de l'altération du sideromélane. Les amygdales et les microfractures sont partiellement ou totalement remplies de zéolites, formées par la percolation de l'eau qui réagit avec la palagonite et la précipitation des éléments chimiques du fluide hydrothermal. Les magnétites-Ti et l'iddingsite sont observées dans les fractures et en bordure des olivines. La progression de l'altération dans le profil du sol, se manifeste par la présence de reliques d'olivine ou sa transformation totale dans les horizons supérieurs, et montre que l'altération est le processus principal de formation des iddingsites. Certaines magnétites-Ti sont zonées avec un enrichissement en Cr au centre, suggérant une origine mantellique. Le diopside expliquent les teneurs élevées en éléments traces. Les données géochimiques montrent que les pyroclastes se situent dans les champs ultrabasique et föiditique sur le diagramme de classification TAS. Les sols de P1 et P2 comportent, respectivement, les horizons A, Bi, C et un A érodé, C, tandis que P3 et P4 sont constitués des horizons A et C. Les sols montrent une matrice argileuse rougeâtre et brunâtre et sont friables avec une consistance plastique. Leurs microstructures sont granulaires, simples microaggrégats de grains et d'intergrains et, les aggrégats sont indifférenciés. Les constituants minéralogiques de la roche sont la biotite, l'hématite, la magnétite, l'ilménite, les pyroxènes, l'olivine, l'halloysite, la goethite, l'anatase et le rutile. La fraction argileuse est marquée par la présence d'halloysite, de ferrihydrite et de petites quantités d'allophane. Tous les sols peuvent être classés comme Andosols non-allophaniques. Les caractéristiques micromorphologiques ressemblent à des Andosols d'autres îles volcaniques (Pico, Faial, Terceira, Canarias, Santa Fé). La prédominance de l'halloysite dans la fraction argileuse suggère que l'allophane serait une phase intermédiaire issue de l'altération rapide du sidéromélane favorisée par les conditions climatiques de l'IT. La géochimie totale montre que dans tous les profils Al, Fe et Ti s'accumulent en raison de leur faible mobilité et que Ca, Na, K et Mg sont les plus intensément lixiviés. Les profils situés aux altitudes inférieures ont tendance à présenter des valeurs en K et Mg plus élevées dans l'horizon A en raison de l'influence des projections salines et de dépôt d'éléments chimiques des niveaux supérieurs. Pour P1 et P3, les éléments Ti, Mn, Fe, Co, Cr, Ni, V, Zr, S ont été enrichis dans les sols et leurs concentrations relatives sont liées à perte d'éléments mobiles pendant le processus de formation du sol. Zn et Cu se concentrent sur un horizon A de profils P3 et P4 avec une concentration plus élevée de matière organique et des fragments de pyroclastes inaltérés. Les terre rares, principalement les terre rares légères, sont enrichies dans le profil situé à basse altitude (258 m), en raison de la contribution des niveaux plus élevés de l'île. Le profil de haute altitude a montré une anomalie positive en Ce due à une exposition plus longue aux intempéries.

Mots clés : Île de Trindade, Andosols, roches volcaniques, pyroclastites

Résumé Allongé

Au Brésil, la situation géopolitique et économique des trois dernières décennies a incité le gouvernement à soutenir fortement la recherche scientifique dédiée au domaine maritime national, incluant les cinq îles océaniques: Trindade et Martin Vaz, Abrolhos, Fernando de Noronha, Atol das Rocas et São Pedro et São Paulo. Les efforts déployés par le gouvernement fédéral, la Marine et les entreprises brésiliennes ont été mis en commun pour créer des programmes d'incitation à la recherche sur les îles comme le PROTRINDADE, pour Trindade et Martin Vaz et le PROARQUIPÉLAGO, pour São Pedro et São Paulo. La superficie de l'ensemble de ces cinq îles est de 3,6 millions de km². La richesse de leur biodiversité leur a valu le surnom de Amazon Blue. La plupart des recherches menées dans les îles océaniques brésiliennes jusqu'à ce jour, porte sur la flore et la faune marines, négligeant globalement les milieux terrestres. Cette lacune, souvent responsable de la mauvaise gestion de ces territoires, nécessitait donc d'être comblée. Les quelques études pédologiques déjà effectuées sur les îles océaniques brésiliennes montrent, dans la plupart des cas, que les singularités et endémismes sont liés aux caractéristiques du sol et de la roche mère, le plus souvent de nature volcanique. Une prédominance des sols jeunes est généralement observée, mais même lorsqu'ils sont profondément altérées, de nombreuses caractéristiques du matériau source sont conservés. Pour ces raisons, une meilleure connaissance des milieux terrestres dans les îles océaniques du Brésil et par conséquent de leurs sols, nécessite d'élucider la façon dont se produit l'altération d'un susbstrat géologique diversifié, compte tenu des modifications chimiques, minéralogiques et morphologiques impliquées. C'est dans ce contexte que s'inscrit ce travail concernant l'Île de Trindade (IT). L'IT est située dans l'Atlantique Sud, 1140 km au large de la côte brésilienne. Elle fait partie d'une vaste chaîne volcanique sous-marine d'orientation est - ouest, nommée Vitória-Trindade, et représente la partie supérieure d'un édifice volcanique de plus de 5,2 km de haut. Trindade est une île émergée depuis le Cénozoïque, soit à peu près depuis trois millions d'années. Elle est constituée de coulées et intrusions basiques alcalino sodiques, nettement sous saturées en silice, et de plusieurs pyroclastes. Ces éruptions ont eu lieu durant tout le Quaternaire jusqu'àu début de l'Holocène. Ainsi à l'exception de certains dépôts côtiers colluviaux, de récifs d'algues, de dunes et de plages, l'île entière est formée par des matières volcaniques extrusives et intrusives. Dans ce cadre lithologique diversifié, des sols enrichis en minéraux inhabituels dans les régions tropicales, allophanes et autres minéraux argileux, se sont développés. Peu de données sont disponibles concernant la genèse et l'évolution de ce type de minéraux secondaires, ainsi que leurs liens avec les de microsystèmes associés. Cette problématique est l'objet de cette étude. Ainsi, dans cette thèse, nous avons identifié et caractérisé les principaux produits d'altération et nous avons établi leur origine lithologique. Nous avons ensuite étudié la genèse et l'évolution des principales espèces minérales secondaires, en particulier les allophanes et les minéraux argileux. Puis, nous avons évalué les principales transformations morphologiques et géochimiques des minéraux primaires (les roches) et secondaires (le manteau d'altération), et identifié et comparé les differents niveaux d'altération. Nous avons ainsi pu confirmer la présence d'Andosols sur l'IT. Cette thèse a été divisée en 9 chapitres qui présentent les méthodologies, les résultats et les principales conclusions. Le premier chapitre présente la problématique, les objectifs spécifiques du travail, et la région d'étude. Les deuxième et troisième chapitres présentent les fondements théoriques qui ont guidé les travaux, en mettant l'accent sur le contexte géologique et géomorphologique de la zone d'étude et l'état actuel des altérations dans les îles océaniques (îles brésiliennes de Trindade, Fernando de Noronha, São Pedro e São Paulo, mais également autres îles des archipels des Açores, Galápagos, Cap Vert, Canaries). Le quatrième chapitre décrit les méthodes utilisées. Le cinquième chapitre concerne l'étude des pyroclastes, leur composition et leur produits d'altération. Les échantillons ont été recueillis au Vulcão do Paredão de l'Holocène (profil P1) et à la Formation Morro Vermelho du Quaternaire ancien (profils P2 and P3) sur l'IT. Les pyroclastes de P1 et P2 sont interprétés comme des dépôts de brèches volcaniques, tandis que le pyroclastes de P3 est un dépôt de lapilli. P4 présente des fragments de roches avec une composition minéralogique différente des autres profils suggérant un autre événement de dépôt de bombes pyroclastiques. Les éruptions associées peuvent être considérées comme stromboliennes. Les pyroclastes sont de couleur gris foncé avec certaines régions altérées rougeâtres. Les données pétrologiques et minéralogiques ont révélé un mélange de biotite, de goethite, d'ilménite, d'anatase, de magnétite, d'hématite, de pyroxène, de zéolite et d'olivine comme principaux minéraux. L'observation de lames minces par microscopie optique montre des structures vésiculaires et amygdaloïdes, avec une texture hypocrystalline et une masse vitreuse de sidéromélane qui se transforme en palagonite, indiquant clairement une éruption phréato-magmatique. Les analyses par microscopie infrarouge ont permis d'identifier la présence d'halloysite dans les zones à palagonite, suggérant l'altération du sidéromélane en minéraux tubulaires phyllosilicatés. Les amygdales et les microfractures sont partiellement ou entièrement remplies de zéolites, qui sont formées par précipitation des éléments chimiques du fluide hydrothermal issu de la percolation de l'eau qui réagit avec la palagonite. Les iddingsites et les Ti-magnétites sont présentes dans les fractures et les bords des olivines. Certains Ti-magnétites sont zonées avec un noyau riche et un bord pauvre en Cr, suggérant une origine du magma issue du manteau profond. Le diopside expliquent la haute teneur en éléments traces. Les données géochimiques montrent que les pyroclastes sont sous-saturés en silice et sont situés dans le domaine des roches ultrabasiques et les foïdites dans le diagramme de classification TAS. Le sixième chapitre porte sur l'altération des phénocristaux d'olivine dans trois profils de sol qui ont été développés sur des roches pyroclastiques de l'IT, similaires à celles étudiées dans le chapitre précédent, prélevées à différentes altitudes et degrés de développement. La microscopie optique, la microanalyse par microsonde électronique, la microscopie électronique à balayage, la diffraction des rayons X et l'analyse thermique et thermogravimétrique différentielle ont été utilisées pour déterminer la micromorphologie et les transformations géochimiques résultant du processus d'altération. Les analyses micromorphologiques ont montré des phénocristaux fracturés d'olivine incolores avec un fort relief en lumière polarisée. Ces cristaux sont euhedraux et de forme irrégulière, et distribués dans une matrice brun rougeâtre foncé composée de pyroxène, magnétite, ilménite, halloysite, hématite et anatase. En lumière polarisée, les olivines présentent une bordure d'iddingsite brun rougeâtre sur les fractures et les côtés, qui envahit progressivement les olivines jusqu'à un remplacement complet en haut du profil du sol où le degré de développement est plus élevé. Par microssonde électronique, les olivines ont été identifiées comme étant de la forsterite et l'iddingsite a une composition chimique avec Si, Fe, Mg, Al, Ca, Na, K, Mn et Ti, avec une teneur prédominante et variable en Fe, Si et Mg. La composition chimique et les caractéristiques optiques sont compatibles avec celles trouvées dans les sites d'iddingsite qui peuvent se former par l'altération des olivines due à l'oxydation du fer ferreux en fer ferrique et au lessivage du magnésium. Les caractéristiques microscopiques de l'olivine ne nous ont pas permis d'identifier les altérations antérieures par des processus deutériques ou hydrothermaux. Cependant, l'évolution du profil du sol, qui montre l'altération progressive des olivines, présente sous forme de reliques puis totalement transformées dans les horizons supérieurs, permet de conclure que l'altération est le principal processus de formation d'iddingsite. Cette découverte est corroborée par la présence d'une altération plus intense des cristaux d'olivine dans le sol situé à l'altitude la plus élevée pour la même lithologie. Les septième chapitre est une étude qui confirme la présence d'Andosols dans l'IT. La caractérisation minéralogique, micromorphologique, physique et chimique de quatre profils de sols (P1, P2, P3 e P4) a été réalisée. Les P1 et P2 ont respectivement des horizons A, Bi, C et A érodé, C; et les sols de P3 et P4 ont des horizons A et C. Les sols montrent une matrice d'argile rougeâtre et brunâtre, sont friables et ont une consistance plastique. Ses microstructures sont granulaires. Les échantillons sont constitués de simples grains et de micrograins interaggrégats et, les aggrégats sont indifférenciés. Les constituants minéralogiques sont la biotite, l'hématite, la magnétite, l'ilménite, le pyroxène, l'olivine, l'halloysite, la goethite, l'anatase et le rutile. La fraction argileuse est marquée par la présence d'halloysite, de ferrihydrite et d'allophane en petites quantités . Tous les sols présentent des propriétés andiques et peuvent être classés comme Andosols non-allophaniques. En outre, les caractéristiques micromorphologiques ressemblent aux Andosols d'autres îles volcaniques décrites dans la littérature. La prédominance de l'halloysite dans la fraction argileuse issue de l'altération du sidéromélane suggère que l'allophane serait une phase intermédiaire de cette transformation rapide favorisée par les conditions climatiques de l'IT. Le huitième chapitre montre le comportement géochimique des éléments majeurs, mineurs, traces et terres rares (TR) lors de l'évolution pédogénétique des quatre profils de sol (P1, P2, P3 et P4). Le contenu absolu des éléments chimiques a été calculé et les pertes et les gains de ces éléments ont été évalués à l'aide de l'équilibre chimique de masse pour deux profils, le P1 situé à plus haute altitude (460 m) et le P3 à basse altitude (258 m). La géochimie totale a montré que dans tous les profils, Al, Fe et Ti s'accumulent en raison de leur faible mobilité et Ca, Na, K et Mg, sont les plus intensément lixiviés. Les profils situés aux altitudes inférieures ont tendance à avoir des valeurs en K et Mg plus élevées dans l'horizon A en raison de l'influence des projections salines et du dépôt d'éléments chimiques venant des niveaux supérieurs. Dans les profils situés à 460m et 258m, les éléments Ti, Mn, Fe, Co, Cr, Ni, V, Zr, S ont été enrichis dans les sols et les augmentations de ces concentrations sont liées à la perte de poids totale liée à la perte d'éléments plus mobiles au cours du processus de formation du sol. Les teneurs plus élevées en Zn et Cu dans l'horizon A des P3 et P4 seraient une conséquence d'une plus grande quantité de complexes d'acides humiques liés à ces éléments. En outre, tous les horizons des P3 et P4 contiennent encore plusieurs fragments reliques de la roche parentale, qui pourraient contribuer à l'enrichissement en Zn et Cu. Les TR présente un enrichissement dans le profil situé à basse altitude (258 m), principalement en TR légères , en raison de la contribution des niveaux plus élevés de l'île. La normalisation des concentrations des TR sur la chondrite montre une augmentation des concentrations de TR dans tous les profils. Le P1 présente des anomalies positives en Ce plus fortes que pour les autres profils (P2, P3 et P4) en raison de l'influence plus marquée des intempéries dans ce profil. Le neuvième chapitre présente des conclusions sur l'origine et les principaux produits d'altération des pyroclastes recueillis dans le Vulcão do Paredão et la Formation Morro Vermelho. Les roches recueillies dans les dépôts pyroclastiques ont été formées au cours d'une éruption strombolienne et phréato-magmatique, et le magma a une origine mantélique d'une profondeur de moins de 50 km. Ces conclusions sont étayées par la présence de matériaux grossiers (blocs) et de palagonite dans les pyroclastes, ainsi que par la présence de spinelles avec des noyaux enrichis en Cr et un enrichissement modéré des TR dans le magma. Les principaux produits d'altération observés sont des olivines iddingsitisées, le sidéromélane palagonitisé, les zéolites et les halloysites. La première étape de l'altération se manifeste par la formation de palagonite issue de l'interaction du magma avec l'eau de mer. Au cours de cette étape, l'altération de sidéromélane en palagonite est associée à la perte des éléments chimiques Na, Ca et Mg et à un enrichissement en Fe. Après refroidissement total de la roche, une deuxième étape d'altération est provoquée par l'interaction de l'eau météorique avec les pyroclastes, ayant pour conséquence une deferruginisation des zones palagonitisées (palagonites blanches), la formation de zéolite sur les bords des palagonites et d'halloysite dans les zones palagonitisées, et l'altération des olivines en iddingsites composés d'hématites et de goethites. La transformation des pyroclastes en sol est marquée par la présence de minéraux secondaires tels que l'halloysite, la goethite, l'hématite, le rutile, l'anatase, la ferrihydrite et quelques allophanes. Ces sols présentent des propriétés andiques et peuvent être classés comme Andosols non-allophaniques du fait de la présence prononcée d'halloysite et de complexes humiques d'Al. La faible quantité d'allophane pourrait s'expliquer par la transformation rapide de l'allophane en halloysite en raison des conditions climatiques de l'IT. Dans les profils d'altitude élevée et basse, les éléments Ti, Mn, Fe, Co, Cr, Ni, V, Zr, S sont accumulés dans les sols et les augmentations de leurs concentrations sont liées à la perte de poids totale par la perte d'éléments plus mobiles pendant le processus de formation du sol. Zn et Cu se concentrent sur l'horizon A des profils qui présentent une plus grande concentration de matière organique et qui conservent des fragments de pyroclastes inchangés. Les TR, principalement les TR légères, sont enrichies dans le profil de basse altitude, du fait de la contribution des apports en éléments venant des altitudes plus élevées. Le profil de haute altitude a montré une anomalie positive en Ce due à une exposition plus longue aux intempéries.

Présentation

Cette recherche présente des études sur les systèmes d'altération et la genèse des sols dans les pyroclastes de l'Île de Trindade, Atlantique Sud. Cette étude a été divisée en chapitres qui présentent les étapes méthodologiques, les résultats et les principales conclusions obtenues.

- **Chapitre 1**: présente le thème abordé, les problèmes à étudier, la question directrice, les objectifs du travail et et l'emplacement d'étude.

- **Chapitre 2 e 3**: présentent le fondement théorique qui a guidé l'élaboration des travaux, en mettant l'accent sur l'examen du contexte géologique et géomorphologique de la zone d'étude et sur l'état actuel des changements dans les îles océaniques, respectivement.

- **Chapitre 4** : présente les méthodes utilisées lors de la recherche.

- **Chapitre 5**: présente la caractérisation macro et micromorphologique, minéralogique et chimique des pyroclastes et de leurs produits d'altération, recueillis à 3 points à différentes altitudes de l'Île Trindade.

- **Chapitre 6** : discute de l'iddingsitisation des olivines trouvées dans ces pyroclastes.

- **Chapitre 7**: présente la caractérisation des sols par l'altération des pyroclastes et la découverte de la présence d'Andosols non allophaniques sur l'Île de Trindade.

- **Chapitre 8**: montre l'évolution géochimique des pyroclastes vers le sol.

- **Chapitre 9**: présente la synthèse des conclusions obtenues dans ce travail.

CONSIDÉRATIONS GÉNÉRALES

1.1– INTRODUCTION

Au Brésil, la situation géopolitique et économique au cours des trois dernières décennies, a soutenu une grande incitation à la recherche scientifique dirigée au domaine maritime national, y compris les cinq îles océaniques: Trindade et Martin Vaz, Abrolhos, Fernando de Noronha, Atol das Rocas et São Pedro et São Paulo. Les efforts déployés par le gouvernement fédéral, la Marine et les enterpreneurs brésiliens ont été rassemblés pour créer des programmes d'incitation à la recherche sur des îles comme le PROTRINDADE, pour Trindade et Martin Vaz et le PROARQUIPÉLAGO, pour São Pedro et São Paulo. Ce territoire comprend une surface de 3.6 millions de km², avec une richesse de biodiversité qui assure le surnom de Amazon Blue.

Des recherches menées dans les îles océaniques brésiliennes jusqu'à ce jour, correspond la pluspart à des études sur la flore et la faune marines, trois peut sur les milieux terrestres. Dont se détachent les études développées par Almeida (1955, 1961, 1965) relatifs à la géologie et Alves (1998, 2006) sur la botanique. D'autres contributions pertinentes à la géologie sont Milet-Mureau (1797) apud Almeida (1961), Prior (1900), Veltheim (1950), Soares (1964), Cordani (1970) et Weaver (1990). En ce qui concerne les sols, la recherche se révèle encore plus rares, étant connu les travaux de Batistela (1993) et Marques (2004) sur les sols du Fernando de Noronha; Paul Vageler (Veltheim 1950), Clément (2006), Clement *et al*. (2006, 2009, 2011) et Sá (2010) sur les sols de la Trindade; Oliveira (2008) sur la São Pedro et São Paulo, et l'île Rata à Fernando de Noronha. Cette lacune souvent responsable de la mauvaise gestion de ces environnements de connaissances, indique un défi à être surmonté.

En général, la plupart des études sur les sols de l'îles océaniques (Cardoso 1958, Nunes 1962, Faria 1974, Lima 2003, Marques 2004) a montré que la plupart de ces singularités et endémisme sont liés à l'association entre les caractéristiques le sol et le matériau source, le plus souvent de nature volcanique. Cette association représenterait la prédominance des sols plus jeunes et même lorsqu'il est profondément altéré, en conservant de nombreuses caractéristiques du matériau source, ce qui est commun. Pour ces raisons, l'avance dans la compréhension des milieux terrestres dans les îles océaniques du Brésil et par conséquent leurs sols, imprègne la nécessité d'élucider la façon dont se produit la transformation du cadre géologique diversifié dans leurs manteaux d'altération respectifs, compte tenu des modifications chimiques, minéralogiques et morphologiques impliqués.

1.2 – QUESTION DE GUIDAGE

Les résultats jusque-là obtenus sur l'Île de Trindade (Clemente 2006, Clemente *et al.* 2006; Schaefer 2010, Oliveira 2008), suggèrent que l'interaction entre les roches, le climat, le relief, les organismes et le temps, occur d'une façon tout à fait atypique dans les îles océaniques. Cela parce que, du point de vue géologique, climatique et biologique, ces milieux présentent des caractéristiques uniques de formation et d'évolution; tout en étant assez récente dans le temps et géologique, souffrent l'influence directe de l'ocean. En conséquence, sont observés des sols hautement différenciés par rapport à ceux trouvés dans les continentes. Dont ont été reconnu dans les préceptes de Bockheim (2005), comme étant endémiques; soulignant la nécessité de les étudier d'une façon approfondie (Cardoso 1958, Pissarra *et al.* 1965, Faria 1974). L'endémisme des sols se manifeste à la fois par l'existence des classes (types) difficiles à classer par le système de classification adopté au Brésil, lorsque la présence de certaines classes seulement ont été vérifiés sur les îles océaniques, compte tenu de tout le territoire national. De plus, l'Île de Trindade présente des sols enrichis en minéraux inhabituels dans les régions tropicales, y compris des alophanes et d'autres types d'argiles. Jusqu'à présent, peu est connu sur la genèse et l'évolution des ces espèces minéraux secondaires sur l'Île de Trindade, insi que leur relation avec le changement de microsystèmes associés. Ces questions constituent l'objet de cette étude.

1.3 – OBJECTIFS ET BUTS

1.3.1- Objectif général

Cette étude vise à étudier les microsystèmes d'altération associés aux roches volcanoclastique de l'Île de Trindade, à comprendre leur évolution chronologique et à mettre en évidence les transformations minéralogiques, géochimiques et morphologiques impliquées.

1.3.2- Objectifs spécifiques

- Identifier et caractériser les principaux produits de l'altération et établir leur affiliation lithologique;

- Comprendre la genèse et l'évolution des principales espèces minérales secondaires, en mettant l'accent sur les minéraux non cristallines et les minéraux argileux;

- Évaluer les principales transformations morphologiques et géochimiques des compositions minérales primaires (roche) et secondaires (manteau d'altération), identifier et relier les modèles et les degrés d'altération minérale et;

- Confirmer la présence d'Andosols sur l'Île de Trindade.

1.4 – LOCALISATION

L'Île de Trindade, d'une surface de 13 km^2, appartient à l'État d'Espírito Santo et est située dans l'Atlantique Sud à 1140 km de la côte brésilienne (**Figure 1.1**) à des coordonnées de 20 '31'30' S, 29'19'30' O. L'île fait partie d'une vaste chaîne volcanique sous-marine orientée est-ouest, appelée Vitória-Trindade, et constitue la partie supérieure d'un bâtiment volcanique de plus de 5,2 km de haut. Selon Alves *et al.* (2006), l'extension à l'ouest de la zone de fracture Vitória-Trindade sur la rive continentale correspond à l'alignement Vitória-Trindade (**Figure 1.2**).

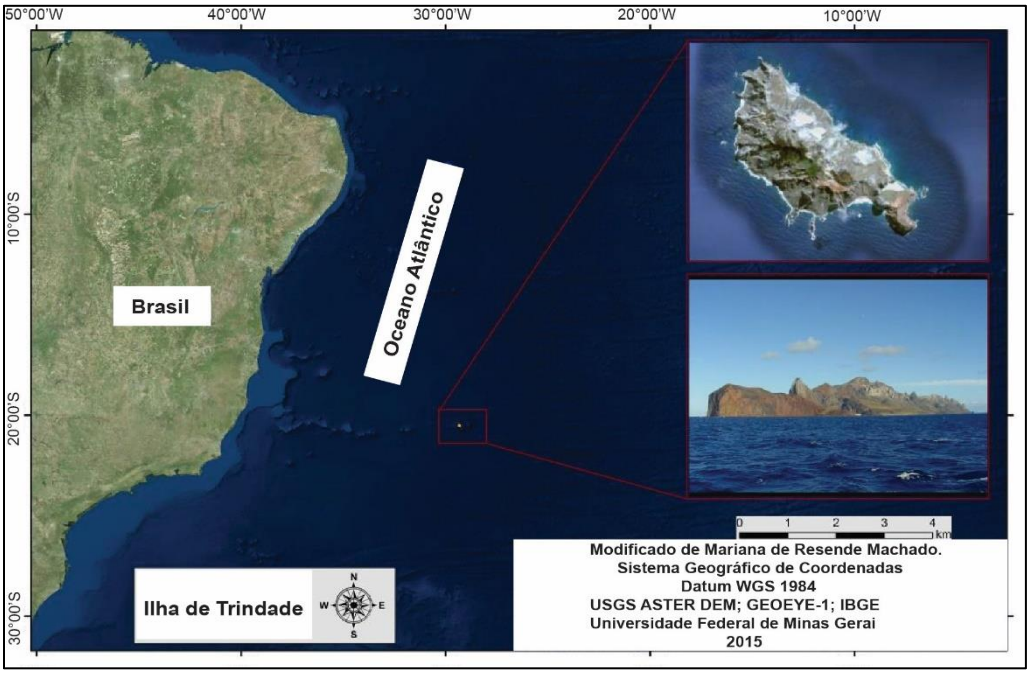

Figure 1.1: Representação espacial da Ilha de Trindade (Brasil).

Figure 1.1: Représentation spatiale de l'Île de Trindade (Brésil).

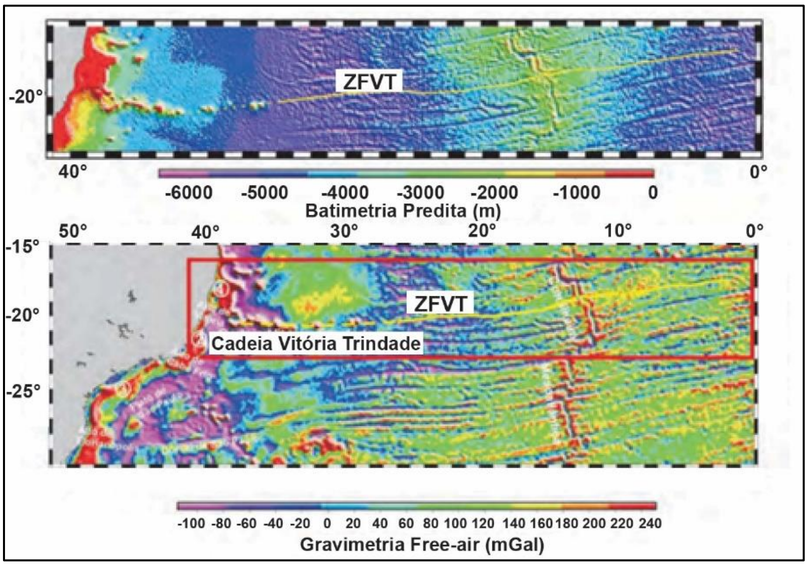

Figure 1.2: Mapas de batimetria e gravimétrica Free-air mostrando localização do Lineamento Vitória-Trindade como continuidade da Zona de Fratura Vitória-Trindade. Fonte: Alves *et al*. (2006).

Figure 1.2: Cartes de Bathymetry et Gravimetric Free-air montrant l'emplacement de la ligne Vitória-Trindade comme continuité de la zone de fracture Vitória-Trindade (ZFVT). Le NNW de l'élinage apparaît la Banque d'Abrolhos (1). Source : Alves *et al*. (2006).

L'accès à l'Île de Trindade est donné par des expéditions scientifiques d'une durée moyenne de 3 jours par bateau grâce à l'accord avec la Marine Brésilienne.

CHAPITRE 2

ASPECTOS FISIOGRÁFICOS E CONTEXTO GEOLÓGICO

2.1 – CLIMA E VEGETAÇÃO

Segundo Soares (1964) a Ilha de Trindade apresenta clima do tipo oceânico tropical com temperatura média de 25 °C, sendo o mês de fevereiro o mais quente (30 °C) e o de agosto o mais frio, com temperatura em torno de 17 °C. Está sob o domínio dos ventos alísios de sudeste (Almeida 2002). A pluviosidade média anual é baixa (924 mm), com duas estações anuais, uma seca nos meses de janeiro a março, e outra úmida nos meses de julho a agosto (Sá 2010). De acordo com Clemente (2006b) a ilha apresenta microclimas variados em diferentes posições topográficas. Nas partes mais baixas e secas do setor norte da ilha predomina um microclima semelhante ao semi-árido e nas regiões mais altas, a partir de 400 metros de altitude, o clima é mais úmido com chuvas orográficas.

De acordo com Almeida (2002) a Ilha da Trindade apresenta vegetação do tipo campestre, com ervas, gramíneas e ciperáceas nas regiões baixas e superfícies do vulcanismo ankaratrítico nas regiões de piroclastos do platô axial. Também são encontradas vegetação arbórea como samambaias gigantes de até 6 m (**Figura 2.1**) de altura e comunidades de fetos arborescentes gigantes (*Cyathea trindadensis*) nas vertentes dos morros fonolíticos. Em estudos de uma topossequência da Ilha, Clemente *et al*. (2009) encontraram a espécie endêmica *Cyperus atlanticus* consideradas do tipo rasteira; e nas altitudes mais elevadas, vegetação de maior densidade com destaque das espécies *Myrsine floribunda*, com cobertura herbácea mista de *Pytyrogramma*, *Cyperus*, Bulbostyls e nas regiões onde não existe erosão aparente, indivíduos jovens de *Cyathea*.

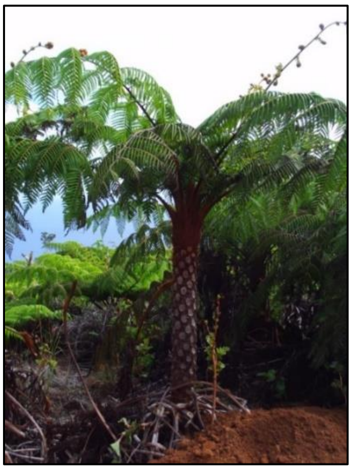

Figura 2.1: Espécie de samambaia gigante (*Cyathea trindadensis*) no domínio da Sequência Desejado.

Figure 2.1: Espèces de fougères géantes (*Cyathea trindadensis*) dans la domination de la Séquence Desejado.

2.2 – GEOMORFOLOGIA

Castro (2010) descreveu os aspectos geomorfológicos da ilha de Trindade através de um conjunto de formas diferenciadas caracterizadas por: Domínio Planalto Axial (Almeida 1961); Domínio de Vertentes Costeiras (Almeida 1961 apud Castro & Antonello, 2006) e; Domínio Litorâneo (Castro & Antonello, 2006).

2.2.1- O Domínio do Planalto Axial

São encontradas as maiores elevações da ilha, onde se originam todos os cursos de água importantes, assim como numerosas incisões que drenam as escarpadas vertentes (**Figura 2.2**). Esse domínio é formado por derrames fonolíticos, graziníticos e nefeliníticos, intercalados em tufos. O planalto apresenta elevação acima de 350 m com um relevo de morros separados por profundos vales. No centro da ilha ocorrem cristas elevadas que correspondem aos principais divisores de águas. Essas cristas apresentam-se sustentadas em derrames fonolíticos constituídas pelos picos do Desejado (600 m), Trindade (590 m), Verde (553 m), São Bonifácio (570 m) e Grazinas (477 m).

Figura 2.2: Derrames fonolíticos da Sequência Desejado em região de maior elevação da Ilha de Trindade.

Figure 2.2: Déversements phonolytiques de la Séquence Desejado dans la région de plus haute altitude de l'Île de Trindade.

2.2.2- Domínio de Vertentes Costeiras

Ocorrem superfícies rochosas abruptas que descem ao mar, das quais se erguem os picos fonolíticos (Almeida 1961 apud Castro & Antonello 2006). Outra feição morfoestrutural da ilha é o Vulcão do Paredão formado por ruínas de um edifício vulcânico alto (acima de 200 m), semidestruído pelo mar. A sul, são encontrados paredões de tufos, falésias verticais com altura de aproximadamente 200 m (**Figura 2.3**); a oeste, as vertentes voltadas para os morros fonolíticos caem suavemente, em quase perfeita coincidência com a superfície original do cone vulcânico. Os declives caracterizam-se, em geral, por escarpas abruptas, principalmente na face voltada para o quadrante sudoeste. A rede de drenagem caracteriza-se por caráter torrencial de mediana competência. A periodicidade do fluxo é limitada ao período chuvoso. Na estação seca, as vazões dos córregos são pouco expressivas.

Figura 2.3: Paredão de tufos provavelmente da Sequência Desejado.

Figure 2.3: Mur de touffe probablement de la Séquence Desejado.

2.2.3- Domínio Litorâneo

Reflete de certa forma, a resistência da estrutura em que se estabeleceu. As saliências, geralmente, acham-se suportadas por rochas eruptivas que se destacam no traçado geomorfológico. As mais proeminentes pontas são caracterizadas por grandes corpos fonolíticos, diques, como ocorrem nas pontas da Crista do Galo, Cinco Farilhões, Sul e Noroeste. Destacam-se também antigos condutos vulcânicos (*necks*) constituídos pelo morro Pão de Açúcar (392 m) e as pontas do Príncipe e Monumento

(Castro & Antonello 2006). A plataforma de abrasão esculpida pela ação marinha é relativamente estreita e descontínua, destacando o baixo Sueste como a mais expressiva. As pontas do Túnel e Paredão (**Figura 2.4**) participam da mais destacada saliência do litoral da Trindade.

Figura 2.4: Ponta do Vulcão do Paredão que resistiu a erosão marinha.

Figure 2.4 : Pointe du Volcan do Paredão qui a résisté à l'érosion marine.

2.3 – GEOLOGIA REGIONAL

A Ilha de Trindade é formada por cinco episódios vulcânicos de derrames e intrusões de rochas subsaturadas em sílica com acentuado teor sódico-alcalino. Estes episódios vulcânicos foram descritos por Almeida (1961 *apud* Castro & Antonello 2006) da base para o topo: Complexo de Trindade, Sequência Desejado, Formação Morro Vermelho, Formação Valado e Vulcão do Paredão (**Figura 2.5**). Sobre os derrames vulcânicos ocorrem os depósitos holocênicos que representam uma pequena parcela das unidades estratigráficas ocorrentes na ilha (Castro & Antonello 2006) (**Figura 2.5**). Tais derrames vulcânicos e depósitos holocênicos são descritos a seguir.

2.3.1- Complexo Trindade

O Complexo Trindade constitui o episódio vulcânico mais antigo de Trindade e está presente

na maior parte da ilha (**Figura 2.6**). É um conjunto heterogêneo de rochas piroclásticas variadas associadas principalmente ao vulcanismo fonolítico (Almeida 2006). Os piroclastos são recortados por diques de composição nefelinítica, fonolítica, olivina analcítica, analcita basanítica, gauteítica e outros. Recentemente Pires *et al.* (2016) fizeram datações radiométricas por $^{40}Ar/^{39}Ar$ e identificaram que o pico da atividade vulcânica fonolítica-nefelinítica ocorreram entre 3.9 e 2.5 M.a. Os grandes volumes de depósito vulcânico preservados na ilha apresentaram idades entre 3.0 e 2,5 M.a.

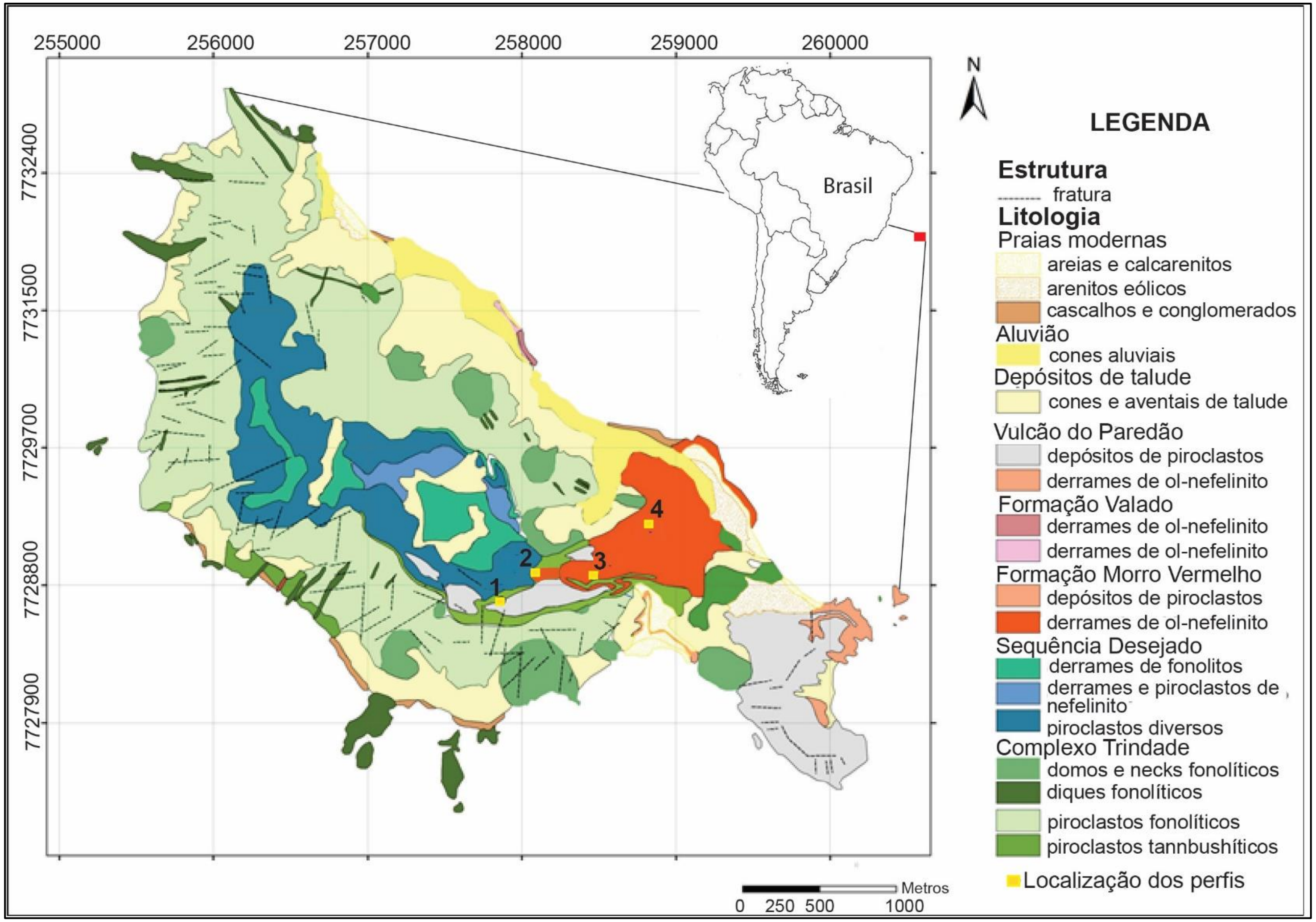

Figura 2.5: Mapa Litológico da Ilha de Trindade. Modificado de Patrício (2012).

Figure 2.5: Carte lithologique de l'Île de Trindade. Modifiée de Patrício (2012).

Figura 2.6: Fonolitos e nefelinitos do Complexo Trindade. Fonte: Clemente (2006a).

Figure 2.6: Phonolites et néphélinites du Complexe Trindade. Source: Clemente (2006a).

2.3.2- Sequência Desejado

Sobre a superfície de erosão do Complexo de Trindade ocorre a Sequência Desejado constituída de derrames de fonolitos e nefelinitos intercalados com camadas de piroclastos da mesma composição (**Figura 2.2**). De acordo com Pires *et al*. (2016), esse vulcanismo apresenta entre 2.5 M.a a cerca de 1.6 M.a.

2.3.3- Formação Morro Vermelho

A Formação Morro Vermelho ocorre no alto vale do Córrego Vermelho, região central da ilha, como resultado de uma erupção explosiva de lavas ankaratríticas (variedade melanocrática de olivina nefelinito com biotita) (**Figura 2.7**). Cordani (1970) indica que as erupções não seriam mais antigas que 170.000 anos.

2.3.4- Formação Valado

No litoral norte da ilha entre as praias dos Cabritos e dos Portugueses ocorrem depósitos do grande cone aluvial do córrego do Valado contendo intercalações de piroclastos e derrames de lava tannbushíticas (olivina-nefeliníticas) (**Figura 2.8**). A erupção aparentemente se processou a partir de

uma fenda situada a meia encosta, paralela à costa atual, em sítio onde existem diversos diques de tannbushito (olinvina-nefelinito) de estrutura escoriácea (Almeida 2002). Tendo em vista a geomorfologia da ilha, Almeida (2002, 2006) supõe uma idade pós-glacial ao vulcanismo Valado.

Figura 2.7: Lavas ankaratríticas erodidas da Formação Morro Vermelho. Fonte: Clemente (2006a).

Figure 2.7: Laves ankaratritiques érodées de la Formation Morro Vermelho. Source: Clemente (2006a).

Figura 2.8: Tannbuchitos da Formação Valado. Fonte: (Clemente 2006a).

Figure 2.8: Tannbuchites de la Formation Valado. Source: (Clemente 2006a).

2.3.5- Vulcão do Paredão

O vulcão do paredão localiza-se na porção oriental da ilha (**Figura 2.4**). Segundo Almeida (2002) este vulcão testemunha a última erupção na ilha e derradeira atividade magmática em território brasileiro. O cone do vulcão é formado pelo acúmulo de piroclastos variados como tufos lapilíticos e cineríticos contendo bombas rotacionais, blocos, agregados e aglutinados de lava melanefelinítica, basanítica e tefrítica. As datações geocronológicas realizadas por Pires *et al.* (2016) registraram idades de 0.25 M.a. para os depósitos vulcânicos do Vulcão do Paredão. De acordo com Pires *et al.* (2016) esse evento representa a atividade vulcânica mais recente do território brasileiro.

2.3.6- Depósitos Holocênicos

De acordo com Castro & Antonello (2006) os depósitos holocênicos são representados pelos depósitos eólicos, praias, aluviões, recifes algálicos e depósitos de encosta (**Figura 2.9**). Os depósitos eólicos escalonares (dunas) são provenientes das contribuições exclusivas de tufos vulcânicos, materiais piroclásticos e recifes algálicos (Castro 2010).

Figura 2.9: Depósitos de praias e depósitos de encostas na Praia do Príncipe.

Figure 2.9: Dépôts de plages et de dépôts à flanc de colline sur la Praia do Príncipe.

CHAPITRE 3

ESTADO DA ARTE: SISTEMAS DE ALTERAÇÃO EM ILHAS OCEÂNICAS

3.1 – AS ROCHAS PIROCLÁSTICAS BÁSICAS E SEUS PRODUTOS DE ALTERAÇÃO

As rochas piroclásticas são rochas vulcanoclásticas formadas pela fragmentação em consequência das erupções vulcânicas ou dos processos explosivos, sendo que os fragmentos podem ser de cristais individuais ou fragmentos de cristais, vidro vulcânico ou rocha. Os piroclastos podem ser distinguidos pelo seu tamanho como bombas e blocos (> 64 mm), lápilis (entre 64 mm e 2 mm), e grãos de cinzas (< 2mm); e os depósitos piroclásticos como aglomerados (quantidade de bombas maior que 75 %), brechas piroclásticas (quantidade de blocos maior que 75 %), brechas de tufos (quantidades de bombas e/ou blocos entre 25 % e 75 %), tufos de lápilis (quantidade de bombas e/ou blocos menor que 25 %, e ambos lápilis e cinzas menor que 75%), *lapillistone* (quantidade de lápilis maior que 75 %), tufos ou tufos de cinza (quantidade de cinza maior que 75 %), (Le Maître *et al*. 2002).

Através do mundo os depósitos piroclásticos de composição máfica e ultramáfica são comumente encontradas em ilhas vulcânicas e alguns exemplos podem ser encontrados na Ilha de Santa Maria/Açores (tufos hidromagmáticos basáltico, Larrea *et al*. 2018); no monte marinho Loihi /Hawaí e em Ilha Isabela/Galápagos (piroclastos de composição toleítica; Clague *et al*. 2003 e Reynolds & Geist 1995); Ilha de Trindade e de Fernando de Noronha (piroclastos de melanephelinitos; Almeida 2006).

Os piroclastos de composição ultramáfica descritos nas ilhas oceânicas apresentam em sua composição, vidro vulcânico do tipo sideromelano e minerais como olivina, piroxênios, anfibólios e feldspatóides. Como principais produtos de alteração são encontrados zeólitas, palagonita e iddingsita (Antonello *et al*. 2009).

Em erupções vulcânicas marinhas o sideromelano altera-se para palagonita através da interação com a água do mar em temperatura ambiente (Peacock 1926, Moore 1966), mas também podem se formar pela interação da água meteórica (Hay & Iijima 1968) após a consolidação do magma. Von Waltershausen (1845) foi o primeiro a descrever a palagonita como uma substância resinosa transparente e de coloração amarela e marrom em vidros basálticos alterados e hialoclastitos na região da Palagônia (Sicília). Mais tarde Peacock (1926) distinguiu a palagonita em duas variedades – gel-palagonita e fibro-palagonita. A palagonita é um material heterogêneo composto de argilominerais (esmectitas, caulinita, ilitas), zeólitas, óxidos (hematita, ilmenita) e hidróxidos (goethita, gibbsita), gipsita, apatita (Peacock &

Fuller 1928, Eggleton & Keller 1982, Furnes 1984, Jercinovic *et al.* 1990, Zhou *et al.* 1992, Daux *et al.* 1994, Stroncik & Schmincke 2001) e durante sua formação ocorre a oxidação do Fe, aumento de H_2O, e perda de CaO, Na_2O, SiO_2 e Al_2O_3 (Peacock 1926, Correns 1930, Moore 1966, Hay & Iijima 1968).

Zeólitas são comumente encontradas como produtos de alteração em depósitos piroclásticos máficos. Nesses depósitos elas provêm da alteração do sideromelano e os tipos mais comuns de serem encontrados são philipisitas e chabazitas devida a baixa quantidades de sílica, mas natrólita, gornadita, analcima e outras zeólitas de baixa sílica também podem aparecer, (Sheppard & Hay 2001). Alterações de sideromelano para zeólitas foram descritas em tufos palagonitizados de Oahu, Havaí (Hay & Iijima 1968, Iijima & Harada 1969) e Islândia (Nayudu 1964). De acordo com Kristmannsdóttir & Tómasson (1978), heulandita, stilbita e analcima podem se formar em temperaturas abaixo de 100°C. Barrows (1980) descreveu heulandita, clinoptilolita, mordenita, analcima, thomsonita, erionita e chabazita em grossas sequências vulcânicas em Nevada atribuídas a um processo que envolve a circulação de líquido meteórico de baixa temperatura em um sistema hidrológico aberto.

Outro tipo de feição de alteração encontrado em piroclastos de composição máfica é olivina iddingsitizada. Os primeiros estudos sobre a iddingsita foram retratados por Lawson (1893) em rochas basálticas da região da Califórnia. Lawson (1893), descreveu iddingsita como uma substância macia, frágil, com clivagem bem desenvolvida e em microscopia óptica, mostram cores variando de marrom a amarelo claro com pleocroismo pronunciado em posição transversal para sua clivagem. Ross & Shannon (1925) e Edwards (1938) propuseram que a iddingsita seria formada durante e após a consolidação do magma. Através de análises DRX, Sun (1957) mostra que a iddingsita é um produto complexo de alteração da olivina e não um único mineral. Haggerty & Baker (1967), Champness (1970), Goode (1974) e Gualtieri *et al.* (2003) observaram a formação de hematita, magnetita e ortopiroxênio durante experimentos de oxidação de alta temperatura em olivina. Além disso, vários autores estudaram iddingsita de alta temperatura (IAT) com composição semelhante (ortopiroxênio, magnetita, hematita, cristobalita e sílica amorfa) dentro de fluxos de basalto continentais e oceânicos (Goff 1996, 1977; Caroff *et al.* 2000, 1999, 1997) e em intrusões gabróicas (Clément *et al.* 2007). A iddingsita de baixa temperatura (IBT) apresenta composição diferente das de IAT, uma mistura íntima de silicatos de ferro hidratado e magnésio (goethite, montmorillonita, illite, clorite) como descrito por Gay & Le Maître (1961), Fawcett (1965), Le Maître *et al.* (1966), Baker & Haggerty (1967), Schandl *et al.* (1990), Schenato *et al.* (2003), Talbi & Honnorez (2003). Gay & Le Maître (1961) descreveram o padrão de DRX de várias fases que ocorrem em IBT: como estruturas de olivina, goethita, hematita, espinélio e outros silicatos. Baker & Haggerty (1967), observaram que a alteração em condições oxidantes a baixa temperatura, provavelmente abaixo de 140 °C, produz iddingsita com goethita e esmectita. Delvigne *et al.* (1979) também propôs que a iddingsita é composta por uma mistura de goethita criptocristalina e possivelmente hematita, com esmectita, clorita, micas e raramente talco. Talbi & Honnorez (2003)

descreveram um material laranja ou avermelhado com composição intermediária entre oxihidroxidos de ferro e filosilicatos, quimicamente semelhante a iddingsita, em basaltos toleíticos que foram afetados pela alteração de baixa temperatura. Através da microscopia eletrônica de transmissão, Eggleton (1984) mostrou saponitas e goethitas em iddingsitas de basaltos na Alemanha. Gerard *et al.* (2007) descreveram a presença de iddingsita em piroclastos basálticos nas ilhas Faial e Pico (Açores). Nas ilhas vulcânicas do território brasileiro, especificamente na Ilha de Trindade, objeto deste estudo, Antonello *et al.* (2009) descreveram rochas de composição basáltica com olivina parcialmente ou totalmente alterada para serpentina, carbonatos e iddingsita. Estudos recentes realizados em meteoritos com olivina (Kuebler 2013, Lee *et al.* 2015) mostraram iddingsita formada durante os estágios finais da consolidação do magma.

3.2 – OS SOLOS DE ILHAS OCEÂNICAS BRASILEIRAS

3.2.1- Arquipélago de Fernando de Noronha

No Atlântico Sul, o arquipélago brasileiro de Fernando de Noronha localiza-se entre as coordenadas 3°50’ e 3°52’ de Latitude Sul e 32°24’ e 32°58’de Longitude Oeste de Greenwich. O Arquipélago é formado por um conjunto de 21 ilhas e 20 ilhotas, sendo que a ilha principal, com 17.6 km^2 de extensão, recebe o mesmo nome do arquipélago.

Em relação à geologia, Almeida (1955) descreveu as seguintes unidades: Formação Remédios, Quixaba e São José e outras rochas sedimentares.

A Formação Remédios localiza-se principalmente na região central da ilha e em sua extremidade ocidental. Também formam as falésias e os blocos rochosos das praias. A Formação Remédios é formada por rochas piroclásticas atravessadas por plugs e diques que representam o penúltimo ciclo vulcânico presente no arquipélago de Fernando de Noronha. Essas rochas apresentam idades entre 12 e 8 milhões de anos. Após um período erosivo com duração de 5 a 6 milhões de anos, ocorreu uma reativação vulcânica produzindo basaltos que recobriram a maior parte das rochas do ciclo anterior. Junto a esta fase ocorreram episódios explosivos menores que deram origem às rochas piroclásticas da Formação Quixaba.

A ilha São José e parte das ilhas Cuscus e de Fora são encontrados derrames de nefelina basanito da Formação São José. Esta formação não é encontrada na ilha principal de Fernando de Noronha.

Os depósitos sedimentares são encontrados em menos que 7.5 % do Arquipélago de Fernando de Noronha e segundo Teixeira *et al.* (2003) correspondem a antigos depósitos eólicos, formados por areia de praia constituída de fragmentos de conchas, de ouriços, corais, algas e poucos minerais

silicáticos ou metálicos ou, ainda de raros fragmentos vulcânicos. Os registros sedimentares mais antigos são do período Pleistoceno, entre 1.8 milhões e 10 mil anos atrás.

O primeiro pesquisador a fazer referências ao solo do Arquipélago foi Almeida (1955). Mais tarde, Jacomine *et al.* (1969) realizaram estudos em nove perfis de solos e constataram uma elevada fertilidade natural para os solos de Fernando de Noronha e a dominância de Cambissolos na porção central da ilha principal. Segundo Mantovani *et al.* (1991), o Arquipélago de Fernando de Noronha apresenta para a formação de solo, condições bastantes distintas das que são encontradas no continente, devido a peculiaridades como o material de origem vulcânica, o relevo movimentado, o clima tropical com estação seca bem definida, além da intensa e constante influência do oceano Atlântico. Montovani *et al.* (1992) relataram a associação de Cambissolos e solos litólicos às rochas ankaratríticas. Ribeiro *et al.* (2003) e Marques *et al.* (2003) descreveram perfis de solos poucos evoluídos pertencentes às classes dos Cambissolos, Vertissolos e Neossolos.

Segundo Marques (2004) os solos mais desenvolvidos do Arquipélago são os Cambissolos Háplicos que ocorrem próximos aos divisores de água ou no terço inferior dos morros fonolíticos, associados a rochas basálticas, fonolíticas e ankaratríticas. Os solos menos intemperizados, os Vertissolos, estão associados às áreas abaciadas, deprimidas, imperfeitamente drenadas e possuem como material de origem o saprolito das rochas piroclásticas e dos tufos da Formação Remédios.

Os Neossolos ocorrem nas encostas e em áreas de sedimentos quaternários, próximas do mar e apresentam distintos materiais de origem que compreendem desde rochas ígneas vulcânicas básicas (ankaratritos) até sedimentos psamíticos carbonáticos de natureza marinha. De acordo com Marques (2004) os Neossolos da Ilha de Fernando de Noronha não puderam ser enquadrados na classificação do SiBICS por apresentarem características incomuns às existentes nos solos do continente e também pela ausência de termos apropriados que pudessem atender às características desses solos. Este autor sugeriu ao SiBICS a inclusão do grande grupo Neossolo Litólico Fragmentário e do Neossolo Regolítico Psamítico carbonático-bioclástico.

No extremo nordeste do Arquipélago de Fernando de Noronha localiza-se a Ilha Rata. Nesta ilha, Oliveira (2008) realizou o levantamento de quatro perfis de solos que foram classificados como Neossolos e Cambissolos. Segundo Oliveira (2008) os Neossolos localizam-se preferencialmente nas partes baixas da ilha, em terraço marinho soerguido carstificado e tem como material de origem os carstes arenitos calcíferos da Formação Caracas. Os Cambissolos por sua vez se originam das lavas ankaratríticas da Formação Quixaba e dos calcarenitos que ocorrem sobre os ankaratritos. Oliveira (2008) ainda relata que estes solos sofreram processo de fosfatização que se relacionam à ocupação da maior parte da ilha por ninhais, em condições de clima seco, com vegetação de menor porte e solos menos erodidos. Em consequência os solos se tornaram ricos em P e minerais fosfáticos.

3.2.2- Arquipélago de São Pedro e São Paulo

O arquipélago de São Pedro e São Paulo (ASPSP) localiza-se no Atlântico Norte em aproximados 1000 km de distância da costa brasileira. É formado por dez ilhas e diversas saliências rochosas que se situam próximas à Dorsal Meso-Atlântica (Oliveira 2008).

Segundo Campos *et al.* (2005) as rochas formadoras do embasamento do ASPSP são peridotitos que em maior parte apresentam-se serpentinizados por fluxos hidrotermais. Apenas na Ilha Belmont são encontrados alguns locais que não sofreram processo de serpentinização. Campos *et al.* (2003) apresentam duas Unidades fundamentais de caráter bio-litoclásticas para a Formação São Pedro e São Paulo: a Unidade Atobás formada por conglomerados e a Unidade Viuvinhas formada por arenitos.

De acordo com Oliveira *et al.* (2008) estão depositados abundantes excrementos de aves sobre as rochas do ASPSP. Esses excrementos são enriquecidos em fósforo e estão diretamente relacionados com o intemperismo dos peridotitos. Segundo Oliveira *et al.* (2008) ocorrem associados aos peridotitos produtos de fosfatização como crostas, espeleotemas, fosfatos percolados, coberturas esverdeadas, guano e solos fosfatizados.

Na porção oeste da elevação do Morro do Farol as crostas fosfáticas ocorrem associadas aos peridotitos milonitizados sem serpentinização. A composição química dessa crosta está relacionada aos elementos químicos dos dejetos animais e não à rocha subjacente.

Os espeleotemas ocorrem nas bordas e no interior das fraturas dos peridotitos, associados ou não às crostas fosfáticas. Os espeleotemas fosfáticos são formados através da percolação de soluções ricas em fósforo. Os fosfatos percolados contribuem na gênese dos espeleotemas e tem como mecanismo propursor para sua formação as fraturas existentes nos peridotitos milonitizados e serpentinizados.

As coberturas esverdeadas apresentam-se relacionadas ao saprolito de algumas amostras de peridotito serpentinizado. Esta crosta seria formada através da interação geoquímica com o saprolito e não somente por acumulação superficial de excrementos das aves. O guano apresenta-se na forma de depósitos muito pouco espessos, localizados em posições abaciadas da ASPSP. Estes são formados por apatitas biogênicas e fragmentos de rochas.

Em relação aos solos, Oliveira *et al.* (2008) encontraram alguns “bolsões” que se localizam em algumas regiões da Ilha Belmonte. Estes são entendidos como produtos indiretos do intemperismo dos peridotitos e alguns se relacionam com restos de material de construção que foram submetidos a processos pedogenéticos e, portanto, apresentam requisitos necessários à sua classificação como solo. Estes solos são fosfatizados pela constante deposição de excrementos das aves.

3.2.3- Ilha de Trindade

Estudos pedológicos preliminares foram realizados por Paul Vageler (Veltheim 1950) na expedição “João Alberto” em 1950. Mais tarde Clemente (2006) e Clemente *et al*. (2006a, 2006b, 2009, 2011) realizaram estudos mais detalhados em uma topossequência que não abrange todo o território da ilha. Neste trabalho foi realizado um esboço preliminar da classificação de solos onde foram registradas 4 ordens: Neossolos, Nitossolos, Cambissolos e Organossolos. Dentre esses solos alguns não existem no continente: os Cambissolos Hísticos de rochas alcalinas e os Organossolos associados a florestas monodominantes de Samambaias Gigantes (*Cyathea sp.*).

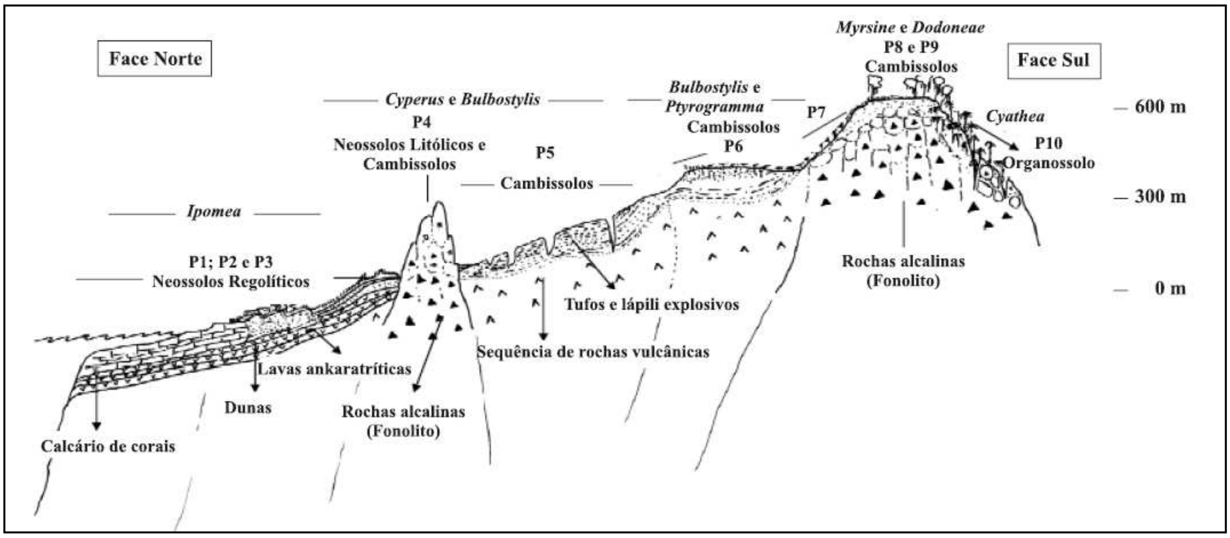

Figura 3.1: Topossequência estudada por Clemente *et al.* (2009) que indica os 10 perfis de solo posicionados em relação ao tipo litológico, as diferentes espécies de vegetação e a classificação de solos. Fonte: Clemente *et al.* (2009).

Figure 3.1: Toposséquence étudiée par Clemente *et al.* (2009) qui indique les 10 profils de sol positionnés par rapport au type lithologique, aux différentes espèces de végétation et à la classification des sols. Source: Clemente *et al.* (2009).

Em estudos mais recentes, Sá (2010) coletou amostras em 22 perfis, o que possibilitou estudar regiões não abrangidas por Clemente *et al.* (2009), inclusive as que apresentam influência Ornitogênica. De acordo com Sá (2010) a Ilha apresenta três ordens de solos com base no SIBICS (EMBRAPA 2006): Neossolos, Cambissolos e Organossolos.

Os Neossolos estão presentes em cerca de 55 % do território da ilha. Ocorrem em maior proporção nas áreas mais baixas e/ou secas, mas também nas regiões de afloramento rochoso relacionado a locais de acentuado declive. Em menores proporções, estes solos ocorrem nas áreas deposicionais como em taludes ou cones aluviais. Como subclasses são encontrados os Neossolos Litólicos típicos e fragmentários e os Neossolos Regolíticos.

Os Cambissolos ocupam cerca de 30 % da ilha, e aparecem nas porções medianas a elevadas da paisagem onde o clima é ameno. Nas regiões mais baixas e secas ocorrem os Cambissolos Háplicos Ta; nas áreas medianas mais aplainadas e úmidas, em elevações a partir de 400 m, ocorrem os Cambissolos Háplicos Alíticos; e nas regiões mais altas e aplainadas do planalto axial (do Desejado e de Trindade) ocorrem os Cambissolos Haplicos Ta Distróficos.

Os Organossolos estão presentes em aproximados 10 % da ilha. Os Organossolos Fólicos Fíbricos ocorrem nas altas encostas e nos vales estreitos abaixo do planalto axial na região sul da ilha de clima mais frio e úmido. Segundo Sá (2010), o aporte elevado de material orgânico recalcitrante depositado pela vegetação de *Cythea delgadii* associada à pobreza e quase inexistência de (meso e micro) fauna (Barth 1958, Clemente *et al*. 2009) e clima Nebular condicionam a formação insólita de um horizonte hístico muito espesso e a formação de Organossolos em relevo escarpado, atípico para essa classe. Esses solos também não sofrem acumulação de água como os solos com horizonte superficial hístico das regiões continentais. Os Organossolos de Trindade por se formarem em condições atípicas são considerados como solos restritos e endêmicos da Ilha de Trindade.

Nos Neossolos, Cambissolos e Organossolos, Sá (2010) registrou solos com influência atual e/ou pretérita de aves marinhas. Esses solos foram classificados como ornitogênicos por serem formados pela mineralização dos dejetos das aves e a interação dos produtos com o substrato mineral (Schaefer *et al*. 2004, Simas *et al*. 2007).

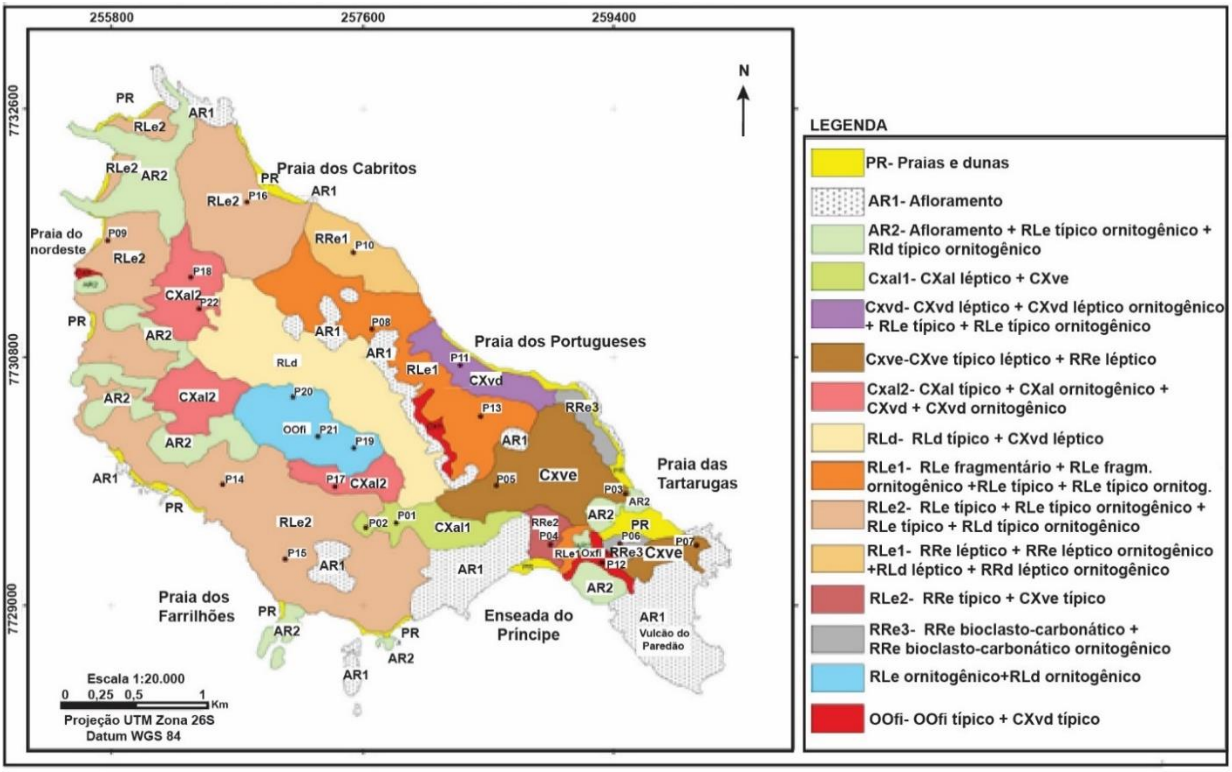

Figura 3.2: Mapa detalhado de solos com a posição dos 22 perfis onde foram realizadas coletas de amostras. Modificado de Sá (2010).

Figure 3.2: Carte détaillée des sols avec la position des 22 profils où des échantillons de collections ont été recueillis. Modifié de Sá (2010).

3.2.3.1- *Os solos com indícios de propriedades ândicas na Ilha de Trindade*

De acordo com FAO (2006) as propriedades ândicas resultam principalmente do moderado intemperismo de depósitos piroclásticos. Segundo a Soil Survey Staff (2014) para que um solo tenha propriedades ândicas é necessária a presença de menos de 25 % de carbono orgânico total e que sejam atendidos um dos seguintes critérios: i) os valores de ($Al_{(oxilato)}$ + ½$Fe_{(oxilato)}$) > 2 %, a densidade volumétrica do solo igual ou menor a 0.90 kg dm^{-3} e a retenção de fosfato de valor igual ou maior a 85 %; ou ii) relação ($Al_{(oxilato)}$+ ½$Fe_{(oxilato)}$) = > 0.4 e < 2.0, retenção de fosfato > 25 %, 30 % ou mais de partículas no tamanho areia e silte; e pelo menos 5 % de vidro vulcânico na TFSA. O primeiro critério é aplicado a solos que apresentam alto grau de intemperismo e o segundo critério é aplicado a solos de baixo grau de intemperismo. Tais propriedades devem compor 60 % ou mais do perfil do solo.

Na Ilha de Trindade, Clemente *et al.* (2009) observou alguns indícios da existência de solos com propriedades ândicas atestada pela aparente presença de material alofânico na base de um perfil de solo localizado no platô onde ocorrem piroclastos da Formação Morro Vermelho. Em solos provenientes de rochas fonolíticas e rochas básicas da ilha, Sá (2010) encontrou valores de ph em NaF acima de 9.4, o que indica a presença de minerais de baixa cristalinidade (Fields & Perrot 1966, Brydon & Day 1970). Também foram observados valores de 25 % ou mais de retenção de fosfatos e a maioria dos solos apresentaram relação ($Al_{(oxilato)}$+ ½$Fe_{(oxilato)}$) > 0.4. A proporção de vidro vulcânico na TFSA não foi obtida para esses solos, portanto não puderam ser enquadrados no grupo dos Andossolos pouco desenvolvidos.

3.3 – OCORRÊNCIA DE ANDOSSOLOS NO MUNDO E SUAS CARACTERÍSTICAS

Os Andossolos ocorrem em cerca de 1.24 milhões de km^2 (aproximadamente 1 %) da área terrestre global (Takahasi & Shoji 2002), em diversos climas (**Figure 3.3**), preferencialmente em regiões de vulcanismo ativo ou recentemente extinto, (Shoji *et al.* 1993). Esses são encontrados na região do círculo de fogo do Pacífico, nas Ilhas Aleutas, na Península Kamchatka da Russia, no Japão, nas Ilhas Filipinas, Indonésia, Papua Nova Guiné, Ilhas Salomão, Vanatua, Nova Zelândia, Rifte Valey na África, costa oeste da Itália, Ilhas Havaianas, Oeste da Índia, Irlanda, Ilhas Canárias e em outras ilhas.

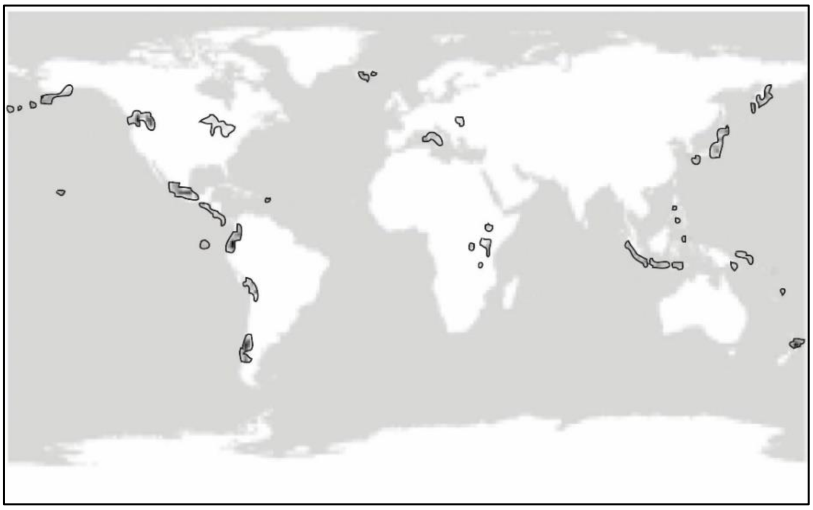

Figura 3.3: Localização de Andossolos no mundo. Modificado de Soil Survey Staff (1999).

Figure 3.3 : Localisation d'Andosols dans le monde. Modifié de Soil Survey Staff (1999).

Os Andossolos, são equivalentes aos Andosols, Andisols, Kurobokudo, respectivamente na WRB (2015), Soil Survey Staff (2014) e USCSJ 2nd (2002) e são caracterizados pela presença de propriedades ândicas e quantidades de minerais pouco cristalinos (alofana, ferrihidrita) ou paracristalino (imogolita) ou complexos húmicos ligados ao Al.

Andossolos podem ser divididos em alofânicos e não alofânicos com base na composição mineralógica dos argilominerais, (Shoji 1984). Andossolos alofânicos são caracterizados por conterem predominantemente alofana e imogolita na fração argila, (Saigusa *et al.* 1980). De acordo com Shoji *et al.* (1985) os Andossolos não alofânicos apresentam predominância de complexos húmicos de Al e Fe e argilominerais 2:1, sendo que a inibição da formação da alofana seria devido ao fornecimento de uma grande quantidade de matéria orgânica da vegetação em condições de ph 5 ou menos.

Os Andossolos podem ser encontrados sobre diversos tipos de rochas vulcânicas (andesito, dacito, cinzas vulcânicas, basaltos e ignimbritos) e não vulcânicas (gabros, anfibolitos, granulitos básicos, biotita-xisto, filitos anfibolíticos).

Nos Arquipélagos de Açores e da Madeira em Portugal vários estudos caracterizaram Andossolos desenvolvidos sobre rochas basálticas e piroclastos também de composição basáltica, com características alofânicas e não alofânicas: Ilha Santa Maria (Madeira 1980), Ilha São Jorge (Madruga 1995), Ilha do Pico (Madeira *et al.* 1996; Pinheiro *et al.* 2001), Ilha da Madeira (Madeira *et al.* 1994); e de traquitos e piroclastos de mesma composição: Ilha São Miguel (Ricardo *et al.* 1977, 1978/79), Ilha Terceira (Pinheiro 1990), Ilha Graciosa (Medina & Grilo 1981), Ilha Faial (Madeira *et al.* 2002).

Na Ilha da Madeira e do Pico os Andossolos apresentaram características não alofânicas atribuídas à presença de uma particular acumulação de matéria orgânica e à uma maior precipitação (Madeira *et al.* 1994, Pinheiro *et al.* 2001). Nos Andossolos da Ilha da Madeira ainda ocorre uma

predominância de argilominerais do tipo 1:1 (haloisita) e 2:1 (Al-vermiculita), (Madeira *et al.* 2007). Na Ilha de Santa Maria a característica não alofânica é principalmente devido a predominância de complexos húmicos de Al e Fe, (Madeira 1980).

Em Galápagos, Laruelle (1967) constatou a presença de solos com características andossólicas na Ilha de Santa Cruz, com densidade volumétrica menor que 0,85 g/cm^3 e domínio de material amorfo na fração argila, cujo material parental é de natureza basáltica. Mais tarde Sedov *et al.* (2010) em sua classificação micromorfológica, observaram uma micromassa isotrópica típica de Andossolos proveniente de cinzas vulcânicas.

Na Nova Zelândia os Andossolos alofânicos cobrem cercar de 12.5 % do país e apresentam argilominerais pouco cristalizados em vez de complexos húmicos ligados ao Al. Esses solos ocorrem sobre rochas eruptivas andesíticas, depósitos de pomes riolíticas e depósitos de piroclastos andesíticos, riolíticos e basálticos (Lowe & Palmer 2005). No sul da Austrália eles compreendem cerca de 0.001 % do território e encontram-se em regiões de vulcanismo basáltico de cerca de 5000 anos (Lowe & Palmer 2005).

Na região leste do vulcão Ercyes na Turquia ocorrem Andossolos alofânicos sob climas áridos e semi-áridos que provém de diversos materiais vulcânicos, como andesitos, dacitos, cinzas vulcânicas, basaltos e ignimbritos (Kılıç *et al.* 2018).

No vulcão Nevada de Toledo no México Central, ocorrem Andossolos soterrados que apresentam como principais constituintes na fração argila a haloisita. O contrário ocorre em Andossolos modernos que são constituídos principalmente de alofanas (Sedov *et al.* 2003).

Na Itália, próximo ao lago Vico, Quantim *et al.* (1985) observaram sob um depósito de lápilis fonolíticos um vulcão extinto, a presença de Andossolos caracterizados por conterem haloisita na base do perfil e alofana no topo do perfil.

No Brasil, Dumig *et al.* (2008) foram os primeiros a detectarem Andossolos na América do Sul fora do raio de influência do vulcanismo recente da região da Cordilheira dos Andes. Esses Andossolos foram estudados nas regiões altas do nordeste do Rio Grande do Sul sobre riodacitos do Cretáceo-Jurássico e são do tipo não alofânicos.

Micromorfologicamente os Andossolos descritos pelo mundo apresentam uma microestrutura granular bem separada no topo do perfil que muda para eunálica, quitônica e monica grossa em direção a base de um perfil de solo, (Sedov *et al.* 2010). A micromassa apresenta em geral uma b-fábrica indiferenciada devido a presença de amorfos ou componentes coloidais criptocristalinos (alofana, imogolita, ferrihidrita), Kawai (1969). Exemplos de estudos micromorfológicos em Andossolos com tais características podem ser encontrados na Ilha Pico e Faial, (Gerard 2007); Ilha Terceira, (Pinheiro *et al.* 2003); Ilhas Canarias, (Benayas *et al.* 1980, Sanchez Dias 1978); Ilha de Santa Fé, (Morrás 1978).

CHAPITRE 4

METODOLOGIA

Os procedimentos adotados neste estudo visam contemplar os objetivos propostos e estão organizados nas etapas e atividades discriminadas a seguir.

4.1- 1ª ETAPA – ESCRITÓRIO (PRÉ-CAMPO)

Nessa etapa foram desenvolvidas as atividades de levantamentos pré-campo de dados, materiais e bibliografias. Os dados e materiais dizem respeito a todo o conjunto de informações e produções cartográficas disponíveis para a área de estudo, incluindo imagens de satélite, cartas planialtimétricas e mapeamentos (geológico, geomorfológico, pedológico, vegetacional, etc.). As bibliografias, por sua vez, referem-se tanto informações específicas sobre o estado da arte do conhecimento sobre os solos e produtos de alteração da Ilha da Trindade, como solos de ilhas vulcânicas e a alteração de tais rochas de uma maneira geral (conceitual e de estudos de caso). Essas informações visam orientar as coletas de campo, bem como fundamentar a análise dos resultados e sua discussão.

4.2- 2ª ETAPA – TRABALHO DE CAMPO

O trabalho de campo visou o reconhecimento da área de estudo e, principalmente, a coleta das amostras. As expedições à ilha têm duração de 60 dias (considerando 8 dias para deslocamentos) e são organizadas pela Marinha do Brasil. O primeiro campo foi realizado entre maio e junho de 2016. Na ocasião, foram coletadas amostras de rochas e saprolitos de quatro perfis, sendo um no Vulcão do Paredão, e outros três na Formação Morro Vermelho, (**Quadro 4.1** e **Figura 2.5**). As orientações para coleta seguiram os levantamentos realizados por Almeida (1961, 2002) e as demais informações obtidas na Etapa 1.

Foram descritas e amostradas em campo as seções de contato entre rochas sãs e suas respectivas alteritas (iso e aloteritas) e solum (horizontes pedogenéticos). As descrições destacaram as principais variações morfológicas em escala macroscópica, bem como através do uso de uma lupa (20X). Aspectos como cor (MUNSELL 1994), texturas e estruturas foram destacadas nos distintos perfis descritos e após, foram coletadas amostras para análises laboratoriais. As amostras foram identificadas e acondicionadas para transporte ao continente.

Quadro 4.1: Descrição geral dos perfis durante a coleta em campo.

Tableau 4.1: Description générale des profils lors de la collecte sur le terrain.

Perfil	Localização	Altitude (m)	Rochosidade	Pedregosidade	Material de Origem e Formação Geológica	Erosão
1	257867/ 7729600; platô ankaratrítico; topo	460	Não rochosa	Moderadamente pedregosa	Solo derivado de Piroclasto; Vulcão do Paredão	Extremamente forte
2	257916/7729828, media vertente superior	351	Ligeiramente rochosa	Muito pedregosa	Solo derivado de Piroclasto; Formação Morro Vermelho	Extremamente Forte
3	258467/ 7729761; media vertente inferior	258	Muito rochosa	Muito pedregosa	Solo derivado de Piroclasto; Formação Morro Vermelho	Extremamente forte
4	258826/ 7730121; vertente da costa; base	72	Rochoso	Muito pedregoso	Solo derivado de Piroclasto; Formação Morro Vermelho	Extremamente Forte

4.3- 3ª ETAPA – LABORATÓRIO

Diferentes análises objetivam a caracterização das amostras coletadas em campo.

4.3.1- Análise Textural

A análise granulométrica das frações areia, silte e argila foi realizada no Laboratório de Análise de Solo Viçosa Ltda pelo procedimento da EMBRAPA (1999). Após agitação lenta (16 h), utilizando hexametafosfato de sódio como dispersante, o silte e a argila foram determinados pelo método da pipeta, ao passo que a areia grossa e a fina foi separada por peneiramento. As proporções de cada fração foram plotadas no diagrama triangular para obter a classe textural.

4.3.2- Análises Mineralógicas

4.3.2.1- *Contagem de vidro vulcânico*

Foram realizadas análises em lupa de aumento Nikon C-POL para a identificação de vidro vulcânico entre a fração silte grosso e areia grossa dos solos. Cinco gramas deste material foram pesados e após foram selecionados o vidro vulcânico sob lupa de aumento para uma posterior quantificação.

4.3.2.2- ***Difratometria de Raios-X***

As análises mineralógicas por Difratometria de Raios-X (DRX) foram realizadas em duas etapas. A primeira etapa foi realizada para caracterização mineralógica sobre amostras totais e da fração argila abaixo de 2 µm, 1 µm e 0.5 µm. O detalhamento das análises da fração argila teve como objetivo inicial identificar se as amostras apresentariam material amorfo. Depois da primeira etapa analítica por DRX, foi efetuada uma segunda etapa em amostras na fração argila (< 2 µm) saturadas com Ca^{2+}, deferrificadas com ditionito-citrato-bicarbonato de sódio (DCB) de acordo com a metodologia de Meha & Jackson (1960), imediatamente tratadas com formamida e desidratadas à 110 °C durante 6 h. A primeira etapa analítica foi realizada em difratômetro Panalytical Empyrean (CuKα, 45 KV e 40 mA) no DEGEO/ Universidade Federal de Ouro Preto/Brasil e a segunda etapa foi realizada em difratômetro Philips X ' Pert Pro Diffraction (CuKα, 40 KV, 40 mA) no IC2MP/Université de Poitier/França. O intervalo de escaneamento da fração total foi de 2 to 70 °, com passo de 0.02 ° (2 (θ)/min) e das análises da fração argila foram no intervalo de 2 a 35 º, com passo 0.4 ° (2 (θ)/min). Os difratogramas foram interpretados no software X'Pert HighScore Plus e através de padrões da literatura (Brindley & Brown 1980).

4.3.2.3- ***Análise térmica diferencial e termogravimétrica (ATD-TG)***

A ATD-TG foi realizada para melhorar a caracterização e a identificação das fases constituintes da fração argila. As amostras foram analisadas no instrumento TGA Q50 V20.10 com atmosfera de nitrogênio, pressão máxima de 1.4 kgf cm^{-2} e taxa de aquecimento de 10 °C min^{-1}. Os dados foram analisados por meio do software TA Universal Analysis.

4.3.2.4- ***Infravermelho***

A Espectroscopia no Infravermelho foi utilizada para auxiliar as análises mineralógicas por Difração de Raios-X. As análises foram realizadas no Instituto IC2MP, Universidade de Poitiers/França usando Espectrômetros de Transformada de Fourrier Thermo Nicolet, série Nexus 5700, para análises das frações de argila. Alíquotas de 1mg de amostra foram previamente pulverizadas em almofariz de ágata e pesadas em balança de precisão de cinco casas decimais. As amostras foram misturadas com 150 mg de KBr (brometo de potássio) espectroscópico. A mistura foi prensada durante cinco minutos à uma pressão 7 Pa e após foram secos em mufla à 120 °C durante 20 h. Os espectros de infravermelho médio (4000-400 cm^{-1}) foram obtidos usando fonte de luz branca, beamsplitter KBr, resolução de 4 cm^{-1}, velocidade óptica de 0.4747 cm s^{-1} e 100 varreduras.

Foram realizadas análises em lâminas delgadas para identificação de argilominerais nas feições

de alteração das rochas. Os equipamentos utilizados foram Espcectômetro de Transformada de Fourier Thermo Nicolet, series Nexus 5700 acoplado com microscópio Thermo Scientific Nicolet Continum do instituto IC2MP/Université de Poitiers/França. No microscópio, os espectros de infravermelho próximo (8000-4000 cm^{-1}) foram obtidos usando fonte de luz branca, beamsplitter CaF_2, resolução de 4 cm^{-1}, velocidade óptica de 0.3165 cm s^{-1} e 100 varreduras.

As análises de infravermelho próximo também foram realizadas diretamente na fração argila condicionada em frascos de vidro para serem comparadas com as análises pontuais das lâminas delgadas. Essas análises foram feitas nas mesmas condições de aquisição em que foram obtidos os espectros das lâminas delgadas, com a única diferença na velocidade que foi de 0.12659 cm s^{-1}.

4.3.3- Análise Petrográfica e Micromorfológica

As análises petrográficas e micromorfológicas foram feitas em seções delgadas e polidas previamente impregnadas ou não em microscópio petrográfico Zeis no laboratório do Departamento de Geolologia/UFOP. Para as descrições micromorfológicas dos solos foram utilizados os preceitos de Stoops (2003).

As microanálises por Microscopia Eletrônica de Varredura (MEV) foram realizadas nos sítios previamente selecionados durante os estudos micromorfológicos, visando determinar fases minerais não identificáveis ao microscópio óptico convencional, caracterizando-as morfologicamente.

4.3.3.1- *Análise por Microscópio Eletrônico de Transmissão (MET)*

As imagens da fração argila foram realizadas no MET JEOL 2011 Bruker Esprit no CinaM-CNRS, Université de Aix-Marseille. As argilas foram depositadas em tubo de ensaio e realizadas a diluição até que o líquido ficasse límpido. As amostras foram passadas em ultrassom para que houvesse a dispersão dos agregados de argila. Após esse procedimento as amostras foram depositadas em grades Formvar revestidas com filme de carbono. Regiões alteradas das rochas foram raspadas e, em seguida, depositadas em resina para serem feitos cortes em ultramicrótomo. Os cortes também foram depositados em grades revestidas com filme de carbono.

4.3.4- Análises Químicas

4.3.4.1- *Química parcial do solo*

As análises de química parcial dos solos foram realizadas no Laboratório de Solos da Universidade Federal de Viçosa utilizando os padrões da (EMBRAPA 2017). Foram medidos o pH em H_2O (solo:solução 1:2.5); pH em NaF (Pansu & Gautheyrou 2006); os teores de P em mg dm^{-3} (Defelipo & Ribeiro 1981); os teores de K, Ca, Mg e Al em cmolc dm^{-3}; e a partir deles foram calculados a soma de bases trocáveis (SB), a capacidade de troca catiônica efetiva (CTC(t)) e a capacidade de troca catiônica potencial a ph 7 (CTC(T)) em cmolc dm^{-3}; e os índices de saturação de bases (V) e de alumínio (m) em %. O teor de matéria orgânica (MO) em g kg^{-1} foi medido pelo carbono orgânico total, obtido pelo método Walkley-Black, multiplicado por 1.72. O P remanescente (Prem) foi calculado de acordo com Alvares *et al.* (2000) e a retenção de P em porcentagem foi calculada da seguinte maneira: P do branco menos P na solução de equilíbrio (Prem).

4.3.4.2- ***Análises de química total por ICP-OES e ICP-MS***

As análises dos elementos maiores e menores foram realizadas no ICP-OES Agilent Technologies 725 e dos elementos terras raras (ETR) no ICP-MS Agilent Technologies 7700 no Laboratório LGqA do DEGEO/UFOP.

Para digestão total de 0.1g de cada amostra, foram utilizados 1ml de peróxido de hidrogênio, 3 ml de HCl a 10 mol L^{-1}, 6 ml de HNO_3 a 10 mol L^{-1}, 20 ml de HNO_3 a 2 mol L^{-1} e 4 ml de HF concentrado. O percentual de SiO_2 foi calculado de forma relativa pela diferença para 100 % na soma dos principais elementos e perda ao fogo (LOI).

4.3.4.3- ***Microquímica por MEV-EDX***

Imagens de elétrons dispersivos e análises químicas semi-quantitativas por Elétron Dispersivo de Raios-X (EDX) foram feitas para analisar, respectivamente, o hábito e a composição de olivinas e indigsitas. As análises foram realizadas no microscópio eletrônico de varredura (MEV) acoplado com EDX Jeol JSM-6510 com uma tensão operando-se de 20 KV do DEGEO/UFOP.

4.3.4.4- ***Microquímica por Microssonda Eletrônica***

As microananálises de olivinas, piroxênios, zeolitas, espinélios, sideromelano, palagonita e feldspatos foram realizadas com microssonda eletrônica JEOL JXA-8230 no Laboratório de Microanálises do DEGEO/UFOP. As condições de aceleração e voltagem foram 15 kV e 20 nA, e as correções da matriz ZAF foram aplicadas. O tempo de contagem em picos/background foram 10/5 s para todos elementos, exceto o sódio e bário que foram de 20/10 s e 30/15 s respectivamente. Para os

elementos Si, Al, Na, Mg, Fe, Cr, Ti, Ca, Ni, K, Mn, Ba as análises pontuais foram calibradas com quartzo-TAP, córindon-TAP, jadeita-TAP, óxido de magnésio-TAP, almandina- LIFH, óxido de cromo-LIF, rutilo-LIF, rodonita-LIF, magnetita-LIF, augita- PETJ, AN100-PETJ anortoclásio- TAPH, microclina- PETL, sanidina-PETJ, rodonita-LIF, barita- PETH. O FeO foi considerado como a quantidade do ferro total obtido através da microssonda. A água para as zeólitas foi calculada diminuindo a soma total dos cátions por 100 %.

Mapas microquímicos de olivina também foram obtidos pela microssonda para ilustrar as distribuições de elementos químicos. As condições operacionais foram: aceleração de 15 kV, corrente de feixe de 20 nA e 20 ms de tempo de permanência por ponto (modo de estágio). Os mapas mostram distribuições de elementos quantitativos. Mapas microquímicos de olivina foram realizados para os elementos Fe e Mg e foram calibrados com almandina-LIFH e olivina-TAP. Os cristais foram analisados por perfis transgranulares.

As fórmulas minerais foram calculadas com base em 4 oxigênios para olivina, 6 oxigênios para o piroxênios (diopsídio) e, 98 e 36 oxigênios para zeólitas (heulandita e chabazita) de acordo com (Deer *et al*. 1992).

4.3.4.5- ***Extração seletiva de Al, Si e Fe***

A extração seletiva de Al, Si e Fe foi realizada com pirofosfato de sódio (Blackmore *et al*. 1981), oxalato de amônio (MacKeague & Day 1966) e ditionito-citrato-bicarbonato de sódio (Meha & Jackson 1960, Holmgreen 1967) e a determinação do conteúdo desses elementos químicos pelo ICP-OES para quantificação de fases amorfa e cristalina.

Uma quantidade de 0.25 g de amostras de solo seco (< 2 mm) foi adicionada em tubos de polietileno de 50 mL com 20 mL de uma mistura de solução de citrato de sódio tribásico bihidratado a 0.4 mol L^{-1} e bicarbonato de sódio a 1 mol L^{-1}; uma solução de ácido oxalato-oxálico de amônio 0.2 mol L^{-1} (pH 3.0) e 0.1 mol L^{-1} de pirofosfato de sódio. A mistura foi aquecida entre 75 °C e 80 °C. Depois de atingir a temperatura juntou-se 1g de pó de ditionito de sódio sob agitação constante por 1 minuto e, ocasionalmente, por 5 min. Duas porções de 1 g de ditionito foram adicionadas após dez minutos de reação com agitação constante entre intervalos de dez minutos cada. A extração foi repetida 5X até que um resíduo de cor branca ou cinza fosse obtido. O ácido oxalato-oxálico de amônio e a solução de pirofosfato de sódio foram agitados por 12 h no escuro. Todas as amostras foram centrifugadas por 5X durante 10 min após a adição de accofloc (0.4 %) e os supernadantes foram coletados para a determinação de Al, Fe e Si em ICP-OES.

Quantificação de alofanas e ferridritas- A relação A1: Si da alofana foi calculada a partir da razão [A1(o)-Al(p)]/Si(o) e a quantidade de alofana na amostra foi estimada por multiplicação de Si(o) pelo fator dado por Parfit (1990a): as proporções atômicas de Si(o) próximas a 1.0, 1.5, 2.0, 2.5, 3.0, 3.5 foram multiplica pelos fatores 5, 6, 7, 10, 12, 16, respectivamente. O conteúdo de ferrihidrita foi determinado pela multiplicação dos valores de Fe(o) por 1.7 (Parfitt & Childs 1988).

4.3.5- Densidade Aparente

O cálculo da densidade das rochas e dos solos foram realizados de acordo com a metodologia da EMBRAPA (2018).

4.3.5.1- *Densidade das rochas*

A densidade das rochas foi efetuada pelo método do torrão parafinado. O torrão foi elaborado com dimensões que mantivessem um volume de 100 cm^3 para serem comparados com o mesmo volume do anel volumétrico onde foram realizadas as coletas de solo. Os torrões secos ao ar foram mergulhados em parafina fundida (60 °C – 65 °C) e foram deixados para esfriarem. Após o esfriamento os torrões foram pesados em um béquer graduado previamente com o peso zerado. O béquer foi pesado com a água até a marca graduada máxima. Após foi inserido o torrão parafinado no béquer vazio e seco, e inserido água até a marca máxima. Os pesos do torrão seco ao ar, da parafina, do torrão parafinado, da água e do torrão parafinado com a água foram anotados para efetuarem os cálculos de densidade das rochas de acordo com a seguinte equação:

$$\boldsymbol{Dr = \frac{Pt}{(Va - Vat) - Pp}}$$

Sendo que: Dr= densidade da rocha, em g cm^{-3}; Pt= peso do torrão, em g; Va= volume da água, em cm^3; Vat= volume da água com o torrão, em cm^3 ; $Pp=(m_{tp}-m_t)/0.9$; m_{tp}= massa do torrão parafinado, em g; m_t= massa do torrão, em g. Obs.: P_p= peso da parafina, em g; densidade da parafina comercial=0.9 g cm^{-3}.

4.3.5.2- *Densidade dos solos*

A amostragem do solo foi realizada em anel volumétrico de 100 cm^3, evitando-se a compactação do solo no interior do cilindro e a perda de estrutura do solo. No laboratório as amostras foram pesadas em balança com precisão de 0.01 g e após foram inseridas em estufa para secagem à 105 °C. Após a secagem foram efetuadas novamente a pesagem. O cálculo da densidade foi realizado através da divisão

entre a massa da amostra de solo seco a 105 °C, em gramas; e o volume do cilindro, em cm^3.

4.3.6- Balanço de Massa

O balanço de massa foi efetuado sobre os perfis que apresentaram amostras com estrutura conservada (perfis 1 e 3). Foram calculadas as perdas e ganhos da alteração isovolume através da metodologia de Millot & Bonifas (1955). A expressão utilizada para o cálculo foi a seguinte:

$$\mathbf{t\ \% = 100.[(ds.xs/dr.xr) -1]}$$

Sendo que: t % = taxa de mobilidade (perda, quando negativo; e ganho, quando positivo); ds= densidade do solo (produto de alteração); dr= densidade da rocha (material de origem); xs= teor do elemento no solo, e xr= teor do elemento na rocha.

CHAPITRE 5

LES PYROCLASTES ET LEURS PRODUITS D'ALTERATION[1]

ABSTRACT

This paper reports the composition and alteration products of pyroclasts in the Holocene Paredão volcano (pyroclast 1) and Late Quaternary Morro Vermelho Formation (pyroclasts 2 and 3) of Trindade Island, South Atlantic, Brazil using combined macromorphological, micromorphological, mineralogical and geochemical techniques. The pyroclasts 1 and 2 are interpreted as volcanic breccia deposits, whereas pyroclast 3 is a lapilli deposit. They are dark gray in color with some altered reddish regions and show vesicles and amygdales structures with small greenish crystals of 2.0 mm scattered throughout the matrix. The eruptions can be regarded as Strombolian-type by producing pyroclastic deposits with coarse fragments with high vesicularity and fluidal shape that indicate magmatic degassing and fragmentation. Petrologic and XRD data revealed a mixture of biotite, goethite, ilmenite, anatase, magnetite, hematite, pyroxene, zeolites, and olivine as their main mineral components. Optical microscopy analysis confirms the vesicular and amygdaloid structures, with a hypocrystalline texture and a pale brown stained vitreous mass classified as sideromelane, due to its basaltic composition. The sideromelane changes to a reddish brown and yellowish-brown staining material identified as palagonite, clearly indicating a phreatomagmatic eruption that occurs when the ascending magma comes into contact with water. Infrared analyses in the palagonitized regions revealed the presence of halloysite, suggesting alteration of sideromelane to tubular clay minerals. Amygdales and microfractures are partially or totally filled with zeolites, which are formed by the percolation of water that reacts with the palagonite and precipitation of chemical elements of hydrothermal fluid. Reddish dark brown iddingsite and anhedral crystals of titaniferous magnetites occur in the fractures and edges of the olivine. These crystals are also dispersed in the matrix while some of them are zoned with Cr-rich core and Cr-poor edge, suggesting a deep mantle origin of the magma. The high trace elements content can be related to clinopyroxene (diopside) that include these elements. Geochemical data show that the pyroclasts are undersaturated in silica, plotting in the ultrabasic and foidites fields on the TAS classification diagram.

Keywords: Palagonite; Halloysite; Zeolites; Infrared

---

[1] Article soumis au magazine "Journal of South American Earth Science" avec le titre "Mineralogical and geochemical signatures of Quaternary pyroclasts alterations at the volcanic Trindade Island, South Atlantic".

5.1 – INTRODUCTION

The Trindade Island is a small Brazilian island of ~13 km^2 and located in the South Atlantic (**Figure 5.1**). The Island is part of an extensive east-west-oriented underwater volcanic chain, called Vitória-Trindade, and constitutes the upper portion of a volcanic building of ~5.2 km high. The Vitória-Trindade Chain corresponds to the western extension of the Trindade Victory Fracture Zone, located at 18°40' in the Mid Atlantic Ridge (Alves *et al.* 2006). The Island is formed by five different volcanic episodes of lava flows and intrusions of poor silica rocks with accentuated sodium-alkaline content (Almeida 1961). These volcanic episodes were described by Almeida (1961) from bottom to top as: Trindade complex, Desejado sequence, Morro Vermelho Formation (MV), Valado Formation and Vulcão do Paredão Formation (VP) (**Figure 5.1**). The volcanic spills are overlain by the Holocene deposits that represent a small portion of the stratigraphic units occurring on the island (Castro & Antonello 2006) (**Figure 5.1**). Particularly in MV and VP formations, there are several pyroclasts such as lapilli and ash tuffs containing rotational lumps, blocks, aggregates and agglutinates of melanefelintic, basanite and tephrytic lava. Cordani (1970) suggested an eruption age by potassium-argon dating method of 0.17 Ma for the MV deposits. However, Pires *et al.* (2016) a recorded a 0.25 Ma age for the VP volcanic deposits and suggests that this volcanism represents the most recent volcanic activity of the Brazilian territory.

Studies of volcano stratigraphy and eruption geological models in the area of the Paredão Volcano (Pasqualon 2017) and Morro Vermelho Formation (Luz 2016) showed intercalation of nephelinitic flows and pyroclastic deposits, leading to the interpretation of heterogeneous volcanism characterized by a Hawaiian initial phase, and a Strombolian final phase. The Hawaiian phase would be formed exclusively by 'A'a flows and Strombolian phase by pyroclasts deposits of breccia and lapilli being composed mainly of basaltic scoria.

The petrological and geochemical studies of the olivine-nephelinites in the VP rocks showed strongly fractionated REE patterns in the melanephelinites and basanites–tephrites, suggesting the presence of garnet as a probable residual phase and generation of melt at about 100 km depth (Marques *et al.* 1999). Bongiollo *et al.* (2015) recently used geochemical modeling to show that the nephelinites in Trindade Island were from magmas derived at a minimum of 1490 °C and 3 Gpa (> 100 km depth).

Studies to date have focused on the petrogenesis and age of lava flows and intrusions on Trindade Island. Except for studies of alteration of olivine crystals of the pyroclasts (Mateus *et al.* 2018), there is still a deficiency of studies with emphasis on alteration of these rocks such as the features of palagonization and zeolitization. Therefore, this study used combined macromorphological, micromorphological, mineralogical and geochemical techniques to examine the composition, alteration products, and origin of the pyroclasts in MV and VP formations.

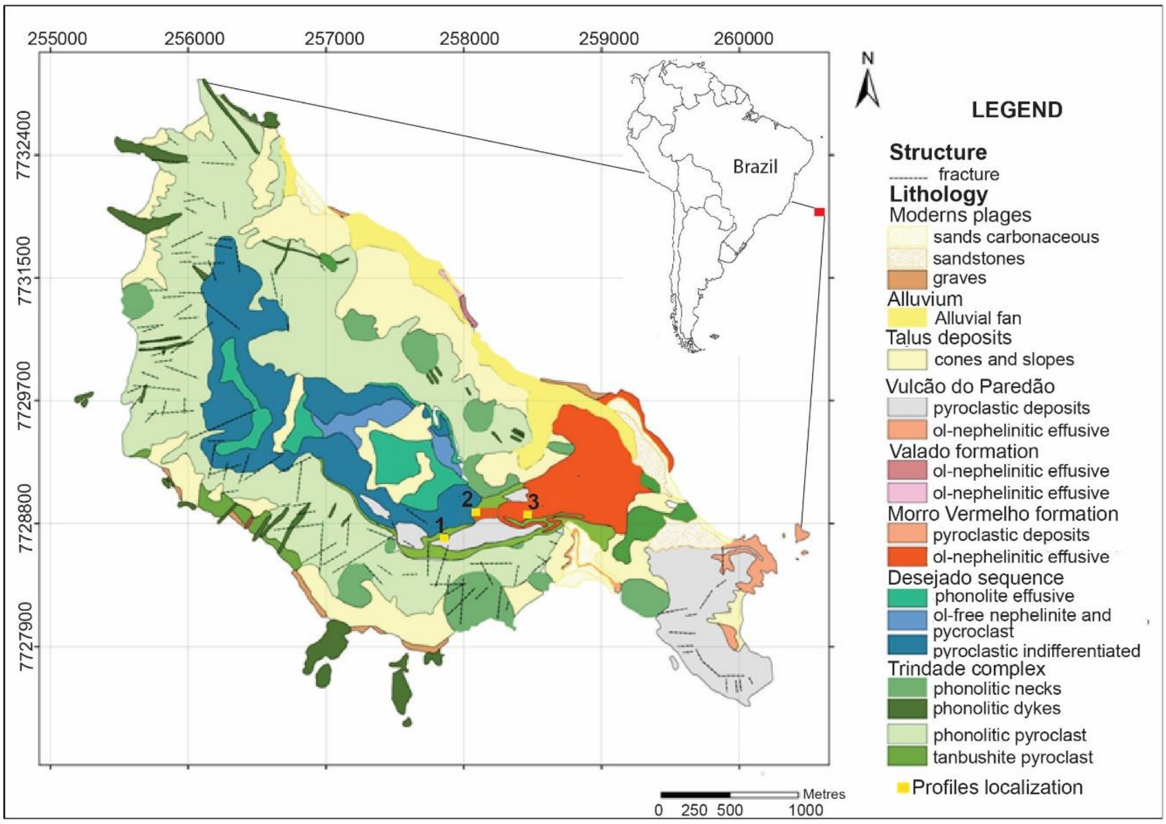

Figure 5.1: Geological map of Trindade Island and the regions of collection of pyroclasts 1, 2 and 3. Modified of Patrício (2012).

Figure 5.1: Carte géologique de l'Île de Trindade et des régions de collecte des pyroclastes 1, 2 et 3. Modifié de Patrício (2012).

5.2 – METHODOLOGY

The pyroclastic rocks were collected from the Holocene VP (the latest event) and the Late Quaternary MV formation. Macromorphologically, the coloration and the mineral constituents of the rocks were observed with the aid of a magnifying glass of 20x. The pyroclasts were measured and classified according to the systematic of the IUGS (Le Maître 2002) taking into account the size of the clasts. The petrological description including mineralogy, texture, estimation of the percentage of minerals and photographic images were performed in polished thin sections using a Zeiss microscope coupled with a camera.

More detailed mineralogical information was obtained on the samples using X-Ray Diffraction (XRD) technique. The samples were initially gently powdered in agate mortar and sieved with 250 mesh. The samples were analyzed at a scanning interval of 2 to 70 °2θ with a step size of 0.02 ° 2θ/s using a CuKα radiation and power 45 KV and 40 mA on a Panalytical diffractometer at the Universidade Federal

de Ouro Preto (DEGEO/UFOP), Brazil. The diffractograms were interpreted with X'pert HighScore Plus software and compare with standards (Brindley & Brown 1980). The Transform Fourier Thermo Nicolet, Nexus 5700 series infrared spectrometer coupled with Thermo Scientific Nicolet Continum microscope was used to complement the XRD mineralogical analyses at the IC2MP institute, Université de Poitiers, France. These analyses were performed on clay fractions and point analyses in thin sections. In microscope the near-infrared spectra (8000-4000 cm^{-1}) were obtained using source of white light, beamsplitter CaF_2, resolution of 4 cm^{-1}, optical velocity of 0.3165 cm s^{-1} and 100 scans. The spectra of clay fraction were obtained with the same condition of acquisition in thin sections, but with velocity of 0.12659 cm s^{-1}.

Image analyses of the clay minerals were performed with a JEOL 2011 Bruker Esprit Transmission Electron Microscope (TEM) at CinaM-CNRS, Aix Marseille University. The suspended clay separates were deposited onto carbon coated Formvar film Cu grids. The palagonitized regions were scraped and then deposited in resin to be made cuts in ultramicrotome. The cuts were deposited in grids.

The chemical analyses of the major and trace element compositions of the samples were measured in the ICP-OES Agilent Technologies 725 while the rare earth elements (REE) were performed in the ICP-MS Agilent Technologies 7700 at DEGEO/UFOP LGqa Laboratory. For total digestion of 0.1 g of each sample, 1 mL of hydrogen peroxide, 3 mL of HCl at 10 mol L^{-1}, 6 mL of HNO_3 to 10 mol L^{-1}, 20 ml of HNO_3 to 2 mol L^{-1} and 4 mL of HF concentrate were used. The percentage of SiO_2 was calculated in a relative way by the difference to 100 % in the sum of the main elements and LOI.

The microanalyses of the pyroxenes, zeolites, spinels, sideromelane and palagonite were performed with electron microprobe JEOL JXA-8230 at the Microanalysis Laboratory of the DEGEO/UFOP. The acceleration and current conditions were 15 kV and 20 nA, and corrections of the common ZAF matrix were applied. The counting time in the peaks/background were 10/5s for all elements except the sodium that was 20/10s (Na, Si, Al, Mg, Fe, Cr, Ti, Ca, Ni, K, Mn). The punctual analyses were calibrated with jadeite-TAP, rutile-LIF, sanidine-PETJ, magnesium-TAP oxide, chromium-LIF oxide, AN100-PETJ, corindon-TAP, rodonite-LIF, quartz-TAP, magnetite-LIF. The FeO was considered as the amount of total iron obtained through the microprobe. The H_2O for zeolites was calculated by decreasing the total sum of cations by 100 %.

5.3 – RESULTS

The pyroclastic rocks collected in the VP (pyroclast 1) and MV formations (pyroclasts 2 and 3) were classified according to their sizes (Le Maître 2002). The pyroclasts 1 and 2 are classified as volcanic breccia deposit because they contain more than 75 % of angular and subangular fragments of 140.0 mm (blocks) (**Figures. 5.2a**, **c**). In addition, pyroclast 1 contains fragments between 2.0 and 40.0 mm (lapilli) in smaller proportions (**Figure 5.2b**). The pyroclast 3 belongs to a lapilli deposit containing more than 75% of 2.00 to 20.00 mm (lapilli) fragments (**Figures. 5.2d**, **e**). Macroscopically, all the pyroclasts have dark gray coloration with some brownish to reddish regions, and vesicular and amygdaloid structures (**Figure 5.2**). The matrix of the pyroclasts contain scattered small green crystals (~ 2.0 mm). Owing to the fine-grained size (< 1.0 mm) of the matrix constituents, it is difficult to distinguish their mineral composition in macroscopic view.

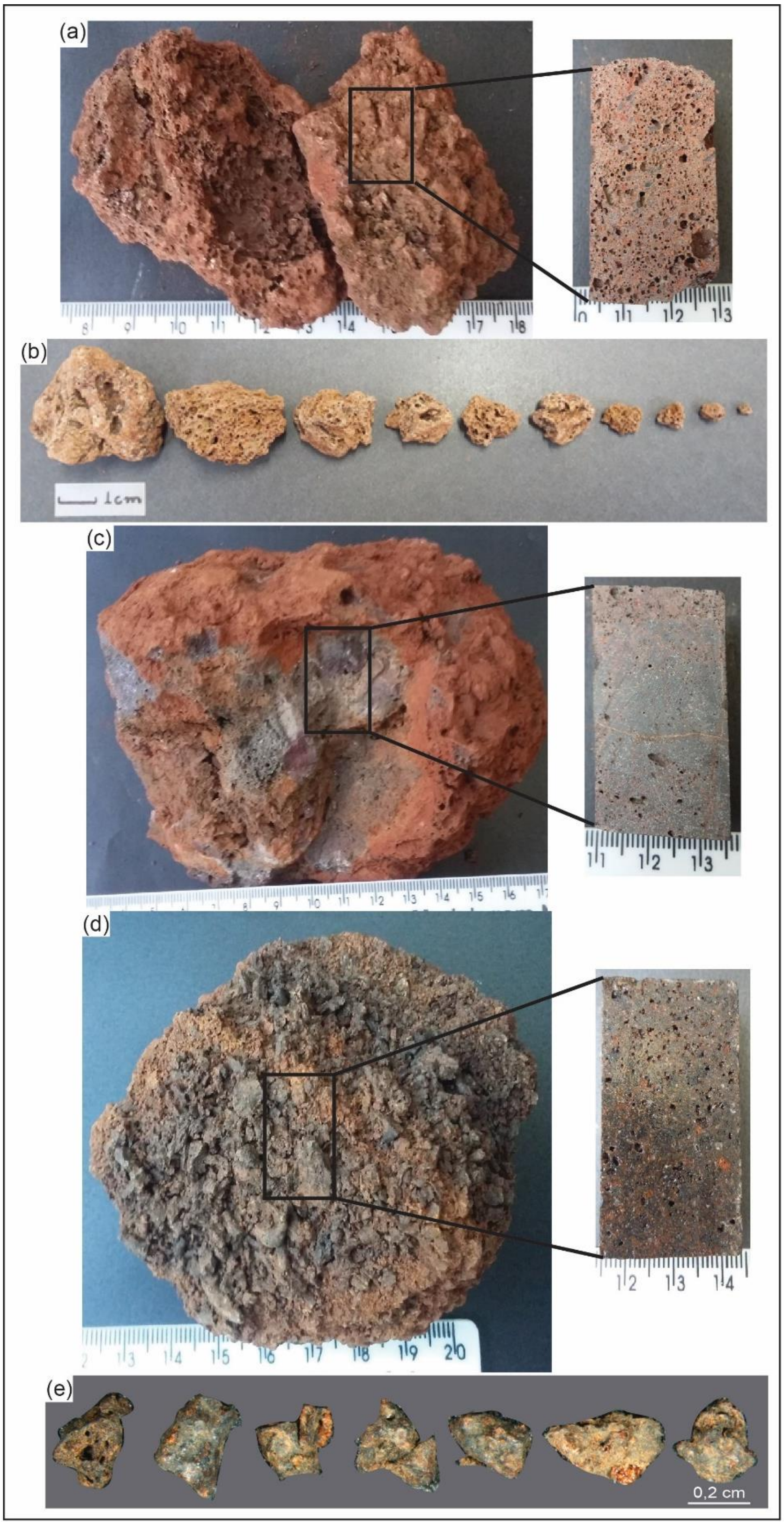

Figure 5.2: (**a**) Pyroclast 1 of Vulcão do Paredão formation showing reddish-colored alteration features. On the right, sample where the blade was made for the micromorphological description. (**b**) Image showing lapilli of different sizes in pyroclast 1. (**c**) Pyroclast 2 of the Morro Vermelho formation, with the altered edges of reddish coloration. On the right, image of the sample where the blade was made for the micromorphological description.

(**d**) Pyroclast 3 of the Morro Vermelho formation. On the right is the sample where the blade was made for micromorphological description. It is possible to observe reddish-colored alteration features. (**e**) Image showing smaller lapilli grains of 2mm with alteration features.

Figure 5.2: (**a**) Pyroclaste 1 de la Formation Vulcão do Paredão Pyroclast 1 montrant des caractéristiques d'altération de couleur rougeâtre. Sur la droite, échantillon où la lame a été faite pour la description micromorphologique. (**b**) Image montrant des lapilli de différentes tailles dans le pyroclaste 1. (**c**) Pyroclast 2 de la Formation Morro Vermelho, avec les bords altérés de la coloration rougeâtre. Sur la droite, image de l'échantillon où la lame a été faite pour la description micromorphologique. (**d**) Pyroclast 3 de la Formation Morro Vermelho. Sur la droite se trouve l'échantillon où la lame a été faite pour la description micromorphologique. Il est possible d'observer les caractéristiques d'altération de couleur rougeâtre. (**e**) Image montrant de plus petits grains de lapilli de 2mm avec des dispositifs d'altération.

Microscopically the pyroclast 1 are altered and show reddish brown vitreous matrix (**Figure 5.3a**) that is attributed to exposure to intense alteration. Some regions of pyroclasts 2 have grayish stains because of the presence of unaltered portions of the rock (**Figure 5.3e**). However, fragments in pyroclast 3 are yellowish brown in color (**Figure 5.3j**). All the pyroclasts have hypocrystalline textures and vesicular and amygdaloid structures (**Figures. 5.3a**, **d**, **j**). The pyroclasts are composed of a pale brown vitreous mass in 50 % of thin section area, which are isotropic in crossed polarized light and occurs around olivine, pyroxene and spinel crystals. Bulk rock XRD analyses show that the matrix of these pyroclasts are essentially composed of biotite, goethite, ilmenite, anatase, magnetite, hematite, pyroxene and olivine (Mateus *et al.* 2018).

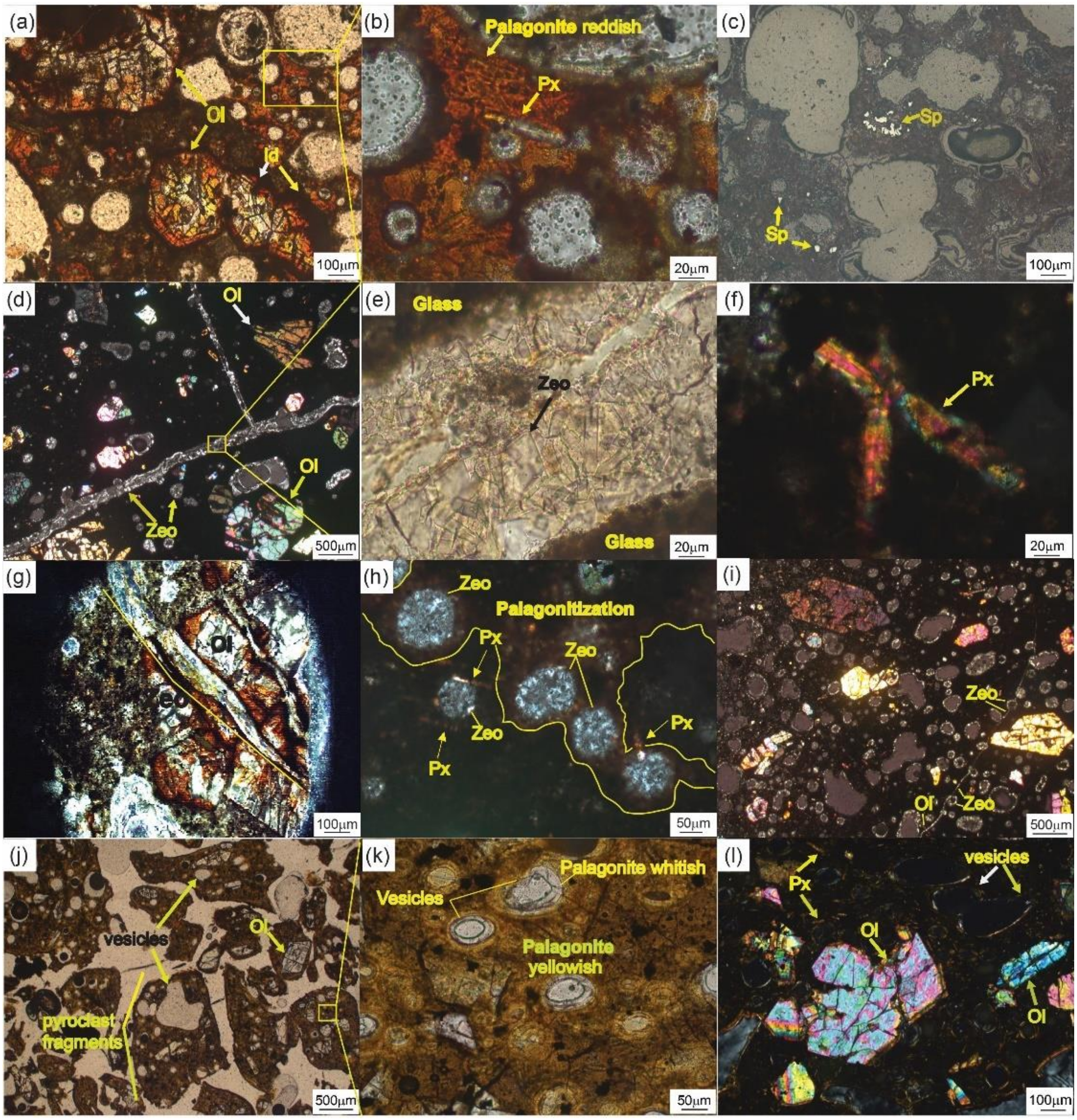

Figure 5.3: Pyroclast 1: (**a**) PPL photomicrograph from the euhedral olivine phenocrystals with altered borders for iddingsite wrapped by reddish brown matrix. (**b**) PPL photomicrograph from the prismatic pyroxene near vesicles wrapped in palagonite. (**c**) Reflected light photomicrograph showing the crystals of spinel in the matrix.

Pyroclast 2: (**d**) XPL photomicrograph showing hypocrystalline structure, veins and vesicles partially and totally filled by zeolites. (**e**) PPL photomicrograph from the rhombohedral zeolites with low relief and glass volcanic grayish. (**f**) XPL photomicrograph from the pyroxenes intercrossed. (**g**) PPL photomicrograph showing vein of zeolite cutting olivine crystal. (**h**) PPL photomicrograph showing hypocrystalline structure and partial vesicles and fully filled by zeolites. (**i**) XPL photomicrograph from vein of zeolite cutting vesicles filled by zeolite.

Pyroclast 3: (**j**) XPL photomicrograph from the fragments of 2mm pyroclasts with vesicles structure. (**k**) PPL photomicrograph showing fully palagonitized glass and region with white palagonite. (**l**) XPL photomicrograph from the hypocrystalline matrix with vesicles and small crystals of pyroxenes around phenocrystals of fractured olivines. Some olivine crystals are euhedral. XPL = cross polarized light; PPL = plane polarized light; Ol = olivine; Px = pyroxene; Sp = spinel, Zeo = zeolite.

Figure 5.3: Pyroclaste 1: (**a**) Photomicrographie par LPP du phénocristaux d'olivine euhedral avec les frontières modifiées pour le site d'iddingite enveloppé par la matrice brun rougeâtre. (**b**) Photomicrographie par LPP du

pyroxène prismatique près des vésicules enveloppées dans la palagonite. (**c**) Photomicrographie par lumière réfléchie montrant les cristaux de spinelle dans la matrice.

Pyroclaste 2 : (**d**) Photomicrographie par LPX montrant la structure hypocrystalline, les veines et les vésicules partiellement et totalement remplies par des zéolites. (**e**) Photomicrographie par LPP des zéolites rhombohedral avec le bas relief et le grisâtre volcanique de verre. (**f**) Photomicrographie par LPX des pyroxènes croisés. (**g**) Photomicrographie par LPP affichant la veine du cristal d'olivine de découpage de zéolite. (**h**) Photomicrographie par LPP affichant la structure hypocrystalline et vésicules partielles et entièrement rempli par des zéolites. (**i**) Photomicrographie par LPX à partir de veines de vésicules de découpe de zéolite remplies par la zéolite.

Pyroclaste 3: (**j**) Photomicrographie par LPX à partir des fragments de pyroclastes de 2 mm avec structure de vésicules. (**k**) Photomicrographie par LPP affichant le verre entièrement palagonitisé et région avec la palagonite blanche. (**l**) Photomicrographie par LPX de la matrice hypocrystalline avec vésicules et petits cristaux de pyroxènes autour des phénocristaux d'olivines fracturées. Certains cristaux d'olivine sont euhedral. LPX= Polariseur croisés; LPP= Lumière polarisée; Ol = olivine; Px = pyroxéne; Sp = spinelle ; Zeo = zéolite.

Glass – The vitreous mass (glass) is classified as sideromelane due to the basaltic composition of the pyroclasts (**Table 5.1**; **Figures. 5.4b**, **c**). The sideromelane changes to a reddish brown (**Figure 5.3b**) and yellowish brown (**Figure 5.3k**) materials identified as palagonites. In pyroclast 1, the glass is totally palagonitized and it is possible to find only sideromelane in pyroclasts 2 and 3. The reddish colorations are due to a high degree of alteration and high Fe content. In some portions, palagonite is whitish (**Figure 5.3k**) due to leaching of Fe in the reddish brown and yellowish brown palagonite. This process is similar to what was observed in palagonites of Iceland (Thorseth *et al.* 1990). Chemical analyses of the palagonite showed a loss of alkali and alkaline-earth elements (Na, Ca, Mg) and enrichment of Fe and water in relation to the sideromelane (**Table 5.1**) in the reddish and yellowed regions. This composition is similar to those found in palagonites from previous studies such as Peacock (1926, 1928), Thorseth *et al.* (1990), Stroncik & Schmincke (2001, 2002) and Pauly *et al.* (2011). The infrared analyses in the palagonitized regions of pyroclasts 1 and 2 showed the presence of halloysite (**Figure 5.5**). Notably, the characteristic bands of halloysite are observed at about 7070, 7200, and 4530 cm^{-1}. The two former bands are attributed to the first overtones of the Al_2OH stretching vibrations and the latter band to the Al_2OH stretching plus bending combination mode (Madejová *et al.* 2011). Images of TEM confirm the presence of tubular halloysite in the clay fraction of the altered and palagonitized portions of the pyroclasts. The diameter of the spherules and tubes ranges from 0.1 to 0.2 μm (**Figure 5.6**). Figure 5.6b shows a halloysite crystal and a fragment of volcanic glass.

Table 5.1: Micropobre analyses of sideromelane and palagonitized regions.

Tableux 5.1: Analyses de microsonde électronique des régions avec sideromelane et régions palagonitized.

	1-palagonite Figure 5.4a				2-sideromelane Figure 5.4c					2-palagonite Figs. 5.4d, f				3-sideromelane Figure 5.4b			3-palagonite Figure 5.4b		
N°	1	2	3	4	1	2	3	4	5	1	2	3	4	1	2	3	4	5	6
										%									
Na_2O	0.30	0.22	0.23	0.49	5.72	5.51	5.44	6.11	6.21	0.23	0.45	1.12	0.42	3.56	3.65	3.68	0.15	0.04	0.07
SiO_2	25.52	29.82	28.37	32.36	54.62	53.92	50.35	54.87	55.64	16.74	30.84	34.66	30.61	40.37	39.88	39.91	31.85	41.83	40.22
Al_2O	14.76	17.79	14.05	15.67	25.01	23.70	23.28	24.62	24.87	16.24	15.05	20.60	21.95	13.18	13.05	13.03	23.33	8.71	7.64
MgO	1.34	1.86	1.65	3.05	0.11	0.69	0.66	0.14	0.17	0.41	2.24	1.27	0.74	5.04	4.99	5.02	0.72	0.86	0.73
ZnO	0.00	0.02	0.00	0.19	0.07	0.04	0.00	0.04	0.02	0.00	0.00	0.00	0.00	0.09	0.01	0.00	0.03	0.07	0.00
FeO	7.41	8.23	8.60	9.58	0.93	1.26	1.24	0.74	0.82	0.33	4.59	3.18	1.06	11.47	11.48	11.43	4.34	14.93	14.10
SrO	0.00	0.00	0.00	0.00	0.01	0.04	0.05	0.04	0.01	0.02	0.16	2.60	0.30	0.00	0.00	0.00	0.00	0.00	0.00
CaO	2.21	2.18	2.94	8.20	1.63	4.18	4.44	2.11	1.07	1.74	4.26	5.27	5.58	14.72	14.51	14.49	1.53	4.37	4.43
Cr_2O	0.00	0.00	0.00	0.30	0.00	0.09	0.14	0.00	0.06	0.11	0.00	0.00	0.08	0.00	0.04	0.05	0.03	0.00	0.04
P_2O_5	0.54	0.47	0.20	2.30	0.38	0.87	0.19	0.83	0.09	0.48	0.83	1.16	1.90	0.80	0.88	0.83	0.33	1.11	1.24
NiO	0.05	0.02	0.00	0.01	0.00	0.02	0.00	0.00	0.02	0.00	0.01	0.03	0.02	0.00	0.00	0.00	0.04	0.00	0.03
K_2O	0.12	0.15	0.18	0.09	0.23	0.13	0.24	0.15	0.16	0.34	0.57	3.60	1.06	3.80	3.91	3.85	0.48	0.58	0.65
MnO	0.07	0.06	0.08	0.09	0.03	0.00	0.06	0.00	0.02	0.00	0.07	0.18	0.00	0.19	0.15	0.17	0.00	0.00	0.00
SO_3	0.04	0.06	0.02	0.13	0.02	0.06	0.07	0.01	0.02	0.47	0.02	0.04	0.07	0.19	0.18	0.16	0.13	0.01	0.00
TiO_2	2.51	2.66	3.97	4.79	0.36	0.42	0.53	0.39	0.49	0.17	3.48	0.29	0.28	5.84	5.82	5.80	0.28	8.17	8.15
Total	54.86	63.53	60.28	77.24	89.11	90.91	86.68	90.06	89.68	37.28	62.56	74.00	64.06	99.24	98.55	98.41	63.25	80.68	77.29

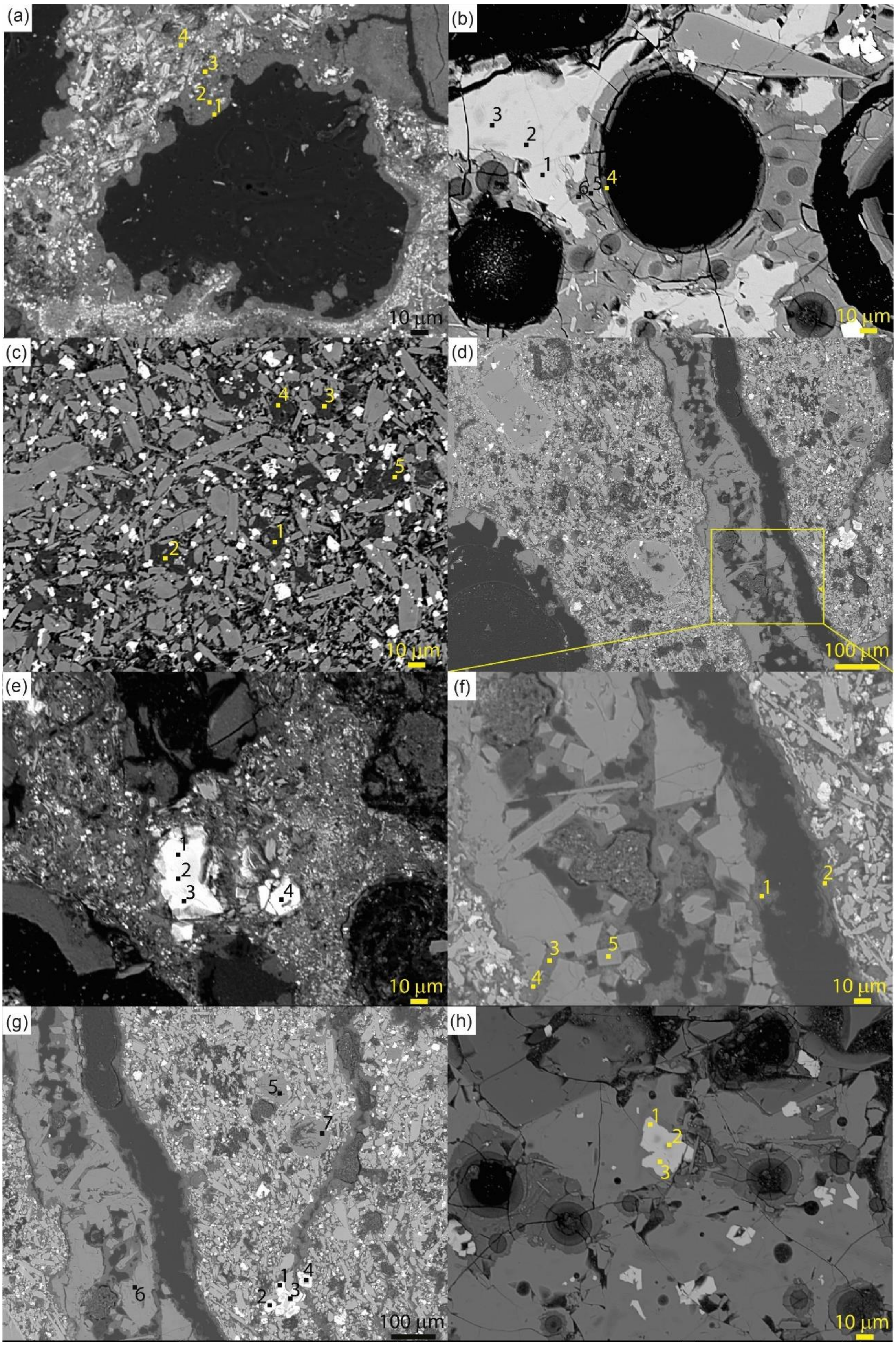

Figure 5.4: SEM photomicrograph and point of microchemical analyses by micropobre of pyroclasts. Pyroclast 1: (**a**) Punctual analysis of the palagonite in the wall and around a vesicle, (**e**) Punctual analysis of two spinel crystals.

Pyroclast 2: (**c**) Punctual analyses in sideromelane in the microlytic matrix, (**d**) and (**f**) Punctual analyses in a fracture filled by zeolites and palagonite. (**g**) Analysis of amygdales filled by zeolites and analysis of spinels crystals.

Pyroclast 3: (**b**) Analysis of sideromelane and its alteration to palagonite., (**h**) Analyses of zoned spinel crystals.

Figure 5.4 : Photomicrographie par MEB et point d'analyse microchimique par microsonde électronique des pyroclastes. Pyroclaste 1: (**a**) Analyse ponctuelle de la palagonie dans le mur et autour d'une vésicule, (**e**) l'analyse ponctuelle de deux cristaux des spinelles.

Pyroclaste 2: (**c**) Analyses ponctuelles dans le sideromelane dans la matrice microlytique, (**d**) et (**f**) analyses ponctuelles dans une fracture remplie par les zéolites et les palagonites. (**g**) Analyse des amygdales remplies de zéolites et analyse des cristaux de spinelles.

Pyroclaste 3: (**b**) Analyse du sideromelane et de son altération en palagonite., (**h**) Analyses des cristaux des spinelles zonés.

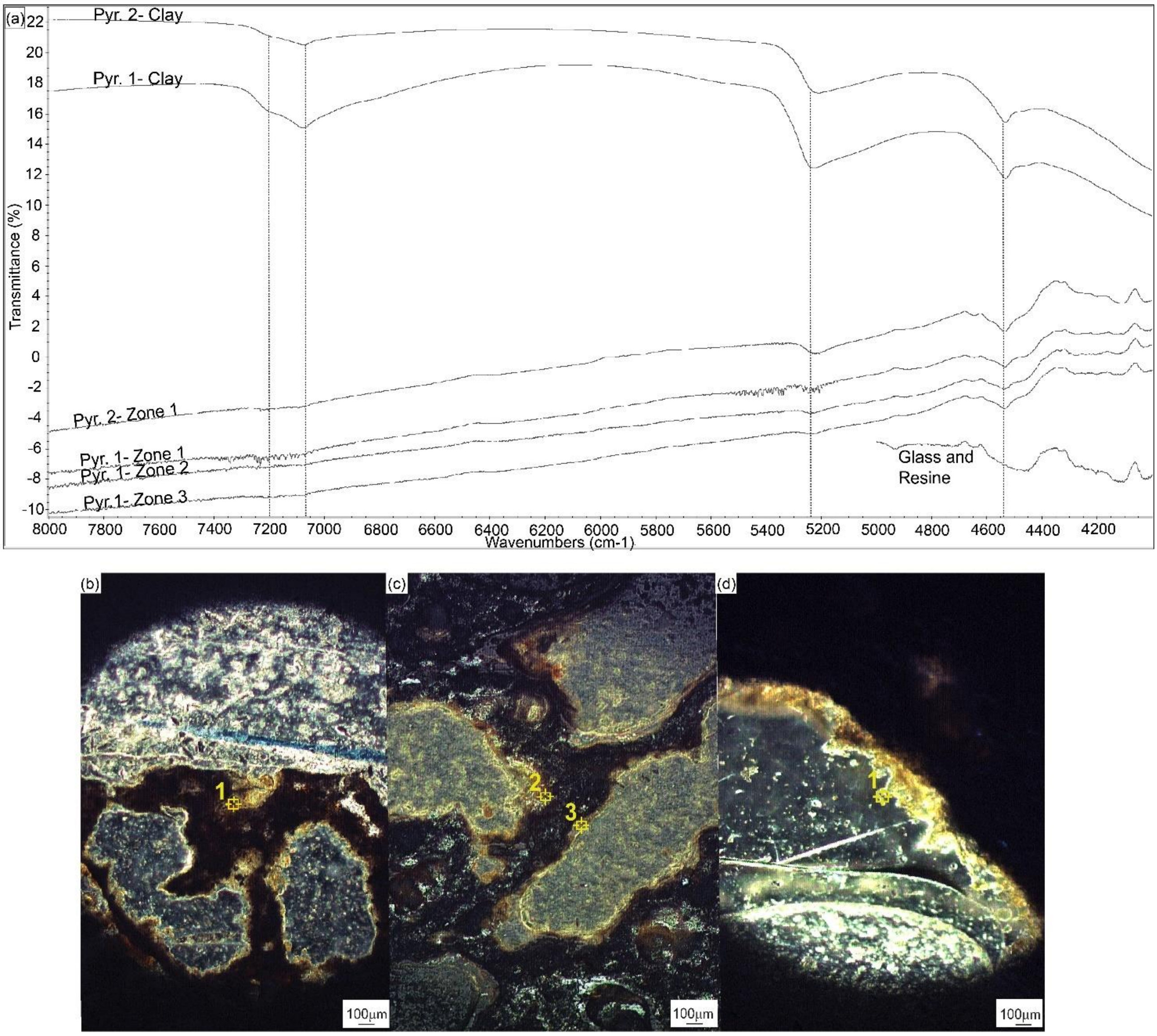

Figure 5.5: (**a**) NIR analysis of clay and palagonitized portions of pyroclast 1 and 2 showing the presence of halloysite. The clay analysis was used to compare the positions of the signals between 7000 and 7230 cm^{-1}, since the signal in the palagonitized region is weak due to thickness and resin of the slender section. The spectrum of resine and glass was obtained to show the regions when occurs signal of resine and glass in spectrum of thin

section. **b**, **c** and **d**) XPL photomicrograph in regions palagonitized and points of the analysis of the pyr. 1 (**b** and **c**) and pyr. 2 (**d**). Pyr=pyroclasts.

Figure 5.5 : (**a**) Analyse d'Infrarouge Proche des parties d'argile et de régions palagonitisées des pyroclaste 1 et 2 montrant la présence d'halloysite. L'analyse de l'argile a été utilisée pour comparer les positions des signaux entre 7000 et 7230 cm^{-1}, puisque le signal dans la région palagonitisée est faible en raison de l'épaisseur et de la résine de la lame mince. Le spectre du verre e de résine a été obtenu pour montrer les régions quand se produit le signal de résine et de verre dans le spectre de la lame mince. (**b**), (**c**) et (**d**) photomicrographie LPX dans les régions palagonitisées et les points de l'analyse du pyr. 1 (**b** et **c**) et pyr. 2 (**d**). Pyr=pyroclaste.

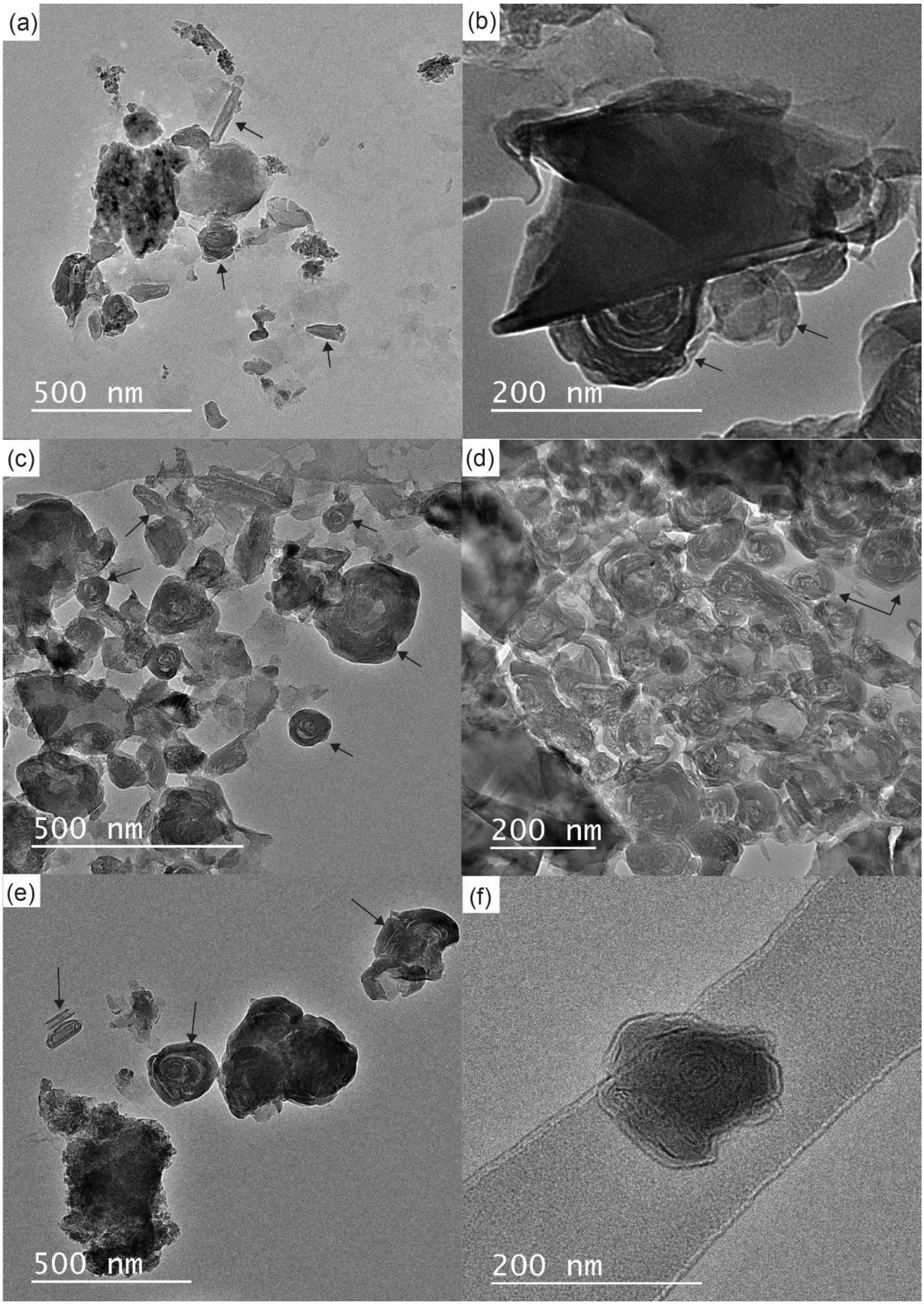

Figure 5.6: TEM images of halloysites in clay fraction of altered regions of the pyroclast 1 (**a**), 2 (**c**), and 3 (**e**) and halloysites in regions with palagonitization (pyroclast 1-**b**, 2-**d** and 3-**f**). In all figures the arrows indicate the tubular halloysite crystals. The figure b shows the fragment of volcanic glass on halloysite crystals. In the lower left corner of figure d occurs a fragment of pyroxene.

Figure 5.6 : Images de MET d'halloysites dans la fraction d'argile des régions modifiées du pyroclaste 1 (**a**), 2 (**c**), et 3 (**e**) et halloysites dans les régions avec palagonitisation (pyroclaste 1-b, 2-d et 3-f). Dans toutes les figures, les flèches indiquent les cristaux tubulaires de l'halloysite. La figure b montre le fragment de verre volcanique sur les cristaux de l'halloysite. Dans le coin inférieur gauche de la figure d se produit un fragment de pyroxène.

Olivine – Olivine is euhedral, forsterite (Fo_{80}) in composition (Mateus *et al.* 2018) and makes up 20 % of the rock in all the pyroclasts. The olivine phenocrysts in pyroclast 1 are essentially altered and fractured with axis sizes greater than 1mm (**Figure 5.3a**). The fractures and edges of these altered and fractured olivine phenocrysts in pyroclasts 1 are filled and corroded with reddish dark brown colored iddingsite (**Figure 5.3a**). However, well preserved olivine phenocrysts with sizes ranging from 0.5mm to 3mm dominate pyroclasts 2 and 3 (**Figures. 3d**, **l**).

Pyroxene – The pyroxenes were observed as very small crystals about of 0.07 mm in the form of microliths in the vitreous matrix and present in trace amount (5 %) in pyroclast 1 (**Figure 5.3b**). Pyroxenes in pyroclast 2 are mostly tiny (0.02 mm), dispersed in the matrix and surround the olivine phenocrysts with high interference colors, and are present in small amount (15 %). However, largest crystals of ~120 mm are rarely found (**Figure 5.3f**). In the pyroclast 3, prismatic pyroxenes, constituting about 25 %, are tiny (~ 0.02 µm) and occur within the microlytic matrix and surrounding the olivine phenocrysts (**Figure 5.3l**). Electron microprobe micro-chemical analyses show that the pyroxenes in pyroclasts 1 and 2 are diopside (**Table 5.2**; **Figure 5.7**). TEM analyses also show occurrence of fragments of pyroxene in clay fraction (**Figure 5.6d**).

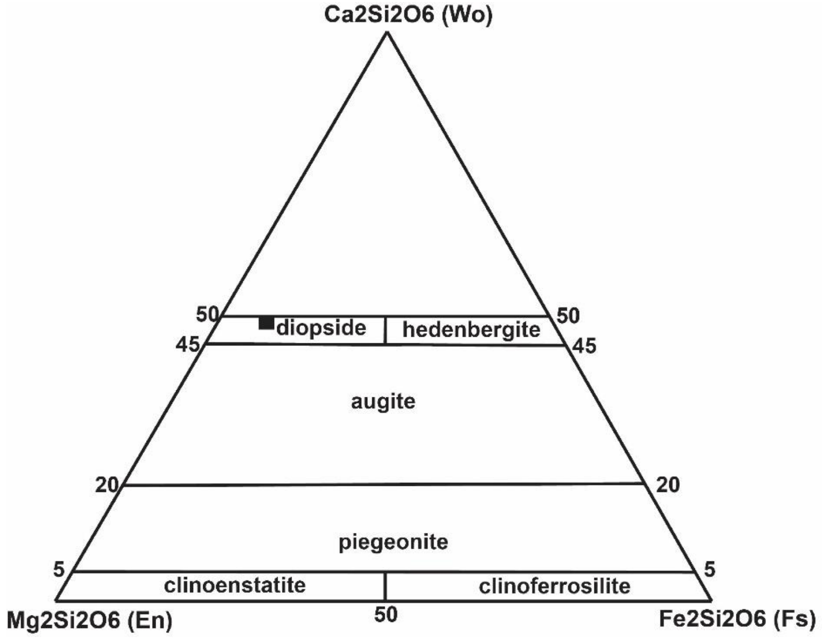

Figure 5.7: Morimoto diagram (1988) modified showing the composition of the clinopyroxene. The square indicates the pyroclasts 1 and 2.

Figure 5.7 : Diagramme de Morimoto (1988) modifié montrant la composition des clinopyroxene. Le carré indique les pyroclastes 1 et 2.

Table 5.2: Micropobre analyses with ions calculated for clinopyroxene.

Tableau 5.2 : Analyses de microsonde électronique avec des ions calculés pour les clinopyroxene.

	1-Diopside	2-Diopside				
Region	Core	Edge	Interm.	Edge	Edge	Edge
SiO_2	41.33	42.79	47.36	47.41	47.30	46.41
TiO_2	6.54	5.61	2.95	3.17	3.48	3.97
Al_2O_3	9.39	8.58	4.37	5.27	5.33	5.42
FeO	7.70	7.61	7.50	6.43	6.74	7.43
MgO	10.93	11.72	16.87	13.67	13.42	13.08
MnO	0.06	0.05	0.14	0.12	0.12	0.13
CaO	23.56	23.87	21.62	23.30	23.73	23.76
Na_2O	0.43	0.46	0.29	0.29	0.32	0.35
Cr_2O_3	0.00	0.00	0.00	0.00	0.00	0.00
NiO	0.00	0.00	0.00	0.00	0.00	0.00
K_2O	0.03	0.02	0.02	0.05	0.03	0.02
Total	100.01	100.71	101.12	99.69	100.47	100.58
Calculation based on 6 oxygens						
Si	1.57	1.61	1.76	1.78	1.77	1.74
Ti	0.19	0.16	0.08	0.09	0.10	0.11
Al	0.42	0.38	0.19	0.23	0.23	0.24
Fe	0.25	0.24	0.23	0.20	0.21	0.23
Mg	0.62	0.66	0.93	0,76	0.75	0.73
Mn	0.00	0.00	0.00	0.00	0.00	0.00
Ca	0.96	0.96	0.86	0.94	0.95	0.95
Na	0.03	0.03	0.02	0.02	0.02	0.03
Cr	0.00	0.00	0.00	0.00	0.00	0.00
Ni	0.00	0.00	0.00	0.00	0.00	0.00
K	0.00	0.00	0.00	0.00	0.00	0.00
Ens	0.34	0.35	0.46	0.4	0.39	0.38
Fs	0.13	0.13	0.12	0.11	0.11	0.12
Wo	0.53	0.52	0.42	0.49	0.50	0.50

Spinels – Spinels are commonly observed dispersed in the matrix of the pyroclasts, and within the fractures and edges of olivine phenocrysts in varying trace amounts (5 – 10 %; **Figure 5.3c**). The crystals are anhedral and are about 0.05 mm in size. Electron microprobe analyses shows that the spinels are titaniferous magnetites, and some crystals display Cr-rich and Cr-poor zones (**Table 5.3**; **Figures 5.4e**, **g**, **h**). Due to the degree of alteration of the spinels, it was difficult and nearly impossible to determine their chemical composition as none of the analysis was close to 100 %.

Table 5.3: Chemical analysis by microprobe of the spinels of the pyroclasts 1, 2 and 3.

Tableau 5.3 : Analyse chimique par microsonde électronique des spinelles des pyroclastes 1, 2 et 3.

	1				2				3		
	Figure 5.4e				Figure 5.4g				Figure 5.4h		
Region No.	Edge 1	Core 2	Edge 3	Core 4	Edge 1	Edge 2	Core 3	Core 4	Edge 1	Core 2	Edge 3
%											
SiO_2	0.04	0.07	0.00	0.06	0.14	0.04	0.03	0.09	0.05	0.00	0.03
Al_2O_3	4.96	6.12	5.44	5.74	2.14	8.29	18.07	7.25	5.18	21.755	5.29
MgO	5.63	9.52	8.09	7.26	1,267	3.83	11.67	4.40	8.01	10.789	8.15
FeO	56.60	50.10	53.13	54.64	71.99	61.453	33.44	62.03	60.61	37.396	59.67
Cr_2O_3	0.88	6.88	6.28	2.48	3.19	5.47	2.96	8.69	1.97	20.434	3.10
MnO	0.36	0.42	0.47	0.77	0.18	0.29	4.07	0.44	0.39	0.13	0.45
TiO_2	21.77	16.70	17.74	20.18	10.392	9.12	2.30	5.34	18.94	4.65	17.93
Total	90.30	89.80	91.15	91.13	89.307	88.501	93.55	88.24	95.75	9549	95.05
Calculation based on 4 oxygens											
Si	0.001	0.002	0.002	0.002	0.002	0.002	0.002	0.002	0.002	0.002	0.002
Ti	0.622	0.561	0.561	0.561	0.561	0.561	0.561	0.561	0.561	0.561	0.561
Al	0.222	0.250	0.250	0.250	0.250	0.250	0.250	0.250	0.250	0.250	0.250
Cr	0.027	0.073	0.073	0.073	0.073	0.073	0.073	0.073	0.073	0.073	0.073
Fe^{+2}	0.506	0.550	0.550	0.550	0.550	0.550	0.550	0.550	0.550	0.550	0.550
Fe^{+3}	1.293	1.139	1.139	1.139	1.139	1.139	1.139	1.139	1.139	1.139	1.139
Mn	0.012	0.024	0.024	0.024	0.024	0.024	0.024	0.024	0.024	0.024	0.024
Mg	0.319	0.400	0.400	0.400	0.400	0.400	0.400	0.400	0.400	0.400	0.400

Zeolite – In pyroclast 2, amygdales and microfractures are partially to completely fill by zeolites (**Figures. 5.3d**, **e**, **h**). The zeolites are small pseudorhombohedral crystals (**Figure 5.3e**), mostly less than 20 µm, with low interference colors, and constitute about 10% in thin section observations. The zeolites filled microfractures sometimes crosscut the olivine crystals (**Figures. 5.3g**, **i**) and vesicles (**Figure 5.3i**), suggesting their latter and secondary crystallization. The zeolites also crystallize in the walls of the palagonitized portions (**Figure 5.4f**).

Electron microprobe analyses of the zeolites in pyroclast 2 shows that they are predominantly heulandite-Ca and chabazite-Ca (**Table 5.4**; **Figs. 5.4f**, **g**). Both the heulandite-Ca and chabazite-Ca are found in the amygdales filled zeolites while those in the microstructure veins are essentially chabazite-Ca. The average calculated structural formula is $(Ca_{3.17}Na_{0.85}K_{4.28})_{8.3}(Si_{21.58}Al_{10.34})O_{72}.26H_2O$ and $Ca_{1.31}(Al_{4.42}Si_{7.6}O_{24}).13H_2O$ for the heulandite-Ca and chabazite–Ca, respectively. The Si:Al ratios are relatively low in the heulandite-Ca (2.08) and chabazite-Ca (1.74).

Table 5.4: Chemical analysis by microprobe of the zeolites of the pyroclast 2.

Tableau 5.4 : Analyse chimique par microsonde életronique des zéolites du pyroclaste 2.

Mineral	Heulandite-Ca	Chabazite-Ca	Chabazite-Ca	Chabazite-Ca
Region	Amygdale filled Figure 5.4g	Fracture Figure 5.4g	Fracture Figure 5.4f	Amygdale partially filled Figure 5.4g
N°	5	6	5	7
		%		
SiO_2	48.21	47.09	45.87	49.18
TiO_2	0.09	0.05	0.00	0.00
Al_2O_3	19.60	23.25	24.02	23.92
FeO	1.06	0.18	0.24	0.32
MgO	0.13	0.20	0.05	0.30
MnO	0.05	0.00	0.00	0.00
CaO	6.60	7.57	8.74	7.52
Na_2O	0.49	0.13	0.36	0.31
K_2O	4.24	0.69	4.98	0.91
Cr_2O_3	0.03	0.04	0.00	0.00
H_2O	19.50	20.80	14.23	17.54
Total	100.00	100.00	100.00	100.00
	Calculation based on 98 oxygens	*Calculation based on 36 oxygens*		
Si	21.58	7.60	8.08	8.16
Ti	0.00	0.00	0.00	0.00
Al	10.34	4.42	4.99	4.68
Fe	0.40	0.02	0.04	0.04
Mg	0.09	0.05	0.01	0.08
Mn	0.02	0.00	0.00	0.00
Ca	3.17	1.31	1.65	1.34
Na	0.85	0.08	0.25	0.20
K	4.84	0.28	2.24	0.38
Cr	0.00	0.00	0.00	0.00
H	65.50	25.18	18.82	21.84

Geochemical of pyroclasts – The pyroclasts are undersaturated with silica (~ 37 %). Na_2O content is higher than K_2O in pyroclasts 1 and 2 but lower in pyroclast 3 (**Table 5.5**). All the pyroclasts plot in the ultrabasic rocks and foidites fields on the $Na_2O + K_2O$ vs SiO_2 TAS classification diagram (**Figure 5.8**; Les Bas *et al.* 1986). The high FeOt, MgO, TiO_2 and CaO contents in all the pyroclasts (**Table 5.5**) are probably due to the presence of ferromagnesian minerals such as magnetites, olivines, ilmenites and clinopyroxenes. The pyroclasts are also enriched in trace elements, such Ba, Cr, Sr, V, Zr, Zn and Ce (**Table 5.5**). The elevated trace elements contents are related to the presence of pyroxenes as shown by Panina & Stoppa (2009) who documented the enrichments of trace elements in clinopyroxenes in foidian olivine in southern Italy. Moreover, the pyroclasts display strong enrichments of light rare earth elements (LREE) over the heavy rare earth elements (HREE) (∑LREE/∑HREE = 12.38 to 13.71; La/Yb= 33.55 to 40.85, **Table 5.5** and **Figure 5.9**).

Table 5.5: Chemical analyses of the major elements, trace and REE in representative samples of pyroclasts of the Vulcão do Paredão (1) and Morro Vermelho (2 and 3). LQ = quantification limit, LOI=loss on ignition.

Tableau 5.5 : Analyses chimiques des principaux éléments, traces et terres rares dans des échantillons représentatifs de pyroclastes du Vulcão do Paredão (1) et du Morro Vermelho (2 et 3). LQ = limite de quantification, LOI=perte au feu.

	Pyroclasts													
	%													
	SiO_2	Al_2O_3	FeO_t	TiO_2	CaO	Na_2O	K_2O	MgO	MnO	P_2O_5	LOI	K_2O/ Na_2O	Total	
1	37.47	14.68	19.58	6.95	5.43	0.53	0.15	4.50	0.30	1.36	9.05	0.28	100.00	
2	37.50	11.95	16.09	5.36	11.15	0.57	0.27	7.37	0.27	1.48	7.99	0.47	100.00	
3	37.81	13.38	18.46	7.31	3.50	0.29	0.48	3.67	0.30	0.86	13.95	1.65	100.00	
	Ppm													
	As	Ba	Co	Cr	Cu	Li	Mo	Ni	Sr	Th	V	Zn	Be	Sb
1	<LQ	1377.45	127.12	252.82	44.73	14.35	<LQ	115.04	1240.76	33.40	248.97	145.55	1.08	<LQ
2	<LQ	1608.22	92.73	363.23	75.9	10.94	<LQ	127.93	1592.12	39.5	302.20	128.11	1.00	<LQ
3	<LQ	1887.55	116.35	472.19	87.47	9.69	<LQ	115.02	566.09	32.02	275.81	172.75	1.13	<LQ
	Zr	Pb	S	Sc	Ga	Y	Cd	In	Cs	La	Ce	Pr	Nd	Sm
1	314.24	<LQ	220.20	34.83	33.44	42.62	1.86	0.15	1.04	101.82	267.19	27.42	109.93	20.58
2	279.70	<LQ	110.88	29.49	28.96	48.56	0.88	0.12	0.75	124.19	299.11	32.55	131.87	24.14
3	308.19	<LQ	65.44	37.16	33.80	41.28	0.50	0.16	0.62	89.93	229.24	23.99	97.44	18.72
	Eu	Gd	Tb	Dy	Ho	Er	Tm	Yb	Lu	Tl	Pb	Bi	Th	U
1	6.34	18.01	2.00	10.1	1.67	4.03	0.46	2.56	0.35	<LQ	4.19	<LQ	8.86	2.51
2	7.28	20.60	2.25	11.26	1.87	4.66	0.53	3.04	0.41	<LQ	10.64	<LQ	11.09	2.68
3	5.85	16.37	1.87	9.67	1.64	4.04	0.48	2.68	0.36	<LQ	12.23	0,043	8.81	2.01

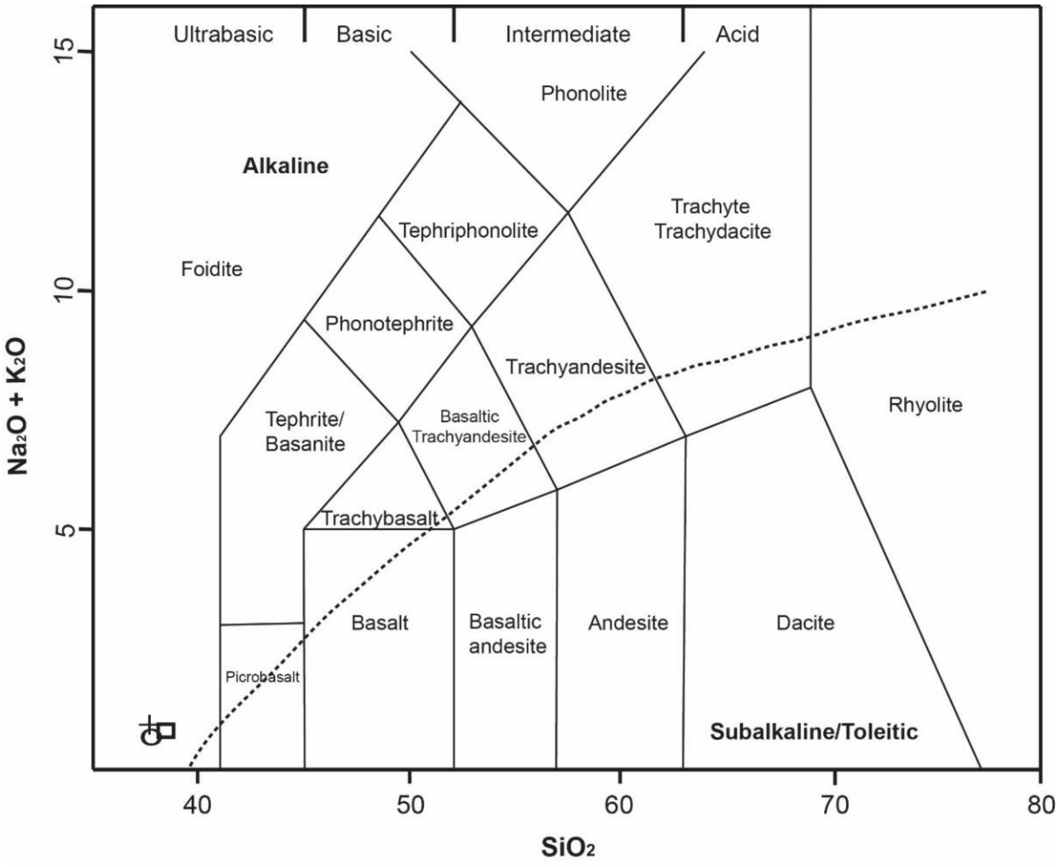

Figure 5.8: TAS diagram (Les Bas *et al*. 1986) for the pyroclasts 1 (circle) of the Vulcão do Paredão and, 2 (cross) and 3 (square), both of Morro Vermelho formation.

Figure 5.8 : Diagramme TAS (Les Bas *et al*. 1986) pour les pyroclastes 1 (cercle) du Vulcão do Paredão et 2 (croix) et 3 (carré), tous deux de la formation de Morro Vermelho.

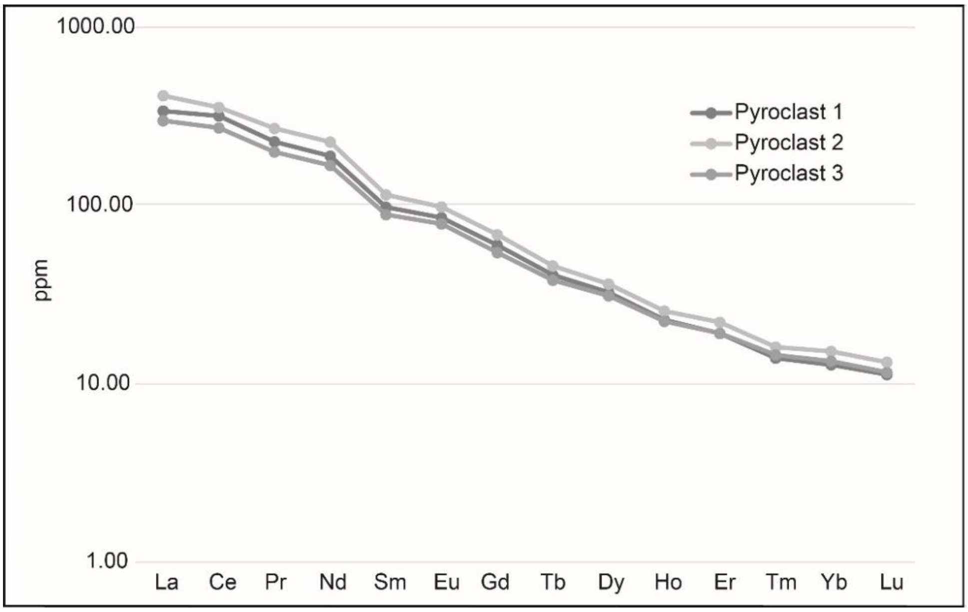

Figure 5.9: Typical chondrite-normalized (McDonough & Sun 1995) rare-earth-element (REE) plots of pyroclasts.

Figure 5.9 : Diagramme des terres rares des pyroclastes normalisé par le chondrite (McDonough & Sun 1995).

5.4 – DISCUSSIONS

5.4.1- The eruption type and the alteration process of pyroclasts

According to Walker and Croasdale (1971), the eruptions during the formation of pyroclastic deposits can be regarded as Strombolian-type by producing initially coarse materials, with a restricted range of sizes. This affirmation is attested in this study by the presence of blocks and lapillis. Additionally, the high vesicularity and fluidal shape presented by the fragments, that indicate degassing and magmatic fragmentation, are characteristic of Strombolian-type eruption (Vergniolle & Brandeis 1996, Vergniolle *et al.* 1996, Houghton *et al.* 1999). The Strombolian-type eruption is supported by studies of Pasqualon (2017) and Luz (2016) on pyroclasts deposits in the areas of this study.

The main alteration products of pyroclasts are: palagonite, iddingsites, halloysite and zeolites.

The palagonite is the result of alteration of sideromelane and its presence is characterized by regions with reddish and yellowish color due to the relative concentration of iron due to the loss of more mobile chemical elements such as Na, K, Mg. An explanation for the formation of palagonite would be a phreatomagmatic eruption that occurred when the ascending magma came into contact with sea water at high tide. The process of palagonitization by the phreatomagmatic eruption has been previously described in volcanic islands, such as the Azores, Hawaii (Wentworth 1926, Stearns & Vaksvik 1935) and Oshima (Nakamura 1961); and in lakes or low ground with a high groundwater in Auckland (Searle 1965), Idaho (Hamilton & Bvers 1963) and Iceland (Einarsson 1965). According to Bonati (1965), hydration of the lava is probably faster at higher temperatures when the lava is still in a molten state. During this phase, the hydrous lava forms directly hydrated glass (palagonite). This process seems to have occurred in the pyroclast 2 because there is a large amount of yellowish brown palagonite with little sideromelane.

Following the complete consolidation of magma and the alteration of volcanic glass as a result of seawater interaction, the pyroclasts underwent a second phase of alteration due to exposure to meteoric water. The presence of halloysite in the palagonitized sideromelane attested by infrared and MET analyses; the crystals of olivine and amigdals cut by zeolites veins, the presence of zeolites crystallized in palgonitized regions; and the presence of iddingsitized olivines (see Mateus *et al.* 2018) corroborate this proposition.

Alterations of sideromelane to zeolites have been described in palagonite tuffs from Oahu, Hawaii (Hay & Iijima 1968, Iijima & Harada 1969) and Iceland (Nayudu 1964). The probable formation of zeolites in pyroclast 2 would to be the reaction of sideromelane with meteoric fluid in temperature around of 100 °C. According to Kristmannsdóttir & Tómasson (1978), heulandite, stilbite and analcime may form at temperatures below 100°C. Barrows (1980) described heulandite, clinoptilolite, mordenite, analcime, thomsonite, erionite and chabazite in thick Miocene volcaniclastic sequences in Nevada attributed to a process involving the circulation of low temperature meteoric fluid in an open hydrologic system. Höller & Wirsching (1980) observed the formation of chabazite, phillipsite, and analcime in the reaction of nephelinite with a solution of 0.01 N NaOH at 150 °C in open system.

In this study, the meteoric water reacted with the vitreous matrix of the rock to form the palagonite and precipitated the Si, Al, Ca, Na, and K in the form of zeolites in the adjacencies of the palagonite, similar to the one described by Hay & Iijima (1968) and Iijima & Harada (1969) in zeolithic palagonite tuffs. The occurrence of zeolites impoverished in silica is due to the low silica contents in the pyroclasts and primary basaltic magma.

In all pyroclasts occur olivines iddingsitized by meteoric water. The difference in the degree of preservation or alteration of olivine phenocrysts between VP (pyroclast 1) and MV (pyroclasts 2 and 3) is related to their position on the sampling profile (Mateus *et al*. 2018). The pyroclast 1 was collected at higher altitude and in a more humid region, exposing it to greater leaching and alteration processes compared to pyroclasts 2 and 3 that were collected from much lower altitude with less exposure to alterations. Mateus *et al*. (2018) argue that the presence of iddingsite in the high altitude and humid region indicates an advanced alteration stage of the olivine crystals during weathering.

5.4.2- Magma genesis considerations

The presence of spinels enriched with chromium and the LREE enrichment indicate that the magma has a mantelic origin (Irvine 1965).

The strongly fractionated REE patterns suggest the presence of garnet as a probable residual phase, implying that melt generation occurred at depths of about 100 km. This interpretation is corroborated by the earlier work of Marques *et al*. (1999), who suggested a garnet magma source at deeper depth (~ 100 km) for the olivine-nephelinites in the VP Formation and proven by Bongiollo *et al*. (2015) through geochemical modeling.

5.5– CONCLUSIONS

The Quaternary pyroclastic rocks of the Vulcão do Paredão (Holocene) and Morro Vermelho (Pleistocene) showed the following products of alteration:

1- sideromelane palagonitized through the interaction of magma with the sea water and subsequently with meteoric water;

2- particularly in the pyroclast 2, the palagonite alters to form zeolite and halloysite through the passage of hydrothermal fluids and meteoric waterduring weathering.

The main factors justifying this assertion are:

1- in the palagonitized regions there is a loss of bases (Na, Ca, Mg) and an enrichment of Fe and water in relation to the sideromelane;

2.1- the chemical analysis by microprobe showed the presence of zeolites alongside the palagonite;

2.2- the point-source analyses of infrared allow to identify halloysite in the palagonite of pyroclast with totally altered sideromelane;

2.3- TEM observations confirm the presence of halloysite in the palagonitized regions.

In addition, the presence of palagonite may indicate a phreatomagmatic eruption for these deposits.

CHAPITRE 6

L'ÁLTERATION DES OLIVINES[2]

ABSTRACT

The alteration of olivine (forsterite) phenocrysts in three soil profiles that were developed on similar pyroclastic rocks from Trindade Island, at different altitudes and degree of development, were investigated in this study. Optical microscopy, Electron Probe Microanalysis (EPMA), Scanning Electron Microscopy (SEM), X-Ray Diffraction (XRD) and Differential Thermal and Thermogravimetric Analysis (DTA-TGA) were used to determine the mineralogical, micromorphological and geochemical transformations resulting from the alteration process. Micromorphological analyses showed fractured phenocrysts of colorless olivines with high relief at plane polarized light. These crystals are euhedral and irregularly shaped and distributed in a dark reddish brown matrix constituted by pyroxenes, magnetites, ilmenites, halloysite, hematite and anatase. At crossed polarized light, the olivine phenocrysts display a rim of reddish brown material in the fractures and in the borders that extinguishes parallel to their extinction direction. This reddish brown material appears to invade the crystal progressively until a complete replacement towards the top of the soil profile of higher altitude and degree of development. The olivine was identified as forsterite type and the reddish brown material has a chemical composition of Si, Fe, Mg, Al, Ca, Na, K, Mn and Ti, with predominant and variable contents of Fe, Si and Mg. The chemical composition and optical features are consistent with that found in iddingsites which may form through the incipient alteration of olivines due to the oxidation of ferrous iron to ferric iron, and with the coordination of magnesium with hydroxyl groups. The microscopic features of olivine did not allow us to identify any previous alteration by either deuteric or hydrothermal processes. However, the advance of the alteration towards the soil profile, leaving only relicts of olivine crystals or reaching their total transformation in the upper horizons, shows that weathering is the main process of iddingsite formation. This finding is corroborated by the presence of greater alteration of olivine crystals in the topmost soil at the highest altitude on the same lithology.

Keywords: iddingsite, forsterite, pyroclastics, Brazil

---

[2] Article publiée au magazine, "Aplyed Clay Scince", v. 160., p. 40-48, 2018, avec le titre "Alteration of olivine in volcanic rocks from Trindade Island, South Atlantic."

6.1 – INTRODUCTION

Iddingsites are formed from the alteration of olivines and are very common in rocks of basic volcanism. The first studies about the iddingsites were portrayed in the 19th century. Lawson (1893) proposed the name iddingsite in honor of the geologist and petrologist Joseph Paxson Iddings, for phenocrysts found in basaltics rocks of the region of California. According to Lawson (1893), the iddingsites in hand samples are soft, brittle, with well developed cleavage and, under optical microscopy, show colors varying from brown to light yellow with pronounced pleochroism in transversal position to their cleavage. The chemical formula of iddingsite, $MgO \cdot Fe_2O_3 \cdot 3SiO_2 \cdot 4H_2O$, was deduced by Ross and Shannon (1925). They concluded that iddingsite would be a deuteric mineral formed at the end of the lava cooling and not a weathering product. Edwards (1938) also proposed that iddingsite was formed during and after the magma consolidation. Through XRD analyses, Sun (1957) showed that the iddingsites are a complex product of olivine alteration and not a single mineral. Haggerty & Baker (1967), Champness (1970), Goode (1974) and Gualtieri *et al.* (2003) observed the formation of hematite, magnetite and orthopyroxene during high temperature oxidation experiments on olivine. Additionally, several authors have studied high-temperature iddingsite (HTI) with similar composition (orthopyroxene, maghetite, hematite, cristobalite and amorphous silica) within continental and oceanic basalt flows (Goff 1996, 1977; Caroff *et al.* 2000, 1999, 1997) and in gabbroic intrusions (Clément *et al.* 2007). Tschegg *et al.* (2010) observed a systematic HTI like corrosion phenomenon of olivine phenocrysts in alkaline lavas and because they did not observed real iddingsite formation they called this phenomenon high temperature corrosion (HTC) of olivine. The low temperature iddingsite (LTI) present composition different from that of HTI, a intimate mixture of hydrous iron and magnesium silicates (goethite, montmorillonite, illite, chlorite) as described by Gay & Le Maître (1961), Fawcett (1965), Le Maître *et al.* (1966), Baker & Haggerty (1967), Schandl *et al.* (1990), Schenato *et al.* (2003), Talbi & Honnorez (2003). Gay & Le Maître (1961) described the XRD standard of several phases that occur in LTI: as olivine-like, goethite-like, hematite-like, spinel-like and silicate structures. Baker & Haggerty (1967), observed that inalteration under oxidizing conditions at low temperature, probably below 140°C, produces iddingsite with goethite and smectite. Delvigne *et al.* (1979) also proposed that the iddingsite is composed by a mixture of cryptocrystaline goethite and possibly hematite, with smectite, chlorite, micas and rarely talc. Talbi & Honnorez (2003) described an orange or reddish material with intermediate composition between Fe-oxyhydroxides and phyllosilicates, chemically similar to iddingsite, in tholeiitic basalts that were affected by low temperature alteration. Through the transmission electronic microscopy, Eggleton (1984) showed saponites and goethites in iddingsites in olivine borders of basanites in Germany. A few years later, Smithetal *et al.* (1987) demonstrated that the olivine alteration model in iddingsites proposed by Eggleton (1984) was applicable to olivine alterations from Australia region. Gerard *et al.* (2007) described the presence of iddingsite in basaltic pyroclasts on Faial and Pico islands (Azores). Recent studies performed on meteorites with iddingsitized olivine

(Kuebler 2013, Lee *et al.* 2015) showed iddingsite formed during the final stages of magma consolidation.

In the volcanic islands of the Brazilian territory, specifically in the island of Trindade, object of this study, Antonello *et al.* (2009) described basaltic composition rocks with partially or totally altered olivines to serpentine, carbonates and iddingsites. However, these studies dealt with an essentially petrographic description, without involving a detailed microscopic and microchemical analysis that allowed to investigate the processes of alteration of the olivines and the evolution of this alteration along the soil profiles. In order to overcome this lack of research in Trindade, the present work aims to investigate the alteration of olivines into iddingsite in the pyroclastic rocks, to define the composition of iddingsite and to understand low temperature conditions of its formation, by using optical microscopy, X-Ray Diffraction (XRD), Differential and Thermo Gravimetric Analysis (DTA-TGA), Electron Probe Microanalysis (EPMA) and Scanning Electron Microscopy (SEM).

6.2 – MATERIALS AND METHODS

Trindade Island, with a surface of 13 km^2, is located in the South Atlantic at 1140 km from the Brazilian coast (**Figure 6.1**). The island is part of an extensive submarine volcanic chain of east-west orientation, denominated Vitória-Trindade, and constitutes the superior portion of a volcanic building rising 5.2 km from the ocean floor (Almeida 2002, Alves *et al.* 2006). The study area is located in the south-eastern part of the island in three soil profiles developed on pyroclastic rocks, MV1, MV2 and MV3, respectively at 460, 351 and 258 m of elevation (**Figure 6.1**).

The MV1 is from the Vulcão do Paredão and, MV2 and MV3 from the Morro Vermelho Formation. Macromorphological descriptions and samplings of pyroclastic rocks and soil horizons were performed on all three profiles (**Figure 6.1**). Particle size was determined by the total dispersion method according to Donagema *et al.* (2011). After vertical shaking for 16 h with sodium hexametaphosphate solution as a dispersant, the clay content was determined by the pipette method, the gravel, coarse and fine sand were separated by sieving, and silt content was obtained by the difference of the sum of the other fractions in relation to the original sample. The structure descriptions were made according to Schoeneberger *et al.* (2012).

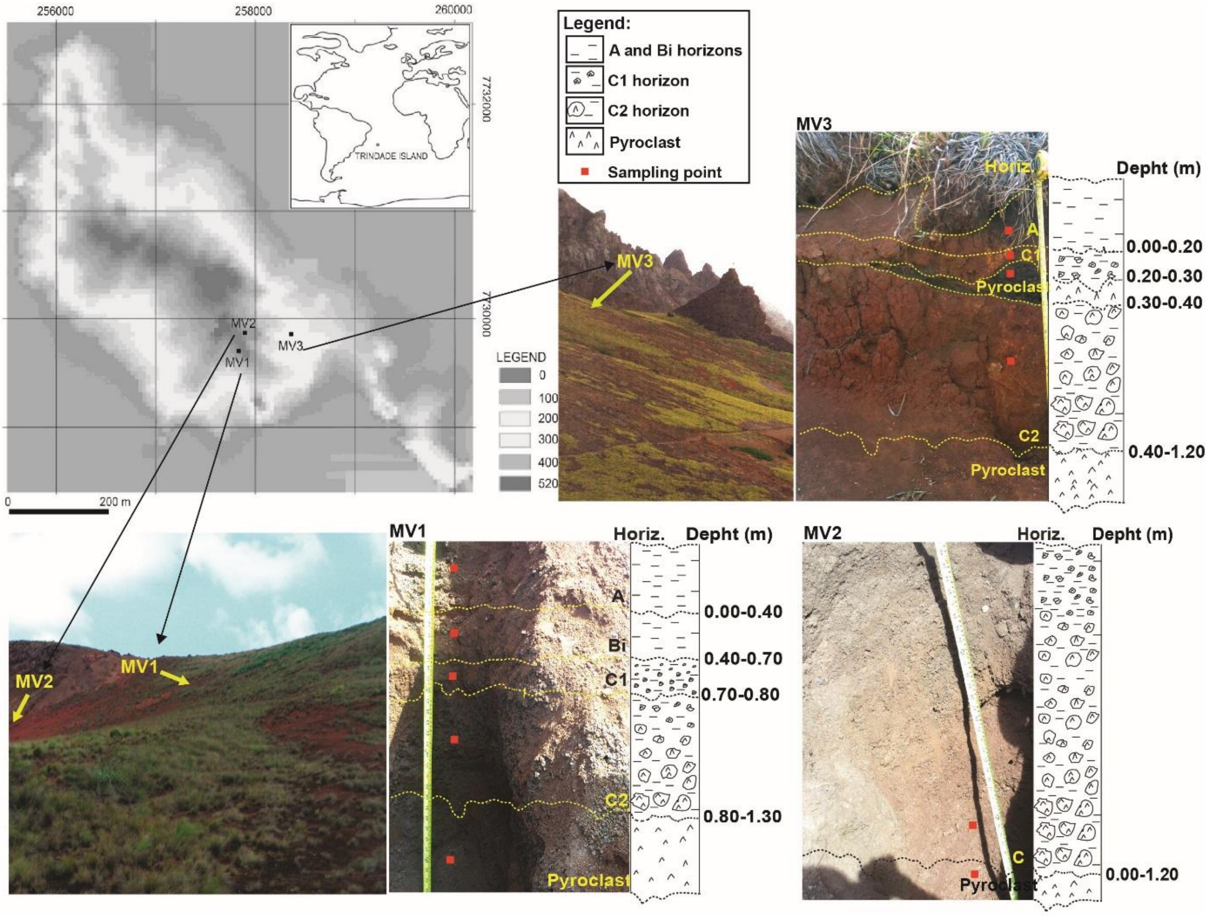

Figure 6.1: Digital elevation model of Tindade Island showing the location of the three soil profiles, MV1, MV2 and MV3 and their respective horizons.

Figure 6.1: Modèle numérique de terrain de l'Île de Tindade montrant l'emplacement des trois profils de sol, MV1, MV2 et MV3 et leurs horizons respectifs.

Particle size was determined by the total dispersion method according to Donagema *et al.* (2011). After vertical shaking for 16h with sodium hexametaphosphate solution as a dispersant, the clay content was determined by the pipette method, the gravel, coarse and fine sand were separated by sieving, and silt content was obtained by the difference of the sum of the other fractions in relation to the original sample. The structure descriptions were made according to Schoeneberger *et al.* (2012).

The mineralogical composition was obtained by X-ray Diffraction (XRD) using an Empyrean Panalytical diffractometer with CuKa radiation. For the bulk random samples, XRD patterns were obtained in the range of 2°–70° 2θ, step of 0.02° 2θ and count of 10″/step. For the clay fraction, oriented preparations were made, air dried, ethylene glycol solvated and heated to 100 °C and 550 °C. XRD patterns were acquired using the same step and counting time but in the range of 2°–35° 2θ. XRD patterns were interpreted using High Score X'Pert Plus software and known patterns from the literature (Brindley & Brown 1980). Differential Thermal and Thermogravimetric analyzes (DTA-TGA) were made to improve the characterization and identification of the constituent clay phases. A TGA Q50

V20.10 instrument was used under nitrogen atmosphere with maximum pressure of 1.4kgf/cm^2, heating rate of 10°C/min. The data were analyzed using TA Universal Analysis software.

Optical microscopic investigations were carried out on eleven thin sections of undisturbed samples of rocks and representative soil horizons from the three soil profiles. A Zeiss trinocular optical microscope (Axiophot model), with an integrated digital camera in conjunction, was used for the petrological and micromorphological descriptions.

Representative samples of fresh and altered olivine crystals in varying degrees were selected for punctual microanalyses with an electron microprobe Jeol JXA8900RL WD/ED combined Microanalyzer and microchemical maps were performed with an electron microprobe JEOLJXA-8230.The electron beam was set at15 kV, 20 nA, 2–5 μm and the common matrix ZAF corrections were applied. Counting times on the peaks/background were 10/5s for all elements (Na, Si, Al, Mg, Fe, Cr, Ti, Ca, Ni, K, Mn). For the punctual analysis the elements were calibrated with jadeite-TAP, rutile-LIF, sanidine- PETJ, magnesium oxide- TAP, chromium oxide- LIF, AN100-PETJ, corundum-TAP, rodonite-LIF, quartz-TAP, magnetite-LIF. For the microchemical maps, the Fe and the Mg were calibrated with almandine-LIFH and olivine-TAP. The olivine crystals were analyzed along transgranular profiles. The mineral formulas were calculated based on 4 oxygens for olivine. The total iron content obtained by the microprobe was considered as FeO. Chemical maps of olivine were also obtained by the microprobe in order to illustrate the distributions of chemical elements. Operating conditions were 15-kV acceleration, 20-nA beam current, and 20-ms dwell time per spot (stage mode). Maps show quantitative element distributions.

Back-scattered electron images and semi-quantitative chemical analyses by Electron Dispersive X-ray (EDX) were made to analyze respectively the habit and composition of iddingsitized olivines. The analyzes were made in Scanning Electron Microscope (SEM) coupled with EDX Jeol JSM-6510 with an operating voltage of 20KV.

6.3 – RESULTS AND DISCUSSIONS

The macromorphological aspects of the analyzed profiles are presented in **Table 6.1**. All the soils described are shallow and have similar morphology and clay texture (**Table 6.1**, **Figure 6.1**). They are composed of the A and C horizons, with or without transitional horizons between them. An exception occurs in MV1, which presents a poorly developed B horizon and in MV2, the absence of the A horizon.

Macroscopically the pyroclasts from the three sampled profiles showed a dark gray color and brownish altered regions, with milimetric light green olivine phenocrysts dispersed in an afanitic matrix.

Table 6.1: Macromorphological description of the MV1, MV2 and MV3 soil profiles.

Tableau 6.1 : Description macromorphologique des profils de sol MV1, MV2 et MV3.

Horizon	**Layers**	**Particule size**				**Wet color**	**Structure**
		> 2 μm		< 2 μm			
		Coarse sand	**Fine sand**	**Silt**	**Clay**		
	m		g kg^{-1}				
MV1							
A	0.00-0.40	26.00	111.00	384.00	478.00	Dark brown 7.5YR3/2	Subangular blocks weak medium to coarse
Bi	0.40-0.70	12.00	78.00	360.00	549.00	Dark brown 7.5YR3/2	Platy weak medium
C1	0.70-0.80	23.00	159.00	399.00	419.00	Dark brown 7.5YR3/4	Angular blocks weak fine
C2	0.80-1.30	68.00	180.00	358.00	394.00	Dark brown 7.5YR3/2	Angular bloscks weak fine
Pyroclast	1.30+	-	-	-	-	Reddish brown 5YR4/3	Massive
MV2							
C	0.00-1.20+	259.00	82.00	251.00	409.00	Strong brown 7.5YR4/6	Angular blocks weak fine to medium
Pyroclast	1.20	-	-	-	-	Reddish brown 5YR4/3	Massive
MV3							
A	0.00-0.20	35.00	67.00	323.00	575.00	Dark brown 7.5YR3/2	Single grains
C1	0.20-0.30	51.00	74.00	298.00	577.00	Reddish brown 7.5YR4/4	Subangular blocks moderate medium to fine
Pyroclast	0.30-0.40	-	-	-	-	Reddish brown 5YR4/3	Massive
C2	0.40-1.00	50.00	22.00	247.00	681.00	Dark reddish brown 5YR3/3	Subangular blocks moderate medium to fine

The XRD patterns of pyroclasts MV1, MV2 and MV3 profiles showed d-spacings of 2.46, 2.51 e 3.88 Å (**Figures 6.2.1**, **5**, **7**) indicating that the olivines are of forsterite type. Additionally, they showed biotite, goethite, magnetite, hematite, ilmenite, anatase and pyroxene. The clayey fraction of the soil profiles is constituted by hematite, goethite, magnetite, anatase and halloysite, with biotite and rutile in MV2 profile, and rutile in MV3 profile (**Figures 6.2.2**, **3**, **4**, **6**, **8** and **9**). The DTA-TGA analyses confirmed the presence of goethite and halloysite, indicated by an endothermic peak at 280 °C and 460 °C respectively (**Annexes**: **Figures 2.1**, **2.2**, **2.3**).

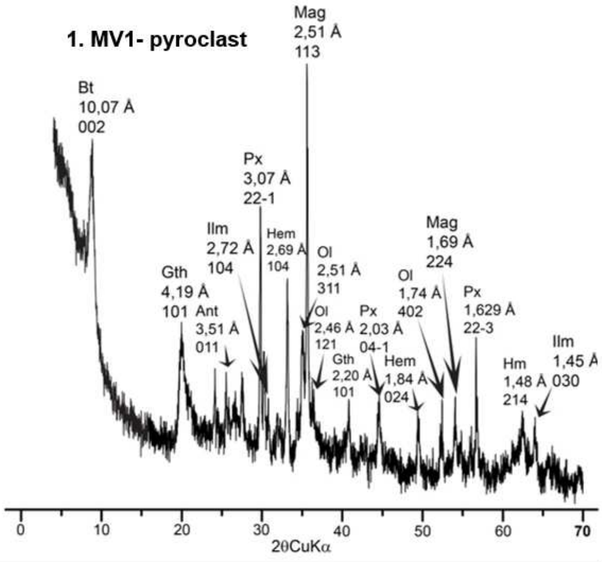
1. MV1- pyroclast
Mag 2,51 Å 113
Bt 10,07 Å 002
Px 3,07 Å 22-1
Ilm 2,72 Å 104
Hem 2,69 Å 104
Gth 4,19 Å 101
Ant 3,51 Å 011
Ol 2,51 Å 311
Ol 2,46 Å 121
Px 2,03 Å 04-1
Gth 2,20 Å 101
Mag 1,69 Å 224
Ol 1,74 Å 402
Px 1,629 Å 22-3
Hem 1,84 Å 024
Hm 1,48 Å 214
Ilm 1,45 Å 030
0 10 20 30 40 50 60 70
2θCuKα

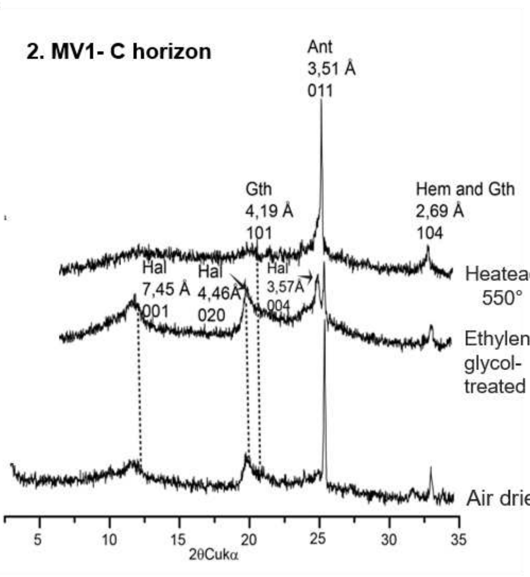
2. MV1- C horizon
Ant 3,51 Å 011
Gth 4,19 Å 101
Hem and Gth 2,69 Å 104
Hal 7,45 Å 001
Hal 4,46Å 020
Hal 3,57Å 004
Heatead 550°
Ethylene glycol-treated
Air dried
5 10 15 20 25 30 35
2θCukα

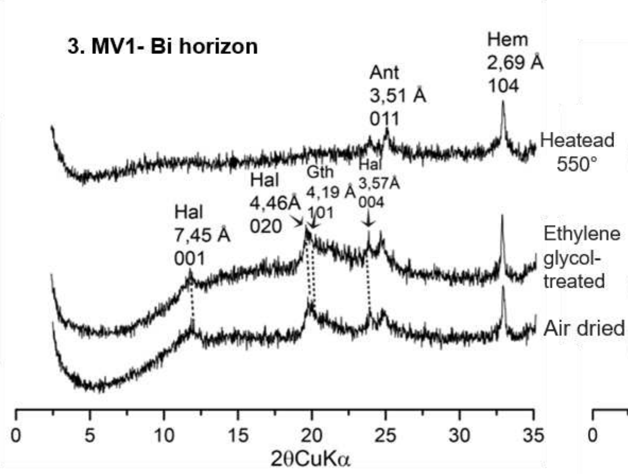
3. MV1- Bi horizon
Hem 2,69 Å 104
Ant 3,51 Å 011
Heatead 550°
Hal 4,46Å 020
Gth 4,19 Å 101
Hal 3,57Å 004
Hal 7,45 Å 001
Ethylene glycol-treated
Air dried
0 5 10 15 20 25 30 35
2θCuKα

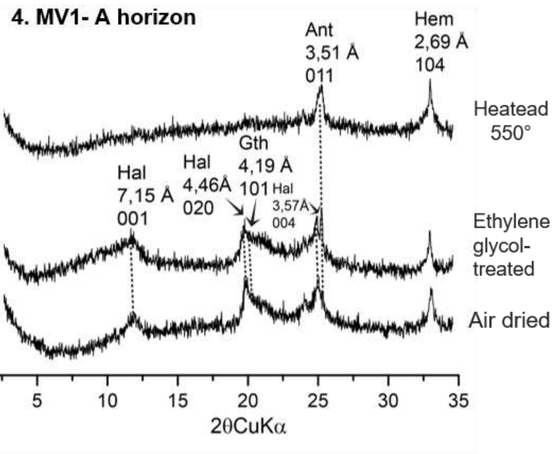
4. MV1- A horizon
Ant 3,51 Å 011
Hem 2,69 Å 104
Heatead 550°
Gth 4,19 Å 101
Hal 7,15 Å 001
Hal 4,46Å 020
Hal 3,57Å 004
Ethylene glycol-treated
Air dried
0 5 10 15 20 25 30 35
2θCuKα

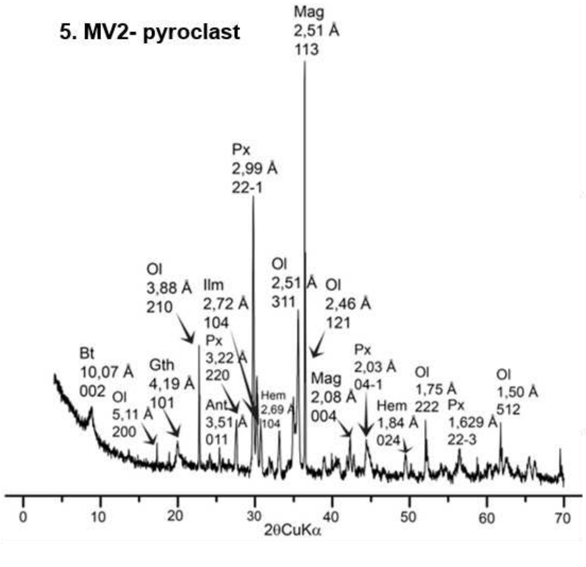
5. MV2- pyroclast
Mag 2,51 Å 113
Px 2,99 Å 22-1
Ol 3,88 Å 210
Ilm 2,72 Å 104
Ol 2,51 Å 311
Ol 2,46 Å 121
Px 3,22 Å 220
Bt 10,07 Å 002
Gth 4,19 Å 101
Ol 5,11 Å 200
Ant 3,51 Å 011
Hem 2,69 Å 104
Mag 2,08 Å 004
Px 2,03 Å 04-1
Ol 1,75 Å 222
Hem 1,84 Å 024
Px 1,629 Å 22-3
Ol 1,50 Å 512
0 10 20 30 40 50 60 70
2θCuKα

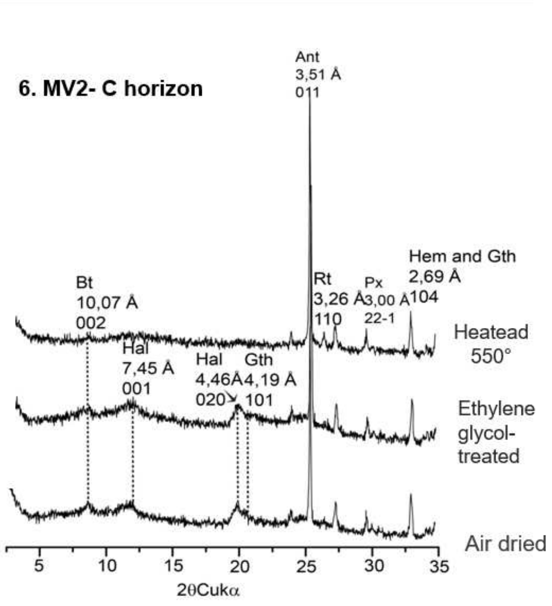
6. MV2- C horizon
Ant 3,51 Å 011
Hem and Gth 2,69 Å 104
Bt 10,07 Å 002
Rt 3,26 Å 110
Px 3,00 Å 22-1
Heatead 550°
Hal 7,45 Å 001
Hal 4,46Å 020
Gth 4,19 Å 101
Ethylene glycol-treated
Air dried
5 10 15 20 25 30 35
2θCukα

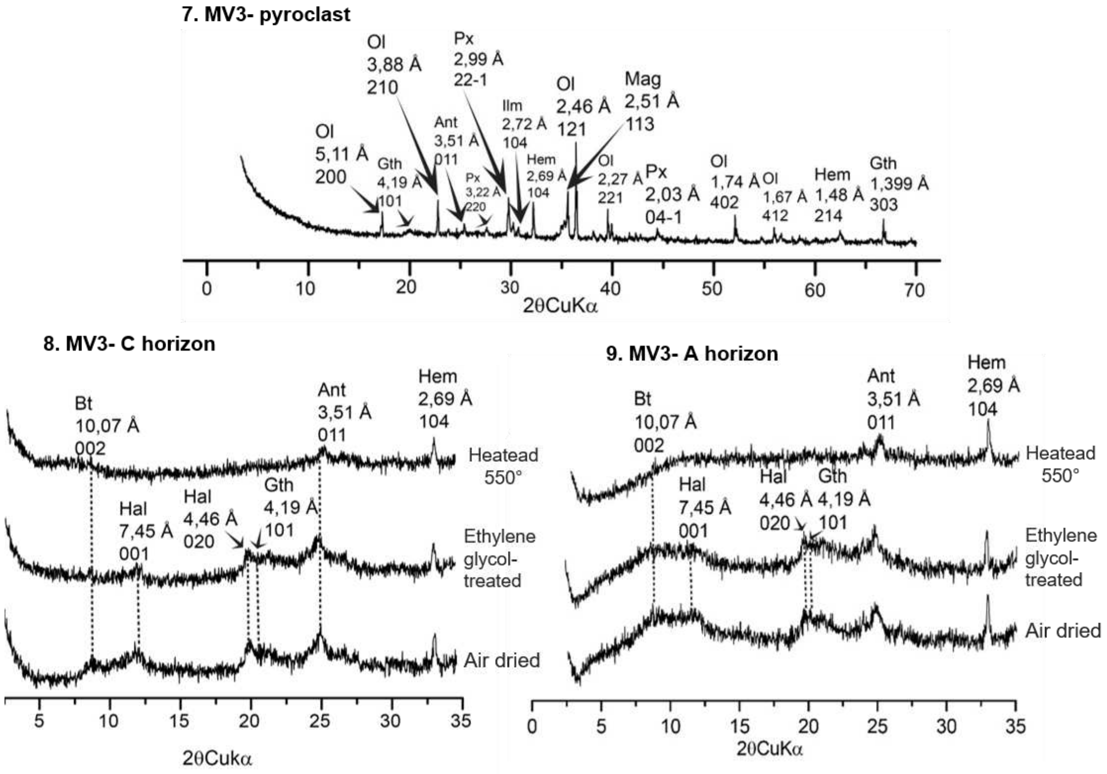

Figure 6.2: 1, 5 and 7. XRD of pyroclast MV1, MV2 and MV3 profiles. 2, 3, 4, 6, 8 and 9. XRD patterns of the clay fraction air dried, ethylene glycol-treated and heated at 550 °C from the C, Bi and A horizons. Bt=biotite, Ol=olivine, Gth=goethite, Ilm=ilmenite, Px=pyroxene, Hem=hematite, Mag=magnetite, Hal=halloysite, Ant=anatase, Rt=rutile.

Figure 6.2 : 1, 5 et 7. DRX des pyroclastes des profils MV1, MV2 et MV3. 2, 3, 4, 6, 8 et 9. Les DRX de la fraction argile séchés, traités à l'éthylène glycol et chauffés à 550 °C des horizons C, Bi et A. Bt=biotite, Ol=olivine, Gth=goethite, Ilm=ilmenite, Px=pyroxene, Hem=hematite, Mag=magnetite, Hal=halloysite, Ant=anatase, Rt=rutile.

Microscopically the pyroclasts showed a vesicular structure and sometimes the vesicles were filled by clay minerals, iron oxide and hydroxide and, in the pyroclast MV2 profile, by zeolites. The texture is porphyritic, the olivine phenocrystals being colorless, with high interference colors, fractured with axis sizes > 1 mm (**Figures 6.3.1**, **4**). They are euhedral and irregularly shaped crystals distributed in a dark reddish brown microlitic matrix constituted by pyroxenes crystals of high interference color and subhedral magnetites (**Figures 6.3.1**, **4**, **5**). A reddish dark brown material (**Figures 6.3.1**, **4**, **7**, **8**) identified as iddingsite, is always present on the edges, fractures and cores of the olivine crystals. However, this iddingsite invasion was much more prominent in the phenocrysts of the MV1 profile (**Figure 6.3.7**). The external outline of the iddingsite is regular and follows the original crystal limits. On the inside, however, the contour line of the olivine core is irregular and denticulated (**Figures 6.3.8**, **9**). This transformation is centripetal and starts in the margins leading to complete pseudomorphosis of the olivine crystals in the C, Bi and A horizons from the MV1 profile (**Figures 6.3.10**,**11**,**12**; **6.5.1**). In the soil horizons of the profiles MV2 and MV3, despite the advance of the pseudomorphosis of the olivine crystals, there are still relicts of unchanged olivine crystals in the C and A horizons (**Figures 6.3.2**, **3**, **6**). This variation of weathering between profiles can be attributed to the higher altitude of the MV1 profile, which leads to a better drainage circulation and, consequently a greater leaching of the basic cations. This fact is highlighted by the greater development of the MV1 profile which it is the only one that contains the Bi horizon.

The microchemical map of the fractured olivine crystal of the pyroclast from the MV1 profile represented in **Figure 6.3.7** showed the iron concentration and Mg loss in the borders and fractures due to the oxidation of ferrous olivine iron and Mg leaching, respectively (**Figure 6.4**).

The microprobe analyzes of unaltered olivine crystals showed an average of 44.55 % of MgO, 40.07 % of SiO_2 e 14.78 % of FeO indicating the forsterite Fo_{84} member (**Table 6.1**) and corroborating with the XRD data (**Figures 6.2.1, 2, 3**). On the margins and inner fractures of the olivines the chemical composition (**Table 6.2**) is similar to that found in iddingsites by Delvigne *et al.* (1979), Eggleton (1984) and Smith *et al.* (1987). In agreement with Ross & Shannon (1925), Sun (1957), Hytonen (1959), Gay & Le Maître (1961), Delvigne *et al.* (1979), Smith *et al.* (1987), Gerard *et al.* (2007) they showed a decrease in SiO_2, FeO and MgO content and an increase in Al_2O_3, Fe_2O_3 and H_2O content (**Table 6.2**). A small input in Na_2O e K_2O similar to iddingsites of Hytonen (1959), Gay & Le Maître (1961), Delvigne *et al.* (1979), Talbi & Honnorez (2003) was also observed (**Table 6.2**). The chemical compositions of smectites of Talbi & Honnorez (2003) show SiO_2 content greater than the iddingsites of this study. This fact suggests a more advanced stage of weathering of the soils and pyroclasts of this study. In the C horizons the iddingsitized olivines were totally depleted in Mg and the dominant iron component gives a dark brownish red color (**Figures. 6.5.1**).

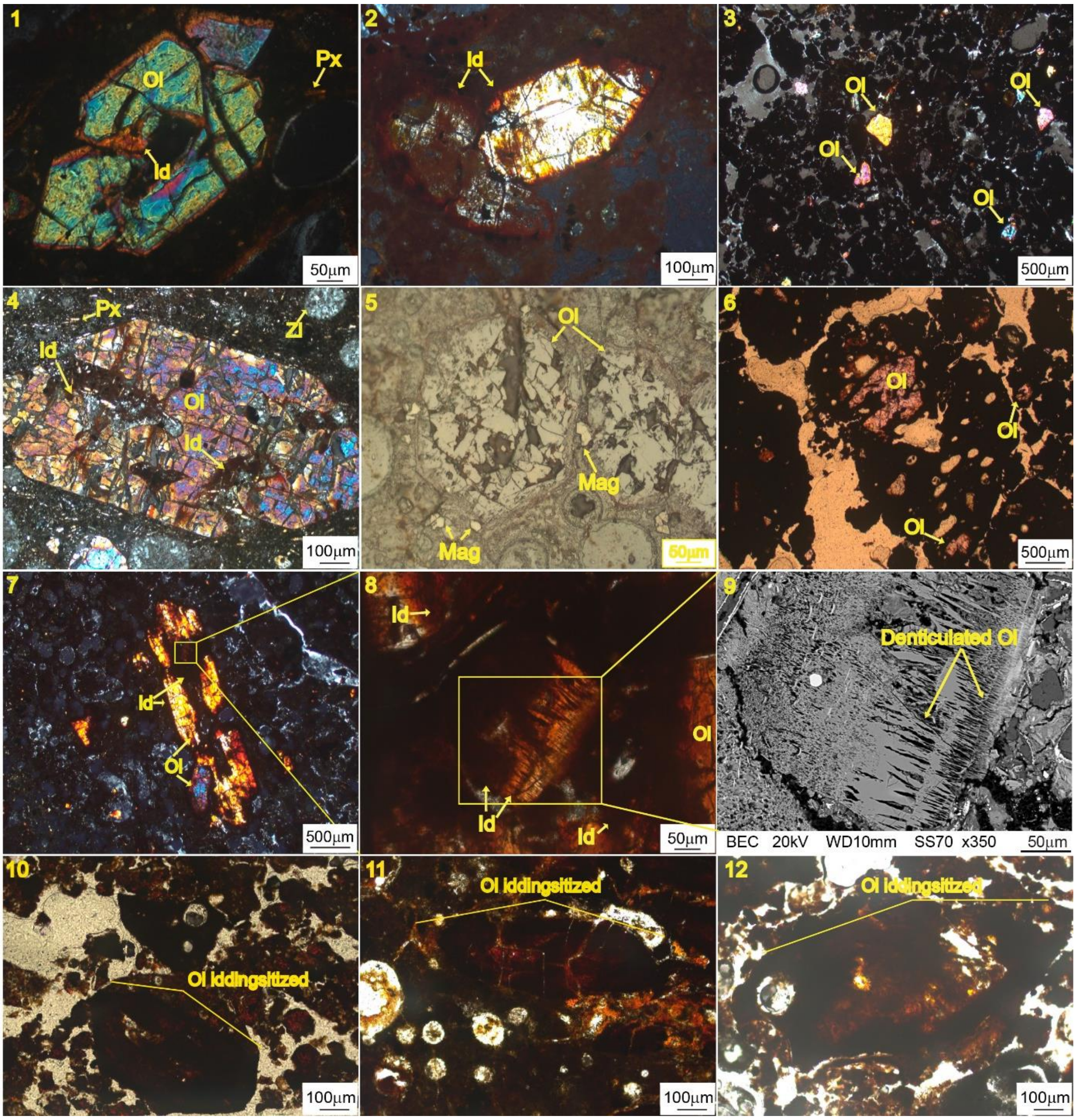

Figure 6.3: **1**. XPL photomicrograph from the pyroclastic MV3 profile showing olivine phenocrystal with iddingsite in the borders, fractures and core surrounded by dark reddish-brown matrix with pyroxenes crystals. **2**. XPL photomicrograph from the C horizon MV3 profile showing olivine phenocrystals well preserved with iddingsite. **3**. XPL photomicrograph from the A horizon from MV3 profile showing relicts of unchanged olivine. **4**. XPL photomicrograph from the pyroclast MV2 profile similar to photomicrograph 1 but with zeolites in the vesicles and fractures. **5**. Reflected light photomicrograph from the pyroclast MV2 profile showing magnetite in the matrix. **6**. XPL photomicrograph from the C horizon MV2 profile showing olivine phenocrystal and relicts. **7**.XPL photomicrograph from the MV1 profile showing pseudomorphosis of the olivine phenocrystal. **8**. Detail of photomicrograph 7 showing the replacement of olivine by iddingsite characterized by denticulated structure due to centripetal penetration of alteration. **9**. SEM photomicrograph showing the denticulated olivine. **10**. PPL photomicrograph from the C horizon MV1 profile showing olivine phenocrystal totally iddingsitized. **11**. PPL photomicrograph from the Bi horizon MV1 profile showing olivine phenocrystal totally iddingsitized. **12**. PPL photomicrograph from the A horizon MV1 profile showing olivine phenocrystal totally iddingsitized. Ol=olivine, Id=iddingsite, Px=pyroxene, Mag=magnetite, Zl=zeolite. XPL:Crossed polarized light. PPL: Plane polarized light

Figure 6.3 : **1**. Photomicrographie par LPX de pyroclastique du profil MV3 montrant le phénocristaux d'olivine avec iddingsite dans les côtés, les fractures et le noyau entouré par la matrice brun-rougeâtre foncé avec des cristaux de pyroxène. **2**. Photomicrographie par LPX d'horizon C du profil MV3 montrant des phénocristaux

d'olivines bien conservés avec iddingsite. **3**. Photomicrographie par LPX du horizon A du profil MV3 montrant des reliques d'olivine inchangée. **4**. Photomicrographie par LPX du pyroclaste du profil MV2 semblable au photomicrographie 1 mais avec des zéolites dans les vésicules et les fractures. **5**. Photomicrographie par lumière réfléchi du pyroclaste du profil MV2 montrant la magnétite dans la matrice. **6**. Photomicrographie par LPX d'horizon C du profil MV2 montrant le phénocristaux olivine et les reliques. **7**. Photomicrographie par LPX du profile MV1 montrant la pseudomorphose du phénocrystal d'olivine. **8**.Détail de la photomicrographie 7 montrant le remplacement d'olivine par iddingsite caractérisé par la structure denticulated due à la pénétration centripète de l'altération. **9**. Photomicrographie par MEB montrant l'olivine dentticulated. **10**. Photomicrographie par LPP d'horizon C du profil MV1 montrant le phénocrystal d'olivine totalement iddingsitisée. **11**. Photomicrographie par LPP du horizon Bi du profil MV1 montrant le phénocristaux d'olivine totalement iddingsitisée. **12**. Photomicrographie par LPP d'horizon A du profil MV1 montrant le phénocristaux d'olivine totalement iddingsitisée. Ol=olivine; Id=iddingsite; Px=pyroxene; Mag=magnetite; Zl=zeolite; LPX=Polariseur croisés; LPP= Lumière polarisée.

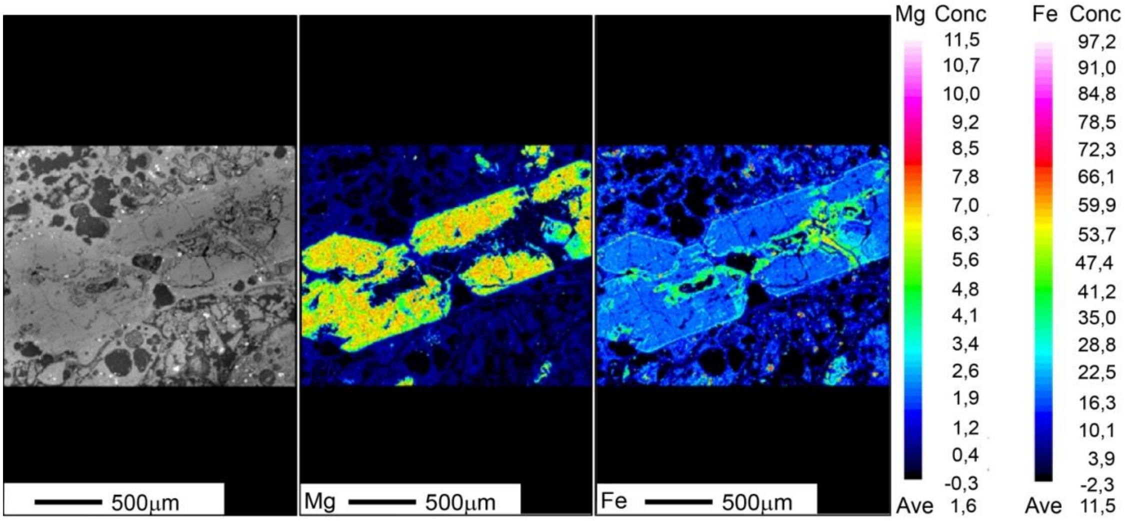

Figure 6.4: Microchemical map of an olivine crystal from the pyroclast MV1 profile showing the Fe concentration and Mg loss in the borders and fractures.

Figure 6.4 : Carte microchimique d'un cristal d'olivine du profil de pyroclaste MV1 montrant la concentration de Fe et la perte de Mg dans les bordures et les fractures.

Table 6.2: Microprobe analyzes showing chemical composition and ions calculated of olivine. Ol=olivine e Id=iddingsite.

Tableau 6.2: Analyse par microsonde électronique de la composition chimique et les ions calculés d'olivine. Ol=olivine et Id=iddingsite.

	MV1-Olivine crystal						**MV2-Olivine crystal**					
Sample	Ol unchanged	Ol unchanged	Ol unchanged	Id	Id	Id	Ol unchanged	Ol unchanged	Ol unchanged	Id	Id	Id
Position	border	center	border	fracture	fracture	border	border	center	border	fracture	fracture	fracture
	%	%	%	%	%	%	%	%	%	%	%	%
SiO_2	39.11	39.33	39.82	25.05	29.30	28.19	40.23	40.39	40.34	27.50	33.40	43.95
TiO_2	0.01	0.02	0.04	1.85	0.17	0.15	0.00	0.01	0.00	3.25	0.51	0.87
Al_2O_3	0.07	0.00	0.04	2.58	2.14	0.62	0.06	0.00	0.08	23.31	15.03	11.66
FeO	14.27	15.52	14.78	-	-	-	13.78	14.51	14.04	-	-	-
Fe_2O_3	-	-	-	25.25	23.14	15.29	-	-	-	7.36	15.49	370
MgO	45.93	44.64	45.38	25.22	29.72	31.53	46.16	45.34	45.75	6.15	25.90	19.94
Na_2O	0.04	0.00	0.02	0.14	0.15	0.01	0.02	0.00	0.01	0.36	0.34	0.24
K_2O	0.00	0.00	0.00	0.20	0.08	0.04	0.00	0.00	0.00	0.52	0.99	7.32
CaO	0.50	0.22	0.54	0.58	0.32	0.20	0.20	0.53	0.22	15.35	1.91	1.29
MnO	0.21	0.22	0.30	0.28	0.15	0.12	0.16	0.31	0.20	1.31	0.42	0.81
Cr_2O_3	0.07	0.04	0.03	0.11	0.16	0.04	0.11	0.04	0.07	0.83	0.53	0.11
H2O	-	-	-	18.75	14.69	23.82	-	-	-	14.07	5.48	10.10
Total	100.20	100.00	100.94	100.00	100.00	100.00	100.71	101.12	100.71	100.00	100.00	100.00
	Calculated ions based on 4 oxygen						*Calculated ions based on 4 oxygen*					
Si	0.98	0.99	0.99	-	-	-	0.99	0.99	0.99	-	-	-
Ti	0.00	0.00	0.00	-	-	-	0.00	0.00	0.00	-	-	-
Al	0.00	0.00	0.00	-	-	-	0.00	0.00	0.00	-	-	-
Fe	0.30	0.33	0.31	-	-	-	0.31	0.31	0.33	-	-	-
Mg	1.72	1.68	1.68	-	-	-	1.69	1.68	1.68	-	-	-
Na	0.00	0.00	0.00	-	-	-	0.00	0.00	0.00	-	-	-
K	0.00	0.00	0.00	-	-	-	0.00	0.00	0.00	-	-	-
Ca	0.01	0.01	0.01	-	-	-	0.01	0.01	0.01	-	-	-
Mn	0.00	0.00	0.01	-	-	-	0.01	0.00	0.00	-	-	-
Cr	0.00	0.00	0.00	-	-	-	0.00	0.00	0.00	-	-	-
Fo	0.85	0.84	0.85	-	-	-	0.86	0.84	0.85	-	-	-
Fy	0.15	0.16	0.15	-	-	-	0.14	0.16	0.15	-	-	-

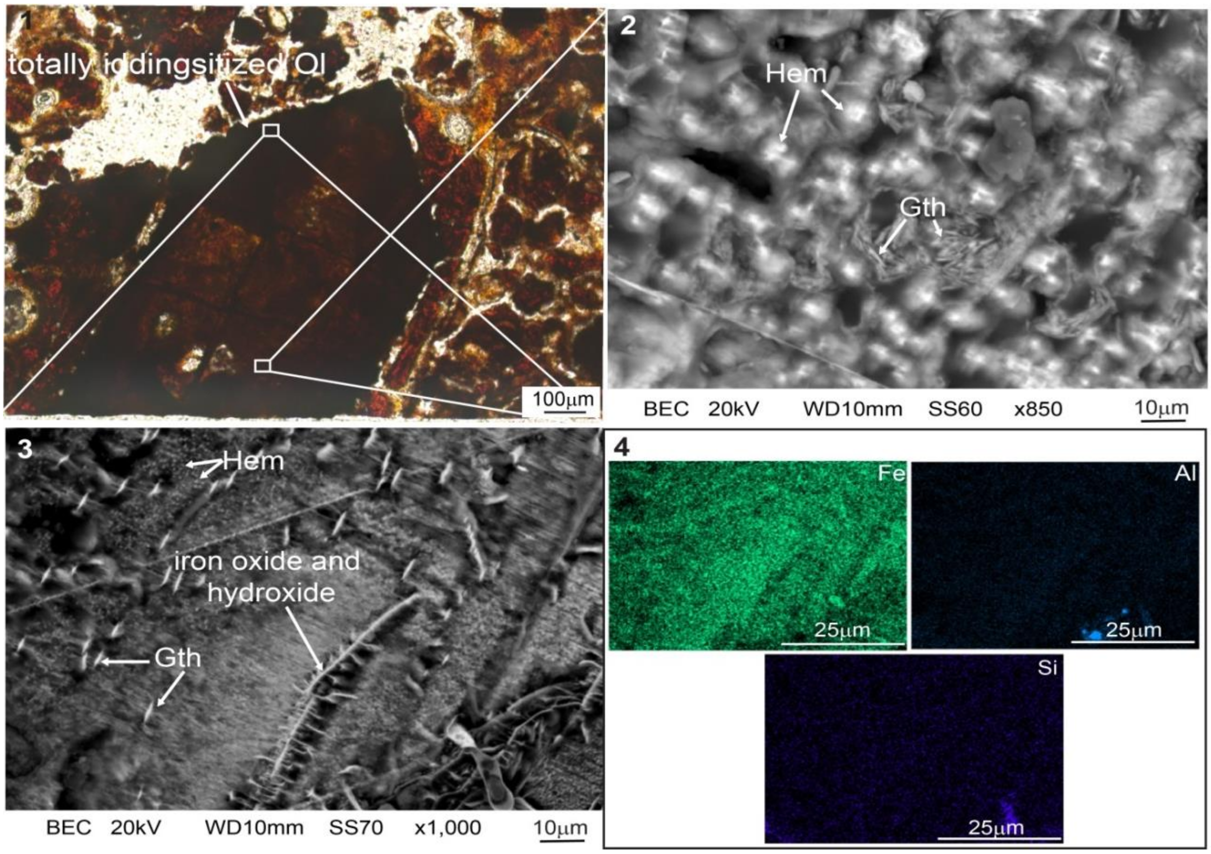

Figure 6.5: **1.** Plane polarized light photomicrograph showing the total pseudomorphosis of olivine in iddingsite from the C horizon of the MV1 profile. **2.** SEM Photomicrography showing granular hematite and aggregates of acicular crystals of goethite. **3.** SEM Photomicrography showing the iron oxides and hydroxides. **4.** Microchemical map of the image 3 showing the concentration of Fe, Al and Si. The Mg content was not detected in the analysis.

Figure 6.5: 1. Photomicrographie par lumière polarisée montrant la pseudomorphose totale d'olivine dans le site d'iddingsite de l'horizon C du profil MV1. 2. Photomicrographie par MEB affichant l'hématite granulaire et les agrégats des cristaux aciculaires de goethite. 3. Photomicrographie par MEB montrant les oxydes de fer et les hydroxydes. 4. Carte microchimique de l'image 3 montrant la concentration de Fe, Al et Si. Le contenu de Mg n'a pas été détecté dans l'analyse.

The SEM photomicrographs showed a porous oriented aggregate of iron oxides and hydroxides (**Figures. 6.5.2**, **3**), characterized by granular hematite and acicular goethite generated by their on oxidation within the remnants olivine crystals. The Al and Si detected (**Figure 6.5.4**) could indicate the presence of a clay mineral phase. However, X-ray diffraction only showed the presence of halloysite. It is possible that all or part of the Al and Si are substituted in the goethite as observed in Smith *et al.* (1987).

The reddish-brown color of iddingsite is common in tropical regions due the presence of hematite that partially replace the goethite (Delvigne *et al.*, 1979). However, serpentinized olivines substituted by carbonates as described by Antonello *et al.* (2009) were not found.

The presence of hematite, which is one of the constituent minerals of HTI, could suggest that the iddingsites of this study could be a pyroclasts, and totally iddingsitized olivines in the C, Bi and A horizons. In the rocks, when iddingsite is present in the cores, it also occurs in the margins and fractures. Additionaly it is understood that the weathering of olivine results in a mixture of phyllosilicates, hematite and goethite (Baker & Haggerty 1967, Delvigne *et al.* 1979, Talbi & Honnorez 2003).

The microscopic and microchemical features observed in this study pointed to iddingsites of meteoric origin due to the following:

a) advanced of the alteration of the olivine crystals towards the upper horizons of the profile,

b) occurrence of totally altered olivine in to iddingsite in the C, Bi and A horizons,

c) composition essentially of iron oxides and hydroxides of the iddingsites,

d) presence of more altered olivine crystals in the topographically higher profile.

6.4 – CONCLUSION

The olivines from piroclasts from Vulcão do Paredão and Morro Vermelho Formation belong to the forsterite type and are partially or completely transformed into iddingsites. In the pyroclast MV1 profile the olivines appear more altered than in the pyroclast MV2 and MV3 profiles because the weathering processes were more pronounced at higher altitudes. In this study, there is no sign of the iddingsite being of deuteric origin. The microscopic and microchemical analysis of the olivine did not allow us to identify any evidence of previous deuteric or hydrothermal processes of alteration. However, the advance in the alteration of the olivine crystals towards the top of the soil profiles, reaching their total transformation and a predominant composition of iron oxides and hydroxides in the upper horizons shows that weathering is the main process of iddingsite formation. This finding is highlighted by the presence of more altered olivine crystals in the topographically higher profile, on the same lithology, due to better drainage and consequently greater leaching.

CHAPITRE 7

LES ANDOSOLS DE L'ÎLE DE TRINDADE[3]

ABSTRACT

The pedological studies carried out so far in Trindade Island (TI) have obtained patchy evidences of allophane, without detailed mineralogical and micromorphological studies to confirm the occurrence of Andosols in TI. Therefore, in this work the mineralogical, micromorphological, physical and chemical characterization of four soil profiles from Vulcão do Paredão (P1) and Morro Vermelho formations (P2, P3 and P4) were carried on the latest volcanic events in Brazil from Trindade Island (TI) with aim to evaluate the presence of Andosols in this oceanic island. Profiles P1 and P2 are developed on pyroclastic bombs, and show, respectively, A-Bi- C and decapitated A-C horizons, whereas P3 and P4 are developed on lapillitic and bomb pyroclasts, show A-C horizons. The soils profiles have a reddish and brownish clayey matrix, are highly friable with and show a plastic consistency. Their microstructures are granular, single grain and intergrain microaggregate, in which aggregates display an undifferentiated b-fabric. The mineralogical constituents of the bulk fraction are biotite, hematite, magnetite, ilmenite, pyroxene, olivine, halloysite, goethite, anatase and rutile. The clay fraction is marked by presence of halloysite, ferrihydrite and little amounts of allophane. All soils presented andic properties and can be classified as non-allophanic Andosols. In addition, micromorphological features closely resemble those reported Andosols from other volcanic islands from elsewhere. The predominance of halloysite in the clay fraction formed by alteration of sideromelane, suggests that allophane would be an intermediate phase of this rapid transformation favored by the wet climate conditions of the highest parts of TI.

Keywords: Volcanic island, Andic properties, Andosols / Andisols, Halloysite

---

[3] Article soumis au magazine "Revista Brasileira de Ciência do Solo" avec le titre "Non-allophanic Andosols of Trindade Island, South Atlantic, Brazil: A New soil order in Brazil".

7.1 – INTRODUCTION

The soils formed from tephras or pyroclastic materials are known as Andisols (Soil Survey Staff 2014), Andosols (WRB 2015) and Kurobokudo (USCSJ 2nd 2002). There are also some Andosols formed from non-tephritic materials, such as volcanic and sedimentary rocks, mixed materials of tephra and loess, etc. (Shoji *et al.* 1993). The Andosols are characterized by the presence of allophane or Al, Si, and humus compounds (Shoji *et al.* 1993). However, Shoji & Ono (1978) reported the occurrence non-allophanic Andosols with Al/Fe humus characterized as Allophanic Andosols (Shoji *et al.* 1985). According to Soil Survey Staff (2014) an Andosol soil must have andic properties in at least 60 % of its profile. The andic properties of a soil are generally acquired during weathering of tephra or other parent materials which contain significant volcanic glass, leading to the formation of amorphous colloidal material as allophane, imogolite, ferrihydrite, or metal-humus complexes. The presence of amorphous materials is inferred from ammonium oxalate extraction of aluminum, iron, and silica (Soil Survey Staff 2014). In the field, the andic soil properties may to be inferred by using 1N sodium fluoride (NaF) (Soil Survey Staff 2014). However, this test may not be specific for allophane as it may also reacts with A1 in Al-humus complexes (Parfitt 1990a).

The volcanic glass content is the percent of volcanic glass (by grain count) in the coarse silt and sand (0.02 to 2.0 mm) fraction (Soil Survey Staff 2014). In addition, the pH (H_2O) > 5, low content of organic matter and base-rich volcanic ash favor the formation of allophane (Dahlgen *et al.* 1993).

According to Soil Survey Staff (2010) the Andosols cover approximately 0.8 % of the Earth's surface, and approximately 60 % of volcanic ash soils occur in tropical countries such as Colombia (Espinosa & Sanabria 2015), Central México (Sedov *et al.* 2003), India (Caner *et al.* 2000), New Zealand (Neall 1977).

The remaining 40 % occur in cooler climate regions and are derived from various types of volcanic rocks, such as andesite, dacite, volcanic ash, basalt and ignimbrite: Chile (Bertrand *et al.* 2008), Argentina (Candam & Broquen 2009), Italy (Vingiani *et al.* 2014, Vingiani *et al.* 2018), France (Grison *et al.* 2015), Germany (Rennert *et al.* 2014), Georgia (Urushadze *et al.* 2011), Turkey (Kiliç *et al.* 2018), Kamchatka Peninsula of Russia (Litvinenko & Zakharikhina 2009); and on non-volcanic rocks as gabbros, amphibolites, basic granulites, biotitic schists, amphibolitic phyllites: Spain (Bech-Borras *et al.* 1977, Garcia-Rodeja *et al.* 1987).

Particularly, in volcanic islands there a number studies identified Andosols, such as in the Portuguese Azores and Cape Verde archipelago: São Miguel Island (Ricardo *et al.* 1977), Santa Maria and Graciosa (Madeira 1980, Medina & Grilo 1981), Terceira (Pinheiro 1990), Madeira (Madeira *et al.* 1994), Faial and São Jorge (Madruga 1995), Pico (Madeira *et al.* 1996, Pinheiro *et al.* 2001), Fogo (Faria 1974), Santo Antão (Constantino *et al.* 1979b), Sal (Dinis & Matos 1993), Brava (Diniz & Matos

(1999b), São Nicolau (Diniz & Matos 1999a) and São Vicente (Diniz & Matos 1994a); in Galápagos: Santa Cruz Island (Sedov *et al.* 2010); França: Reunion Island; Espanha: Canárias Island (Fernandez-Calilas *et al.* 1975); Japan (Adjadeh & Inoue 1999); Indonesia (Devnita 2014, Hikmatullah 2008); Hawaiian Islands, Philippine Islands, Aleutas Islands and Solomon Islands.

In Brazil, studies showing the occurrence of Andosols are rare and Schaefer *et al.* (2016) were the first to postulate their presence in oceanic island. Dumig *et al.* (2008) were the first to detect non-allophanic Andosols in South America outside the radius of influence of the recent volcanism of the Andes region. These Andosols were described in the northeastern of Rio Grande do Sul state and were developed from rhyodacite (Jurassic–Cretaceous volcanism).

Trindade Island (TI) is located in the mid-Atlantic with a surface of 13 km² and formed mostly by extrusive volcanic material and/or hyperabissal sodium-alkaline lava of Quaternary age (Almeida 2002, 2006). Previously, Clemente *et al.* (2009) observed evidences of soils with andic properties and, described a material similar to allophane at the base of a highland soil profile on tuffs, at the same location of (P1) of the present study. In soils developed from phonolitic and basic rocks of TI, Sá (2010) found pH values in NaF above 9.4, suggesting the presence of low crystallinity minerals, possibly allophane (Fields & Perrot 1966, Brydon & Day 1970). Consistently, phosphate retention values equal to or greater than 25 % and [Al (oxalate) + ½ Fe (oxalate)] > 0.4 were also observed (Sá 2010). Clemente (2006) and Machado (2016) verified the presence of volcanic glass in thin section in soils of TI, but a quantitative study was not performed, so they could not be clearly classified as Andosols.

Thus, the pedological studies carried out so far in TI have obtained patchy evidences of allophane, without detailed mineralogical and micromorphological studies to confirm the occurrence of Andosols in TI. To fill this gap, the present study aims to develop a combined mineralogical, micromorphological, physical and chemical characterization of selected soils developed on TI pyroclasts in order to evaluate the presence of Andosols (**Figure 7.1a**) and, assess the pedo-environmental condition of their occurrence.

7.2 – METHODOLOGY

7.2.1- Soil collection

Soil, rocks and saprolites samples from four profiles were collected, one in the Vulcão do Paredão formation (VP) and three in the Morro Vermelho formation (MV) (**Table 7.1**). The contact sections between rocks and their respective alterites (iso and alloalterite) and solum (pedogenetic horizons) were described and sampled in the field according to the standard guidelines (Santos *et al.* 2015). The descriptions highlighted the main morphological variations at macroscopic scale, combined with the use of a magnifying glass (20 X). Aspects such as color (Munsell 1994), textures and structures were described (**Table 7.1**).

Table 7.1: Physical properties of TI soils.

Tableu 7.1: Propriétés physiques des sols TI.

Hor.	**Layer**	**Particle size**							**Color**		**Consistence**		**Plast.**	**Structure**	**BD**	**VG**
		< 2mm						**2mm>x >2µm**								
		Coarse sand	Fine sand	Silt	Clay	Silt/ Clay	Textural class		Wet	Dry	Dry	Moist				
	m	**g kg^{-1}**						**%**							**g cm^{-3}**	**%**
P1- VP																
A	0.00-0.40	26.0	111.0	384.0	478.0	0.80	Clay	52.1	7.5YR3/2 Dark brown	7.5YR3/2 Dark brown	L	FR	SP	SBK weak medium to coarse	0.75	5.4
Bi[1] / Bw[2]	0.40-0.70	12.0	78.0	360.0	549.0	0.65	Clay	45.0	7.5YR3/2 Dark brown	7.5YR4/4 Brown	SH	FI	SP	PL weak mediun	0.93	5.0
C1	0.70-0.80	23.0	159.0	399.0	419.0	0.95	Clay	58.1	7.5YR3/4 Dark brown	7.5YR4/6 Strong brown	L	FR	SP	ABK weak fine	0.93	7.4
C2	0.80-1.30	68.0	180.0	358.0	394.0	0.91	Clay loam	60.6	7.5YR3/2 Dark brown	7.5YR4/6 Strong brown	L	VFR	SP	ABK weak fine	0.71	12.76
Pyr	1.30^{+}	-	-	-	-	-	-	-	5YR4/3 Reddish brow	7.5YR5/2 Brown	-	-	-	MA		
P2- MV																
C	0.00-1.20	259.0	82.0	251.0	409.0	0.61	Clay	59.2	7.5YR4/6 Strong brown	7.5YR4/6 Strong brown	S	VFR	P	ABK weak fine to mediun	1.16	8.10
Pyr	1.20^{+}	-	-	-	-	-	-	-	5YR4/3 Reddish brow	7.5YR5/2 Brown	-	-	-	MA	-	-
P3- MV																
A	0.00-0.20	35.0	67.0	323.0	575.0	0.56	Clay	42.6	7.5YR3/2 Dark brown	7.5YR3/2 Dark brown	L	L	SP	SGR	0.72	4.16
C1	0.20-0.30	51.0	74.0	298.0	577.0	0.51	Clay	42.3	7.5YR4/4 Brown	7.5YR4/4 Brown	VH	VFI	P	SBK moderate medium to fine	1.01	16.66
Pyr	0.30-0.40	-	-	-	-	-	-	-	5YR4/3 Reddish brown	7.5YR5/2 Brown	-	-	-	MA	-	
C2	0.40-1.00	50.0	22.0	247.0	681.0	0.36	Very clayey	31.9	5YR3/3 Reddish Strong	7.5YR3/4 Dark brown	H	VFI	P	SBK moderate medium to fine	0.96	3.50
P4- MV																
A	0.00-0.20	120.0	66.0	497.0	316.0	1.57	Silt clay loam	68.3	10YR4/3 Brown	10YR5/3 Brown	S	FR	P	SGR ABK	0.71	5.9
C1	0.20-0.35	107.0	48.0	582.0	263.0	2.21	Silt	73.7	10YR3/3 Strong Brown	10YR5/3 Brown	S	FI	SP	ABK weak fine	1.38	0.59
C2	0.35-0.57^{+}	283.0	50.0	459.0	209.0	2.20	Silt loam	79.2	10YR4/3 Brown	10YR5/3 Brown	S	FR	SP	MA	-	0.66

Sand, silt and clay, determined by Pipette method, and bulk density, determined by volumetric ring method. Pyr= pyroclasts; BD= bulk density; VG= volcanic glass; L= loose; SH= slightly hard; S= soft; H= hard; FR= friable; FI= firm; VFR= very friable; VFI= very firm; SBK= subangular blocky; Pl= platy; ABK= angular blocky; MA= massive; SGR= single grain; SP= Slightly plastic; P= Plastic. 1 – Coding of horizon according to Brazilian Soil Classification System (Santos *et al.* 2018); 2 – Coding of horizon according to Soil Taxonomy (Soil Survey Staff 2014).

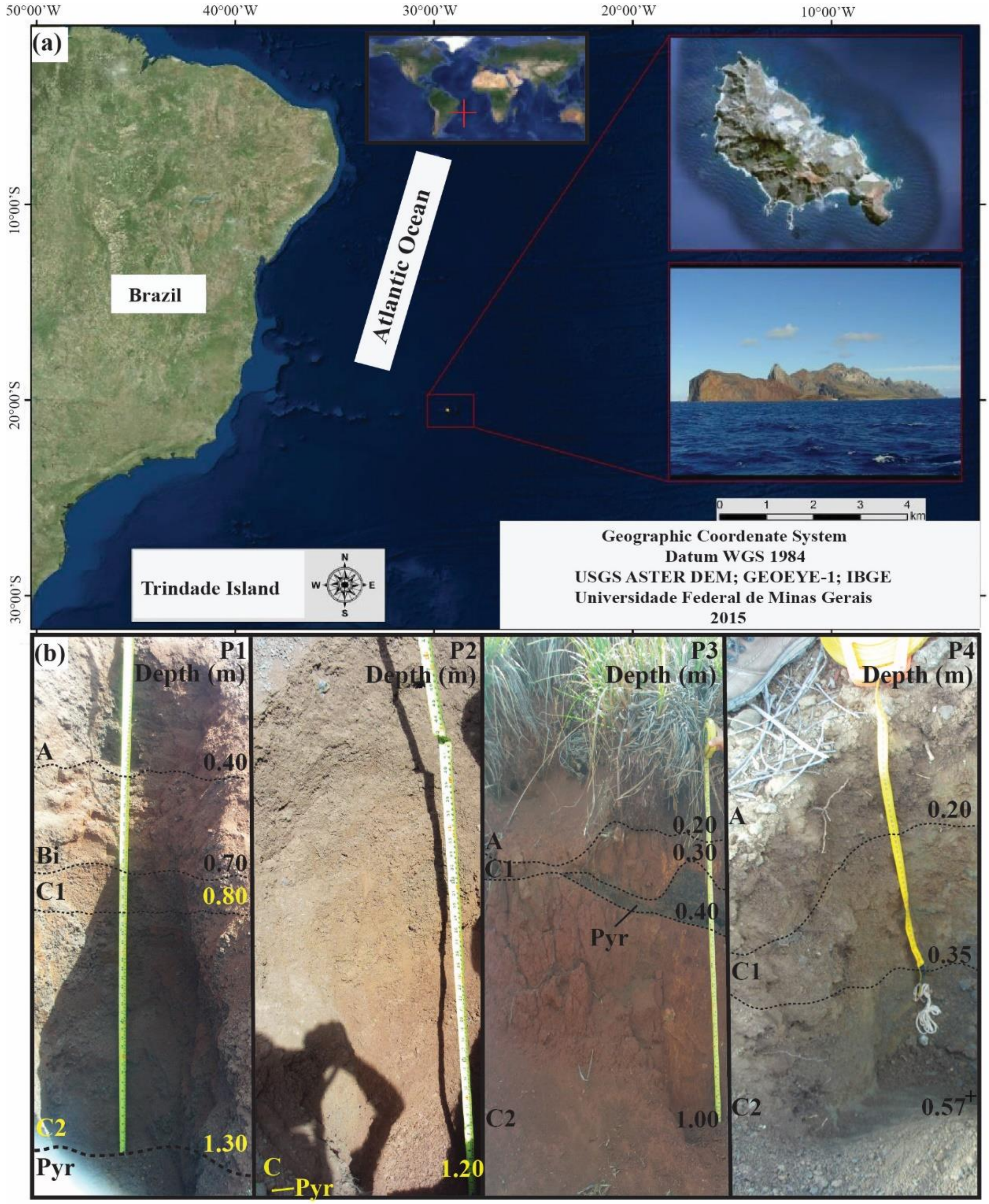

Figure 7.1: (**a**) Location of TI in South Atlantic Ocean. Elaborated by Mariana Rezende Machado. (**b**) Location of profiles in VP (P1) and MV formations (P2, P3 and P4) and description of pedological horizons. Modified of Mateus *et al*. (2018). A=A horizon, Bi= Bi horizon, C1= C1 horizon, C2= C2 horizon, Pyr= pyroclasts.

Figure 7.1 : (**a**) Localisation des IT dans l'océan Atlantique Sud. Élaboré par Mariana Rezende Machado. (**b**) Localisation des profils dans les formations VP (P1) et MV (P2, P3 et P4) et description des horizons pédologiques. Modifié de Mateus *et al*. (2018). A=Horizon A, Bi=Horizon Bi, C1=Horizon C1, C2=Horizon C2, Pyr =pyroclastes.

7.2.2- Physical and chemical analyses

The physical and chemical analyses were performed in the Laboratory of Soil Analysis of the Federal University of Viçosa, following international standard procedures (Teixeira *et al.* 2017). The contents of sand, silt and clay fractions were measured after slow agitation (16 hours) using chemical dispersion with 10 mL of NaOH 1 mol L^{-1} and the proportions of each fraction were plotted in the triangular diagram to obtain the textural class. Coarse and fine sand were separated by sieving and, silt and clay were determined by the pipette method.

The bulk density was performed by volumetric cylinder method (Almeida *et al.* 2017). The samples collected in the field in metallic cylinders of 100 g cm^{-3} and were dried at 105 °C for 48 h, to obtain the soil density.

The quantification of volcanic glass was obtained by separation by a magnifying glass Nikon C-POL it from the coarse silt to sand fractions.

The pH was measured in H_2O (soil: solution 1:2.5) and in NaF (Pansu & Gautheyrou 2006); the Melich-P concentrations was reported in mg dm^{-3} (Defelipo & Ribeiro 1981); the exchangeable contents of K, Ca, Mg and Al in cmolc dm^{-3}, allowed to sum of exchangeable bases (SB), the effective cation exchange capacity CEC (t) and total CEC (T) in cmolc dm^{-3}, base saturation (V) and aluminum saturation (m) in %. Soil organic carbon (OC) content was determined by the Walkley-Black method, while soil organic matter content (OM) was estimated, in g kg^{-1}, by the equation (OC * 1.724). The P remaining (Prem) was calculated according to Alvares *et al.* (2000) and P retention percentage (PR) as follows: P in the blank minus P in the equilibration solution (Prem).

7.2.3- Mineralogical analyses

The identification of the mineralogical phases was performed by X-ray diffractometry (XRD) in the fine-earth fraction and in the clay fraction (< 2 µm). The clay samples were saturated with Ca^{2+}, deferrified with sodium dithionite-citrate-bicarbonate (DCB) according to the methodology of Mehra & Jackson (1960), treated with formamide and dehydrated at 110ºC for 6h. The analyses were carried out in a Panalytical Empyrean (CuKα, 45KV and 40mA) and in the Philips X ' Pert Pro Diffraction (CuKα, 40 KV, 40 mA) diffractometers. The scanning interval for the fine-earth fraction analysis was from 2 to 70 °, with a step of 0.02 ° (2 (θ)/min); and for the analysis of the clay fraction from 2 to 35 °, with step 0.4° (2 (θ)/min). The diffractograms were interpreted by using the X'Pert HighScore Plus software and through the literature references (Brown & Brindley 1980).

The infrared spectroscopy was used to assist the mineralogical analyses. The analyses were performed in the IC2MP Institute, University of Poitiers using Fourrier transform spectrometers (Thermo Nicolet, Nexus 5700 series) for analyses of the bulk and clay fractions. The pressed discs were made with 1 mg of sample and 150 mg of KBr, which were analyzed with natural moisture and then dehydrated at 120 ºC for 20 h and at 200 °C for 4 h to remove absorbed water. The mid-infrared spectra (4000-400 cm^{-1}) were obtained using source of white light, beamsplitter KBr, resolution of 4 cm^{-1}, optical velocity of 0.4747 cm s^{-1} and 100 scans. Clay fraction images were obtained by a Transmission Electron Microscope (TEM) JEOL 2011 Bruker Esprit in the CinaM-CNRS, Aix Marseille University. The suspended clay was deposited on carbon-coated Formvar film Cu grids.

7.2.4- Micromorphological and microchemical analyses

Thin sections of soils and rocks previously impregnated were described in a Zeiss microscope fitted with a digital camera. The micromorphological description of soils was based on Stoops (2003) and (Stoops *et al*. 2018).

The microchemical analyses were performed with electron microprobe JEOL JXA-8230 at the Microanalysis Laboratory of Geology Department/ Federal University of Ouro Preto. The acceleration and current conditions were 15 kV and 20 nA, and corrections of the common ZAF matrix were applied. Counting times on the peaks/background were 10/5 s for all elements (Si, Al, Fe, Ca, Na, K), except for Ba (30/15 s). The point-source analyses were calibrated with quartz-TAP, coridon-TAP, almandine-LIFH, augite- PETJ, anorthoclase- TAPH, microcline- PETL and barite- PETH. The FeO was considered as the amount of total iron obtained through the microprobe.

7.2.5- Selective extraction for allophane and ferrihydrite estimate

Selective extraction of Al, Si and Fe was performed with sodium pyrophosphate (Blackmore *et al*. 1981), ammonium oxalate (MacKeague & Day 1966) and sodium dithionite-citrate-bicarbonate (Mehra & Jackson 1960; Holmgreen 1967) and determination of elemental contents by ICP-OES, for quantification of amorphous and crystalline phases.

The A1: Si ratio of the allophane was calculated from [A1(o)-Al(p)]/Si(o) and the amount of allophane in the sample was estimated by multiplying of Si(o) by the factor proposed by Parfitt (1990a): for AI: Si atomic ratios close to 1.0, 1.5, 2.0, 2.5, 3.0, 3.5, is multiplied Si(o) by the factors 5, 6, 7, 10, 12, 16, respectively. Ferrihydrite content was determined by multiplying Fe(o) values by l.7 (Parfitt & Childs 1988).

7.3 – RESULTS

7.3.1- Physical and chemical properties

The **Table 7.1** shows the macromorphological and physical characteristics of the four soil profiles. P1 is 130 cm thick located at an elevation of 460 m, with A, Bi, C1, and C2 horizons and developed from pyroclastic bombs (**Figure 7.1b**, **Table 7.1**). P2, is 120 cm thick, located at 351 m on deposit of pyroclastic bombs, and has lost most of its A horizon. P3, at an elevation of 258 m, is approximately 100 cm thick and shows A, C1 and C2 horizons, with 10 cm layer of lapillitic pyroclasts between C1 and C2. P4 has a thickness of 57 cm, located at an elevation of 72 m, with a sequence of A, C1 and C2 horizons. Bulk density is low (< 0.9 g cm^{-3}), consistently with soils developed from volcanic ash (Soil Survey Staff 2014).

All soils have high amounts of volcanic glass in the coarse sand fraction of C horizons of P1, P2 and P3 (12.76 %, 8.10 % and 20.96 %), and lower amounts in the A horizon of P4 (4.16 %) (**Table 7.1**, **Figure 7.2**). In P1, the glass is stained (reddish brown to yellowish), showing alteration to palagonite. However, this alteration is only partial in P2, P3 and P4 (**Figure 7.2**).

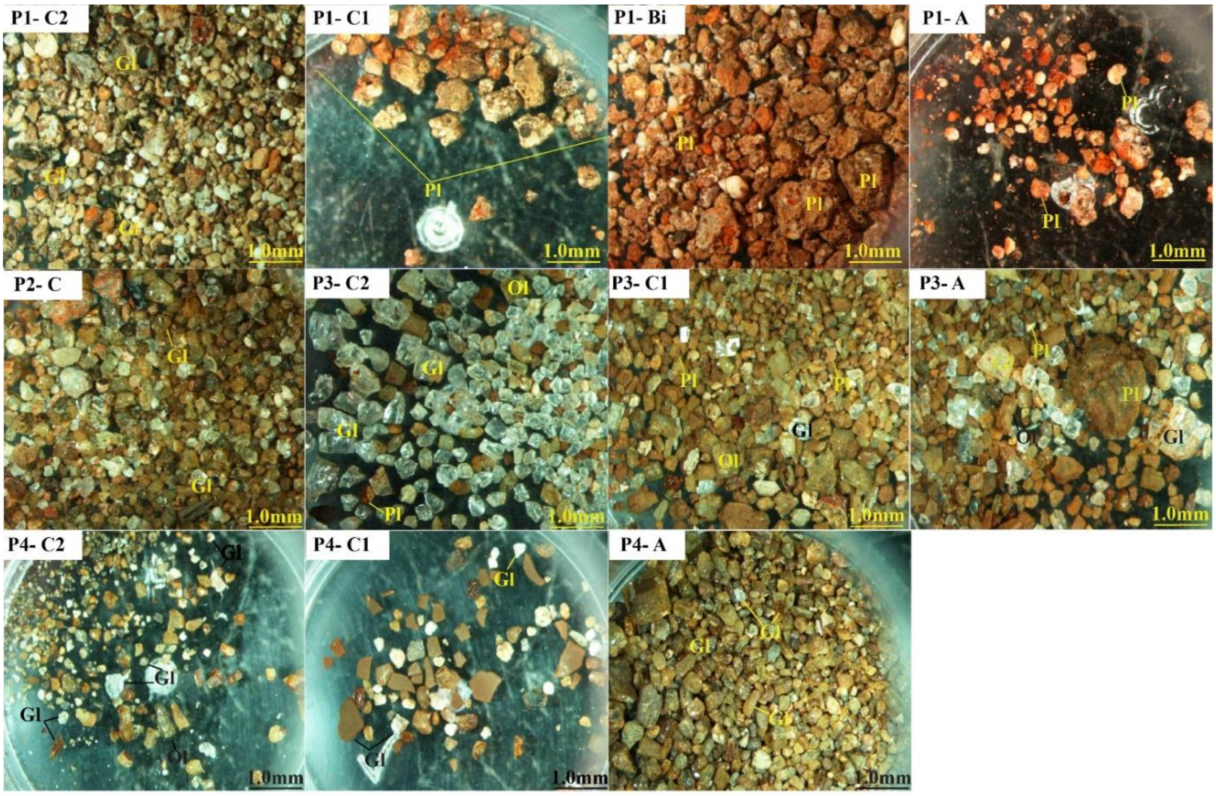

Figure 7.2: Volcanic glass of light-yellow color in the coarse sand of P1, P2, P3 and P4. It is noted than the amount of palagonitized volcanic glass increases in all horizons of P1 and, in C1 and A of P3. Gl= volcanic glass, Pl= palagonite, Ol=olivine.

Figure 7.2 : Verre volcanique de couleur jaune clair dans le sable grossier de P1, P2, P3 et P4. Il est noté que la quantité de verre volcanique palagonitisé augmente dans tous les horizons de P1 et, en C1 et A de P3. Gl=Verre volcanique, Pl=palagonite, Ol=olivine.

The bases saturation of P1 (VP) is lower than P2, P3 e P4 (MV) decreasing to the A horizon (**Table 7.2**). P1 is located at the highest altitude, hence it is exposed to more intense weathering promoting greater leaching (K^+, Na^+, Ca^{2+}, Mg^{2+}), resulting in lower pH values in H_20 (between 4.82 and 6.01). The pH in NaF is greater than 9.5 in all horizons, except A and C2 of P3. The sum of exchangeable bases (EB), effective CEC (CEC(t)) and potential CEC (CEC(T)) are high, which suggest little weathered young soils. A slight increase of EB is seen in the A horizon highlighting the influence of organic surface. The bases saturation (V) is lower than 50 % in A, Bi and C1 of P1, and above 50 % in all others (P2, P3 and P4) (**Table 7.2**). This characterizes the P1 as a dystrophic and the other profiles as eutrophic. The content of exchangeable aluminum (Al^{+3}) is high in A, Bi, C1 horizon of P1, with a marked value in A horizon (4.2 cmolc kg^{-1}). In all other soils the content of Al^{+3} is null. The available phosphorous showed similar values to soils on tuffs described by (Clemente *et al.* 2009); and phosphorous may be attributed to sideromelane (0.8 % in pyroclasts of P2 and P3), and 2.3 % in palagonitized sideromelane of P1 (Mateus *et al.*, submitted article, a). The sodium saturation in the C2 horizon of P1 and P4 represent a solodic character (sodium saturation between 6 % and 15 %). The phosphate retention (PR) is high in all horizons with values between 65 % and 97 %; in contrast, the total organic carbon contents (TOC) are low (**Table 7.2**).

7.3.2- Selective extraction of Si, Al and Fe

The Table 7.3 shows selective extraction for the four soil profiles. For all profiles the values of Al(o) are higher than Al(d), indicating higher concentration of Al in amorphous phases. The iron and silicon contents show an inverse behavior. Lower Fe(o) and Si(o) amounts than F(d) and Si(d), suggest a predominance of well- crystalline minerals in all profiles.

The soils are more enriched in Al–humus complexes than in Fe and Si–humus complexes. In particular, the values of Al–humus complexes are higher in P2, P3 and P4.

The relationship of Al(p) and Al(o) are between 0.37 and 1.22, with greater values in P3 (0.84, 0.72 and 1.22) and lower in P4 (0.37 and 0.46).

The ratio [A1(o)-Al(p)]/Si(o) values are lower in P2 (0.48) and greater in P4 (2.51), indicating a lower (3.56 g kg^{-1}= 0.36 %) and higher (31.85 g kg^{-1}= 3.19 %) contribution of allophane, respectively.

The amounts of ferrihydrite are high in all profiles, with higher value in C1 of P4 (135.66 g kg^{-1} =13.57 %).

7.3.3- Micromorphology, mineralogical and microchemical properties

The pyroclasts (**Figure 7.3a**) show a vesicular and amygdaloid structures, and show sideromelane altered to palagonite. Mineralogically they consist of biotite, hematite, magnetite, ilmenite, pyroxene (diopside), olivine (forsterite), zeolites (chabazite and heulandite) (Mateus *et al.* submitted article, a). The pedological horizons of all profiles have the same minerals in the fine-earth, in addition goethite, anatase and halloysite. Oligoclases and anorthoclases (**Table 7.4**; **Figure 7.4**) of 3.0 mm size occur in 2 % of thin section in C2 and C1 (**Figure 7.3j**) from the P4 profile.

The C horizons show coarse material composed by dark brown very altered subangular fragments of vesicular pyroclasts (**Figures 7.3b**, **g**, **k**), besides a reddish brown clayey micromass composed of fine biotite, halloysite, hematite, goethite, anatase, magnetite (**Figures 7.5a**, **b**, **c**, **d)** **(Annexes, Figures 1.1.1** à **1.2.3**). Halloysite is the only clay mineral resulting from pyroclasts weathering (**Figures 7.6a**, **b**, **c**, **d**), and shows a tubular habitus, annotated with the presence of granular hematite and acicular goethite (**Figures 7.7a**, **c**, **e**, **f**) (**Annexes**, **Figures 3.1** à **3.7**). In particular, the infrared spectra of pyroclasts from P3 showed a less crystalized signature, probably sideromelane (**Figure 7.6c**).

Table 7.2: Chemical properties of soils of the VP and MV.

Tableau 7.2 : Propriétés chimiques des sols du VP et du MV.

Pedon	Hor.	Prof.	pH			P^{5+}	K^+	Na^+	Ca^{2+}	Mg^{2+}	Al^3	H^++Al^3	EB	CEC(t)	CEC(T)	V	m	ISN	TOC	Pre	PR
		m	H_20	HC	Na						$cmol_c$ dm^{-3}						%		$g\ kg^{-1}$	mg	%
P1	A	0.00-0.40	4.8	3.8	9.6	0.15	0.1	0.8	1.16	1.52	4.2	11.60	3.63	7.83	15.23	23.	53.	5.63	2.15	2.20	96.3
	Bi^1 /	0.40-0.70	5.0	3.9	9.8	0.06	0.1	0.7	0.95	1.79	1.9	9.60	3.61	5.51	13.21	27.	34.	5.41	1.45	2.60	95.6
	C1	0.70-0.80	4.9	7.2	9.6	0.07	0.1	0.7	1.04	2.94	2.5	9.70	4.86	7.36	14.56	33.	34.	4.91	0.00	2.6	95.6
	C2	0.80-1.30	6.0	4.7	9.7	0.20	0.2	2.8	1.39	7.87	0.1	6.30	12.2	12.36	18.56	66.	0.8	15.0	0.00	3.80	93.6
P2	C	0.00-1.20	7.5	6.1	9.5	11.8	0.4	0.7	12.0	7.95	0.0	2.30	21.1	21.14	23.44	90.	0.0	3.05	7.19	20.1	66.5
P3	A	0.00-0.20	6.7	5.4	9.2	0.59	1.5	1.6	7.85	11.0	0.0	5.90	22.0	22.07	27.97	78.	0.0	5.82	18.03	8.90	85.1
	C1	0.20-0.30	7.3	5.9	9.8	0.43	1.2	0.7	9.08	7.84	0.0	2.80	18.8	18.87	21.67	87.	0.0	3.30	12.99	7.80	87.0
	C2	0.30-1.00	7.7	6.1	9.4	0.42	1.3	1.1	9.23	9.70	0.0	2.30	21.4	21.43	23.73	90.	0.0	5.03	0.69	6.50	89.1
P4	A	0.00-0.20	7.1	7.1	9.5	16.0	0.5	0.8	9.86	8.36	0.0	4.30	19.5	19.59	23.89	82.	0.0	3.46	9.39	19.2	68.0
	C1	0.20-0.35	7.2	5.6	9.5	13.9	1.0	1.0	8.12	6.87	0.0	2.30	17.1	17.11	19.41	88.	0.0	5.47	2.15	21.2	64.6
	C2	0.35-	7.4	-	9.7	12.2	1.1	1.2	7.32	6.62	0.0	2.30	16.4	16.40	18.70	87.	0.0	6.84	2.15	20.6	65.6

pH(H_2O)= pH in water-saturated soil paste (1:2.5); K+1 (Mehlich 1); Ca^{2+}, Mg^{2+}, and Al^{3+} (KCl 1 mol L^{-1}); H+Al (Calcium acetate 0.5 mol L^{-1}-pH 7.0); EB= exchangeable bases sum; CEC(t)= effective cation exchange capacity; CEC(T)= potential cation exchange capacity (at pH 7.0); V= bases saturation; m= aluminum saturation; ISNa= sodium saturation; TOC= total organic carbon (Yeomans & Bremner 1988) ; Prem =P remaining; PR= P retention. 1 – Coding of horizon according to Brazilian Soil Classification System (Santos *et al.* 2018); 2 – Coding of horizon according to Soil Taxonomy (Soil Survey Staff 2014).

Table 7.3: Selective dissolution and mineralogical properties of soils of VP and MV.

Tableau 7.3: Dissolution sélective et propriétés minéralogiques des sols du VP et du MV.

Pedon	**Hor**	**Al(o)**	**Fe(o)**	**Si(o)**	**Al(d)**	**Fe(d)**	**Si(d)**	**Al(p)**	**Fe(p)**	**Si(p)**	**Aph$^{(1)}$**	**Fh $^{(2)}$**	**Al(o)+ 0.5Fe(o)**	**Al/Si$^{(3)}$**	**Al(p)/ Al(o)**	**Fe(p)/ Fe(o)**	**Fe(o)/ Fe(d)**
		g.kg^{-1}												**atomic ratio**			
P1	**A**	11.31	21.1	2.23	6.36	108.5	5.85	7.08	0.43	0.29	15.59	35.87	21.86	1.89	0.62	0.02	0,19
	Bi^1 / Bw^2	9.21	18.05	2.10	5.42	82.11	4.92	6.18	0.28	0.22	12.57	30.68	18.23	1.44	0.67	0.01	0,22
	C1	11.53	21.52	2.90	6.13	96.35	4.94	5.34	0.38	0.33	17.38	36.58	22.29	1.77	0.46	0.02	0,22
	C2	10.57	19.11	2.99	5.58	71.87	5.19	3.93	0.28	0.32	20.95	32.49	20.12	2.23	0.37	0.01	0,26
P2	**C**	8.40	20.18	3.56	6.17	70.86	9.56	6.90	0.56	0.60	3.56	21.88	18.49	0.41	0.82	0.02	0,28
P3	**A**	8.96	24.77	3.49	6.87	92.93	5.64	7.56	0.62	0.54	17.45	42.11	21.34	1.05	0.84	0.02	0,27
	C1	11.29	26.75	2.98	7.70	86.84	4.90	8.19	0.58	0.47	17.90	45.70	24.76	1.64	0.72	0.02	0,31
	C2	8.39	24.55	3.86	5.85	103.06	7.11	10.28	27.29	4.30	3.86	41.73	20.66	0.48	1.22	1.11	0,24
P4	**A**	12.10	19.96	3.18	5.29	25.39	7.61	6.05	0.86	0.69	31.85	33.93	22.08	2.52	0.50	0.04	0,79
	C1	11.40	20.75	4.17	6.17	23.32	9.02	6.38	0.62	0.76	29.19	135.66	21.77	2.05	0.56	0.03	0,89
	C2	10.80	17.47	3.99	5.49	19.03	9.50	11.79	0.58	0.79	19.94	29.70	19.53	0.74	1.09	0.03	0,92

(1) Allophane: Si(o) multiplied by a factor Parfitt (1990); (2) ferrihydrite: Fe(o)* 1.7; (3) (Al(o) -Al(p)/Si(o). 1 – Coding of horizon according to Brazilian Soil Classification System (Santos *et al*. 2018); 2 – Coding of horizon according to Soil Taxonomy (Soil Survey Staff 2014).

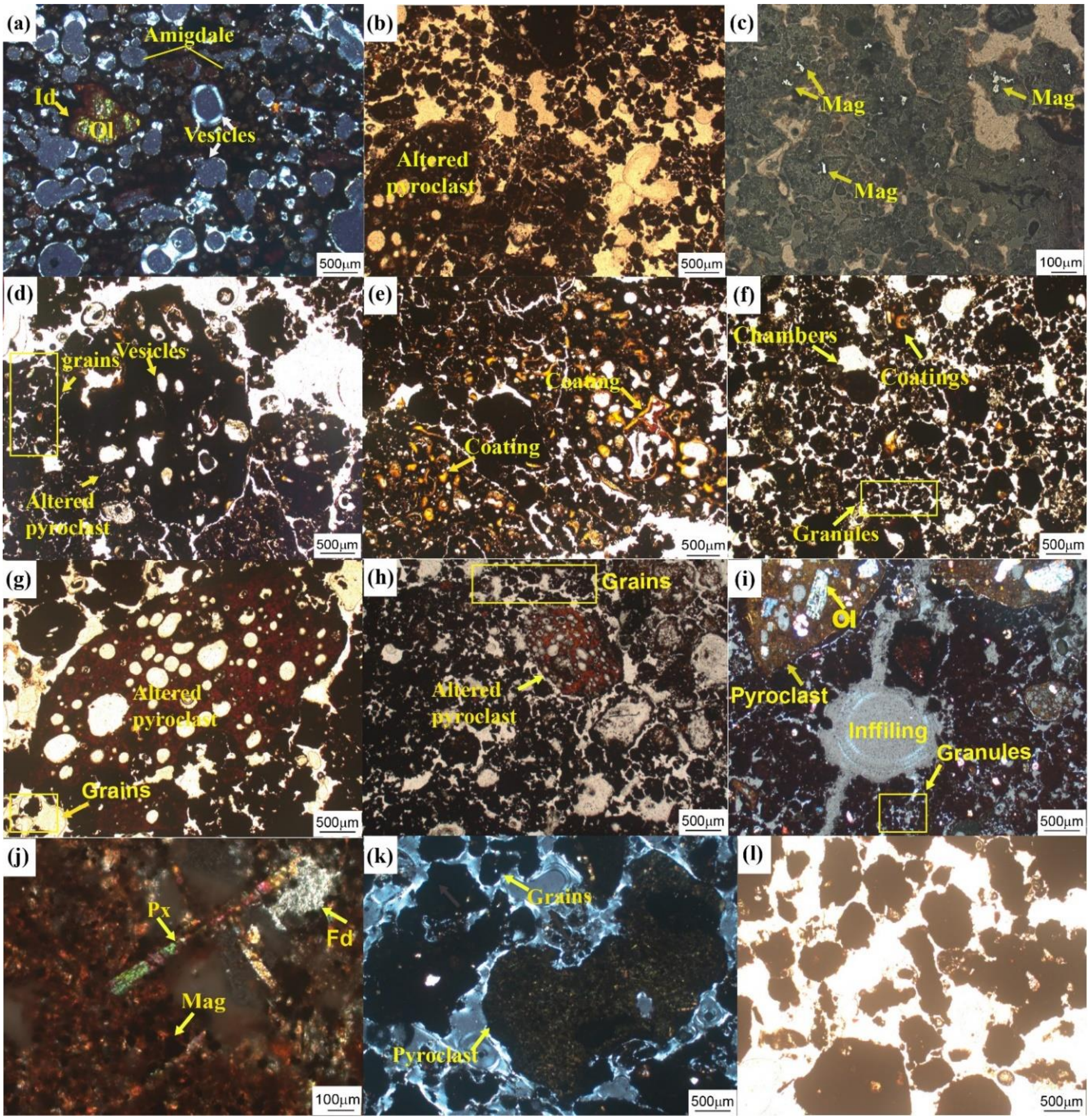

Figure 7.3: (**a**) XPL photomicrograph of pyroclasts from P1 showing vesicles and olivine iddingsitized. (**b**) PPL photomicrograph of C2 horizon from P1 showing altered vesicular pyroclasts and a simple grains microstructure evidenced by coarse monic c/f related distribution. (**c**) Reflected light photomicrograph of C1 horizon from P1 showing magnetite crystals in the clay matrix and pyroclast fragments. (**d**) PPL photomicrograph of Bi horizon from P1 showing altered pyroclast fragments divided into smaller fragments. (**e**) PPL photomicrograph of Bi horizon from P1 showing coatings of clay and c/f chitonic distribution. (**f**) PPL photomicrograph of A horizon from P1 showing granular and intergrain microaggregate microstructures and coating of clay. (**g**) PPL photomicrograph of C horizon from P2 showing pyroclast fragment with sideromelane totally palagonitized and grains of altered pyroclasts of 250mm. (**h**) PPL photomicrograph of C2 horizon from P3 showing the simple grains microstructure and pyroclasts fragments less altered than in P1. (**i**) XPL photomicrograph of A horizon from P3 showing pyroclast fragment with unaltered Ol, granules of clay aggregates with undifferentiated b-fabric and infilling. (**j**) XPL photomicrograph of C2 horizon from P4 showing pyroclast fragment with pyroxenes, magnetites and feldspar. (k) XPL photomicrograph of C1 horizon from P4 showing pyroclast fragment and aggregates of clay. (**l**) PPL photomicrograph of A horizon from P4 showing granular microstructure.
Ol=olivine; Id=iddingsite; Px=pyroxene; Mag=magnetite; Fd= feldspar; XPL=Crossed polarized light; PPL=Plane polarized light.

Figure 7.3: (**a**) Photomicrographie par LPX de pyroclastes de P1 montrant des vésicules et des olivines iddingsitisées. (**b**) Le photomicrographie par LPP de l'horizon C2 à partir de P1 montrant des pyroclastes vésiculaires altérés et une microstructure de grains isolées démontrée par la distribution grossier/fine de type *monic* (type de modèle de distribution des constituants grossiers et fins dans lesquels seules des particules d'une plage de taille (ou matériau amorphe) sont présentes) grossier. (**c**) Photomicrographie par lumière réfléchie de l'horizon C1 de P1 montrant cristaux des magnétites dans la matrice d'argile et les fragments de pyroclaste. (**d**) Photomicrographie par LPP de horizon Bi de P1 montrant des fragments de pyroclaste alterés et divisés en fragments plus petits. (**e**) Photomicrographie par LPP de horizon Bi de P1 montrant des revêtements d'argile et de distribution grossier/fine *chitonic* (type de modèle de distribution des constituants grossiers et fine dans lesquels les particules les plus grossières sont complètement ou partiellement recouvertes de matériaux plus fine). (**f**) Photomicrographie par LPP de l'horizon A de P1 montrant des microstructures granulaires et intergrains micro-agrégées et cutans d'argile. (**g**) Photomicrographie par LPP de l'horizon C de P2 montrant fragment de pyroclaste avec sideromelane totalement palagonitisée et grains de pyroclastes altérés de 250mm. (**h**) Photomicrographie par LPP de l'horizon C2 de P3 montrant les microstructure grains isolées et fragments de pyroclastes moins altérés que dans P1. (**i**) Photomicrographie par LPX d'horizon A de P3 montrant un fragment de pyroclaste avec Ol inaltéré, granules d'agrégats d'argile avec une *b-fabric* (disposition spatiale des constituants du sol) indifférencié et pédotubule. (**j**) Photomicrographie par LPX de l'horizon C2 de P4 montrant un fragment de pyroclaste avec pyroxènes, magnétites et feldspaths. (**k**) Photomicrographie par LPX de l'horizon C1 de P4 montrant un fragment de pyroclaste et des agrégats d'argile. (**l**) Photomicrographie par LPP d'un horizon de P4 montrant la microstructure granulaire.

Ol=olivine; Id=iddingsite; Px=pyroxène; Mag=magnetite; Fd= feldspath; LPX= Polariseur croisés ; LPP= Lumière polarisée.

Table 7.4: Microchemical analyses in feldspars crystals in C2 horizon, P4.

Tableau 7.4 : Analyses microchimiques dans cristaux de feldspars à l'horizon C2, P4.

	Crystal A				**Crystal B**			**Crystal C**		
Region	**Edge**	**Edge**	**Edge**	**Interm.**	**Edge**	**core**	**Edge**	**Edge**	**Edge**	**Edge**
Point	**1**	**2**	**3**	**4**	**1**	**2**	**3**	**1**	**2**	**3**
					%					
SiO_2	60.15	60.27	59.20	61.67	62.07	62.49	62.21	60.32	59.37	59.43
Al_2O_3	24.61	24.35	25.03	24.01	23.17	22.99	23.19	24.315	24.048	24.62
FeO	0.39	0.47	0.35	0.36	0.34	0.33	0.38	0.34	0.34	0.32
CaO	4.06	3.65	4.15	3.46	2.56	2.56	2.54	3.44	3.28	2.99
Na_2O	7.37	7.42	7.40	7,83	7.72	7.64	7.67	7.50	7.19	6.94
K_2O	1.72	1.81	1.51	2.09	2.71	3.14	2.84	1.96	2.16	2.60
BaO	0.00	0.00	0.00	0.00	0.00	0.00	0.00	0.00	0.00	0.00
Total	100.52	100.32	100.59	99.33	98.57	99.15	100.54	100.34	96.38	96.90
Si	2.72	2.74	2.70	2.76	2.80	2.81	2.80	2.74	2.74	2.73
Al	1.31	1.30	1.34	1.27	1.23	1.22	1.23	1.30	1.31	1.33
Fe	0.01	0.02	0.01	0.01	0.01	0.01	0.01	0.01	0.01	0.01
Ca	0.20	0.18	0.20	0.17	0.12	0.12	0.12	0.17	0.16	0.15
Na	0.65	0.65	0.65	0.68	0.68	0.67	0.67	0.66	0.64	0.62
K	0.10	0.10	0.09	0.12	0.16	0.18	0.16	0.11	0.13	0.15
Ba	0.00	0.00	0.00	0.00	0.00	0.00	0.00	0.00	0.00	0.00
Xca=Ano	20.9	19.0	21.5	17.2	13.0	12.7	12.8	17.8	17.4	16.0
Xna=Ab	68.6	69.8	69.3	70.4	70.7	68.7	70.1	70.1	69.0	67.4
XK=Or	10.5	11.2	9.3	12.4	16.3	18.6	17.1	12.1	13.6	16.6

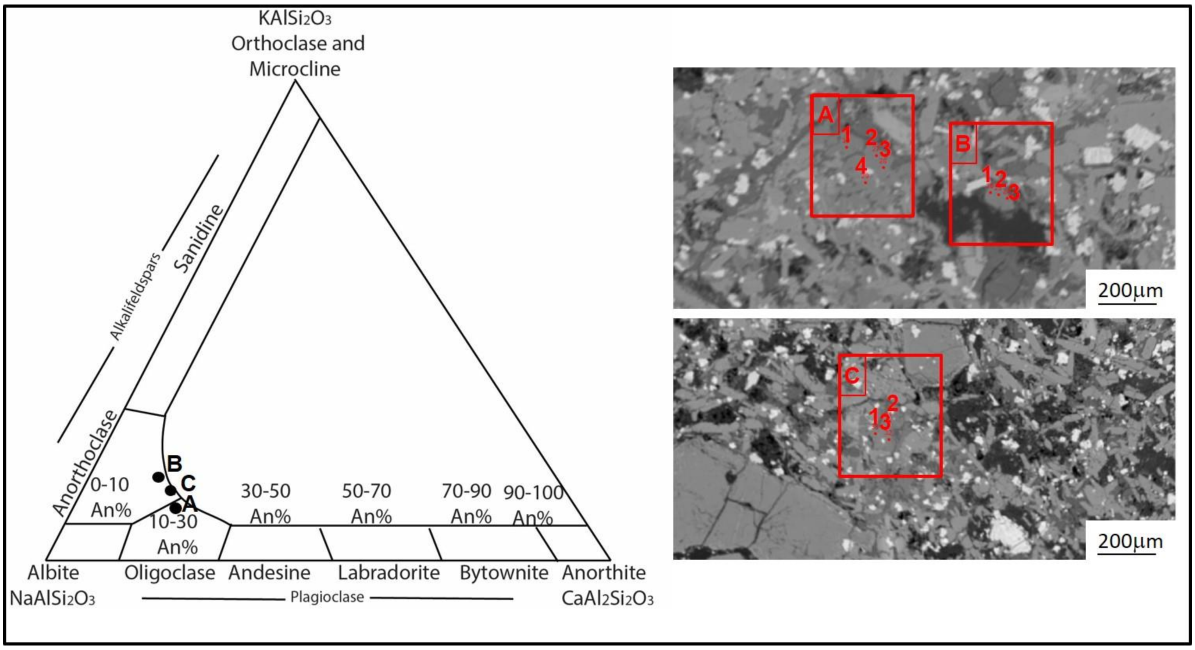

Figure 7.4: Feldspar diagram and SEM images in C2 horizon. The plot of microchemical analyses in the diagram shows that the crystal A is an oligoclase and, B and C are anorthoclase.

Figure 7.4 : Diagramme de feldspar et images de MEB à l'horizon C2. Le point d'analyses microchimiques dans le diagramme montre que le cristal A est une oligoclase et, B et C sont anorthoclase.

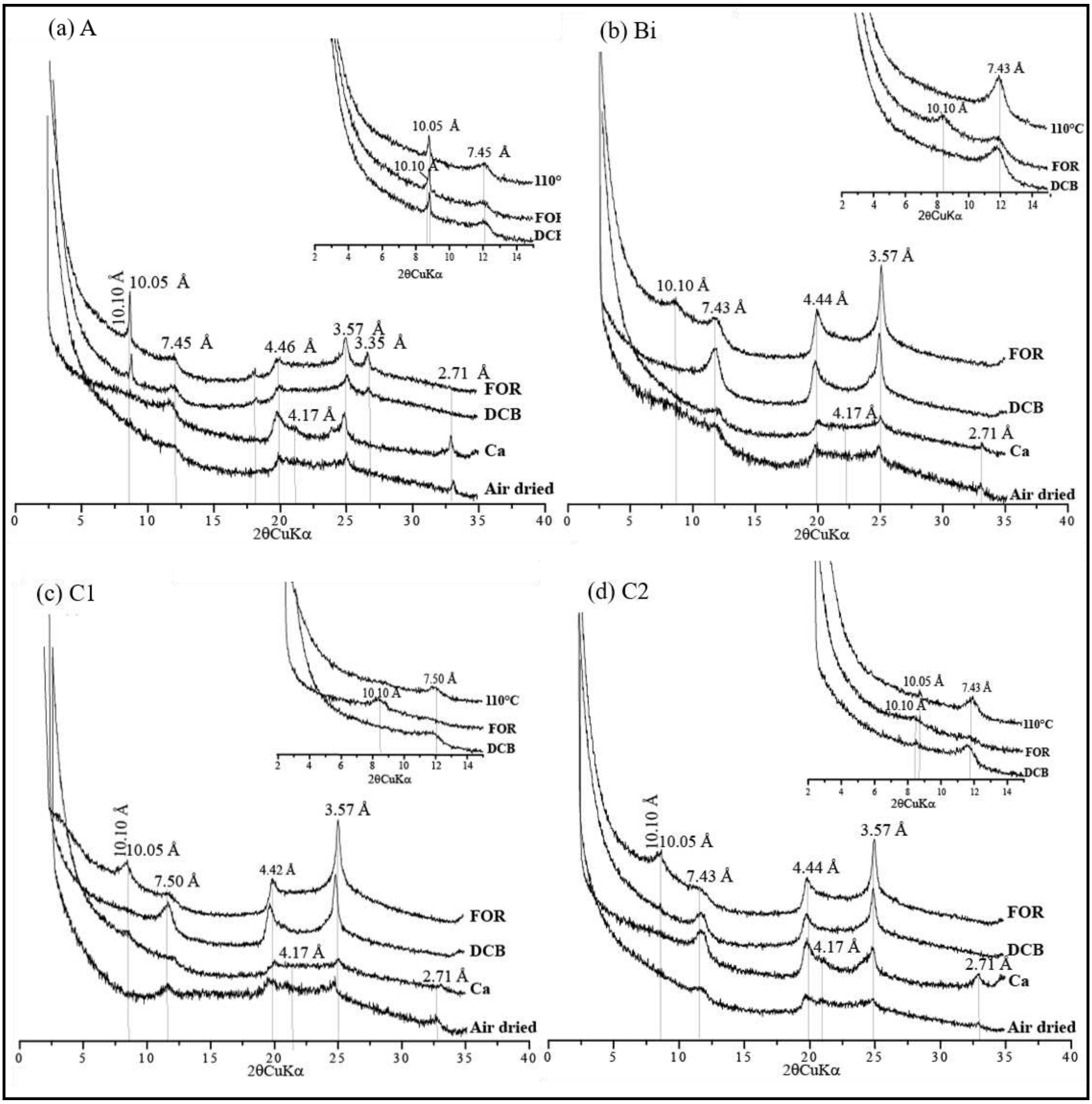

Figure 7.5: (**a**), (**b**), (**c**) and (**d**): XRD of P1 of clay fraction air dried, saturated with Ca^{2+} (Ca), deferrified with sodium dithionite-citrate-bicarbonate (DCB) and saturated with formamide (FOR). Biotite= 10.10 Å; 3.35 Å; Halloysite = 10.05 Å; 7.45 Å, 4.46 Å, 3.57 Å; Hematite=2.71Å.

Figure 7.5 : (**a**), (**b**), (**c**) et (**d**) : DRX de P1 de la fraction argile séché à l'air, saturé avec Ca^{2+} (Ca), deferrifié avec dithionite-citrate-bicarbonate de sodium (DCB), saturé avec formamide (FOR) et chauffé à 110°C. Biotite= 10.10 Å, 3.35 Å; Halloysite=10.05 Å, 7.45 Å, 4.46 Å, 3.57 Å; Hématite= 2.71Å.

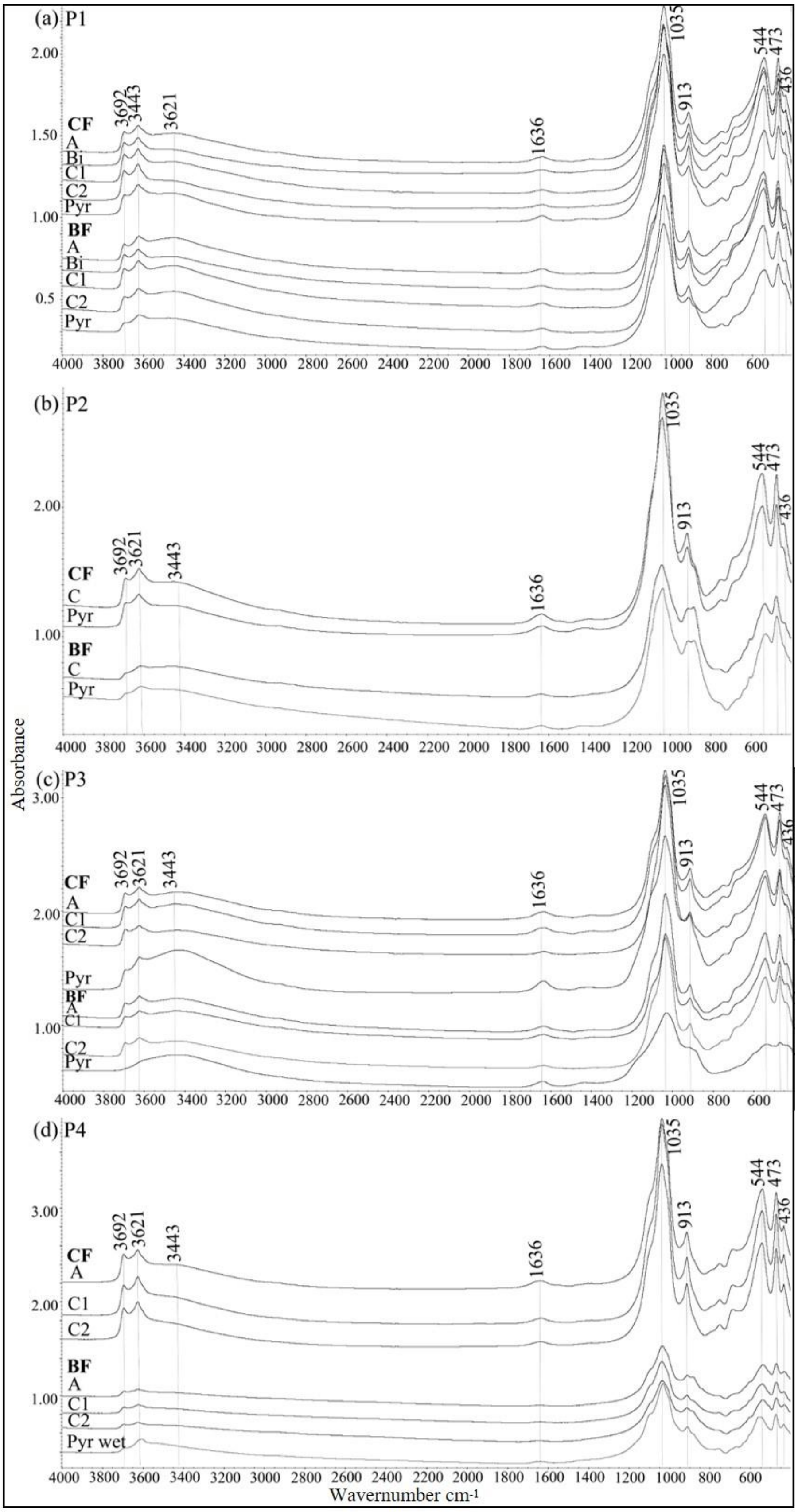

Figure 7.6: **(a), (b), (c)** and **(d):** MIR images of pedological horizons of P1, P2, P3 and P4 showing the spectrum of halloysite. In P3 is noted the presence of piques of material non crystalline in region between 400 cm^{-1} and 950 cm$^{\mathbf{-1}}$**.**

Figure 7.6: (**a**), (**b**), (**c**) et (**d**): Images d'Infrarouge Moyen des horizons pédologiques de P1, P2, P3 et P4 montrant le spectre de l'halloysite. En P3 est noté la présence de piques de matériaux non cristallins dans la région entre 400 cm^{-1} et 950 cm^{-1}.

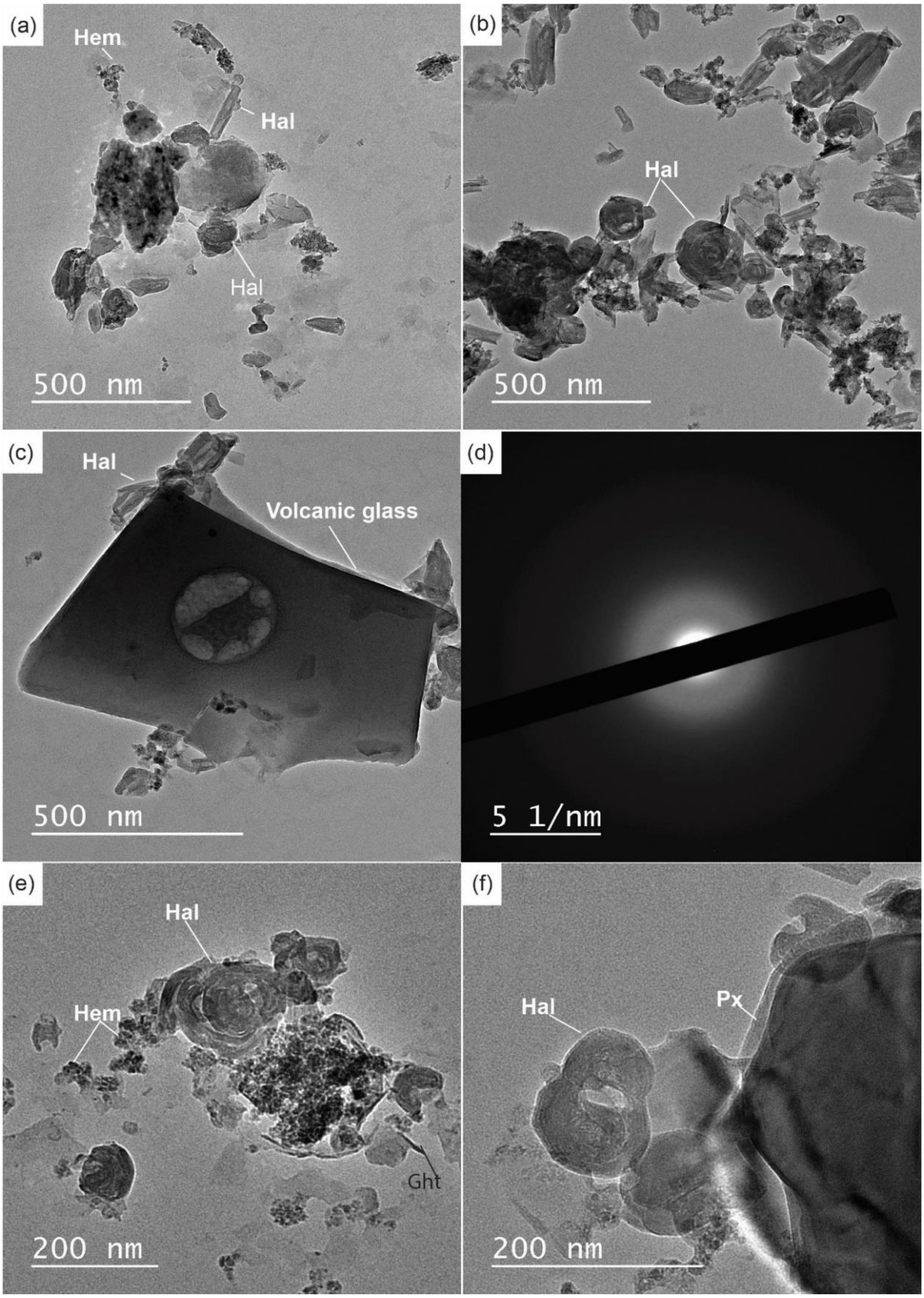

Figure 7.7: TEM images of fraction clay of P1. (**a**) Tubular halloysite and iron oxides (hematite) in pyroclast. (**b**) Halloysite tubular in C2 horizon. Is noted that the halloysite are very crystallized. (**c**) Volcanic glass and halloysite in C2 horizon. The figure (**d**) showed the microdiffraction with characteristic of amorphous material. (**e**) Tubular

halloysite and iron oxyhydroxides (hematite globular and goethite acicular) in Bi horizon. (**f**) Tubular halloysite near of crystal of pyroxene in A horizon. Hal= halloysite; Hem= hematite; Ght=goethite, Px=pyroxene.

Figure 7.7: Images de MET de la fraction argile de P1. (**a**) Halloysite tubulaire et oxydes de fer (hématite) dans le pyroclaste. (**b**) Halloysite tubulaire à l'horizon C2. Est noté que l'halloysite sont très cristallisés. (**c**) Verre volcanique et halloysite à l'horizon C2. La figure (**d**) a montré la microdiffraction avec la caractéristique du matériel amorphe. (**e**) Halloysite et oxyhydroxides de fer (hématite globulaire et goethite aciculaire) dans l'horizon Bi. (**f**) Halloysite tubulaire près du cristal de pyroxène dans horizon A. Hal= halloysite; Hem= hématite; Ght=goethite, Px=pyroxéne.

The c/f related distribution is coarse monic in C horizons (**Figure 7.3b**), changing to chitonic and eunalic in Bi and A horizons, showing a single grain and intergrain microaggregate microstructure, respectively at the bottom and top of the profiles (A and Bi horizons), (**Figures 7.3b**, **f**, **h**, **i**). In Bi and A horizons the pyroclasts fragments are split into smaller fragments characterizing the transition from simple grain to intergrain microaggregate microstructure (**Figures 7.3d**, **f**, **i**).

The typical granular microstructure also occurs in the A horizon (**Figures 7.3f, l**). The pyroclasts fragments and olivine and magnetite crystals decrease in size and quantities towards to the surface. At the bottom (C2 horizon), pyroclasts fragments of 15.0mm size, subhedral magnetite of 0,1mm size and altered olivines of 2.0mm size occur, respectively, in sizes of 5.0mm, 0.03mm and 1.0 mm at the top (A horizon) of the profile.

Aggregates occur in Bi and A horizons and show undifferentiated b-fabric micromass (**Figure 7.3i**). As pedological features, reddish and yellowish clay coatings occur, evidencing illuviation of fine colloidal materials (**Figures 7.3e**, **f**) and infillings of clay due to the bioturbation (**Figure 7.3i**).

7.4 – DISCUSSIONS

The presence of andic properties on TI soils was evaluated using the criteria in both the Soil Taxonomy (Soil Survey Staff 2014), for moderate or weakly weathered soils, and WRB FAO (2015). Recently, in 2018, the Brazilian Soil Classification System – SiBCS (Santos *et al.* 2018) incorporated this property, using the same criteria as the WRB (2015) (**Table 7.5**).

Table 7.5: Diagnostic criteria to andic properties according to (I) Soil Taxonomy (Soil Survey Staff 2014) for moderately weathered soils, WRB (2015) and SiBCS (Santos *et al.* 2018), and (II) Soil Taxonomy for weakly weathered soils.

Tableu 7.5: Critères diagnostiques aux propriétés andiques selon (I) Soil Taxonomy (Soil Survey Staff 2014) pour les sols modérément altérés, WRB (2015) et SiBCS (Santos *et al.* 2018), et (II) Taxonomie du sol pour les sols faiblement altérés.

		I				II						
Pedon	**Hor.**	**$A \geq 2$**	**$BD \leq 0.9$**	**$PR \geq 85$**	**AP**	**$TOC < 25$**	**$A \geq 0.4$**	**$PR \geq 25$**	**sand and silt ≥ 30**	**$VG \geq 5$**	**B**	**AP**
		%	**kg dm^{-3}**	**%**		**%**						
P1	A	2.20	0.75	96.33	*	0.00	2.20	96.33	52.1	5.4	39.77	*
	Bi[1] / Bw[2]	1.80	0.93	95.66		1.45	1.80	95.66	45.0	5.0	33.12	
	C1	2.23	0.93	95.66		2.15	2.23	95.66	58.1	7.4	42.24	*
	C2	2.00	0.71	93.66	*	0.00	2.00	93.66	60.6	12.76	44.24	*
P2	C	1.85	1.16	66.55		7.19	1.85	66.55	59.2	8.1	37.01	*
P3	A	2.13	0.72	85.16	*	18.03	2.13	85.16	42.6	20.96	54.24	*
	C1	2.50	1.01	87.00		12.99	2.50	87.00	42.3	16.66	55.72	*
	C2	2.06	0.96	89.16		0.69	2.06	89.16	31.9	3.5	35.69	
P4	A	2.21	0.71	68.00		9.39	2.21	68.00	68.3	5.9	40.43	*
	C1	2.17	1.38	64.66		2.15	2.17	64.66	73.7	0.59	34.50	
	C2	1.95	-	65.66		2.15	1.95	65.66	79.2	0.63	31.10	

TOC= total organic carbon; PR= phosphate retention; A= (Al(o) +½ Fe(o) B= [(Al(o) +½ Fe(o)]*(15.625) + (volcanic glass content, percent) ≥ 36.25; AP=andic properties; *horizon with all criteria met. .1 – Coding of horizon according to Brazilian Soil Classification System (Santos *et al.* 2018); 2 – Coding of horizon according to Soil Taxonomy (Soil Survey Staff 2014).

According to Soil Survey Staff (2014), soil with andic properties must have less than 25 % of total organic carbon (TOC), with one of the following criteria that must to be met: 1) for moderately weathered soil: the values of [Al(o) + ½Fe(o)] > 2 %; the bulk density of soil equal or minor than 0.90 g cm^{-3} and phosphate retention equal or minor than 85 %; or 2) for weakly weathered soil: ratio [Al(o)+ ½Fe(o)] $\geq$ 0.4 %; phosphate retention $\geq$ 25 %; 30 % or more of sand and silt particles; volcanic glass content $\geq$ 5 % and [(Al(o) +½ Fe(o)].(15.625) + (volcanic glass content in %) $\geq$ 36.25. In addition, the andic properties quoted in criteria 1 or 2 should occur 60 % of the soil profile. For WRB (2015) and SiBCS (Santos *et al.* 2018), only the parameters shown in 1 are taken into account.

Considering the Soil Taxonomy criteria 1, WRB and SiBCS, only three horizons (P1A, P1C2, P3A) met all criteria. The main attribute not met was the bulk density, since only the A horizons of P1, P3 and P4, and C2 horizon of P1 showed density lower than 0.90 g cm^{-3}. However, except for the P4C1 horizon (**Table 7.2**), the values are not much greater than 0.9 g cm^{3}, varying between 0.93 and 1 g cm^{-3}, so very close to the limit.

The soils of TI have met criterion 2 of the Soil Survey Staff (2014), because they contain less than 25 % of TOC (**Table 7.2**) and are weakly weathered. The presence of primary minerals in A and B horizons (glass, olivine, pyroxenes, feldspar), inside and outside of altered pyroclast fragments, including in the clay fraction, corroborate the low weathering degree of these soils (**Figures 7.3k**, **o**, **r** and **7.6f**). P1, P2 and P3 all have andic properties by this criterion in 60 % of their profiles (**Table 7.5**). Only the Bi horizon of P1 showed a value lower than of the sum [(Al (O) + 1/2 Fe (o)] * (15.625) + (volcanic glass content in %) $\geq$ 36.25, while the C2 horizon of P3 presented less than 5 % of volcanic glass, and therefore only, these two horizons do not follow criterion 2. P4 soil did not have 5 % volcanic glass in 60 % of the profile, and therefore does not meet criterion 2, either (**Table 7.5**). It is important to emphasize that the C2 horizon of P4 consists of fragments of mineralogical composition different from the other profiles, suggesting a different volcanic event of pyroclastic bomb deposition.

In addition, based on criterion 2, the andic properties detected were: ratio Al(o) $_+$ ½Fe(o) higher than 0.4 % (**Table 7.5**); phosphate retention (PR) greater than 25 % in all horizons, with values between 65 and 97 % (**Table 7.2**); the sand and silt amount exceeding 30 % in all profiles (**Table 7.1**), corroborating less weathered soils; also, all horizons, excluding the C2 and C1 of P4 and C2 of P3, showed at least 5 % of glass volcanic in the coarse sand fraction in part of the profile (**Table 7.1**, **Figure 7.2**).

Pyroclasts fragments consisting of palagonized glass corroborate the content of more than 5 % of volcanic glass in the < 2mm fraction (**Figures 7.3b**, **e**, **h**, **j**, **n**, **o**).

NaF values greater than 9.4 also indicate the presence of non-crystalline minerals. However, all profiles presented little amounts of allophane (between 0.36 and 3.19 %), and the Si(o) content ≥ 0.6 % further suggests the presence of these amorphous materials. The pH (H_2O)>5 in all profiles and low content of organic material would contribute the allophane formation (Dahlgen *et al.* 1993). The values of the Fe(o)/Fe(d) ratio are also high in all profiles indicating the presence of no crystalline minerals and a poorly weathered soil (**Table 7.5**).

Although the selective extractions indicated the presence of amorphous minerals, mineralogical analyzes (XRD, Infrared and TEM) were not capable of detect their presence, although halloysite was found. Consistently, in Cabo Verde Island, halloysitic soils with high amounts Al–humus complexes were classified as non-allophanic Andosols (Madeira *et al.*1994). Accordingly, soils of the present study have an undifferentiated b-fabric characteristic of the gradual replacement of allophane by halloysite, and illuviation features in all horizons, particularly more pronounced in the Bi horizon of P1, shows that they are Andosols intermediate to soils with more crystalline clays (Stoops *et al.* 2018).

The classification of non-allophanic horizons requires some properties, such as: Alp/Alo of 0.5 or more, and/or Si(o) concentration of less than 6 g kg^{-1}; and thickness of 25 cm or more (Eguchi & Tamura 2012, USCS 2002). All profiles of this study have Si(o) concentration less than 6 g kg^{-1} and thickness of 25 cm or more, so, they can be classified as non-allophanic Andosols. Alternative names for allophane-like materials which could be used are defective kaolin allophane or halloysite-like allophane, when Al:Si ratio value are near 1 (Yoshinaga 1986) or proto-imogolite allophane and imogolite-like, when this ratio is between 2 and 4 (Farmer & Fraser 1979, Parfitt & Wilson 1985). In this case, the soils of P1 and P3 would present halloysite-like allophane, whereas P4 a proto-imogolite allophane and imogolite-like. According to the WRB (2015) soils in which allophane, imogolite and similar minerals are predominant, have silandic properties (Si(o) content of ≥ 0.6 % or an Al(p)/Al(o) of < 0.5).

We suggest that sideromelane is the likely precursor of halloysite. The study of Mateus *et al.* (submitted article, a) on the alteration of pyroclasts of TI showed the presence of little quantities of halloysite in regions when occur altered sideromelane (palagonite). In addition, the halloysite of P4 also has feldspars as possible precursors (oligoclase and anorthoclase), besides volcanic glass.

Soils with andic properties, also considered non-allophanic, have already been recognized in the Brazilian territory. In a pioneer report, Ker (1988) suggested the possibility of soils with andic properties in southern Brazil. Later, Gama *et al.* (1992) also suggested that soils from Acre could possess this character. None of the above studies have demonstrated allophanic soils, and only Dümig *et al.* (2008) who effective reported the first Andosols of Brazil, identified in the northeast plateau of the Rio Grande do Sul state. From this study, WRB (2015) began to recognize Andosols originated from non-volcaniclastic parent materials in humid regions.

Recently, Santos Junior (2017) confirmed the presence of non-allophanic Andosols in the escarpment of Serra Geral Formation, in the states of Santa Catarina and Rio Grande do Sul. This author identified eight Aluandic Andosols, and two Histosols with andic properties. The organometallic complexes formed in the cold-humid-high elevation areas explained the formation of soils with andic properties associated with non-volcanoclastic rocks.

TI soils show an unusual situation, with non-allophanic soils derived from typic pyroclastic materials. As previously described, the other non-allophanic soils in Brazil occur because of cold climate conditions and the role of the organic matter. Studies of soil genesis on Late Quaternary pyroclastic rocks, scorias, tuffs and ashes of basaltic composition from the Federal Republic of Cameroon (Sieffermann & Millot 1969) showed that in tropical climates, with average annual precipitation between 1.5 and 1.6 m, and a marked dry season marked and in less leached zones, there is a rapid neoformation of halloysite through allophane as an intermediate phase, maintaining lower amounts of allophane. In our study at TI, we have found similar characteristics: pyroclasts of basaltic composition and tropical oceanic climate with average annual rainfall between 926 mm and a marked dry season, between January and March. Therefore, the climatic conditions of the island could contribute to the rapid formation of halloysite from an allophane precursor, helping to explain the small amounts of allophane in these soils.

According to Sedov *et al.* (2010) Andosols show a well-developed medium granular microstructure at the top which changes to coalesced microstructures towards to the bottom of profile, very similar to those reported here, but less stable than microgranular microstructures of Latosols (Oxisols). The A horizons showed a granular microstructure, with an undifferentiated b-fabric typical of Andosols on pyroclasts from oceanic islands Pico and Fail in Azores (Gerard 2007); Terceira (Pinheiro *et al*. 2003); Canarias, (Benayas *et al*. 1980, Sanchez Diaz 1978); and Santa Fé (Morrás 1978).

Despite the criteria in the WRB (2015) can be considered satisfactory for the SiBCS (Santos *et al*. 2018), they fail to meet the specificities of TI soils. Soil Taxonomy will offer better conditions to incorporate soils with andic properties with different degrees of the development. Thus, we believe that the criteria currently adopted by Soil Survey Staff (2014) are more adequate for keying out soils like those of Trindade Island, in the SiBCS.

There is no place for Andosols in the SiBCS. Using the current system (Santos *et al*. 2018), the soils of this study would be classified as CAMBISSOLO HÁPLICO Sódico típico (P1), with A moderate, presence of Bi horizon and lower base saturation (< 50 %), (**Table 7.2**); NEOSSOLO REGOLÍTICO Eutrófico típico (P3) and NEOSSOLO REGOLÍTICO Eutrófico solódico (P4). P3 has A moderate, absence of B, lithic contact at a depth greater than 0.50 m, with semi-altered pyroclasts fragments within the C; P4 is different from P3, because it presents a solodic character (sodium saturation between 6 and 15 % in C2 horizon) (**Table 7.2**).

Using the WRB (2015), only pedon (P1) can be classified as Andosol (**Table 7.6**). The others are classified as Regosols, but this class does not admit the andic suffixes as supplementary qualifiers. The reason why some pedons, such as P3, have not been classified as Andosols is because even though they have the andic properties on the A horizon, they are 20 cm thick, whereas a minimum of 30 cm is required by the WRB/FAO System. According to Soil Survey Staff (2014), P1, P2 and P3 are all Andisols, respectively Alic and Typic Hapludand.

Table 7.6: Classification of TI soils according to SiBCS (2018), WRB (2015) and Soil Taxonomy (Soil Survey Staff 2014).

Tableau 7.6 : Classification des sols IT selon SiBCS (2018), WRB (2015) et Soil Taxonomy (Soil Survey Staff 2014).

Pedon	SiBCS	WRB	ST
P1	Cambissolo Háplico Sódico Típico	Vitric Aluandic Andosol	Alic Hapludand
P2	Neossolo Regolítico Eutrófico típico	Eutric Leptic Regosol	Typic Hapludand
P3	Neossolo Regolítico Eutrófico típico	Eutric Leptic Regosol	Typic Hapludand
P4	Neossolo Regolítico Eutrófico solódico	Sodic Eutric Leptic Regosol	Typic Udipsamments

7.5 – CONCLUSIONS

1 - The soils of TI present andic properties and should be classified as Andosols, and meeting the criteria to be classified as non-allophanic Andosols. In addition, the micromorphological features are like the Andosols described from elsewhere.

2 - The Andosols in TI are non-allophanic for a different reason, compared with other non-allophanic Andosols already reported in Brazil. In Trindade Island, soils are derived from pyroclastic materials, and the silandic conditions are weakened by the rapid weathering under warmer climates. Other non-allophanic soils in the southern highlands of Brazil have andic properties because were formed under cold-mesothermic climate conditions.

3 - The predominance of halloysite in the clay fraction is consistent with the non-allophanic character of TI soils. Halloysite was formed by alteration of sideromelane, in which allophane is the intermediate phase.

4 – These unique TI soils should be recognized in the SiBCS as special soils, and the adoption of Soil Taxonomy criteria for weakly weathered soils allows us to key them out as non-allophanic Andosols.

CHAPITRE 8

EVOLUTION GEOCHIMIQUE DES PROFILS[4]

ABSTRACT

The geochemical behavior of the major, minor, trace and rare earths elements (REEs) in soil profiles from ultramafic volcanoclastic rocks of the Vulcão do Paredão and Morro Vermelho Formation from Trindade Island (TI) was analyzed in this study. With chemical composition determination, losses and gains were calculated through the chemical mass balance for two profiles along the slope: one located at higher altitude (460 m) and the other at lower altitude (258 m). In all profiles Al, Fe and Ti accumulate due to their low mobility, whereas Ca, Na, K and Mg are the most intensely leached. Soils located at lower altitude show higher K and Mg values in the surface due to the contribution of saline sprays. Leaching of the REEs from higher to the lower slope led to the enrichment of these elements, especially the light REEs, in the low lying (258 m) soil. The high altitude profile showed Ce positive anomaly due to longer exposure to weathering. The geochemical balance shows a relative enrichment of Ti, Mn, Fe, Co, Cr, Ni, V, Zr, S related to the loss of mobile elements during the soil formation process, despite the youthful nature of these volcanic rocks.

Keywords: Geochemical balance, REEs, Inductively coupled plasma atomic emission spectroscopy (ICP-AES).

---

[4] Article soumis au magazine “Brazilian Journal of Geology” avec le titre “Geochemical evolution of soils on the latest pyroclastic volcanic rocks of Trindade Island, South Atlantic”.

8.1– INTRODUCTION

The distribution and migration of the chemical elements, and the chemical reactions during weathering and soil formation processes are essential in pedogeochemical studies (Carvalho 1995). The meteoric water reacts with most rock minerals, and new stable mineral phases are formed under new physicochemical conditions (Carvalho 1995). In this process some chemical elements are leached out, while others are concentrated.

To study the distribution and migration of chemical elements along the soil profile, the chemical mass balance between the parent material and the alteration products is used, an isovolumetric change (Millot & Bonifas 1955).

In the Brazilian territory there are few studies on the geochemistry of soils from volcanic oceanic islands, specifically on the latest pyroclasts. Of the existing studies, few report the geochemical evolution of soil formation. Among them there are the studies of Oliveira (2008) and Oliveira *et al.* (2014) that showed the soil phosphatization process of Rata Island (Fernando de Noronha Archipelago) due to the interaction of bird excrement with olivine nephelinites (ankaratritic lavas), and that of Oliveira *et al.* (2009) than report high levels of Cu, Pb, Zn, As, U, and Sr in besides soils of this island due to the interaction of bird excrement with mafic rocks, and anomalous concentrations of Ba, Nb, Ta, Cr, Hf, V and Zr due to the geochemical inheritance of local basalts. In the Fernando de Noronha Island, Oliveira *et al.* (2011a) showed that soils developed from mafic rocks (nepheline basalts) presented higher contents Fe, Co, Ni and Cr and Oliveira *et al.* (2011b) showed that soils from these rocks concentrate REEs, preferably the heavy REEs (HREEs).

In basaltic pyroclasts from Azores there are studies on the behavior of REEs (Freitas & Pacheco 2010, Vieira *et al.* 2004), showing a predominance in light REEs elements (LREEs) and positive Ce and Er negative anomalies. In soils developed on phonolitic pyroclasts in Cape Verde also occur positive Ce anomalies (Marques *et al.* 2018).

In Trindade Island, despite studies by Clemente *et al.* (2012) have shown the availability of trace elements in soils from different eruptive materials, there are still deficiencies in studies showing the behavior of chemical elements in these soils, including REEs and the chemical mass balance. To fill this gap, the present study aims to bring more information about the geochemical evolution from the pyroclasts to the soil and to evaluate the distribution and quantification of losses and gains of major, minor, trace and REEs.

8.2 – METHODOLOGY

The sampling was carried out along four alteration profiles covering the pedological horizons and semi-altered ultramafic pyroclastic rocks of the Vulcão do Paredão and Morro Vermelho Formation, located at different altitudes of Trindade Island (**Figure 8.1**).

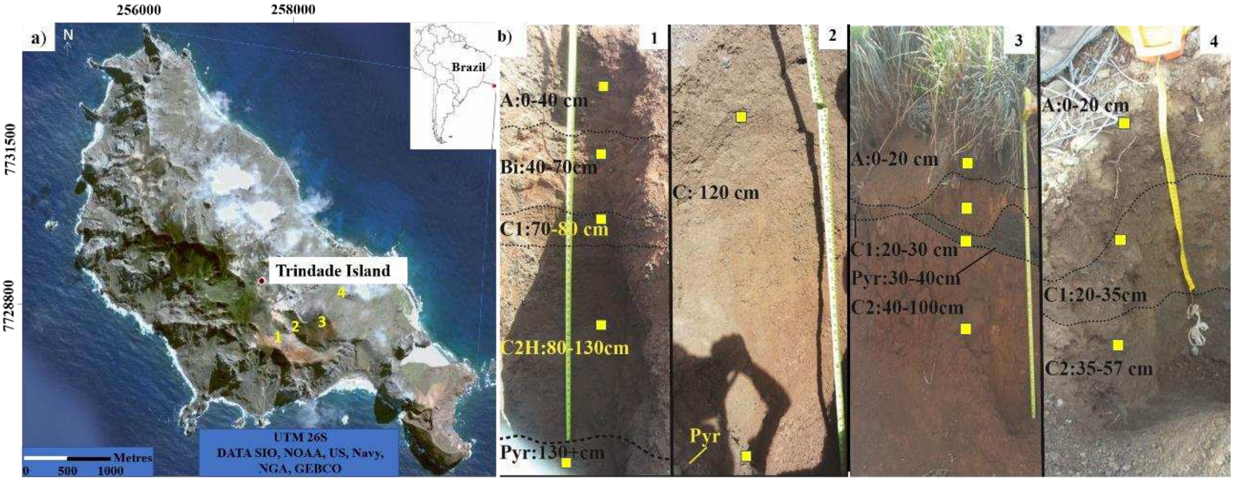

Figure 8.1: a) Satellite image of Trindade Island with location of 1, 2, 3 and 4 profiles. b) Image of profiles 1, 2, 3 and 4 showing sampling point. Modified of Mateus *et al*. (2018).

Figure 8.1 : a) Imagerie satellite de l'Île Trindade avec situation de profils 1, 2, 3 et 4. b) Image des profils 1, 2, 3 et 4 montrant le point d'échantillonnage. Modifié de Mateus *et al*. (2018).

The undeformed soil samples were collected by using a volumetric ring, maintaining the original structure of the material to determine the apparent density.

8.2.1- Geochemical analysis

For the chemical analyzes, the samples of weathered rocks and soils were air-dried and then manually sprayed in agate mortar and sieved to 150 # (granulometry less than 0.105 mm), individualizing aliquots of about 50 g.

The chemical analyses of the major (Al, Si, Fe, K, Mg, Na, Ca, P), minor (Ti, Mn) and trace elements (Ba, Co, Cr, Cu, Li, Ni, Sr, Th, V, Zn, Be, Zr, S, Sc, Ga, Y, Cd, In, Cs, Tl, Pb, Bi, U) were obtained by ICP-OES Agilent Technologies 725 while the rare earth elements (REEs) by ICP-MS Agilent Technologies 7700 at the LGqa Laboratory of DEGEO/UFOP. For total digestion of 0.1 g of each sample, 1 mL of hydrogen peroxide, 3 mL of HCl per 10 mol L^{-1}, 6 ml of HNO_3 per 10 mol L^{-1}, 20 mL of HNO_3 per 2 mol L^{-1} and 4 mL of HF concentrate were used. The percentage of SiO_2 was calculated in a relative way by the difference to 100 % in the sum of the main elements and LOI.

8.2.2- Apparent bulk density, absolute contents and geochemical balance

For this analysis the most complete profiles were chosen, including, at the base, the presence of pyroclasts and, at the top, the A horizon.

The determination of bulk density was made for the weathered rocks by paraffin clod method and for the soils by volumetric ring method, (Embrapa 2018).

The density values were incorporated in the calculation of losses and gains of the elements from the altered rock to the soil, so that the volume variation could be fixed. The absolute contents of each chemical component of profiles 1 and 3 were then calculated using the contents of the elements obtained by chemical analysis and the density measurement of the respective samples. For the quantitative evaluation of the losses and gains of chemical elements during the pedogenetic processes, the chemical mass balance calculations were performed using the Millot & Bonifas (1955) precepts.

8.2.3- Mineralogy and physical characteristics

Table 8.1 summarizes the main physical and mineralogical characteristics of the four soil profiles according Mateus *et al.* (submitted article, b) and Mateus *et al.* (2018).

Table 8.1: Physical and mineralogical characteristics of the profiles (Mateus *et al.* submitted article, a and b) and Mateus *et al.* (2018).

Tableau 8.1 : Caractéristiques physiques et minéralogiques des profils (Mateus *et al.* article soumis, a et b) et Mateus *et al.* (2018).

Profile	Location	Altitude (m)	Source material and geological formation	Erosion	Pyroclast mineralogy	Soil mineralogy
1	257867/7729600 top	460	Cambisols pyroclast derivative Vulcão do Paredão	Extremely strong	Ol, Px, Bt, Mag, Ilm, Hem, sideromelane, sideromelane palagonitized	Ol, Px, Bt, Mag, Ilm, Hem, Hal, Fh, Gth, Ant, sideromelane palagonitized
2	257916/7729828 Upper middle strand	351	Regosols pyroclast derivative Morro Vermelho Formation	Extremely strong	Ol, Px, Bt, Mag, Ilm, Hem, Zl, sideromelane, sideromelane palagonitized	Ol, Px, Bt, Mag, Ilm, Hem, Hal, Fh, Gth, Rt, sideromelane palagonitized
3	258467/7729761 Lower middle strand	258	Regosols pyroclast derivative Morro Vermelho Formation	Extremely strong	Ol, Px, Bt, Mag, Ilm, Hem, sideromelane, sideromelane palagonitized	Ol, Px, Bt, Mag, Ilm, Hem, Hal, Fh, Gth, Rt, sideromelane palagonitized
4	258826/7730121 strand of the coast; base	72	Regosols pyroclast derivative Morro Vermelho Formation	Extremely strong	-	Ol, Px, Bt, Fd, Mag, Ilm, Hem, Hal, Fh, Gth, Rt

Bt= Ti-biotite, Ol=olivine (forsterite), Ilm=ilmenite, Px=pyroxenes (diopside), Mag=magnetite, Fp=feldspars (anorthoclase, oligoclase), Zl=zeolite (chabazite, heulandite), Hem=hematite, Gth=goethite, Ant=anatase, Rt=rutile, Hall=halloysite, Ferryhidrite= Fh.

8.3 – RESULTS

8.3.1- Geochemistry

Pyroclasts show the predominance of SiO_2, FeO_t, Al_2O_3, TiO_2, CaO, MgO and P_2O_5 among the major and minor elements (**Table 8.2**), due to the presence of forsterite, clinopyroxene (diopiside), Ti-biotite, Ti-magnetite, ilmenite and sideromelane (**Table 8.1**). In particular, CaO value in the profile 2 is higher than TiO_2 due to the presence of calcium zeolites (Ca-chabazite and Ca-heulandite) added to the presence of clinopyroxenes. K_2O, Na_2O and MnO occur in small quantities and are mainly related to volcanic glass (sideromelane) which constitutes approximately 50 % of the rock. The pyroclasts from profile 3 contain K_2O values greater than Na_2O due to the higher amounts of Ti-biotite. The high LOI values are due to the presence of sideromelane and palagonite that contain water in their composition. Among the trace and REEs, Ba, Cr, Sr, V, Zr and Ce are those that show similar contents in all pyroclasts.

Table 8.2: Bulk chemistry analysis of major, minor, trace elements, and REEs from the soil profiles 1, 2.3 and 4. LQ= quantification limits; LOI= loss on ignition, Py= pyroclasts.

Tableau 8.2 : Analyse en chimie total des élements principaux, traces et des terres rares des profils de sol 1, 2.3 et 4. LQ=Limites de quantification; LOI= perte au feu, Pyr= pyroclaste.

	1					**2**		**3**				**4**		
	A	**Bi**	**C1**	**C2**	**Pyr**	**C**	**Pyr**	**A**	**C1**	**C2**	**Py**	**A**	**C1**	**C2**
							%							
SiO_2	28.2	21.94	26.91	30.02	37.47	34.67	37.50	27.61	26.11	23.96	37.81	33.80	32.03	39.16
FeO_t	31.45	36.88	31.15	26.73	19.58	20.37	16.09	28.87	29.43	35.46	18.46	21.50	19.49	16.74
Al_2O_3	17.18	17.10	17.24	18.01	14.68	13.19	11.95	13.90	15.17	13.88	13.38	12.17	12.39	11.35
TiO_2	10.18	10.70	10.20	8.92	6.95	7.08	5.36	9.89	10.25	10.95	7.31	6.75	6.36	5.63
CaO	0.09	0.08	0.10	0.10	5.43	7.47	11.15	0.65	0.96	1.00	3.50	7.35	9.86	11.43
MgO	0.90	0.81	0.84	1.04	4.50	5.10	7.37	1.90	2.07	2.16	3.67	7.97	6.55	7.47
P_2O_5	0.39	0.31	0.37	0.45	1.36	1.23	1.48	0.86	1.04	0.90	0.86	1.56	1.29	1.27
Na_2O	0.05	0.07	0.07	0.17	0.53	0.41	0.57	0.18	0.19	0.23	0.29	0.48	0.63	0.92
K_2O	0.03	0.04	0.05	0.07	0.15	0.37	0.27	0.63	0.68	0.88	0.48	0.32	0.27	0.34
MnO	0.48	0.39	0.47	0.45	0.30	0.34	0.27	0.36	0.38	0.41	0.30	0.27	0.24	0.22
LOI	11.05	11.68	12.60	14.03	9.05	9.79	7.99	15.15	13.71	10.17	13.95	7.82	10.89	5.48
Total	100.00	100.00	100.00	100.00	100.00	100.00	100.00	100.00	100.00	100.00	100.00	100.00	100.00	100.00
							mg kg^{-1}							
Ba	2724.73	2916.77	2907.94	2293.72	1377.45	1426.84	1608.22	1422.68	1439.27	1786.25	1887.55	1069.01	850.11	852.91
Co	252.51	257.73	248.08	185.76	127.12	86.38	92.73	176.60	177.42	193.78	116.35	122.91	74.05	69.07
Cr	751.27	643.95	596.31	478.44	252.82	578.50	363.23	683.44	714.72	682.87	472.19	560.56	269.56	218.10
Cu	64.10	57.27	54.58	64.37	44.73	80.54	75.90	74.01	84.62	76.33	87.47	60.45	56.30	82.09
Li	9.24	10.07	15.20	22.07	14.35	12.55	10.94	22.76	26.46	23.95	9.69	10.85	<LQ	<LQ
Ni	226.73	232.70	232.73	204.51	115.04	119.72	127.93	187.52	223.57	184.52	115.02	145.57	108.55	80.91
Sr	482.29	615.96	625.91	567.67	1240.76	1054.46	1592.12	469.31	428.65	724.35	566.09	821.77	871.48	858.86
Th	40.12	39.46	37.80	30.50	33.40	37.97	39.50	26.52	28.34	34.50	32.02	30.88	29.60	30.21

V	313.97	353.05	299.32	247.72	248.97	334.69	302.20	465.91	485.33	425.56	275.81	305.18	247.86	255.17
Zn	211.01	206.70	203.02	202.32	145.55	151.26	128.11	178.16	182.52	215.66	172.75	151.72	134.15	144.44
Be	0.58	<LQ	0.87	1.27	1.08	1.26	1.00	1.21	1.23	1.56	1.13	0.76	0.62	0.99
Zr	439.82	463.95	444.32	373.15	314.24	347.24	279.70	447.85	460.68	511.87	308.19	367.80	325.71	296.98
S	1408.03	1519.63	1260.70	300.59	220.20	262.83	110.88	355.97	564.24	86.81	65.44	213.50	70.96	<LQ
Sc	53.38	53.00	50.04	46.73	34.83	38.78	29.49	43.50	45.54	48.53	37.16	36.04	29.44	28.14
Ga	41.22	42.74	37.75	35.04	33.44	33.64	28.96	38.98	41.77	43.06	33.80	32.83	29.27	26.48
Y	17.53	15.12	12.93	13.86	42.62	51.25	48.56	54.55	54.42	63.60	41.28	43.68	38.52	38.90
Cd	1.73	1.67	1.82	3.23	1.86	1.27	0.88	1.78	2.30	2.71	0.75	0.94	0.63	0.49
In	0.21	0.23	0.19	0.18	0.15	0.15	0.12	0.20	0.21	0.22	0.16	0.15	0.14	0.13
Cs	0.07	0.12	0.15	0.31	1.04	1.59	0.75	1.41	1.48	1.92	0.62	0.51	0.28	0.18
Tl	<LQ	<LQ	<LQ	<LQ	<LQ	<LQ	<LQ	0.14	0.15	0.12	<LQ	<LQ	<LQ	<LQ
Pb	5.74	5.15	4.42	3.19	4.19	5.85	10.64	11.12	10.75	11.70	12.23	4.92	3.64	3.64
Bi	0.12	0.05	<LQ	<LQ	<LQ	<LQ	<LQ	0.06	0.08	0.06	0.043	0.05	0.04	<LQ
U	3.03	2.95	2.62	2.38	2.51	3.23	2.68	3.24	3.55	3.71	2.01	1.62	0.91	1.18
La	38.59	38.41	34.20	34.13	101.82	127.72	124.19	124.05	127.47	164.00	89.93	105.11	91.96	90.85
Ce	254.68	225.13	238.97	253.98	267.19	323.83	299.11	298.14	290.14	329.25	229.24	239.88	206.00	216.34
Pr	9.17	8.57	7.57	10.03	27.42	34.12	32.55	33.69	33.89	40.44	23.99	27.95	24.81	24.75
Nd	37.93	35.42	31.17	42.85	109.93	137.39	131.87	137.46	136.28	169.70	97.44	111.06	98.49	98.66
Sm	9.15	9.14	7.99	11.02	20.58	25.49	24.14	26.09	25.98	31.68	18.72	20.97	18.63	18.58
Eu	3.21	3.22	2.82	3.62	6.34	7.63	7.28	7.88	7.90	9.24	5.85	6.42	5.64	5.61
Gd	8.24	7.61	6.81	8.53	18.01	21.80	20.60	22.33	22.27	25.87	16.37	18.08	16.00	15.95
Tb	0.99	0.93	0.83	1.05	2.00	2.44	2.25	2.52	2.56	2.90	1.87	2.05	1.82	1.81
Dy	5.55	5.16	4.61	5.74	10.10	12.44	11.26	13.12	13.23	14.96	9.67	10.42	9.24	9.24
Ho	0.93	0.86	0.76	0.92	1.67	2.07	1.87	2.17	2.20	2.50	1.64	1.72	1.53	1.52
Er	2.34	2.17	1.93	2.32	4.03	5.14	4.66	5.28	5.38	6.10	4.04	4.20	3.74	3.68
Tm	0.30	0.27	0.24	0.29	0.46	0.58	0.53	0.61	0.63	0.71	0.48	0.48	0.42	0.42
Yb	1.75	1.61	1.46	1.84	2.56	3.36	3.04	3.51	3.55	3.99	2.68	2.67	2.40	2.40
Lu	0.23	0.21	0.18	0.23	0.35	0.46	0.41	0.47	0.47	0.54	0.36	0.36	0.32	0.32

In all soil horizons occur the predominance of SiO_2, Al_2O_3, FeO_t, TiO_2, (**Table 8.2**). The high amounts of FeOt is mainly attributed the presence of semi-altered primary mineral such as Ti-magnetites and secondary minerals such as hematite, goethite and ferrihydrites (**Table 8.1**). TiO_2 is the fourth most abundant element in the profiles 1, 2 and 3 and its presence is related to the presence of rutile, anatase, biotite, magnetite and ilmenite.

The normalization of the REEs' concentrations to chondrite data show higher concentrations of LREEs in all profiles. The profile 1 have positive anomalies of Ce higher than other profiles (2, 3 and 4) (**Table 8.3**; **Figure 8.2**).

8.3.2- Absolute contents and geochemical balance from profiles 1 and 3

Distribution diagrams (**Figure 8.3** and **8.4**) were obtained by the relation of the absolute contents (**Table 8.4**) with the density values. This relationship together with the chemical balance results (**Table 8.5**) allows us to make the following inferences:

8.3.2.1- *Profile 1*

Among the major and minor elements, Si, Al, Fe and Ti show similar behavior. There is a pronounced decrease in absolute contents towards C2 horizon followed by a relative increase to the top of profile. Gains are higher in the Bi horizon with 66.83 % Fe and 36.36 % Ti, and in the C1 horizon with 40.25 % Mn. Na, K, Ca, Mg and P also show similar comportment with a pronounced decrease to the top of the profile, but no peaks of increase. For Mg there is an increase peak in the C1 horizon with stabilization in the A and Bi horizons. Losses are higher in Ca and Na with values around 90 % compared to the altered pyroclast.

Among the trace elements, the absolute contents of Ba, Co, Cr and Ni increase significantly towards the top, with moderate gain in the A horizon, reaching 87.55 %, 19.57 %, 125.57 % and 79.16 %, respectively, in the Bi horizon. For Cu, Th, V, Zn, Zr, S, Pb, Ca, Ga and U there is a decrease from the rock to C2 horizon and a more pronounced increase in the Bi horizon followed by a decrease in the A horizon. Among these elements, S is the one with significant gain of 511.24 % in the Bi horizon while Th, V and Ga have relative loss of 14.20 %, 9.92 % and 11.95 % respectively. Sr and Be behavior is the reverse of Ba, Co, Cr e Ni, that is, occur a decrease towards the top of the profile with higher loss of Sr and Be in the A horizon. The Y presents similar loss in all horizons with values around 70 %.

For the REEs occur a decrease of all elements toward the top of the profile, except Sc that presents increase. Among them, the Dy, Er, Yb, La and Nd show a peak increase in the Bi horizon and, in particular of Ce in the C1 horizon. The geochemical balance shows less loss in the Bi horizon except the Ce which has the lowest value in the C1 horizon. The greatest losses are of LEERs with values around 60-80 %, except the Ce with value between 19-35 %. The HEERs show moderate losses of around 40-60 %.

Table 8.3: Concentration results, in mg kg^{-1}, and their normalization to chondrite (McDonough & Sun 1995), for rare-earth elements in profiles 1,2, 3 and 4.

Tableau 8.3 : Résultats de la concentration, en mg kg^{-1}, et leur normalisation pour la chondrite (McDonough & Sun 1995), pour les éléments de terres rares dans les profils 1,2, 3 et 4.

Prof.	Hor.	La	Ce	Pr	Nd	Sm	Eu	Gd	Tb	Dy	Ho	Er	Tm	Yb	Lu	ΣLREE	ΣHREE	LREE/HREE	La/Lu	Ce/Ce*	Eu/Eu*
1	**A**	128.63	303.19	76.42	65.40	43.57	43.38	27.47	20.20	17.90	12.74	11.14	9.09	8.75	7.42	617.21	114.72	5.38	17.34	2.82	1.21
	Bi	128.03	268.01	71.42	61.07	43.52	43.51	25.37	18.98	16.65	11.78	10.33	8.18	8.05	6.77	572.05	106.11	5.39	18.90	2.54	1.23
	C1	114.00	284.49	63.08	53.74	38.05	38.11	22.70	16.94	14.87	10.41	9.19	7.27	7.30	5.81	553.36	94.49	5.86	19.63	3.03	1.23
	C2	113.77	302.36	83.58	73.88	52.48	48.92	28.43	21.43	18.52	12.60	11.05	8.79	9.20	7.42	626.06	117.44	5.33	15.33	3.01	1.16
	Py	339.40	318.08	228.50	189.53	98.00	85.68	60.03	40.82	32.58	22.88	19.19	13.94	12.80	11.29	1173.52	213.53	5.50	30.06	1.10	1.09
2	**C**	425.73	385.51	284.33	236.88	121.38	103.11	72.67	49.80	40.13	28.36	24.48	17.58	16.80	14.84	1453.84	264.64	5.49	28.69	1.06	1.06
	Py	413.97	356.08	271.25	227.36	114.95	98.38	68.67	45.92	36.32	25.62	22.19	16.06	15.20	13.23	1383.61	243.20	5.69	31.30	1.01	1.07
3	**A**	413.50	354.93	280.75	237.00	124.24	106.49	74.43	51.43	42.32	29.73	25.14	18.48	17.55	15.16	1410.42	274.25	5.14	27.27	1.00	1.07
	C1	424.90	345.40	282.42	234.97	123.71	106.76	74.23	52.24	42.68	30.14	25.62	19.09	17.75	15.16	1411.40	276.91	5.10	28.03	0.96	1.07
	C2	546.67	391.96	337.00	292.59	150.86	124.86	86.23	59.18	48.26	34.25	29.05	21.52	19.95	17.42	1719.07	315.85	5.44	31.38	0.85	1.04
	Py	299.77	272.90	199.92	168.00	89.14	79.05	54.57	38.16	9.67	22.47	4.04	14.55	13.40	11.61	1029.73	168.46	6.11	25.81	1.07	1.10
4	**A**	350.37	285.57	232.92	191.48	99.86	86.76	60.27	41.84	33.61	23.56	20.00	14.55	13.35	11.61	1160.19	218.79	5.30	30.17	0.96	1.08
	C1	306.53	245.24	206.75	169.81	88.71	76.22	53.33	37.14	29.81	20.96	17.81	12.73	12.00	10.32	1017.05	194.10	5.24	29.70	0.94	1.07
	C2	302.83	257.55	206.25	170.10	88.48	75.81	53.17	36.94	29.81	20.82	17.52	12.73	12.00	10.32	1025.21	193.31	5.30	29.34	1.00	1.06

(La/Lu)ch = (La/Lach)/(Lu/Luch) ; Ce/Ce* = (3Ce/Cech)/(2La/Lach + Nd/Ndch), Eu/Eu* = (3Eu/Euch)/(2Sm/Smch + Tb/Tbch); ch=concentration in chondrite.

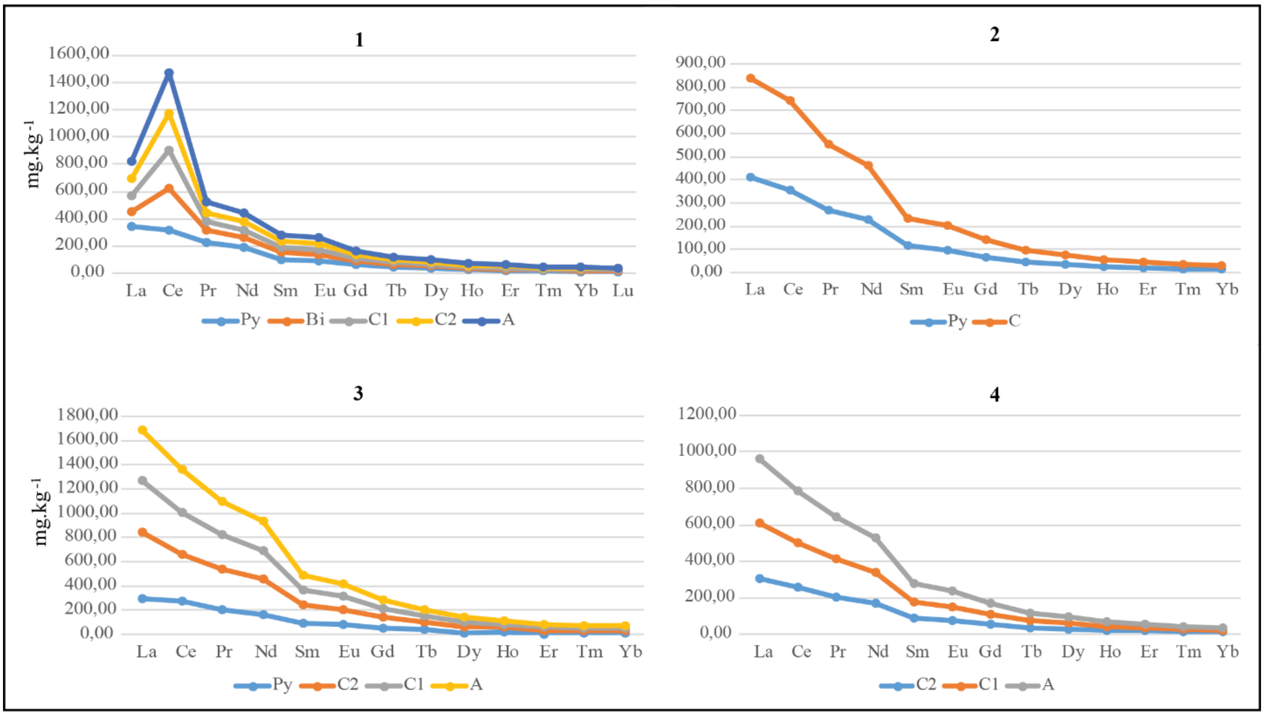

Figure 8.2: Typical chondrite-normalized (McDonough & Sun 1995) rare-earth elements plots of soils and pyroclasts of profiles 1,2,3 and 4.

Figure 8.2 : Des graphiques typiques d'éléments terres rares normalisées en chondrite (McDonough & Sun 1995) de sols et de pyroclastes de profils 1,2,3 et 4.

8.3.2.2- *Profile 3*

Among the major and minor elements, the absolute contents of Fe, Ti and K increase in the C2 and C1 horizon and decrease in the A horizon. The geochemical balance shows higher gain of 39.70 % and 33.33 % for Fe and K, respectively, in the C2 horizon. The elements Si, Al, Ca, Mg, P, Na and Mn decrease towards the top of the profile with more pronounced loss for Ca around 79-90 %.

The absolute contents of Ba, Cu, Sr, Th, Zn, Sc, Ga decrease towards the top of the profile and those of S, Cd, Tl and U increase. Co, Cr, Li, Ni, V, Be, Zr, Y and Cs increase in C2 and C1 horizon and decrease in the A horizon. In and Bi present constant behavior with a small decrease in the A horizon. The geochemical balance shows loss of Ba, Sr, Th, Zn, Sc, Cu, Ga, Be and Y in relation to pyroclast with greater loss in the A horizon around 30-60 %, as opposed to Li, Cd and Cs that show gain in all horizons. Co, Cr, Ni, V and Zr have gains in C2 and C1 horizon and loss in the A horizon. S is the element with the highest gain (559.73 %) between the trace elements. Be and Y behave differently from other trace elements.

For the REEs occur an increase in absolute values from rock to C2 horizon followed by a decrease towards the top of the profile. The geochemical balance shows gain of all elements in the C2 and C1 horizons, except for Ce and Lu that present small loss of 3.11 % and 0.11 %, respectively, and, loss in the A horizon in relation to the pyroclast. In addition, the LREEs show higher gains than the HREEs, between 14-33 % and 9-12 %, respectively.

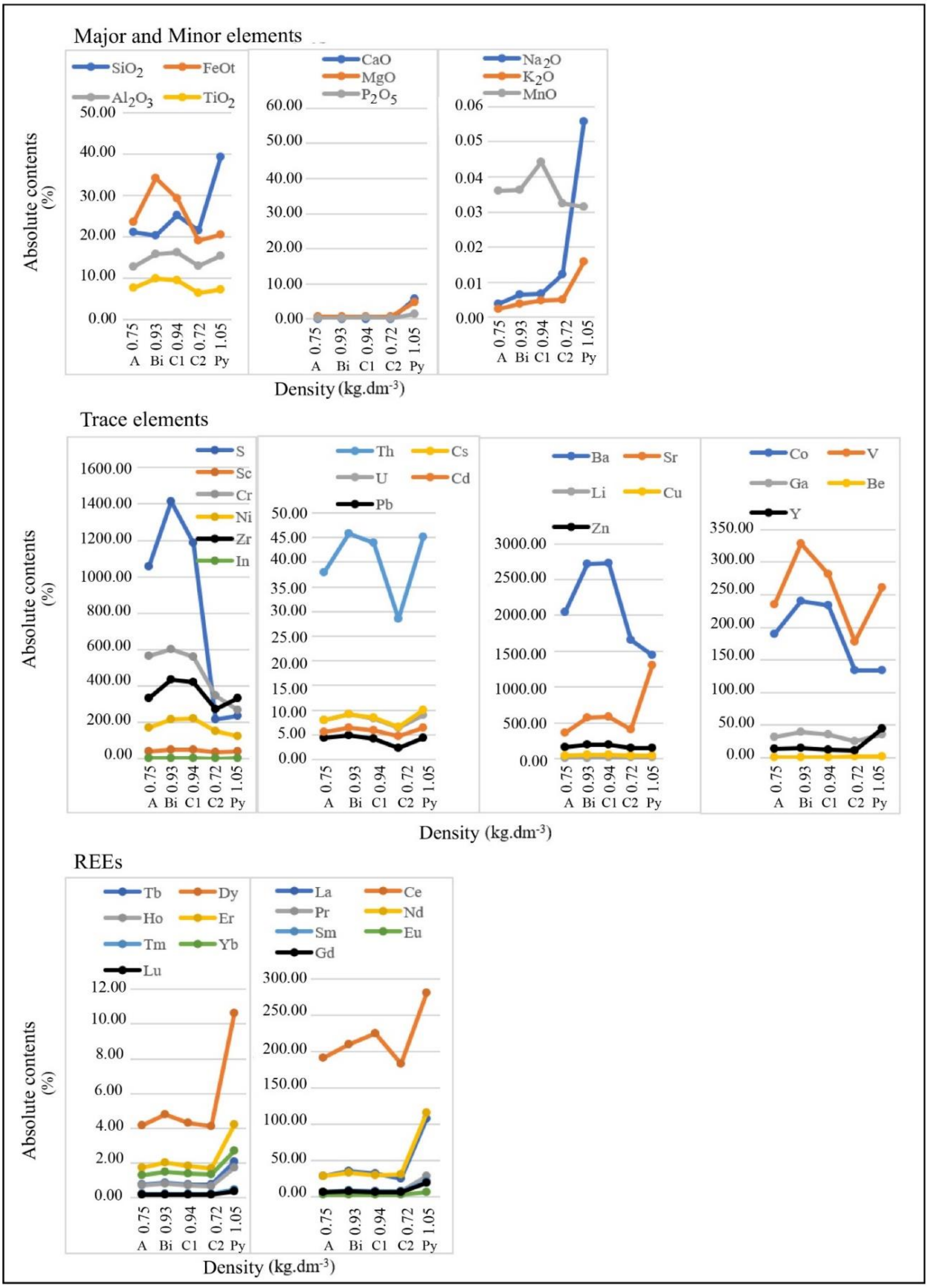

Figure 8.3: Comparison between densities and absolute contents from profile 1.

Figure 8.3 : Comparaison entre les densités et le contenu absolu du profil 1.

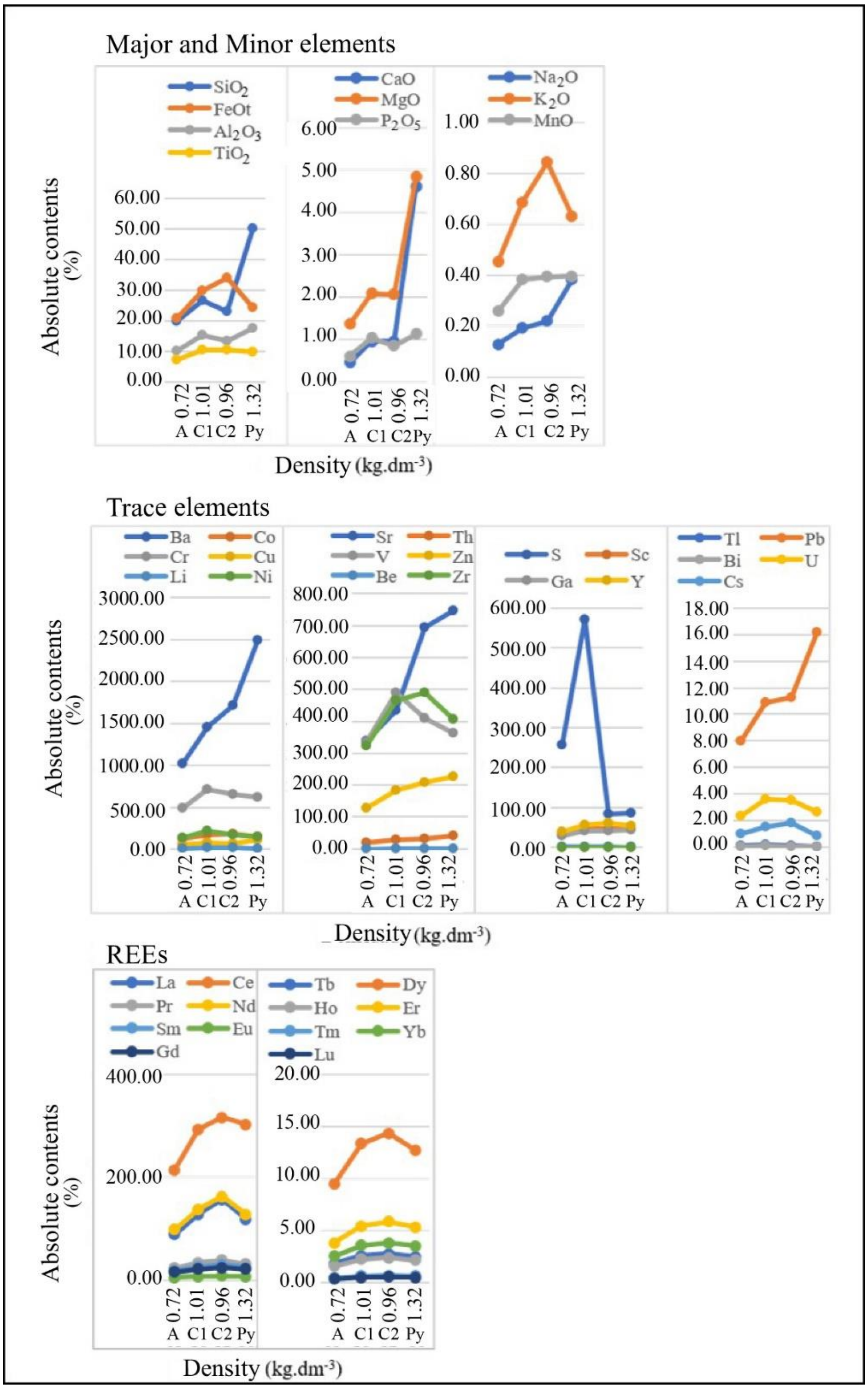

Figure 8.4: Comparison between densities and absolute levels from profile 3.

Figure 8.4 : Comparaison entre les densités et les niveaux absolus du profil 3.

Table 8.4: Absolute values of the major, minor and trace elements and REEs from profiles 1 and 3. Hor= pedological horizons, Py=pyroclast.

Tableau 8.4 : Valeurs absolues des principaux éléments, des éléments secondaires et des terres rares des profils 1 et 3. Hor= horizons pédologiques, Pyr=pyroclaste.

Profiles	**1**					**3**			
Horizons and rocks	**A**	**Bi**	**C1**	**C2**	**Pyr**	**A**	**C1**	**C2**	**Pyr**
					kg dm^{-3}				
Density	0.75	0.93	0.94	0.72	1.05	0.72	1.01	0.96	1.32
					%				
SiO_2	21.15	20.40	25.30	21.61	39.34	19.88	26.37	23.00	49.91
FeO_t	23.59	34.30	29.28	19.25	20.56	20.79	29.72	34.04	24.37
Al_2O_3	12.89	15.90	16.21	12.97	15.41	10.01	15.32	13.32	17.66
TiO_2	7.64	9.95	9.59	6.42	7.30	7.12	10.35	10.51	9.65
CaO	0.07	0.07	0.09	0.07	5.70	0.47	0.97	0.96	4.62
MgO	0.68	0.75	0.79	0.75	4.73	1.37	2.09	2.07	4.84
P_2O_5	0.29	0.29	0.35	0.32	1.43	0.62	1.05	0.86	1.14
Na_2O	0.04	0.07	0.07	0.12	0.56	0.13	0.19	0.22	0.38
K_2O	0.02	0.04	0.05	0.05	0.16	0.45	0.69	0.84	0.63
MnO	0.36	0.36	0.44	0.32	0.32	0.26	0.38	0.39	0.40
					mg dm^{-3}				
Ba	2043.55	2712.60	2733.46	1651.48	1446.32	1024.33	1453.66	1714.80	2491.57
Co	189.38	239.69	233.20	133.75	133.48	127.15	179.19	186.03	153.58
Cr	563.45	598.87	560.53	344.48	265.46	492.08	721.87	655.56	623.29
Cu	48.08	53.26	51.31	46.35	46.97	53.29	85.47	73.28	115.46
Li	6.93	9.37	14.29	15.89	15.07	16.39	26.72	22.99	12.79
Ni	170.05	216.41	218.77	147.25	120.79	135.01	225.81	177.14	151.83
Sr	361.72	572.84	588.36	408.72	1302.80	337.90	432.94	695.38	747.24
Th	30.09	36.70	35.53	21.96	35.07	19.09	28.62	33.12	42.27
V	235.48	328.34	281.36	178.36	261.42	335.46	490.18	408.54	364.07
Zn	158.26	192.23	190.84	145.67	152.83	128.28	184.35	207.03	228.03
Be	0.44	-	0.82	0.91	1.13	0.87	1.24	1.50	1.49
Zr	329.87	431.47	417.66	268.67	329.95	322.45	465.29	491.40	406.81
S	1056.02	1413.26	1185.06	216.42	231.21	256.30	569.88	83.34	86.38
Sc	40.04	49.29	47.04	33.65	36.57	31.32	46.00	46.59	49.05
Ga	30.92	39.75	35.49	25.23	35.11	28.07	42.19	41.34	44.62
Y	13.15	14.06	12.15	9.98	44.75	39.28	54.96	61.06	54.49
Cd	1.30	1.55	1.71	2.33	1.95	1.28	2.32	2.60	0.99
In	0.16	0.21	0.18	0.13	0.16	0.14	0.21	0.21	0.21
Tl	-	-	-	-	-	0.10	0.15	0.12	-
Pb	4.31	4.79	4.15	2.30	4.40	8.01	10.86	11.23	16.14
Bi	0.09	0.05	-	-	-	0.04	0.08	0.06	0.06
U	2.27	2.74	2.46	1.71	2.64	2.33	3.59	3.56	2.65
Cs	0.05	0.11	0.14	0.22	1.09	1.02	1.49	1.84	0.82
La	28.94	35.72	32.15	24.57	106.91	89.32	128.74	157.44	118.71

Ce	191.01	209.37	224.63	182.87	280.55	214.66	293.04	316.08	302.60
Pr	6.88	7.97	7.12	7.22	28.79	24.26	34.23	38.82	31.67
Nd	28.45	32.94	29.30	30.85	115.43	98.97	137.64	162.91	128.62
Sm	6.86	8.50	7.51	7.93	21.61	18.78	26.24	30.41	24.71
Eu	2.41	2.99	2.65	2.61	6.66	5.67	7.98	8.87	7.72
Gd	6.18	7.08	6.40	6.14	18.91	16.08	22.49	24.84	21.61
Tb	0.74	0.86	0.78	0.76	2.10	1.81	2.59	2.78	2.47
Dy	4.16	4.80	4.33	4.13	10.61	9.45	13.36	14.36	12.76
Ho	0.70	0.80	0.71	0.66	1.75	1.56	2.22	2.40	2.16
Er	1.76	2.02	1.81	1.67	4.23	3.80	5.43	5.86	5.33
Tm	0.23	0.25	0.23	0.21	0.48	0.44	0.64	0.68	0.63
Yb	1.31	1.50	1.37	1.32	2.69	2.53	3.59	3.83	3.54
Lu	0.17	0.20	0.17	0.17	0.37	0.34	0.47	0.52	0.48

Table 8.5: Mass balance of profiles 1 and 3.

Tableau 8.5: Bilan de masse des profils 1 et 3.

Profiles	**1**				**3**		
Horizons and rocks	**Py-A**	**Py-Bi**	**Py-C1**	**Py-C2**	**Py-A**	**Py-C1**	**Py-C2**
	%						
SiO_2	-46.24	-48.14	-35.71	-45.06	-60.17	-47.16	-53.91
FeO_t	14.73	66.83	42.42	-6.39	-14.70	21.98	39.70
Al_2O_3	-16.41	3.17	5.14	-15.87	-43.33	-13.25	-24.55
TiO_2	4.62	36.36	31.39	-11.99	-26.20	7.29	8.94
CaO	-98.82	-98.70	-98.35	-98.74	-89.87	-79.01	-79.22
MgO	-85.71	-84.06	-83.29	-84.15	-71.76	-56.84	-57.20
P_2O_5	-79.52	-79.81	-75.64	-77.31	-45.45	-7.47	-23.89
Na_2O	-93.26	-88.30	-88.18	-78.01	-66.14	-49.87	-42.32
K_2O	-85.71	-76.38	-70.16	-68.00	-28.41	8.40	33.33
MnO	14.29	15.14	40.25	2.86	-34.55	-3.08	-0.61
Ba	41.29	87.55	88.99	14.18	-58.89	-41.66	-31.18
Co	41.89	79.57	74.71	0.20	-17.21	16.68	21.13
Cr	112.25	125.60	111.15	29.77	-21.05	15.82	5.18
Cu	2.36	13.40	9.24	-1.32	-53.85	-25.98	-36.54
Li	-54.01	-37.85	-5.17	5.46	28.12	108.94	79.75
Ni	40.78	79.16	81.11	21.90	-11.07	48.73	16.67
Sr	-72.24	-56.03	-54.84	-68.63	-54.78	-42.06	-6.94
Th	-14.20	4.64	1.32	-37.38	-54.82	-32.28	-21.64
V	-9.92	25.60	7.63	-31.77	-7.86	34.64	12.21
Zn	3.55	25.78	24.87	-4.68	-43.75	-19.16	-9.21
Be	-61.64	-	-27.88	-19.37	-41.59	-16.71	0.40
Zr	-0.03	30.77	26.58	-18.57	-20.74	14.37	20.79
S	356.74	511.24	412.55	-6.39	196.71	559.73	-3.52
Sc	9.47	34.78	28.62	-8.00	-36.15	-6.23	-5.02
Ga	-11.95	13.20	1.06	-28.15	-37.10	-5.44	-7.35
Y	-70.62	-68.58	-72.84	-77.70	-27.92	0.87	12.05
Cd	-33.56	-20.48	-12.40	19.08	29.45	134.65	162.79
In	0.00	35.81	13.40	-17.71	-31.82	0.43	0.00
Cs	-95.19	-89.78	-87.09	-79.56	24.05	82.65	125.22
Pb	-2.15	8.86	-5.56	-47.79	-50.41	-32.74	-30.42
Bi	-	-	-	-	-23.89	42.35	1.48
U	-13.77	4.10	-6.55	-34.98	-12.08	35.14	34.24
La	-72.93	-66.59	-69.93	-77.01	-24.76	8.46	32.63
Ce	-31.92	-25.37	-19.93	-34.82	-29.06	-3.16	4.46
Pr	-76.11	-72.32	-75.28	-74.92	-23.40	8.09	22.60
Nd	-75.35	-71.46	-74.62	-73.27	-23.05	7.01	26.66
Sm	-68.24	-60.66	-65.24	-63.28	-23.98	6.19	23.08
Eu	-63.84	-55.02	-60.18	-60.85	-26.53	3.33	14.87
Gd	-67.32	-62.57	-66.15	-67.52	-25.60	4.09	14.93
Tb	-64.64	-58.81	-62.85	-64.00	-26.49	4.75	12.79

Dy	-60.75	-54.75	-59.14	-61.03	-25.99	4.68	12.51
Ho	-60.22	-54.39	-59.26	-62.22	-27.83	2.64	10.86
Er	-58.53	-52.31	-57.13	-60.52	-28.71	1.89	9.81
Tm	-53.42	-48.01	-53.29	-56.77	-30.68	0.43	7.58
Yb	-51.17	-44.30	-48.94	-50.71	-28.56	1.35	8.28
Lu	-53.06	-46.86	-53.96	-54.94	-28.79	-0.11	9.09

8.4 – DISCUSSIONS

According to weather studies of geochemical evolution of soil profiles, in all studied profiles the amount of silica decreases considerably with the advance of weathering, while aluminum, iron and titanium tend to accumulate due to their low mobility. Calcium, sodium, potassium and magnesium are the most intensely leached. In the profile 4, potassium and magnesium values are slightly high in the A horizon due to the position of this profile at a lower altitude. The influence of saline sprays and the deposition of chemical elements from the higher regions increase the amounts of chemical elements in the profiles located at lower altitude, corroborating with Clemente *et al.* (2012).

Profiles located at higher altitudes, such as profile 1 (460 m), are most depleted in the most mobile elements such as Na, Ca, Mg and K. Clemente *et al.* (2012) assigned the low values of CaO to acid pH , to greater degree of weathering in region more elevated of Trindade Island and to small possibility of saline inputs. According to Mateus *et al.* (submitted article, b) acid pH data around 5 were found for C1, Bi and A horizons from the profile 1, which may justify the low CaO values in this profile.

In all profiles the trace elements Ba, Co, Cr, Ni, Sr, V, Zn, Zr, S and Ce are the most abundant and in general, their quantities increase towards the top of the profile. Similar behavior was found in Fernando de Noronha Island for Co, Cr and Ni in soils developed from rocks of mafic composition (Oliveira *et al.* 2011). High values of Ba may be related to Ti-biotite, since Marques (1999) and Green-Wood (1998) reported its presence in heavily zoned Ti-biotite in ultramafic rocks (melanephelinites) from Trindade Island. The presence of ferromagnesian minerals such as olivine, pyroxene and amphibole explain the high content of Ni, Cr, Co, Zn and V. According to Hawes & Webb (1962) Ni, Cr, Co, Cu, Zn and V have similar chemical characteristics and occur in ferromagnesian minerals. Cr contents is high for all soils due to the deep mantelic origin of the pyroclasts and tend to concentrated in the olivine nuclei (Mateus *et al.* submitted article, a). This fact explains the high exchangeable levels of Cr in soils from the Morro Vermelho Formation (Clemente *et al.* 2012). The Cu content from profiles 3 and 4 present similar behavior to the soils of Clemente *et al.* (2012): higher content in near-sea soils, at lower altitude and in younger soils. Another similarity to the Clemente *et al.* (2012) study is the most pronounced Zn content in horizons with greater amount of organic matter such as the A horizon of profile 3 and 4, with values of 18.03 e 9.39 g kg^{-1} in total organic carbon respectively (Mateus *et al.* submitted article, b). According to Abreu *et al.* (2001) high levels of organic matter can complex Cu and Zn retaining these elements in the soil. Therefore, the higher levels of Zn and Cu in the A horizon from profiles 3 and 4 would be a consequence of the greater amounts of complexes of humic acid linked to these elements. In addition, all horizons from the profiles 3 and 4 still contain several relict fragments of the parental rock (Mateus *et al.* article submitted, b) which could contribute to the more pronounced presence of Zn and Cu.

For profiles 1 and 3, the gain of Fe, Ti, Al and Mn are relative, as these elements increase due to the detriment of others such as Si, Na, K, Ca, Mg and P. In relation to trace elements, profile 1 shows moderate mobility of Sr, V, Co, Y, Zr, Pb, Cd, U, Cs, Th, Ga characterized by the loss of these elements from the altered rock to the C2 horizon and a relative enrichment, especially in Bi horizon. Ba, Cr and Ni show enrichment towards to the top of the profile. Li, Zn, Be, Sc do not vary much and show very close values in the rock and in the soil.

Profile 3 has the inverse behavior of profile 1 with high mobility for Ba, Sr, Zn, Pb represented by their marked loss to the top of the profile and a relative enrichment of Cr, Ni, Co, Zr, V, S, Y, Ga, U, Cs from rock to soil with slight loss in the A horizon. According to Hawkes & Webb (1962) Ba and Sr are elements of high mobility, corroborating the geochemical behavior found in the soils of this study. Li, Be, Bi and Tl are constant in the profile 1 e 3.

Alls profiles showed high concentration of LRRE. Featured, the profilse 1 and 2 showed positive Ce anomalies, with higher values in 1. In soils on basaltics pyroclasts from São Miguel island (Azores archipelago) occur similar behavior (Freitas & Pacheco 2010) and in topsoils on phonolitic pyroclasts in Brava Island (Cape Verde archipelago), Marques *et al.* (2018) related the relative Ce enrichment to stronger oxidizing conditions leading to $Ce^{3+} \rightarrow Ce^{4+}$ with preferred retention of this element on the clay-size. This same explanation could be applied to soil from profile 1 since it is the profile that is most weathered (Mateus *et al.* 2018).

The REEs in profile 1 are lost by leaching. The position of this profile in higher regions contributes to the loss of these elements. The opposite occurs in the profile 3 positioned in lower regions, concentrating these elements at the base of the profile (C2 and C1 horizon), highlighting the LREEs that show larger gain than the HREEs. In the Fernando de Noronha Island, the HREEs accumulate in soils on mafic rocks (nepheline basalts) at low altitude (Oliveira *et al.* 2011b). One explanation for this difference would be that the profile studied by Oliveira *et al.* (2011b) developed on older rocks, Morro Quixaba Formation (6.2 Ma; Perlingeiro *et al.* 2013) that the Morro Vermelho Formation (0.17 Ma; Cordani 1970), and consequently the soils formed on these rocks are more weathered and consequently more leached, concentrating more HREE than LREE.

8.5 – CONCLUSIONS

In all profiles Al and Fe accumulate towards to the top due to their low mobility, and, Ca, Na, K and Mg are the most intensely leached. Similarly, Ti, Mn, Co, Cr, Ni, V, Zr, S show relative enrichment due to the leaching of the most mobile elements during the soil formation process.

Lower altitude profiles tend to have higher K and Mg values in A horizon due to the influence of saline sprays.

Zn and Cu are concentrated in A horizon of low altitude profiles that have higher organic matter content and relict fragments of parental rock.

Leaching of the REEs from higher to the lower slope led to the enrichment of these elements, especially the light REEs, in the low lying (258 m) soil. The Ce positive anomalies in high altitude profile (460 m) is because it is more weathered.

CHAPITRE 9

CONCLUSION GÉNÉRALE

Selon les résultats obtenus dans ce travail, il a été possible d'obtenir des conclusions significatives au tour de l'origine, et les principaux produits de l'altération des pyroclastes recueillies dans le Vulcão do Paredão et la Formation Morro Vermelho.

Les roches recueillies dans les dépôts pyroclastiques du Vulcão do Paredão et de la Formation Morro Vermelho ont été formées au cours d'une éruption strombolienne et phréato-magmatique, et le magma formant des ces pyroclastes a une origine manthélique dans les profondeurs de moins de 50 km. Ces conclusions sont étayées par la présence de matériaux grossiers (blocs) et de palagonites dans les pyroclastes, et la présence de spinelles avec des noyaux enrichis en Cr et un enrichissement modéré des éléments de terres rares dans le magma.

Les principaux produits d'altération trouvés étaient les olivinas iddingsitisées, les sidéromélanes palagonitisées, les zéolites et les haloysites. La première étape de l'altération est représentée par la formation de la palagonite par l'interaction du magma avec l'eau de la mer. Au cours de cette étape, les changements de sideromelane à la palgonite avec la perte des éléments chimiques Na, Ca et Mg et un enrichissement de Fe et de l'eau dans la palagonite par rapport au sideromelane. Après refroidissement total de la roche, il y avait une deuxième étape d'altération avec l'interaction de l'eau météorique avec des pyroclastes provoquant une déferruginisation dans les régions palagonitisées (palagonites blanches), formation de zéolites sur les murs des palagonites, argiles de type haloysite dans les régions palagonitisées et l'altération des olivines en iddingsites composés d'hématites et de goethites.

La transformation des pyroclastes en sols est marquée par la présence de minéraux secondaires tels que les haloysites, les goethites, les hématites, le rutile et l'anatase, les ferrihydrites et quelques quantités d'alophanes. Ces sols présentaient des propriétés andic et pouvaient être classés comme Andosols non allophaniques, avec la présence la plus prononcée des halloysites et des complexes humiques d'Al. La faible quantité d'alophane s'expliquerait par la transformation rapide de l'allophane en halloysite en raison des conditions climatiques de l'Île de Trindade.

Dans les profils de haute et basse altitude, les éléments Ti, Mn, Fe, Co, Cr, Ni, V, Zr, S sont accumulés dans les sols et les augmentations de leurs concentrations sont liées à la perte de poids totale par la perte d'éléments plus mobiles pendant le processus de formation du sol. Zn et Cu ont tendance à se concentrer sur l'horizon A de profils qui présentaient une plus grande concentration de matière organique et qui conservait des fragments de pyroclastes inchangés. Le terres rares, principalement les terres rares légéres, sont enrichis dans le profil de basse altitude, en raison de la contribution de ces éléments des régions les plus élevées de l'île. Le profil de haute altitude a montré une anomalie positive en Ce due à une exposition plus longue aux intempéries.

Références bibliographiques

Abreu C. A., Ferreira M. E, Borkert, C. M. Disponibilidade e avaliação de elementos catiônicos: zinco e cobre. 2001. In: Ferreira, M.E, Cruz, M.C.P., Raij, B. van., Abreu, C. A. (eds), *Micronutrientes e elementos tóxicos na agricultura*. Jaboticabal, FAPESP/POTAFOS, 12-150.

Adjadeh T. A. & Inoue K. 1999. Andisols of the Kitakami mountain range, Northeastern Japan: Their characterization and classification. *Soil Science and Plant Nutrition*, 45: 115-130.

Almeida F. F. M. 1955. Geologia e Petrologia do Arquipélago de Fernando de Noronha. Monografia XIII, Departamento Nacional de Prospecção Mineral (DNPM), Rio de Janeiro, 181p.

Almeida F. F. M. 1961. *Geologia e Petrologia da ilha da Trindade*. Rio de janeiro. 197 p. (Monografia, DNPM/DGM).

Almeida F.F.M. 1962. *Petrologia da Ilha da Trindade*. São Paulo. 223p. (Tese para concurso à cátedra, Universidade de São Paulo).

Almeida F. F. M. 2002. Ilha de Trindade – registro de vulcanismo cenozoico no Atlântico Sul. In: Schobbenhaus, C., Campos, D. A., Queiroz, E. T., Winge, M., Berbet-Born, M. L. C. (eds.), *Sítios geológicos e paleontológicos do Brasil*. 1ª ed. Comissão Brasileira de Sítios Geológicos e Paleobiológicos, Brasília, 369-377.

Almeida F. F. M. 2006. Ilhas oceânicas brasileiras e sua relação com a tectônica atlântica. *Terræ Didatica*, 2(1): 3-18.

Almeida B.G, Viana J. H. M., Teixeira W. G., Donagema G.K. Densidade do Solo. 2017. In: Teixeira P. C., Donagema G.K., Fontana A., Teixeira W.G. (eds.), *Manual de métodos de análise do solo*, Embrapa Solos, Rio de Janeiro, 65-67.

Alvarez V. V. H., Novais R. F., Dias L. E., Oliveira J. A. 2000. Determinação e uso do fósforo remanescente. *Boletim Informativo da Sociedade Brasileira de Ciência do Solo*, 25: 27–32.

Alves R. J. V. 1998. *Ilha da Trindade & Arquipélago Martin Vaz – um ensaio geobotânico*. Serviço de Documentação da Marinha, Rio de Janeiro, RJ, Brasil. 144p.

Alves R. J. V. 2006. Terrestrial vascular floras of Brasil's oceanic archipelagos. In: Alves, R. J. V. & Castro, J. W. A. (orgs.). Ilhas oceânicas brasileiras: da pesquisa ao manejo. MMA Secrataria de Biodiversidade e Florestas, Brasília, Brasil, p. 83-104.

Alves E. C., Maia M., Sichel S. E., Campos C. M. P. 2006. Zona de Fratura de Vitória-Trindade no oceano atlântico sudeste e suas implicações tectônicas. *Revista Brasileira de Geofísica*, 24(1): 117-127.

Antonello L. L., Zuccoloto M. E., Castro J. W. A. 2009. In: Mohr, L.V., Castro, J.W., Costa, P.M.S., Alves, R.J.V. (Eds.). Ilhas Oceânicas Brasileiras: da pesquisa ao manejo, Volume II. MMA/Secretaria de Biodiversidade e Florestas, Brasília, pp. 107-124 (Chapter 4).

Baker I., Haggerty E. S. 1967. The alteration of olivine in basaltic and associated lavas. Part II: intermediate and low-temperature alteration. *Contrib. Mineral. Petrol.*, 16: 258-273.

Barth R. 1958. Observações biológicas e meteorológicas feitas na Ilha de Trindade. In: Memórias do Instituto Osvaldo Cruz, 261-279.

Barrows K. J.1980. Zeolitization of Miocene volcanoclastic rocks, southern Desatoya Mountains, Nevada. *Geol Soc. Am. Bull.,* 91: 199-210

Bech-Borras J., Fedoroff N., Sole A. 1977. Etude des andosols d'Olot (Gerona, Espagne). 3e partie: Micromorphologie. *Caih. ORSTOM*, *sér Pédol.*, 15 (4): 381-390.

Benayas J., Fernandez-Caldas E., Tejedor Salguero M.L., Rodriguez-Rodriguez A. 1980. Caracteristicas micromorphologicas de los suelos de una clima secuencia de la vertiente meridional de la Isla de Tenerife. *Anales de Edafología y Agrobiología*, 3: 51-74.

Bertrand S. & Fagell, N. 2008. Nature and deposition of andosol parent material in south-central Chili (36–42°S). *Catena*, 73: 10-22.

Bonatti E. 1965. Palagonite, hyaloclastites and alteration of volcanic glass in the Ocean. *Bull. Volcanol.*, 28(1): 257-269.

Batistella M. 1993. *Cartografia Ecológica do Arquipélago de Fernando de Noronha. São Paulo*. 236 p. (Dissertação de Mestrado (Biociências), Universidade de São Paulo).

Blackmore L. C.; Searle P. L.; Daly B. K. 1981. Methods for chemical analysis of soils. New Zealand Soil Bureau Scientific Repost. 10A, DSIRO, New Zealand.

Bockheim J. G. 2005. Soil endemism and its relation to soil formation theory. *Geoderma*, **129**:109-124.

Bongiolo E. M., Pires G. L. C., Geraldes M. C., Santos A. C., Neumann R. 2015. Geochemical modeling and Nd–Sr data links nephelinite–phonolite successions and xenoliths of Trindade Island (South Atlantic Ocean, Brazil). *J. Volcanol. Geotherm. Res.,* 306: 58–73

Brindley G. W. & Brown G. 1980. *Crystal Structures of Clay Minerals and Their X-ray Identificatino.* Mineralogical Society, London.

Bryndon J. E. & Day J. H. 1970. Use of the Fields and Perrott sodium fluoride test to distinguish the B horizons of Podzols in the field. *Can. J. Soil Sci*, 50 (1): 35-42.

Campos T. F. C., Srivastava N. K., Macambira M. J. B., Petta R. A., Amaral R., Das Virgens Neto J. 2003. A Formação São Pedro e São Paulo: Uma Nova Unidade Litoestratigráfica Quaternária do Atlântico Equatorial Brasileiro. XLI Congresso Brasileiro de Geologia, João Pessoa (PB) Setembro de 2003. *Anais*: 354.

Campos T. F. da C., Das Virgens Neto J., Srivastava N. K., Petta R. A., Hartmann L. A, Moraes J. F. S., Mendes L., Susan R. M. Arquipélago de São Pedro e São Paulo: soerguimento de rochas infracrustais no Oceano Atlântico. In: Winge M., Schobbenhaus C., Berbert-Born M., Queiroz E. T., Campos D. A., Souza C. R. G., Fernandes A. C. S. (eds.) Sítios Geológicos e Paleontológicos do Brasil. http: //www.unb.br/ig/sigep/sitio002/sitio002.pdf.

Candan F. & Broquen P. 2009. Aggregate stability and related properties in NW Patagonian Andisols. *Geoderma*, 154: 42-47.

Caner L., Bourgeon G., Toutain F., Herbillon A. J. 2000. Characteristics of non-allophanic Andisols derived from low-activity clay regoliths in the Nilgiri Hills (Southern India). *European Journal of Soil Science*, 51: 553–563.

Castro J. W. A. 2010. Ilhas Oceânicas de Trindade e Fernando de Noronha, Brasil: Uma visão da Geologia Ambiental. *Revista da Gestão Costeira Integrada*, 10(3): 303-319.

Cardoso J.C. 1958. Caracterização das principais unidades pedológicas do "Esboço da carta dos solos de S. Tomé". Junta de Investigações do Ultramar, Lisboa. Estudos, Ensaios e Documentos, 53-88 p.

Caroff M., Ambrics C., Maury R.C., Cotten J. 1997. From álcali basalt to phonolite in hand-size samples: vapor-differentiation in the Bouzentès lava flow (Cantal, France). *J. Volcanol. Geotherm. Res.*, 79: 47-61.

Caroff M., Guillou H., Lamiaux M., Maury R.C., Guille G., Cotton J. 1999. Assimilation of ocean crust by hawaiitic and mugearitic magmas: an example from Eiao (Marquesas). *Lithos*, 46: 235-258.

Caroff M., Maury R.C., Cotton J., Clément J.P. 2000. Segregation structures in vapor differentiated basaltic flows. *Bull. Volcanol.*, 62: 171-187.

Carvalho, I.G. Fundamentos da geoquímica dos processos exógenos. Salvador, Bureau Gráfica e Editora, 1995. 213p

Castro J. W. A. 2003. Ilhas Oceânicas Brasileiras: Da Pesquisa ao Manejo. Ministério do Meio Ambiente, Brasília.

Castro J. W. A. & Antonello L. L. 2006. Geologia das ilhas oceânicas brasileiras. In: Alves, R.J.V. & Castro, J.W.A. (eds.), *Ilhas Oceânicas Brasileiras: da Pesquisa ao Manejo*. Ministério do Meio Ambiente, Brasília, Brasil, 29-57.

Champness P.E. 1970. Nucleation and growth of iron oxides in olivines, (Mg, Fe)$_2$SiO$_4$. *Min. Mag.*, 37: 790-800.

Clague D. A., Batiza R., Head J., Davis A. S. 2003. Pyroclastic and hydroclastic deposits on Loihi Seamount, Hawaii. In: White, J. D.L., Smellie J.L., Clague D. A. (eds), Explosive Subaqueous Volcanism, American Geophysical Union, pp. 73-95.

Clemente E. P., Schaefer C. E. R. G., Albuquerque Filho M. R., Oliveira F. S., Alves R. W., Melo V. F. 2006a. Solos Endêmicos da Ilha da Trindade. In: Alves, R. V. & Castro, J. W. A. (eds.), *Ilhas Oceânicas Brasileiras: Da Pesquisa ao Manejo*. Ministério do Meio Ambiente, Brasília (DF), 61-82.

Clemente E. P. 2006b. Ambientes Terrestres da Ilha da Trindade, Atlântico Sul: Caracterização do Solo e do Meio Físico Como Subsídio Para Criação de Uma Unidade De Conservação. Viçosa. 210 p. (Tese de doutorado, Solos e Nutrição de Plantas, Universidade Federal de Viçosa).

Clemente E. P., Schaefer C. E., Oliveira F. S., Albuquerque-Filho M. R., Alves R.V., Sá M. M. F., Melo V. S. 2009. Topossequência de solos na Ilha da Trindade, Atlântico Sul. *R. Bras. Ci. Solo*, 33: 1357-1371.

Clemente E. P., Schaefer C. E., Oliveira F. S. 2011. Proposta de zoneamento ambiental para a Ilha de Trindade (ES). Boletim de pesquisa e desenvolvimento. Embrapa Solos, Rio de Janeiro, 27p.

Clemente E. P.; Schaefer C. E. R..; Oliveira F. S.; Marciano, L. C., Clemente A. D. 2012. Geoquímica dos solos da Ilha da Trindade, Atlântico Sul, Brasil. *Geociências*, 31(1): 57-67.

Clément J. P., Caroff M., Dudoignon P., Launeau P., Bohn M., Cotten J., Blais S., Guille G. 2007. A possible link between gabbros bearing High Temperature Iddingsite alteration and huge pegmatoid intrusions: The Society Islands, French Polynesia. *Lithos* 96: 524-542. doi:10.1016/j.lithos.2006.12.001

Cordani U.G.1970. Idade do vulcanismo do Oceano Atlântico Sul. *Boletim IAG USP*, 1: 9-75.

Cordani U. G. & Blazekoviv A. 1970. Idades radiométricas das rochas vulcânicas de Abrolhos. In Congresso Brasileiro de Geologia, 24, Porto Alegre. 1970. Anais... Porto Alegre: v.3, p. 265-27Cordani U. G. 1970. Idade do vulcanismo do Oceano Atlântico Sul. São Paulo: Instituto de Geociências e Astronomia, Boletim IGA, 1: 9-75.

Dahlgen R., Shoji S., Nanzyo M. 1993. Mineralogical characteristics of volcanic ash soils. In: Shogi S., Nanzyo, M., Dahlgren, R. Volcanic ash soils genesis. properties, and utilization, Amsterdam, The Netherlands, 101-143.

Daux V., Crovisier J. L., Hemond C., Petit J. C. 1994. Geochemical evolution of basaltic rocks subjected to weathering: fate of the major elements, rare earth elements, and thorium. *Geochim. Cosmochim. Acta*, 58:4941-4954.

Deer W.A., Howie R.A., Zussman J. 1992. *An introduction to the rock-forming minerals*. England, Longman Scientific & Technical; New York, John Wiley. 712p.

Delvigne J., Bisdom E. B. A., Sleeman J., Stoops G. 1979. Olivines, theirs pseudomorphs and secondary products. *Pedologie*, 29: 247-309.

Devnita R. 2012. Melanic and Fulvic Andisols in Volcanic Soils derived from some Volcanoes in West Java. *Indonesian Journal on Geoscience*, 7: 227-240. DOI 10.17014/ijog.7.4.227-240.

Diniz A.C. & Matos G.C. 1993 - Carta de zonagem agro-ecológica e da vegetação de Cabo Verde. V – Ilha do Sal. *Garcia de Orta, Série Botânica*, 11 (1-2): 9-30.

Diniz A. C. & Matos G. C. 1994a - Carta de zonagem agro-ecológica e da vegetação de Cabo Verde. VI – Ilha de S. Vicente. *Garcia de Orta, Série Botânica*, 12 (1-2): 69-98.

Diniz A. C. & Matos G. C. 1994b - Carta de zonagem agro-ecológica e da vegetação de Cabo Verde. VII – Ilha de Santa Luzia. *Garcia de Orta, Série Botânica*, 12 (1-2): 101-119.

Diniz A. C. & Matos G. C. 1999a - Carta de zonagem agro-ecológica e da vegetação de Cabo Verde. VIII – Ilha de S. Nicolau. *Garcia de Orta, Série Botânica*, 14 (1): 1-54.

Donagema G. K, Campos D.V.B, Calderano S. B, Teixeira W.G., Viana J. H. M. 2011. Manual de métodos de análise do solo. 2 ed. rev. Embrapa Solos, Rio de Janeiro.

Duarte R. H., Horta G. C. M. M. 2012. Barth e a Ilha da Trindade, 1957-1959. História, Ciências, Saúde – Manguinhos, Rio de Janeiro, 19(3): 951-968.

Dümig A., Schad P., Kohok M., Beyerlein P., Schwimmer W., Kögel-Knabner I. 2008. A mosaic of nonallophanic Andosols, Umbrisols and Cambisols on rhyodacite in the southern Brazilian highlands. *Geoderma*, 145: 158-173.

Edwards A.B. 1938. The formation of iddingsite. *American Mineralogist*, 23: 277-28.

Eggleton R. A., Keller J. 1982. The palagonitization of limburgite glass – a TEM study. *Neues Jahrb Miner* 7:321–336.

Eggleton R. A. 1984. Formation of iddingsite rims on olivine: A transmission electron microscope study. *Clays & Clay Minerals*, 32: 1-11.

Eguchi T. & Tamura K. 2012. Characterization of Andosols in Yakushima Island. *Soil Science and Plant Nutrition*, 58: 52-64.

Einarsson T. 1965. The ring-mountains Hverfiall, Lúdent, and Hrossaborg in northern Iceland. Vísindafélag Íslendinga, *Greinar*, 41:1- 28.

EMBRAPA. 2014. *Sistema Brasileiro de Classificação de Solos*. Brasília, Embrapa. 376p.

EMBRAPA. 2011. Manual de Métodos de Análises de Solo. Rio de Janeiro, Embrapa Solos. 230p

Espinosa J. A. S. & Sanabria, Y. R. 2015. Procesos específicos de formación en Andisoles, Alfisoles y Ultisoles en Colombia. *Revista EIA*, 12(2): 85-97.

Faria F.X. 1974. Os solos da Ilha do Fogo (Arquipélago de Cabo Verde). Junta de Investigações científicas do Ultramar. *Rev. Estudos, Ensaios e Documentos*, no129, Lisboa,146 p.

Farmer V.V. & Fraser A. R. 1979. Synthetic imogolite, a tubular hydroxy-aluminium silicate. In: Mortland M. M. & Farmer V. C. (eds), International Clay Conference. Elsevier, Amsterdam, 547-53.

Fawcett J. J. 1965. Alteration products of olivine and pyroxene in basalt lavas from the Isle of Mull. *Min. Mag.*, 35: 55-71.

Fernandez-Calilas E., Tejedors U., Guero M. L.1975. Andosoles de las Islas Canarias. Servicio de Publicacione de la Caja General de Ahorros de Santa Cruz de Tenarife, 29, 210p.

Fields M. & Perrot K. W. 1966. The nature of allophone in soils. III. Gypsum effects on growth and subsoil chemical proprieties. *Soil Sci. Soc. Am. Journal*, 2: 623-629.

Freitas M. C., Pacheco A. M. G. 2010. Soils of Azores islands: elemental characterization with an emphasis on rare-earth elements. *J. Radioanal. Nucl. Chem.*, 283:117-122.

Gama J.R.N.F., Kusuba T., Ota T., Amano Y. 1992. Influência de material vulcânico em alguns solos do Estado do Acre. *Rev. Bras. Cienc. Sol*o, 16: 103-106.

Furnes H. 1984. Chemical-changes during progressive subaerial palagonitization of a subglacial olivine tholeiite hyaloclastite – a microprobe study. *Chem. Geol.*, 43:271-285.

Garcia-Rodeja E., Silva B.M., Macias F. 1987. Andosols developed from non-volcanic materials in Galicia, NW Spain. *J. Soil Sci.*, 38: 573-591.

Gay P., Le Maître R.W., 1961. Some observations on "iddingsite". *The American Mineralogist*, 46: 92-111.

Gerard M., Caquineau S., Pinheiro J., Stoops G. 2007.Weathering and allophane neoformation in soils developed on volcanic ash in the Azores. *European Journal of Soil Science*, 58: 496-515. doi: 10.1111/j.1365-2389.2007.00910.x

Goff F., 1977. Vesicle cylinders in vapor-differentiated basalt flows. Santa Cruz, CA. 181 pp. (PhD Thesis, University of California).

Goff F., 1996. Vesicle cylinders in vapor-differentiated basalt flows. *J. Volcanol. Geotherm. Res.*, 71: 167-185.

Goode A. D. T. 1974. Oxidation of natural olivines. *Nature*, 248: 500-501.

Greenwood J. C. 1998. Barian–titanian micas from Ilha da Trindade, South Atlantic. *Mineral. Mag.*, 62 (5): 687-695.

Grison H., Petrovsky E., Stejskalova S., Kapicka A. 2015. Magnetic and geochemical characterization of Andosols developed on basalts in the Massif Central, France. *Geochem. Geophys. Geosyst.*, 16: 1348-1363.

Gualtieri A. F., Gemmi M., Dapiaggi M. 2003. Phase transformations and reaction kinetics during the temperature-induced oxidation of natural olivine. *Am. Mineral.*, 88: 1560-1574.

Haggerty E. S., Baker I. 1967. The alteration of olivine in basaltic and associated lavas. Part I: high-temperature alteration. *Contrib. Mineral. Petrol.*, 16: 233-257.

Hamilton W., Bvers W. B. 1963. Menan Buttes, cones of glassy basalt tuff in the Snake River Plain, Idaho. *U. S. Geol. Surv.*, 450-E: 114–118.

Hawes H. E. & Webb J. S. 1962. Geochemistry in Mineral Exploration. Elsevier, New York.

Hay R. L., Iijima A. 1968. Petrology of Palagonite Tufts of Koko Craters, Oahu, Hawaii. *Contr. Minera. and Petrol.*, 17:141–154.

Hikmatullah. 2008. Andisols from Tondano Area, North Sulawesi: Properties and Classification. *Jurnal Tanah Tropika*, 13: 77-85.

Holmgreen G. G. S.1967 A rapid citrate-dithionite extractable iron procedure. *Soil Science Society of America* proceedings, 31: 210-211.

Höller H. & Wirsching U. 1980. Experiments on the hydrothermal formation of zeolites from nepheline and nephelinite. In: Rees L. V. C. (ed), Proc. 5th Int'l Conf on Zeolites. Heyden, London, 164–170.

Hytonen K. 1959. On the petrology and mineralogy of some alkaline volcanic rocks of Toror Hills, Mount Moroto, and Morulinga in Karamoja, north eastern Uganda. *Bull. Comm. Géol. Finlande*, 184: 75-132.

Iijima A., Harada K. 1969. Authigenic zeolites in zeolitic palagonite tuffs on Oahu, Hawaii. *Am. Mineral.*, 54: 182-197.

Irvine T. N. 1965. Chromian spinel as a petrogenetic indicator. Part. 1. Theory. *Canad. J. Earth Sci.*, 2: 648- 672.

IUSS Working Group WRB. 2006. World reference base for soil resources. World Soil Resources Reports, N°103. FAO, Rome.

Jercinovic M. J., Keil K., Smith M. R., Schmitt R. A. 1990. Alteration of basaltic glasses from north-central British Columbia, Canada. *Geochim. Cosmochim. Acta*, 54:2679-2696.

Kawai K. 1969. Micromorphological studies of Andosols in Japan. *Bulletin of the National Institute of Agricultural Sciences (Japan)*, 20: 77-154.

Ker J.C. 1988. Caracterização química, física, mineralógica e micromorfológica de Solos Brunos Subtropicais. Viçosa. p. (Dissertação de Mestrado, Solos e Nutrição de Plantas, Universidade Federal de Viçosa).

Kılıç K.; Yalçın H.; Durak A.; Doğan H. M. 2018. Andisols of Turkey: An example from the Cappadocian Volcanic Province. *Geoderma*, 313:112-125.

Kristmannsdóttir H., Tómasson J. 1978. Zeolite zones in geothermal areas, Iceland. In: Sand L.B & Mumpton F.A (eds) Natural Zeolites. Pergammon Press, Oxford, 277-284.

Kuebler, K. E. 2013. A comparison of the iddingsite alteration products in two terrestrial basalts and the Allan Hills 77005 martian meteorite using Raman spectroscopy and electron microprobe analyses. *A Journal of Geophysical Research: Planets*, 118, 803-830. doi:10.1029/2012JE004243.

Larrea P., França Z., Widom E., Lago M. 2018. Petrology of the Azores Islands. In: Kueppers U. & Beier C. (eds.), Volcanoes of the Azores, Active Volcanoes of the World. Springer, Berlin, Heidelberg,147-249.

Laruelle J. 1967. Galápagos. Natuurwetenschappelijk Tijdschrift 47 (1965), 236 p.

Lawson A. C.1893. The geology of Carmelo Bay. *Bull. Dep. Geol. Univ. Calif.*, 1: 1-59.

Le Bas M. J., Le Maître R.W., Streckeisen A., Zanettin B. 1986. A chemical classification of volcanic rocks based on the total alkali–silica diagram. *J. Petrol.*, 27:745-750.

Le Maître, O., Brousse, R., Goni, J., Remond, G. 1966. Sur l'importance de l'apport de fer dans la transformation de l'olivine en iddingsite. *Bull. Soc. Fr. Mineral. Cristallogr.*, 89, 477- 483.

Le Maître R.W., Batema N. P., Dudek A., Keller J., Lameyre J., Le Bas, M.J., Sabine P.A., Schmid R., Sorensen H., Streckeisen A., Woolley A. R., Zanettin B. 1989. *A Classification of Igneous Rocks and Glossary of terms: Recommendations of the International Union of Geological Sciences Subcommission on the Systematics of Igneous Rocks*. Cambridge University Press., New York.

Le Maître R. W., Batema N. P., Dudek A., Keller J., Lameyre J., Le Bas M. J., Sabine P. A., Schmid R., Sorensen H., Streckeisen A., Woolley A. R., Zanettin B. 2002. Igneous Rocks: A Classification and Glossary of terms. Cambridge University Press, New York.

Lee M. R., Tomkinson T., Hallis L.J., Mark D.F. 2015. Formation of iddingsite veins in the martian crust by centripetal replacement of olivine: Evidence from the nakhlite meteorite Lafayette. *Geoquimica et Cosmoquimica Acta*, 154: 49-65.

Lima J. F. W. F. 2003. Caracterização e classificação de Neossolos do Arquipélago de Fernando de Noronha. In CD: XXIX Congresso Brasileiro de Ciência do Solo/ Solo: Alicerce dos Sistemas de produção. Anais. Ribeirão Preto/SP.

Litvinenko Y. S. & Zakharikhina L.V. 2009. Zoning and Geochemical Characterization of Volcanic Soils on Kamchatka. *Geochemistry International*, 47(5), 463-475.

Lowe D. J. & Palmer D. J. 2005. Andisols of New Zealand and Australia. *Journal of Integrated Field Science*, 2: 39-65.

Luz F. R. 2016. Estudo do Vulcanismo da Ilha da Trindade: estratigrafia e petrologia da Formação Morro Vermelho. Monografia. Instituto de Geologia/Universidade Federal do Rio Grande do Sul.

Machado M. R. 2016. *O papel da avifauna na transformação geoquímica de substratos na Ilha da Trindade, Atlântico Sul*. Belo Horizonte. 92p. (Dissertação de Mestrado, Universidade Federal de Minas Gerais).

Mackeague J. A. & Day J. H. 1966. Dithionite and oxalate extractable Fe and Al as aids in differentiating various classes of soils. *Canadian Journal of Soil Science*, 46: 13-22.

McKeague, J.A., Bridon, J.E., Miles, N.M. 1971. Differentiation of forms of extractable iron and aluminum in soils. *Soil Science Society of America Proceedings*, 35: 33-38.

Madeira M. 1980. Esboço Pedológico da Ilha de Santa Maria (Açores). Instituto Nacional de Investigação Cientifica Tropical, Lisboa, Portugal.

Madeira M., Furtado A., Jeanroy E., Herbillon A. J. 1994. Andisols of Madeira Island (Portugal)- Characteristics and classification. *Geoderma*, 62 (4): 363-383.

Madeira M., Pinheiro J., Medina J. 1996. Características físico-químicas e mineralógicas de Andossolos do Arquipélago dos Açores (Portugal) que endurecem irreversivelmente por secagem. Actas do XIII Congresso Latino-Americano de Ciência do Solo, 4-8 de Agosto de 1996, Comissão 02, Trabalho 14, Águas de Lindóia SP (Brasil). (Edição em CD-ROM).

Madeira M., Pinheiro J., Monteiro F. M. G., Fonseca M., Medina J. 2002. Características e classificação dos Solos da Ilha do Faial (Arquipélago dos Açores*). Revista de Ciencias Agrarias*, 25(3/4):53-66.

Madeira M., Pinheiro J., Madruga J., Monteiro F. 2007. Soils of volcanic systems in Portugal. In: Arnalds Ó., Óskarsson H., Bartoli F., Buurman P., Stoops G., García-Rodeja E. (eds.), Soils of Volcanic Regions in Europe. Springer, Berlin, Heidelberg, 69-81.

Madejová J., Balan E., Petit S. 2011. Application of vibrational spectroscopy to the characterization of phyllosilicates and other industrial minerals. In: Christidis G. E. (ed.), Advances in the characterization of industrial minerals, EMU Notes in Mineralogy. European Mineralogical Union and Mineralogical Society of Great Britain and Ireland, Cambridge, 171–226.

Madruga J. S. 1995. *Características e Génese do Horizonte Plácico em Solos do Arquipélago dos Açores*. Dissertação de Doutoramento. Universidade dos Açores, Angra do Heroísmo, Portugal.

Mantovani L. E., Fritzons E., Batistella M. 1991. Solos do Arquipélago de Fernando de Noronha. In: XXIII Congresso Brasileiro de Ciência do Solo. *Anais*. Porto Alegre, SBCS, 263.

Marques R., Vieira B. J., Prudêncio M. I., Waerenborgha J. C., Dias M. I., Rocha F. 2018. Chemistry of volcanic soils used for agriculture in Brava Island (Cape Verde) envisaging a sustainable management. *Journal of African Earth Sciences*, 147: 28–42.

Marques F. A., Ribeiro M. R., Bittar S. M. B., Lima Neto J. A., Jacomine P. K. T. 2003. Caracterização e classificação de Cambissolos e Vertissolos do Arquipélago de Fernando de Noronha. *In*: Congresso Brasileiro de Ciências do Solo, 29. *Anais*. Ribeirão Preto: SBCS, 2003. CD.ROM.

Marques F. A. 2004. *Caracterização e classificação de solos da Ilha de Fernando de Noronha (PE)*. Recife-Pernambuco. 101p. (Dissertação de Mestrado, Solos e Nutrição de Plantas, Universidade Federal Rural de Pernambuco).

Marques L.S., Ulbrich M. N.C., Ruberti E., Tassinari C. G. 1999. Petrology, geochemistry and Sr-Nd isotopes of Trindade and Martin Vaz volcanic rocks (Southern Atlantic Ocean). *J. Volcan. Geoth. Res.*, 93: 191–216.

Mateus A. C. C., Varajão A. F. D. C, Oliveira F. S, Schaefer C. E. 2018. Alteration of olivine in volcanic rocks from Trindade Island, South Atlantic. *Appl. Clay Sci.*, 160: 40-48.

Mateus A. C. C., Varajão A. F. D. C, Petit S., Oliveira F. S., Schaefer C. E. (artigo submetido, a). Mineralogical and geochemical signatures of Quaternary pyroclasts alterations at the volcanic Trindade Island, South Atlantic**.** *Journal of South American Earth Sciences.*

Mateus A. C. C., Varajão A. F. D. C, Oliveira F. S, Petit S., Schaefer, C. E. (artigo submetido, b). Non-allophanic Andosols of Trindade Island, South Atlantic, Brazil: A New soil order in Brazil. *Revista Brasileira de Ciência do Solo*.

McDonough W.F. & Sun S.-S. 1995. The Composition of the Earth. *Chemical Geology*, 120: 223-253.

Medina J. M. B. & Grilo J. T. 1981. Esboço Pedológico da Ilha Graciosa (Açores). Instituto Nacional de Investigação Cientifica Tropical e Universidade dos Açores, Lisboa, Portugal.

Meha J. P. & Jackson M. L.1960. Iron oxides removal from soils and clays by dithionite-citrate-bicarbonate system buffered with bicarbonate sodium. *Clays and Clay Minerals*, 7:317-327.

Milet-Mureau M. L. A. 1797. Voyage de La Pérouse autour du mond. Paris, 2: 26-29.

Millot G. & Bonifas M. 1955. Transformations isovolumetriques dans les phenomenes de laterisation et de bauxitisation. *Bulletin Service Carte Géolique d'Alsace et Lorraine*, 8: 3-20.

Morimoto M. 1988. Nomenclature of pyroxenes. *Min. Mag*, 52: 535-550.

Morrás, H. J. M. 1978. Phosphatic nodules from a soil profile of Santa Fé island, Galapagos. In: Delgado, M. (ed.), Soil Micromorphology. University of Granada, Spain, 1007-1018.

Munsell Soil Color Charts. 2009. Baltimore, Macbeth Division of Kollmorgen Corporation.

Nakamura K. 1961. Stratigraphic studies of the pyroclastics of Oshima Volcano de-posited during the last fifteen centuries. II. Activity of parasitic volcanoes. Sci Pap Coii Gen Educ, Univ Tokyo 11: 281-319.

Nayudi Y. R.1964. Palagonite tufts (hyaloclastites) and the products of post-eruptive processes. *Bull. Volcanol.* 27: 391-410.

Neall, V.E. 1977. Genesis and weathering of Andosols in Taranaki. *Soil Science*, 123: 400-408.

Nunes M. 1962. Os solos da Ilha de São Nicolau (arquipélago de Cabo Verde). Junta de Investigações de Ultramar, Lisboa. Rev. Estudos, Ensaios e Documentos, n°94, Lisboa, 108 p.

Oliveira F. S. 2008. *Fosfatização em solo e rocha em ilhas oceânicas*. Viçosa. 115p. (Dissertação de Mestrado, Programa de Pós Graduação em Solos e Nutrição de Plantas, Universidade Federal de Viçosa).

Oliveira F. S., Shaefer C. E. G. R., Abrahão W. A. P., Clemente E. P., Simas F. N. B. 2014. Soil–geomorphology interactions and paleoclimatic implications of an ornithogenic soil toposequence on Rata Island, Fernando de Noronha Archipelago, South Atlantic. *Journal of South American Earth Sciences*, 52: 119-128.

Oliveira S. M. B., Pessenda L. C. R., Gouveia S. E. M., Fávaro D. I. T., Babinski M. 2009. Evidência Geoquímica de Solos Formados pela Interação de Guanos com Rochas Vulcânicas, Ilha Rata, Fernando de Noronha (PE). *Revista do Instituto de Geociências*, 9 (3): 3-12.

Oliveira S. M. B., Pessenda L. C. R., Gouveia S. E. M., Fávaro D. I. T. 2011a. Heavy metal concentrations in soils from a remote oceanic island, Fernando de Noronha, Brazil. *An. Acad. Bras. Ciênc.*, 83 (4): 1193-1206.

Oliveira S. M. B., Pessenda L. C. R., Babinski M., Gioia S. M. C. L., Fávaro D. I. T. 2011b. Solos Desenvolvidos Sobre Diferentes Rochas Vulcânicas da Ilha de Fernando de Noronha: Padrão de Elementos Terras Raras e Composição Isotópica do Chumbo. *Revista do Instituto de Geociências*, 11 (3): 97-105.

Panina L. I., Stoppa F. 2009. Silicate-carbonate-salt liquid immiscibility and origin of the sodalite-haüyne rocks: study of melt inclusions in olivine foidite from Vulture volcano, S. Italy. Cent. *Eur. J. Geosci.*, 1(4): 377- 392.

Pansu M. & Gautheyrou J. 2006. Handbook of Soil Analysis Mineralogical, Organic and Inorganic Methods. Springer, Berlin.

Parfitt R. L. 1990a. Allophane in New Zealand-A review. *Aust. J. Soil Res.*, 28: 343-360.

Parfitt R. L. & Wilson A. D. 1985. Estimation of allophane and halloysite in three sequences of volcanic soils, New Zealand. *Catena Supp.*, 7: 1-8.

Pasqualon N. G. 2017. Estratigrafia, petrologia e padrões de porosidade dos depósitos do Vulcão do Paredão, Ilha da Trindade, Brasil. Monografia, Instituto de Geologia/Universidade Federal do Rio Grande do Sul.

Patrício R. L. 2012. Mapeamento da Ilha de Trindade, Atlântico Sul. Monografia, Universidade Estadual Paulista.

Pauling B. D., Schiffman P., Zierenberg R. A., Clague D. A. 2011. Environmental and chemical controls on palagonitization. *Geochem. Geophys. Geosyst.*, 12 (12): 1-26.

Peacock M. A. 1926a. The palagonite formation of Iceland. *Geol. Mag.*, 63: 385-399.

Peacock M. A. 1926b. The geology of Videy, southwest Iceland; a record of igneous action in Glacial times. *Trans. R. Soc. Edinburgh,* 5A: 441- 465.

Peacock M. A. 1926c. The petrology of Iceland, part I. The basic turfs. Trans. *Roy. Soc. Edinburgh*, 55: 51-76.

Peacock M. A., Fuller R. E. 1928 Chlorophaeite, sideromelane, and palagonite from the Columbia River Plateau. *Am. Mineral.*, 13: 360-382.

Perlingeiro G., Vasconcelos P.M., Knesel K. M., Thiede D. S., Cordani U. G. 2013. 40Ar/39Ar geochronology of the Fernando de Noronha Archipelago and implications for the origin of alkaline volcanism in the NE Brazil. *J. Volcanol. Geotherm. Res.*, 249: 140-154.

Pinheiro J., Madeira M., Monteiro F., Medina J. 2001. Características e classificação dos Andossolos da Ilha do Pico (Arquipélago dos Açores). *Revista de Ciências Agrárias*, 24 (3 e 4): 48-60.

Pinheiro J., Tejedor Salguero M., Rodriguez-Rodriguez A. 2004. Genesis of placic horizons in Andisols from Terceira Island, Azores – Portugal. *Catena*, 56, 85-94.

Pires G.L.C., Bongiolo E. M., Geraldes M. C., Renac C., Santos A. C., Jourdan F., Neumann R. 2016. New ^{40}Ar/^{39}Ar ages and revised ^{40}K/^{40}Ar data from nephelinitic-phonolitic volcanic successions of the Trindade Island (South Atlantic Ocean). *Journal of Volcanology and Geothermal Research*, 327: 531-538.

Prior G.T. 1900. Petrographic notes on the rock specimens collected in the litle island of Trinidad, South Atlantic, by the Artic Expedition of 1839-1843 under Sir James Clark Ross. *Mineralogical Magazin Journal of the Mineralogical Society*, 22 (58): 317-323.

Rennert, T., Eusterhues, K., Hiradate, S., Breitzke, H., Buntkowsky, G., Totsche, KU. & Mansfeldt, T. 2014. Characterisation of Andosols from Laacher See tephra by wet chemical and spectroscopic techniques (FTIR,.sup.27Al-,.sup.29Si NMR).*Chemical Geology*, 363: 13-21.

Reynolds R. W. & Geist D. J. 1995. Petrology of lavas from Sierra Negra volcano, Isabela Island, Galápagos archipelago. *Journal of Geophysical Research: Solid Earth*, 100(B12): 24537-24553.

Ribeiro M. R.; Marques F. A.; Bittar S. M. B.; Ferraz F. B.; Jacomine, P. K. T.; Lima, J. F. W. F. 2003. Caracterização e classificação de Neossolos do Arquipélago de Fernando de Noronha. In: Congresso Brasileiro de Ciência do Solo, 29. *Anais*. Ribeirão Preto: SBCS, 2003. CD.ROM.

Ricardo R. P., Madeira M. V., Medina J. M. B., Marques M. M., Furtado A. F. S. 1977. Esboço pedológico da Ilha de S. Miguel (Açores). *An. Inst. Sup. Agron.*, 37: 275-385.

Ricardo R. P., Madeira M. A. V., Medina J. M. B. 1978-79. Enquadramento taxonómico dos principais tipos de solos que se admite ocorrerem no Arquipélago dos Açores. *An. Inst. Sup. Agron.*, 38: 167-180.

Ross C. S., Shannon E. V. 1925. The origin, occurrence, composition and physical properties of the mineral iddingsite. *Proc. U. S. Nat. Mus.*, 67: 1-19.

Sá M. M. 2010. *Caracterização ambiental, classificação e mapeamento dos solos da ilha da Trindade, Atlântico Sul*. Viçosa. 58 p. (Dissertação de Mestrado, Programa de Pós-Graduação em Solos e Nutrição de Plantas, Universidade Federal de Viçosa).

Saigusa M., Shoji S., Takahashi T. 1980. Plant root growth in acid Andosols from northeastern Japan: 2. Exchange acidity Y1 as a realistic measure of aluminum toxicity potential. *Soil Sci.*, 130:242-250.

Sanchez Diaz J., Benayas J., Guerra A. 1978. Morphological and micromorphological study of the argillic horizons in the arid and subhumid areas of Gran Canaria (Canary Islands). In: Delgado M. (ed.), Soil Micromorphology. Department of Edaphology, University of Granada, Granada, Spain, 1067-1092.

Santos Junior J.B. 2017. *Solos com propriedades ândicas derivados de litologias da Formação Serra Geral em ambientes altomontanos do sul do Brasil*. Lages. 185 p. (Tese de doutorado, Universidade Estadual de Santa Catarina).

Santos R. D, Lemos R. C, Santos H. G., Ker J. C, Anjos L.H.C., Shimizu S. H. 2013. *Manual de descrição e coleta de solo no campo*. Sociedade Brasileira de Ciência do Solo, Viçosa.

Santos R. D.,Santos H.G, Ker J. C., Anjos L. H. C., Shimizu S. H. 2015. Manual de descrição e coleta de solo no campo. Sociedade Brasileira de Ciência do Solo, Viçosa.

Schaefer C. E. G. R., Simas F. N. B., Albuquerque M. A., Souza, E., Delpupo K. K. 2010. Fosfatização de solos e evolução da paisagem no arquipélago de Abrolhos, BA. *REM: R. Esc. Minas*, 63(4): 727-734.

Schaefer C. E. G. R., Oliveira F. S., Marques F. A. 2017. Solos das ilhas oceânicas. In: Curi N., Ker J. C., Novais R. F., Vidal-Torrado P., Schaefer C. E. G. R. (eds.). Pedologia - Solos dos Biomas Brasileiros. 32ed.Viçosa: SBCS - Sociedade Brasileira de Ciência do Solo.

Schandl E. S., Gorton M. P., Wicks F. J. 1990. Mineralogy and geochemistry of alkali basalts from Maud Rise, Weddell Sea, Antarctica. In: Barker, P.F., Kennett, J.P., *et al.* (eds.), Proc. ODP Sci. Results, vol. 113, pp. 5-14.

Schenato F., Formoso M. L. L., Dudoignon P., Meunier A., Proust D., Mas A. 2003. Alteration processes of a thick basaltic lava flow of the Paraná Basin (Brazil): petrographic and mineralogical studies. *J. South Am. Earth Sci.*, 16: 423-444. doi:10.1016/S0895-9811(03)00098-1

Schoeneberger P. J., Wysocki D. A., Benham E.C., Soil Survey Staff. 2012. Field book for describing and sampling soils, Version 3.0. Natural Resources Conservation Service, National Soil Survey Center, Lincoln, NE.

Searle E. J. 1965. Auckland volcanic district in New Zealand volcanology. Northland, Coromandel, Auckland. *New Zeal. Geol. Surv. Handb.*, *Info Ser.*, 49: 90-103.

Sedov S. N., Solleiro-Reboledo E., Gama-Castro J. E. 2003. Andosol to Luvisol evolution in Central Mexico: timing, mechanisms and environmental setting. *Catena*, 54: 495-513.

Sedov S., Stoops G., Shoba S. 2010. Regoliths and soils on volcanic ash. In: Stoops, G., Marcelino V., Mees F., (eds.), Interpretation of Micromorphological Features of Soils and Regoliths. Elsevier, Amsterdam, 275-303.

Sheppard R.A. & Hay R. L. 2001. Formation of Zeolites in Open Hydrologic Systems. *Reviews in Mineralogy and Geochemistry*, 45(1): 261-275.

Shoji S. & Ono T. 1978. Physical and chemical properties and clay mineralogy of Andosols from Kitakami, Japan. *Soil Sci.*, 126(5): 297-312.

Shoji S. 1984. Andosols. *Kagakutoseibutu*, 22:242-250.

Shoji S.1985. Genesis and properties of non-allophanic Andosols in Japan. *Applied Clay Sci.*, 1:83-88.

Shoji S., Ito T., Saigusa M., Yamada L. 1985. Properties of non allophanic Andosols from Japan. *Soil Sci.*, 140: 264-277.

Shogi S., Nanzyo M., Dahlgren R. 1993. Terminology, concepts and geographic distribution of volcanic ash soils. In: Shogi S., Nanzyo M., Dahlgren R. (eds.), Volcanic ash soils genesis. Properties, and utilization. Elsevier Science Publishers B.V., Amsterdam, 1-5.

Santos, H.G., Jacomine, P.K.T., Anjos, L.H.C., Oliveira, V.A., Lumbreras, J.F., Coelhos, M.R., Almeida, J.A., *et al.* 2018. Sistema Brasileiro de Classificação de Solos. Embrapa, Brasília.

Sieffermann G. & Millot, G. 1969. Equatorial and tropical weathering of recent basalts from cameroon: allophanes, halloysite, metahalloysite, kaolinite and gibbsite. In: Heller L. (ed)., Proceedings of the International Clay Conference Tokyo. Israel Program for Scientific Translations, Jerusalem, 417-429.

Simas F. N. B. 2006. *Solos da Baía do Almirante, Antártica Marítima: mineralogia, gênese, classificação e biogeoquímica*. Viçosa, 153p. (Tese de Doutorado, Solos e Nutrição de Plantas, Universidade Federal de Viçosa).

Simas F. N. B., Schaefer C. E. G. R., Melo V. F. De, Albuquerque- Filho M. R., Michel R. F, Pereira V. V., Gomes M. R. M. 2007. Ornithogenic Cryosols from Maritime Antarctica: phosphatization as soil forming process. *Geoderma*, 138: 191-203.

Smith K.L., Milnes A.R., Eggleton R.A. 1987. Weathering of basalt: formation of iddingsite. *Clays and Clay Minerals*, 35 (6): 418-428.

Soares L. de C. As ilhas oceânicas. 1964. *In* AZEVEDO A. de (ed.) Brasil, a Terra e o Homem, Bases Físicas. (volume 1). São Paulo: Companhia Editora Nacional, p. 341-378.

Soil Survey Staff. 2010. Keys to soil taxonomy, 11th ed. USDA, Natural Resources Conservation Service, Washington, D.C.

Soil Survey Staff. 2014. Keys to soil taxonomy, 12th ed. USDA, Natural Resources Conservation Service, Washington, D.C.

Stearns H. T., Vaksvik K. N. 1935. Geology and ground-water resources of the island of Oahu, Hawaii. Hawaii Division of Hydrography Bulletin 1, U. S. Geological Survey, Hawaii.

Stoops G. 2003. Guidelines for Analyses and Description of Soil and Regolith Thin Sections. Soil Society of America, Inc., Madison.

Stoops G., Sedov S., Shoba S. 2018. Regoliths and soils on volcanic ash. In: Stoops G., Marcelino V., Mees F. (eds.), Interpretation of Micromorphological Features of Soils and Regoliths. Elsevier, Amsterdam, 721-751.

Stroncik N. A., Schimincke H. U. 2001. The evolution of palagonite: crystallization, chemical changes, and element budget. *Geochem. Geophys. Geosyst.*, 2: 2000GC000102.

Stroncik N. A., Schimincke H. U. 2002. Palagonite- a review. *Int. J. Earth Sci.*, 91: 680-697.

Sun M. S. 1957. The nature of Iddingsite in some basaltic rocks of New Mexico. *The American Mineralogist*, 42: 525-533.

Talbi E. H. & Honnorez J. 2003. Low-temperature alteration of mesozoic oceanic crust, Ocean Drilling Program Leg 185. *Geochem. Geophys. Geosyst.*, 4 (5): 1-21.

Teixeira W., Cordani U. G., Menor E. de A., Teixeira M. G., Linsker R. 2003. Arquipélago de Fernando de Noronha o paraíso do vulcão. São Paulo: Terra Virgem, 168p.

Teixeira PC, Donagemma GK, Fontana A, Teixeira WG, organizadores. 2017. Manual de métodos de análise do solo. 3a ed. rev. Brasília: Embrapa Solos.

The Fourth Committee for Soil Classification and Nomenclature, The Japanese Society of Pedology 2003: Unified Soil Classification System of Japan (USCSJ)— 2nd Approximation (2002). Hakuyusha, Tokyo (in Japanese).

Thorseth I. H., Furnes H., Tumyr O. 1990. A textural and chemical study of Icelandic palagonite of varied composition and its bearing on the mechanism of the glass-palagonite transformation. *Geochim. Cosmochim. Acta*, 55: 731-749

Tschegg C., Ntaflos T., Kiraly F., Harangi S. 2010. High temperature corrosion of olivine phenocrysts in Pliocene basalts from Banat, Romania. *Austrian Journal of Earth Sciences*, 103 (1): 101-110.

Urushadze T.F., Blum W. E. H., Sanadze E.V., Kvrivishvili T.O. 2011. Andosols of Georgia. *Eurasian Soil Science*, 44: 969-975.

Veltheim R.V. 1950. Geologia da ilha da Trindade. Relatório prévio da Expedição João Alberto à ilha da Trindade. Rio de Janeiro: [s. n.], (inédito).

Vergniolle S., Brandeis G. 1996. Strombolian explosions: 1. A large bubble breaking at the surface of a lava column as a source of sound. *J. Geophys. Res. Solid Earth*, 101 (B9): 20433–20447.

Vergniolle S., Brandeis G., Mareschal J.C. 1996. Strombolian explosions: 2. Eruption dynamics determined from acoustic measurements. *J. Geophys. Res. Solid Earth*, 101 (B9): 20449–20466.

Vieira B.J., Soares P.M., Prudêncio M.I., Freitas M.C., Rodrigues A.F. 2004. Caracterização química (terras raras e outros elementos) de solos das ilhas de Santa Maria e Terceira (Açores, Portugal). *Geociências*, 16: 5-12.

Vingiani S., Scarciglia F., Mileti F. A., Donato P., Terribile F. 2014. Occurrence and origin of soils with andic properties in Calabria (southern Italy). *Geoderma*, 232-234, 500-516.

Vingiani S., Buonanno M., Coraggio S., D'antonio A., De Mascellis R., Di Gennaro A., Iamarino M., Langella G., Manna P., Moretti P., Terribile F. 2018. Soils of the Aversa plain (southern Italy). *Journal of Maps*, 14: 312-320.

Von Waltershausen W. S. 1845. Über die submarinen Ausbrüche in der tertiären Formation des Val di Noto im Vergleich mit verwandten Erscheinungen am Ätna. *Gött. Stud.*, 1:371-431.

Wada K. 1989. Allophane and imogolite. In: Dixon J. B., Weed S.B. (eds.), Minerals in Soil Enviroments. Soil Society of America, Madison, WI, 1051-1087.

Walter H. S. 2004. The mismeasure of islands: implications for biogeographical theory and the conservation of nature. *Journal of Biogeography*, 31: 177-197.

Weaver B. L. 1990. Geochemical of the highly - undersaturated ocean island basalt suites from the South Atlantic Ocean Fernando de Noronha and Trindade Contributions to Mineralogy and Petrology, 105: 502 -515.

Wilson M. J. 1995. Clay Mineralogy: spectroscopic and chemical determinative methods. Chapman & Hall, London.

Walker G. P.L & Croasdale R. 1971. Characteristics of some basaltic pyroclastics. *Bull. Volcanol.*, 35(2): 303-317

Wentworth C. K. 1926. Pyroclastic geology of Oahu. Bernice P. Bishop. Museum, Bulletin 30, Honolulu, Hawai.

WRB. 2015. World Reference Base for Soil Resources 2014, update 2015 International soil classification system for naming soils and creating legends for soil maps. FAO, Rome.

Yeomans J. M. & Bremner J. C. 1988. A rapid and precise method for routine determination of organic carbon in soil. Commun. *Soil Sci. Plant Anal.*,19:1467-1476.

Yoshinaga N. 1986. Mineralogical characteristics, II. Clay minerals. In: Wada K. (ed.), Ando soils in Japan. Kyushu University Press., Fukuoka-shi, 41–56.

Zhou Z. H., Fyfe W. S., Tazaki K., Vandergaast S. J. 1992. The structural characteristics of palagonite from DSDP Site-335. *Can. Minera.l,* 30:75–81.

ANNEXES

1-Difração de Raios-X dos perfis 1, 2, 3 e 4. Hal= haloisita, Gth= goethita, Hem= hematita, Mag= magnetita, Ant= anatásio, Rt= rutilo, Px=piroxênio, Ol=olivina.

X-ray diffraction of 1, 2, 3 and 4 profiles. Hal= halloysite, Gth= goethite, Hem= hematite, Mag= magnetite, Ant= anatase, Rt= rutile, Px=pyroxene, Ol=olivine.

Diffraction des rayons X de profils 1, 2, 3 e 4. Hal= halloisite, Gth= goethite, Hem= hématite, Mag= magnétite, Ant= anatase, Rt= rutile, Px=pyroxène, Ol=olivine.

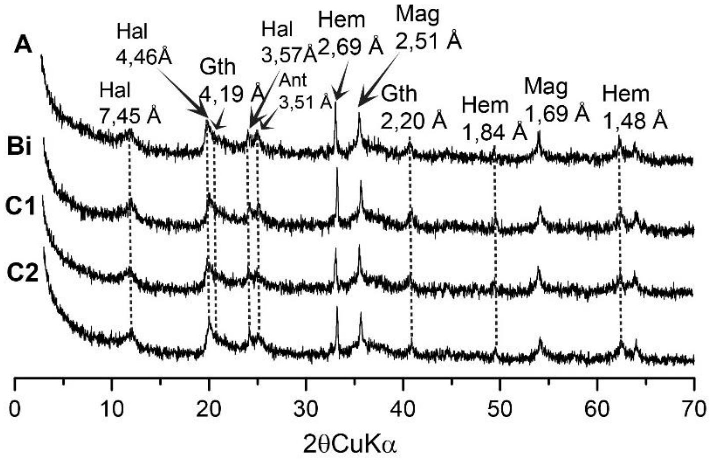

Figura 1.1.1: Fração total do perfil 1.
Figure 1.1.1: Bulk fraction of profile 1.
Figure 1.1.1: Fraction totale du profil 1.

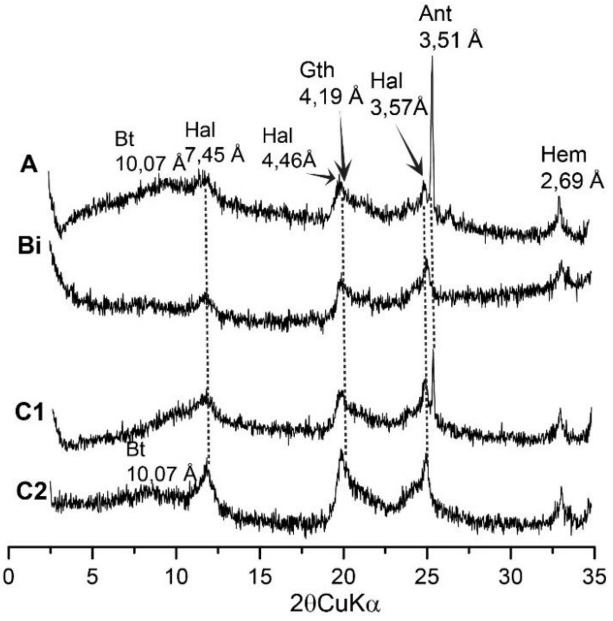

Figura 1.1.2: Fração argila < 2 µm do perfil 1.
Figure 1.1.2: Clay fraction < 2 µm of profile 1
Figure 1.1.2: Fraction argile < 2µm du profil 1.

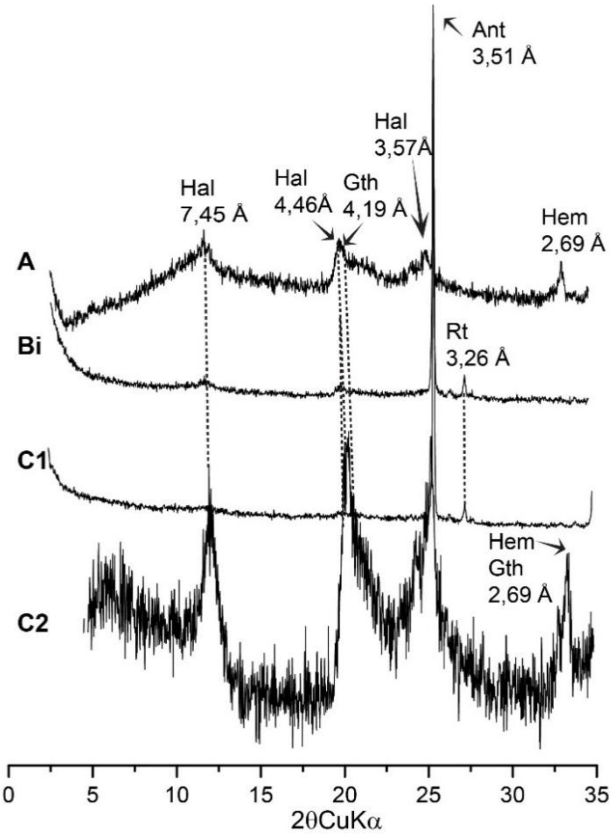

Figura 1.1.3: Fração argila < 1µm do perfil 1.
Figure 1.1.3: Clay fraction < 1µm of profile 1.
Figure 1.1.3: Fraction argile < 1µm du profil 1.

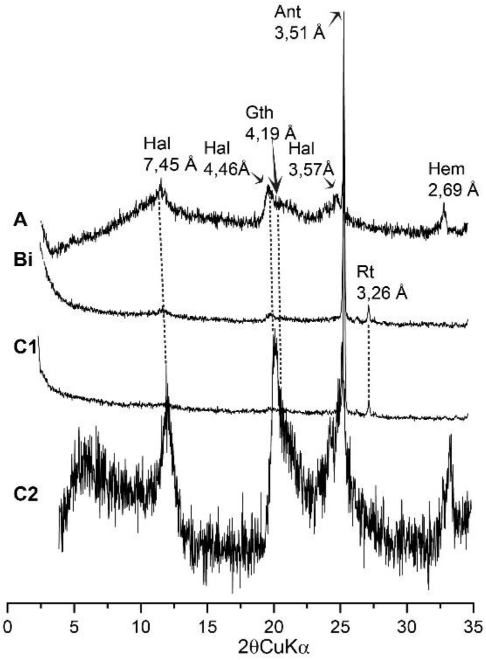

Figura 1.1.4: Fração argila < 0,5µm do perfil 1.
Figure 1.1.4: Clay fraction < 0,5 µm of profile 1.
Figure 1.1.4: Fraction argile < 0,5 µm du profil 1.

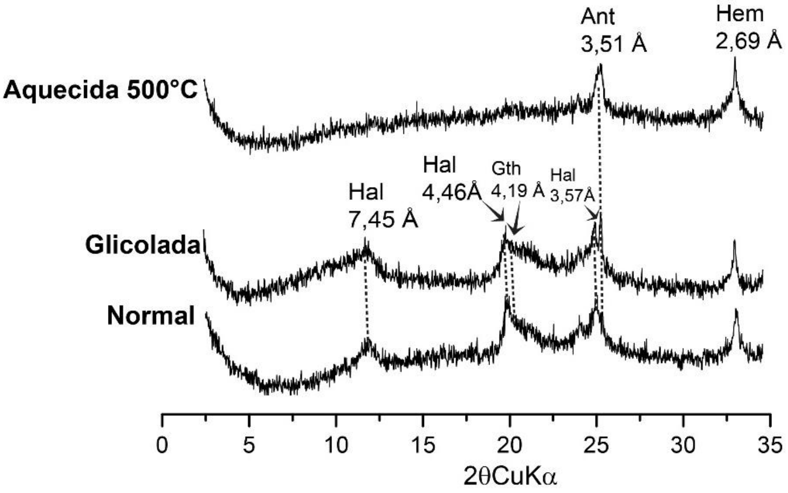

Figura 1.1.5: Fração argila do horizonte A do perfil 1. A amostra aquecida à 550°C mostrou a perda da haloisita.
Figure 1.1.5: Clay fraction of A horizon, profile 1. The sample heated to 550°C showed the loss of halloysite.
Figure 1.1.5: Fraction argile du horizon A, profil 1. L'échantillon chauffé à 550°C a montré la perte d'halloysite.

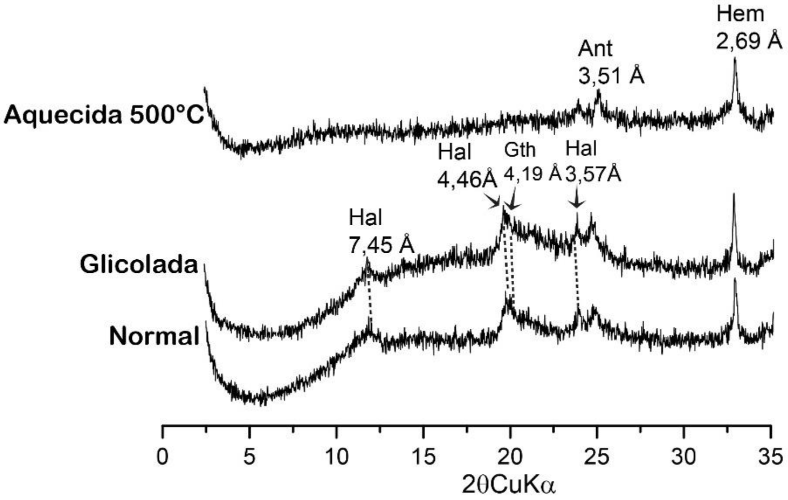

Figura 1.1.6: Fração argila do horizonte Bi do perfil 1. A amostra aquecida à 550°C mostrou a perda da haloisita
Figure 1.1.6: Clay fraction of Bi horizon, profile 1. The sample heated to 550°C showed the loss of halloysite.
Figure 1.1.6: Fraction argile du Bi horizon, profil 1. L'échantillon chauffé à 550°C a montré la perte d'halloysite.

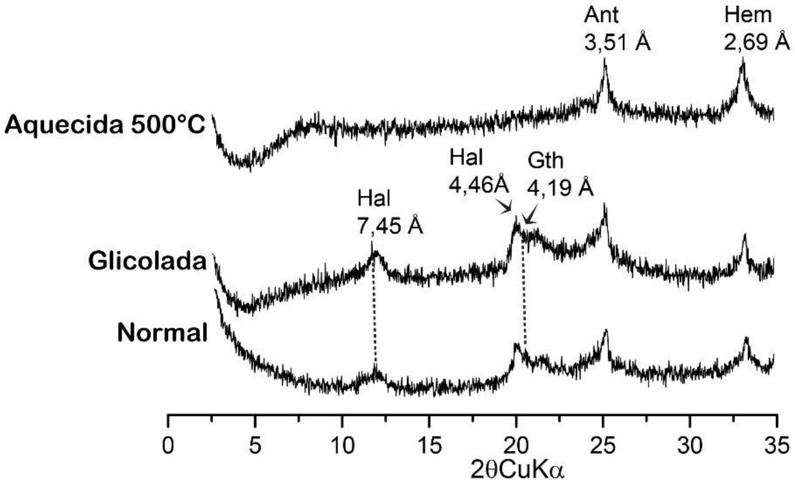

Figura 1.1.7: Fração argila do horizonte C1 do perfil 1. A amostra aquecida à 550°C mostrou a perda da haloisita.
Figure 1.1.7: Clay fraction of C1 horizon, profile 1. The sample heated to 550°C showed the loss of halloysite.
Figure 1.1.7: Fraction argile du C1 horizon, profil 1. L'échantillon chauffé à 550°C a montré la perte d'halloysite.

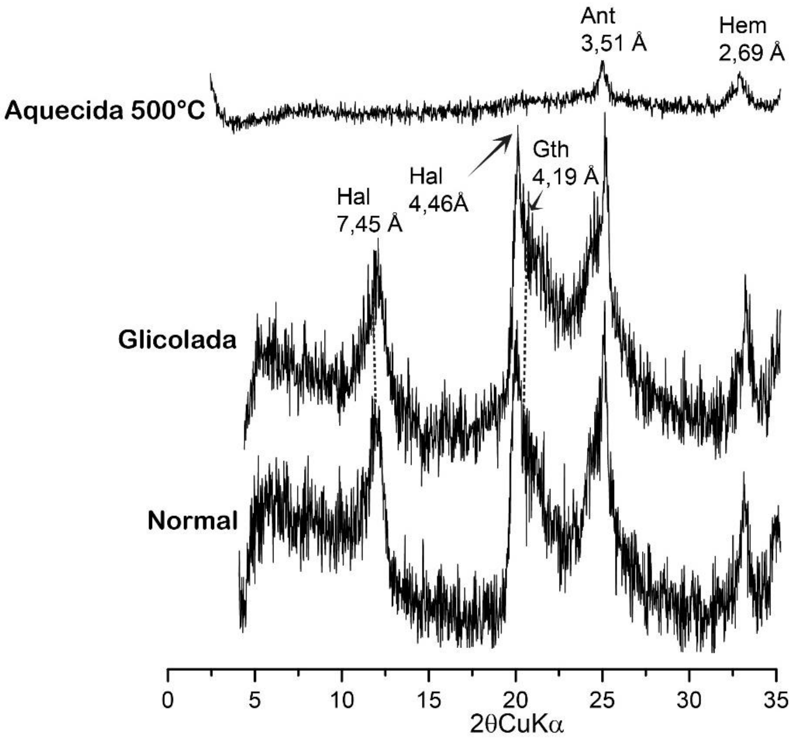

Figura 1.1.8: Fração argila do horizonte C2 do perfil 1. A amostra aquecida à 550°C mostrou a perda da haloisita.
Figure 1.1.8: Clay fraction of C2 horizon, profile 1. The sample heated to 550°C showed the loss of halloysite.
Figure 1.1.8: Fraction argile du C2 horizon, profil 1. L'échantillon chauffé à 550°C a montré la perte d'halloysite.

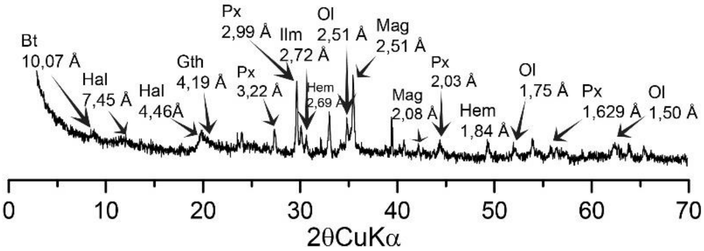

Figura 1.1.9: Fração pó total do perfil 2.
Figure 1.1.9: Bulk fraction of profile 2.
Figure 1.1.9: Fraction totale du profil 2.

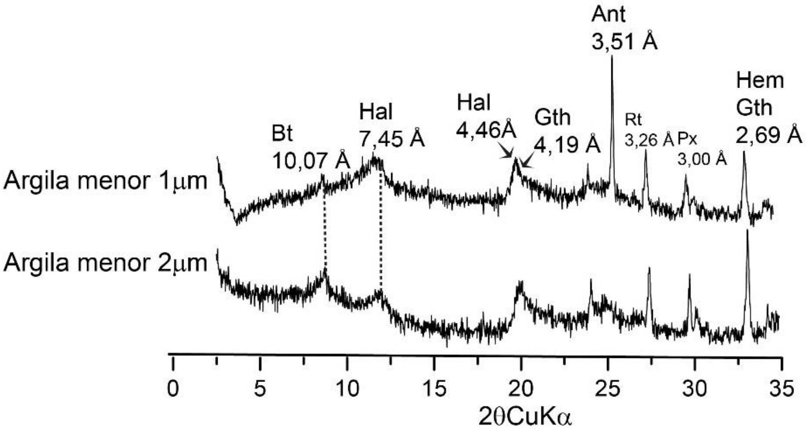

Figura 1.1.10: Fração argila < 2µm e <1µm do perfil 2.
Figure 1.1.10: Clay fraction < 2µm and <1µm of profile 2.
Figure 1.1.10: Fraction argile < 2µm and <1µm du profil 2.

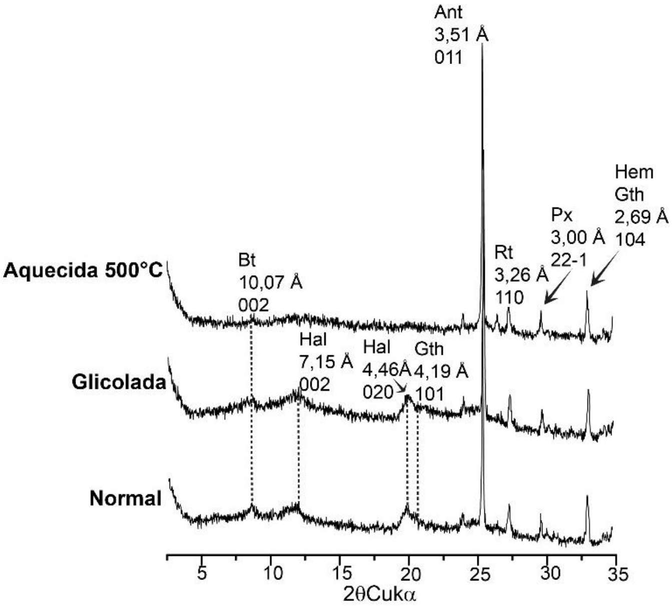

Figura 1.1.11: Fração argila do horizonte C do perfil 2. O aquecimento à 550°C mostrou a perda da haloisita
Figure 1.1.11: Clay fraction of C horizon, profile 2. The sample heated to 550°C showed the loss of halloysite.
Figure 1.1.11: Fraction argile du C horizon, profil 2. L'échantillon chauffé à 550°C a montré la perte d'halloysite.

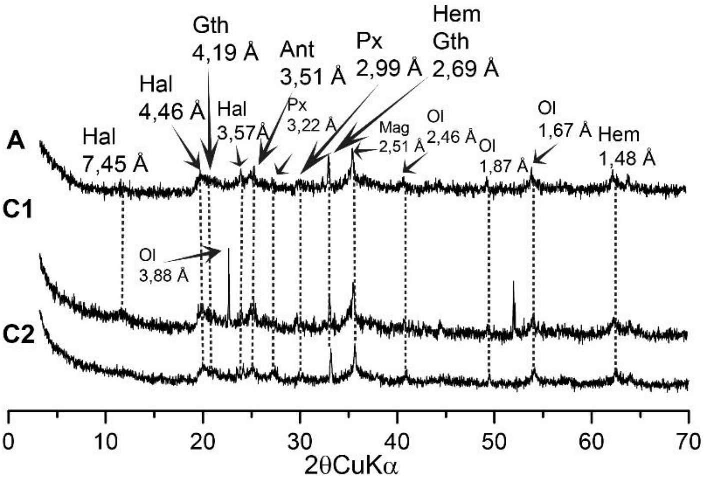

Figura 1.1.12: Fração pó total do perfil 3.
Figure 1.1.12: Bulk fraction of profile 3.
Figure 1.1.12: Fraction totale du profil 3.

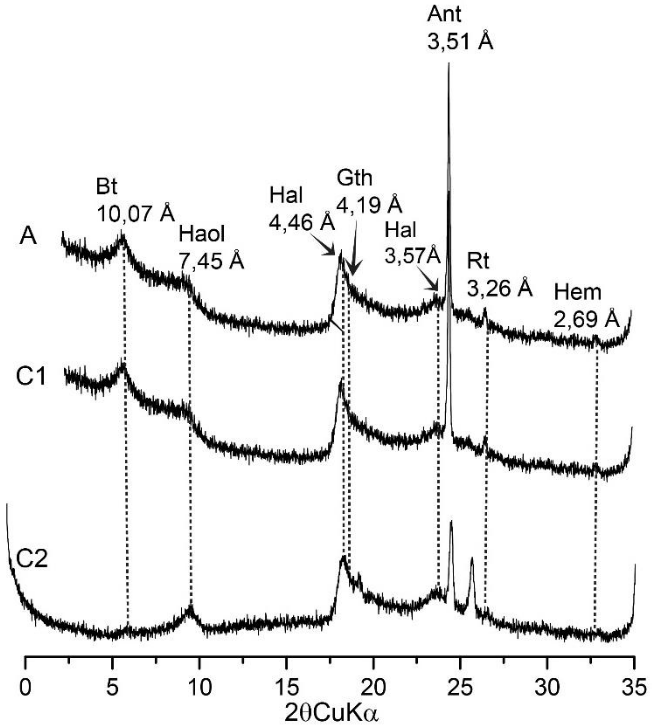

Figura 1.1.13: Fração argila < 2µm do perfil 3.
Figure 1.1.13: Clay fraction < 2µm of profile 3.
Figure 1.1.13: Fraction totale du profil 3.

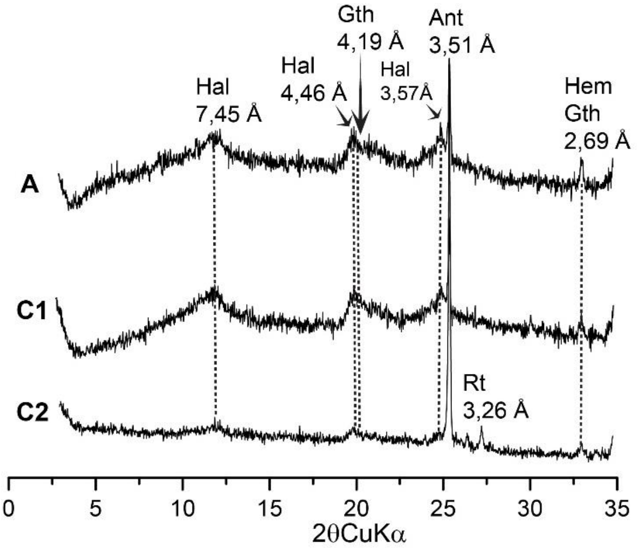

Figura 1.1.14: Fração argila < 1μm do perfil 3.
Figure 1.1.14: Clay fraction < 1μm of profile 3.
Figure 1.1.14: Fraction totale < 1μm du profil 3.

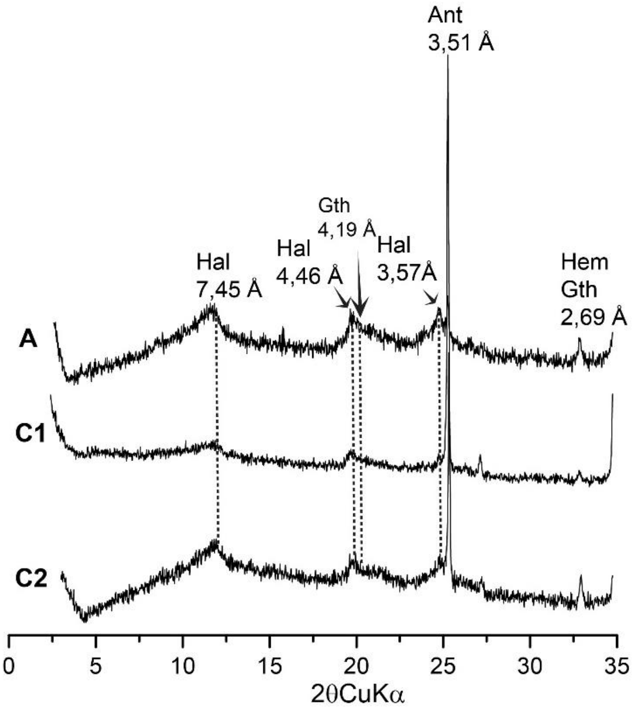

Figura 1.1.15: Fração argila menor que 0,5μm do perfil 3.
Figure 1.1.15: Clay fraction < 0,5μm of profile 3.
Figure 1.1.15: Fraction totale < 0,5μm du profil 3.

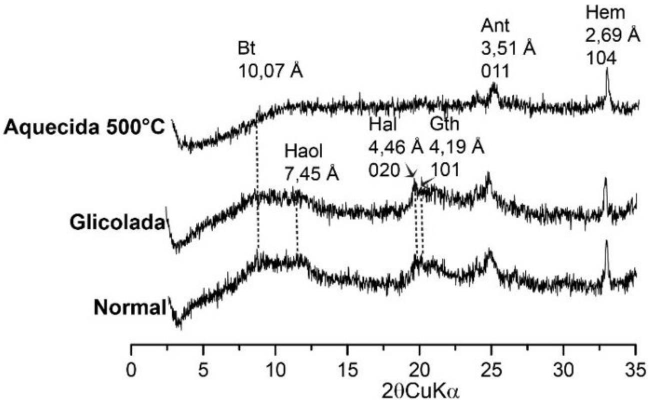

Figura 1.1.16: Fração argila do horizonte A do perfil 3. O aquecimento à 550°C mostrou a perda da haloisita.
Figure 1.1.16: Clay fraction of A horizon, profile 3. The heated to 550°C showed the loss of halloysite.
Figure 1.1.16: Fraction argile du horizon A, profil 3. L'échantillon chauffé à 550°C a montré la perte d'halloysite.

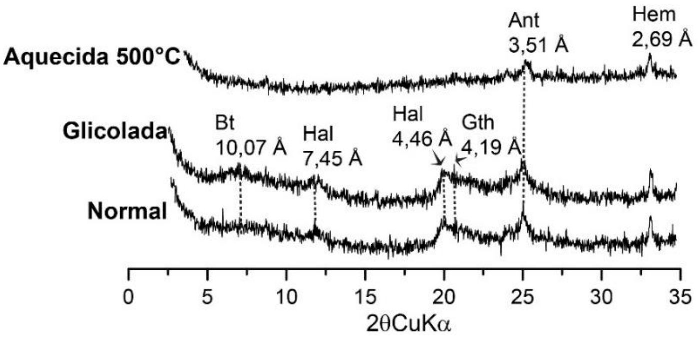

Figura 1.1.17: Fração argila do horizonte C1 do perfil 3. O aquecimento à 550°C mostrou a perda da haloisita.
Figure 1.1.17: Clay fraction of C1 horizon, profile 3. The heated to 550°C showed the loss of halloysite.
Figure 1.1.17: Fraction argile du horizon C1, profil 3. L'échantillon chauffé à 550°C a montré la perte d'halloysite.

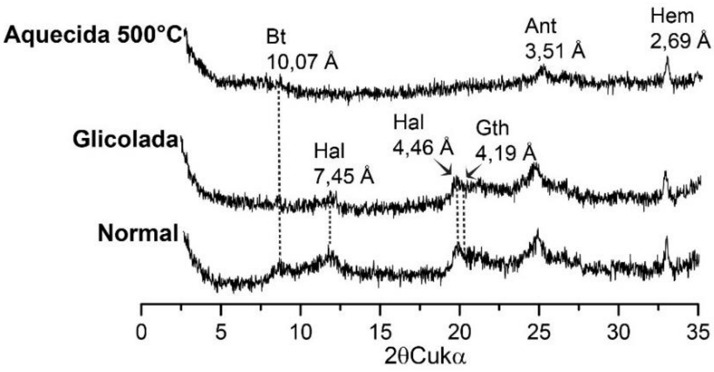

Figura 1.1.18: Fração argila do horizonte C2 do perfil 3. O aquecimento à 550°C mostrou a perda da haloisita.
Figure 1.1.18: Clay fraction of C2 horizon, profile 3. The heated to 550°C showed the loss of halloysite.
Figure 1.1.18: Fraction argile du horizon C2, profil 3. L'échantillon chauffé à 550°C a montré la perte d'halloysite.

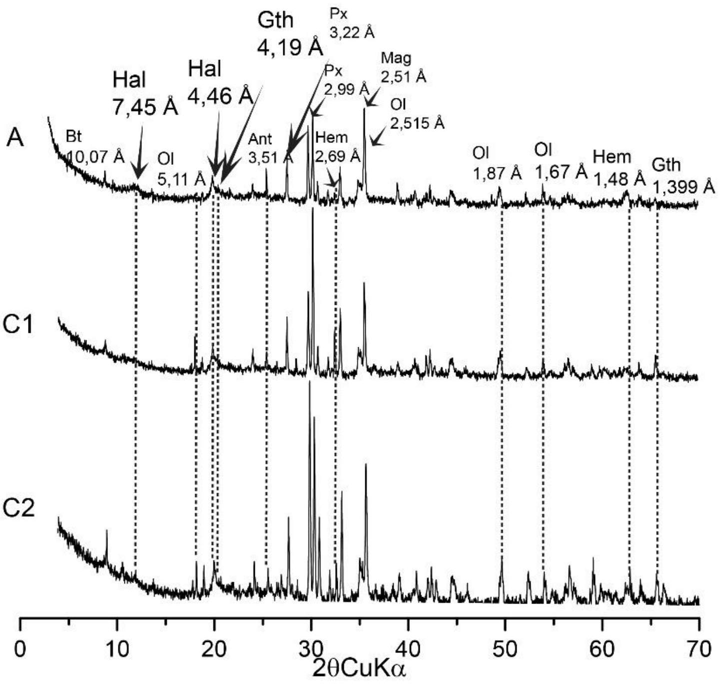

Figura 1.1.19: Fração pó total do perfil 4.
Figure 1.1.19: Bulk fraction of profile 4.
Figure 1.1.19: Fraction totale du profil 4.

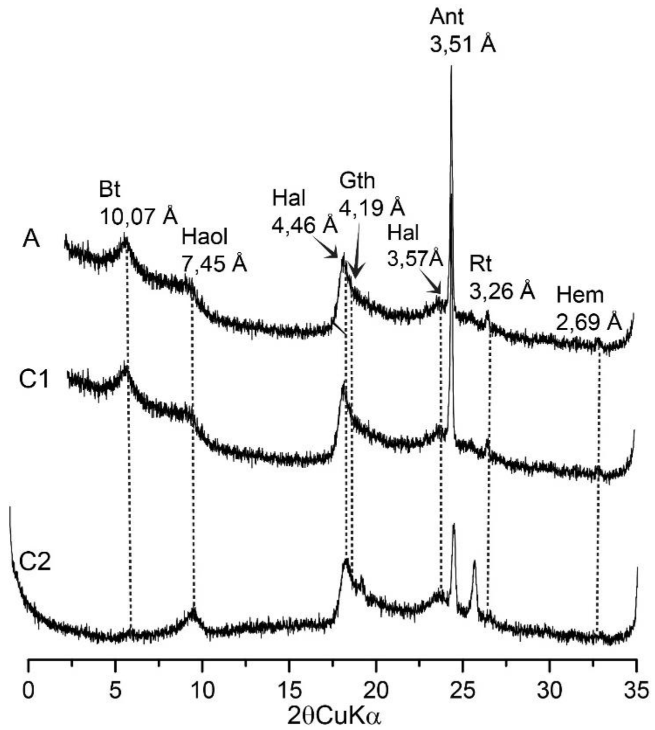

Figura 1.1.20: Fração argila < 2µm do perfil 4.
Figure 1.1.20: Clay fraction < 2µm of profile 4.
Figure 1.1.20: Fraction argile < 2µm du profil 4.

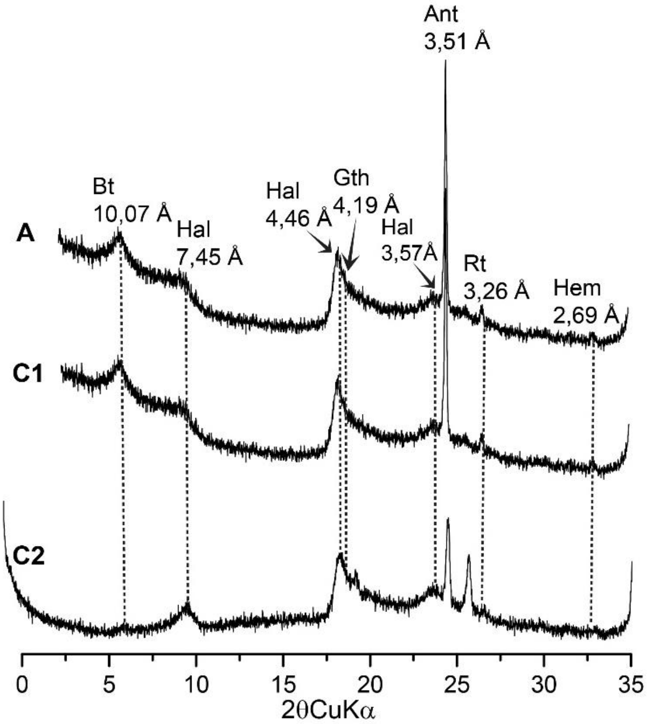

Figura 1.1.21: Fração argila < 1µm do perfil 4.
Figure 1.1.21: Clay fraction < 1µm of profile 4.
Figure 1.1.21: Fraction argile < 1µm du profil 4.

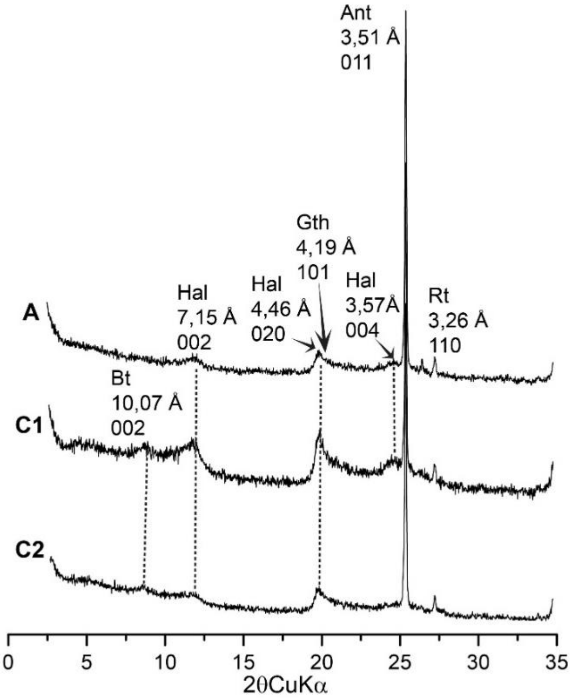

Figura 1.1.22: Fração argila < 0,5µm do perfil 4.
Figure 1.1.22: Clay fraction < 0,5µm of profile 4.
Figure 1.1.22: Fraction argile < 0,5µm du profil 4.

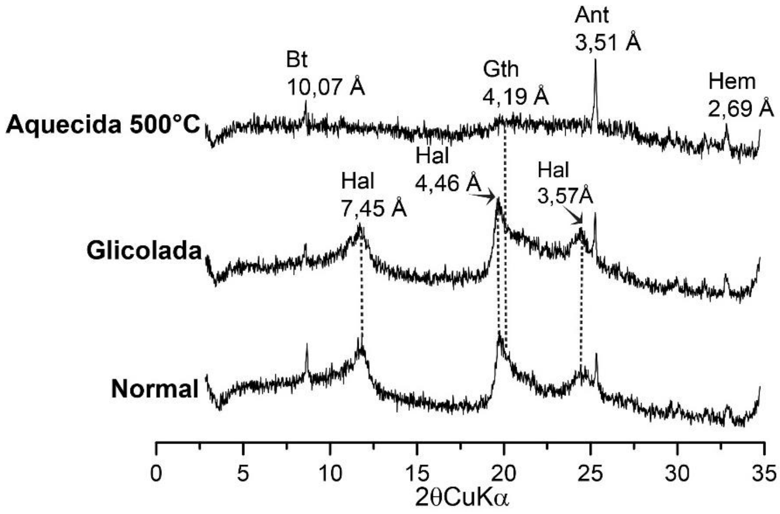

Figura 1.1.23: Fração argila do horizonte A do perfil 4. O aquecimento à 550°C mostrou a perda da haloisita.
Figure 1.1.23: Clay fraction of A horizon, profile 4. The heated to 550°C showed the loss of halloysite.
Figure 1.1.23: Fraction argile du horizon A, profil 4. L'échantillon chauffé à 550°C a montré la perte d'halloysite.

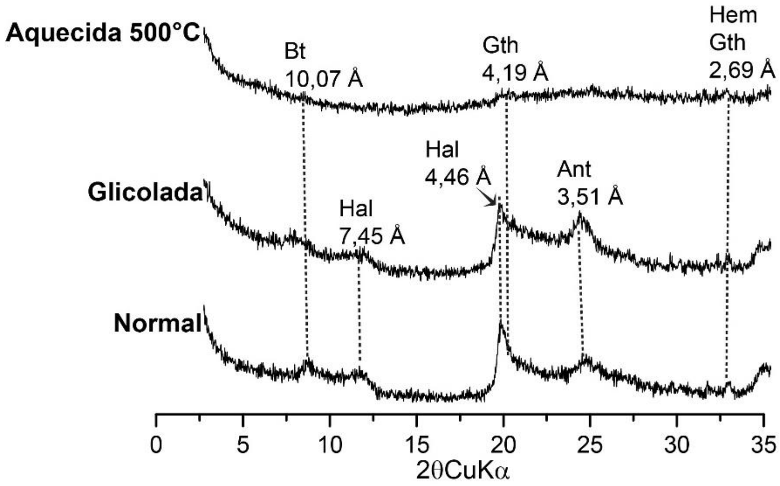

Figura 1.1.24: Fração argila do horizonte C1 do perfil 4. O aquecimento à 550°C mostrou a perda da haloisita.
Figure 1.1.24: Clay fraction of C1 horizon, profile 4. The heated to 550°C showed the loss of halloysite.
Figura 1.1.24: Fraction argile du horizon C1, profil 4. L'échantillon chauffé à 550°C a montré la perte d'halloysite.

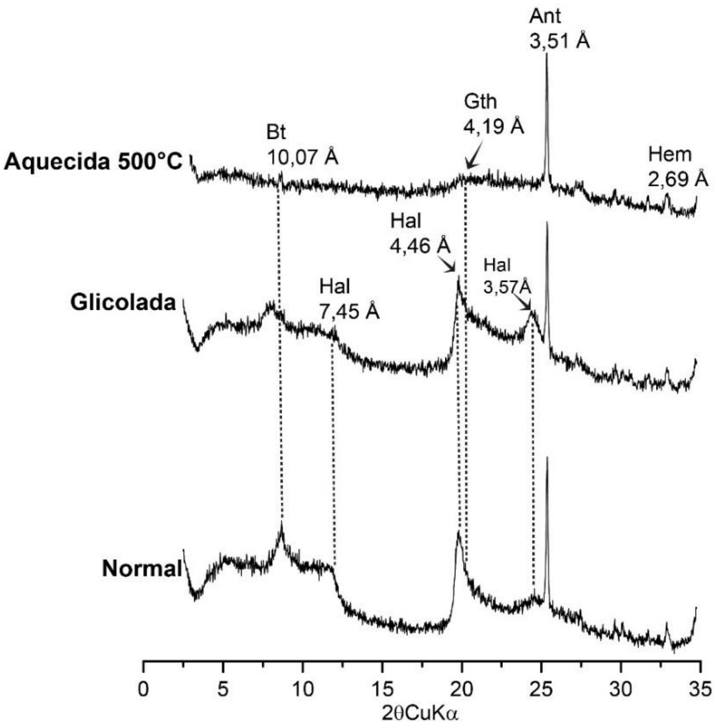

Figura 1.1.25: Fração argila do horizonte C2 do perfil 4. O aquecimento à 550°C mostrou a perda da haloisita.
Figure 1.1.25: Clay fraction of C2 horizon, profile 4. The heated to 550°C showed the loss of halloysite.
Figure 1.1.25: Fraction argile du horizon C2, profil 4. L'échantillon chauffé à 550°C a montré la perte d'halloysite.

1.2- Fração argila dos horizontes A, C1 e C2 do perfil 4 saturada com Ca, deferrificada com ditionitro-citrato-bicarbonato de sódio (DCB) e tratada com formamida. A passagem da haloisita 7Å para haloisita 10Å pode ser verificada através do tratamento com formamida.

Clay fraction of A, C1 and C2 horizon from profile 4 saturated with Ca^{2+} (Ca), deferrified with sodium dithionite-citrate-bicarbonate (DCB) and saturated with formamide (FOR). The passage of haloisite 7Å to haloisite 10Å can be verified through treatment with formamide.

Fraction d'argile de l'horizon A, C1 et C2 du profil 4 saturé de Ca^{2+} (Ca), déferrifié avec du sodium dithionite-citrate-bicarbonate (DCB) et saturée avec formamide (FOR). Le passage de la haloisite 7Å à haloisite 10Å peut être vérifié par le traitement avec le formamide.

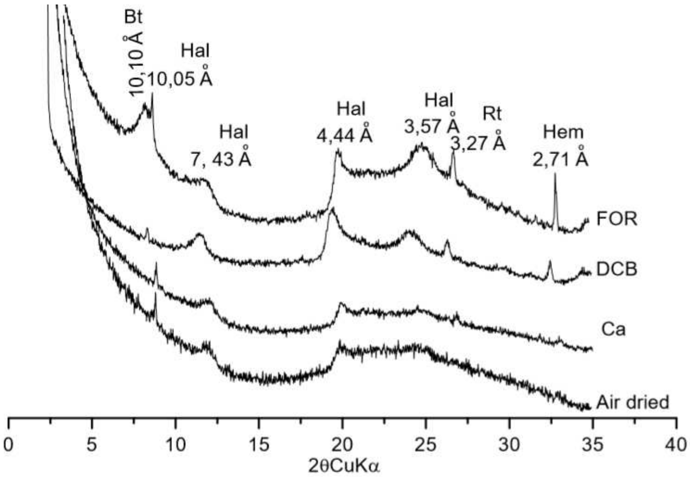

Figura 1.2.1: Horizonte A/ Horizonte A/A horizon/Horizon A.

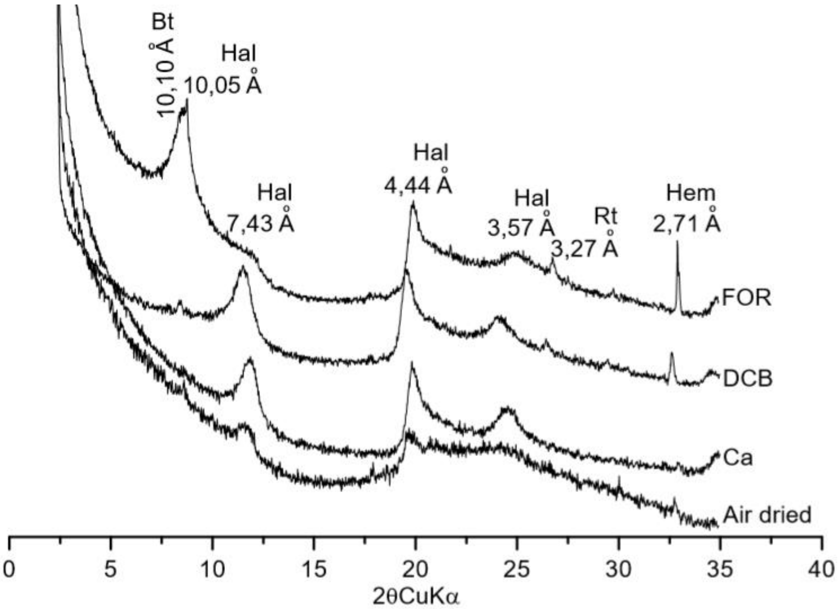

Figure 1.2.2: Horizonte C1/ C1 horizon/Horizon C1.

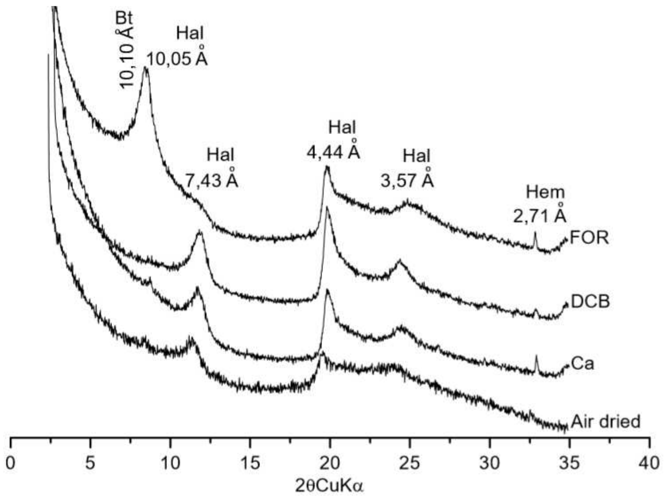

Figura 1.2.3: Horizonte C2/C2 horizon/Horizon C2.

2-Análise termodiferencial e termogravimétrica dos horizontes C2, C e C2 respectivamente do perfil 1,2 e 3.

Differential Thermal and Thermogravimetric analyzes (DTA-TG) from C2, C, C2, respectively from profiles 1, 2, and 3.

Analyse Thermique Différentielle (ATD) et Thermogravimétrique (TG) de C2, C, C2, respectivement à partir des profils 1, 2 et 3.

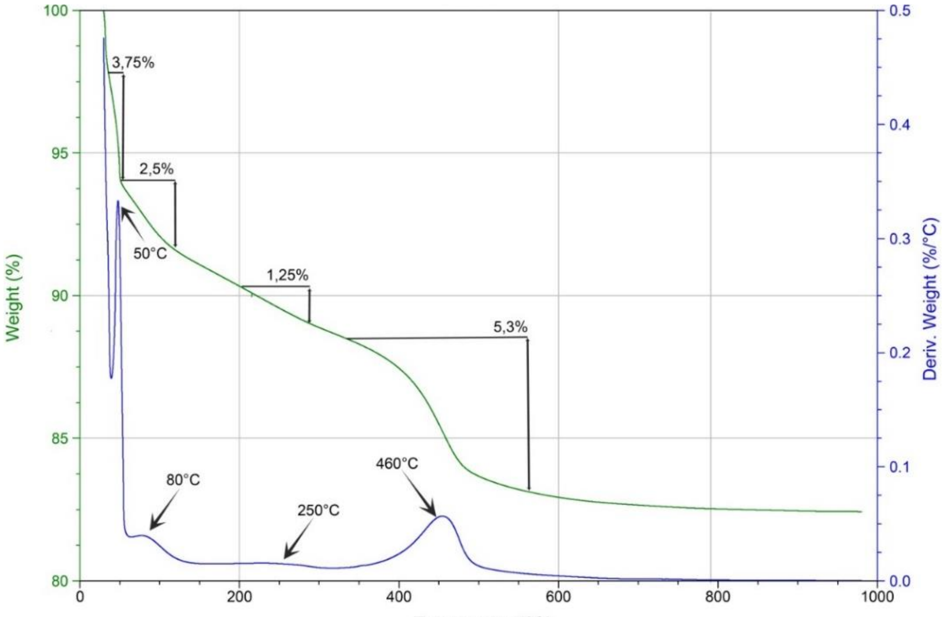

Figura 2.1: A análise termodiferencial indica a presença de goethita (perda de hidroxila a 250°C) e haloisita (perda de hidroxila a 460°C) e a termogravimétrica indica a perda de 12,8% em massa no horizonte C do perfil. 2.

Figure 2.1: DTA indicate the presence of goethite (hidroxil loss in 250°C) and halloysite (hidroxil loss in 460°C) and the TG indicate the loss of 12,8% in mass in C2 horizon from profile 1.

Figure 2.1 : L'ATD indiquent la présence de goethite (perte de hidroxil à 250°C) et d'halloysite (perte de hidroxil à 460°C) et la TG indique la perte de 12,8 % en masse à l'horizon C2 à partir du profil 1.

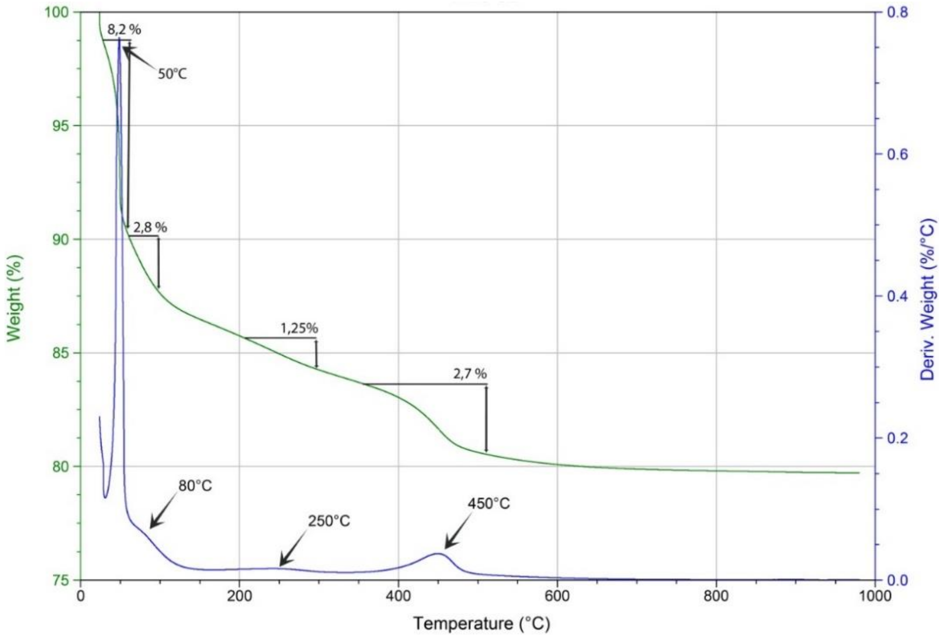

Figura 2.3: A análise termodiferencial indica a presença de goethita (perda de hidroxila a 250°C) e haloisita (perda de hidroxila a 450°C) e a termogravimétrica indica a perda de 14,95% em massa no horizonte C2 do perfil 3.

Figure 2.3: DTA indicate the presence of goethite (hidroxil loss in 250°C) and halloysite (hidroxil loss in 450°C) and the TGA indicate the loss of 14,95% in mass in C2 horizon from profile 3.

Figure 2.3: L'ATD indiquent la présence de goethite (perte de hidroxil à 250°C) et d'halloysite (perte de hidroxil à 450°C) et la TG indique la perte de 14,95 % en masse à l'horizon C2 à partir du profil 3.

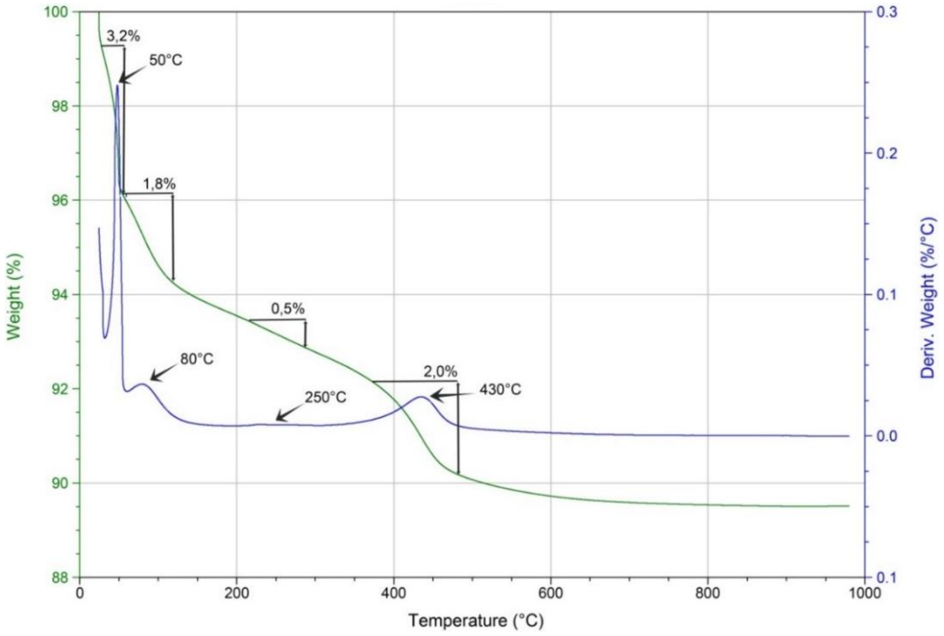

Figura 2.2: A análise termodiferencial indica a presença de goethita (perda de hidroxila a 250°C) e haloisita (perda de hidroxila a 430°C) e a termogravimétrica indica a perda de 7,5% em massa no horizonte C do perfil 2.

Figure 2.2: DTA indicate the presence of goethite (hidroxil loss in 250°C) and halloysite (hidroxil loss in 430°C) and the TGA indicate the loss of 7,5% in mass in C2 horizon from profile 2.

Figura 2.2: L'ATD indiquent la présence de goethite (perte de hidroxil à 250°C) et d'halloysite (perte de hidroxil à 430°C) et la TG indique la perte de 7,5 % en masse à l'horizon C à partir du profil 2.

3-Imagens de MET mostrando halloisita tubular nos perfis 2, 3 e 4.

TEM images showed tubular halloysite in profiles 2, 3 and 4.

Les images de MET ont montré l'halloysite tubulaire dans les profils 2, 3 et 4.

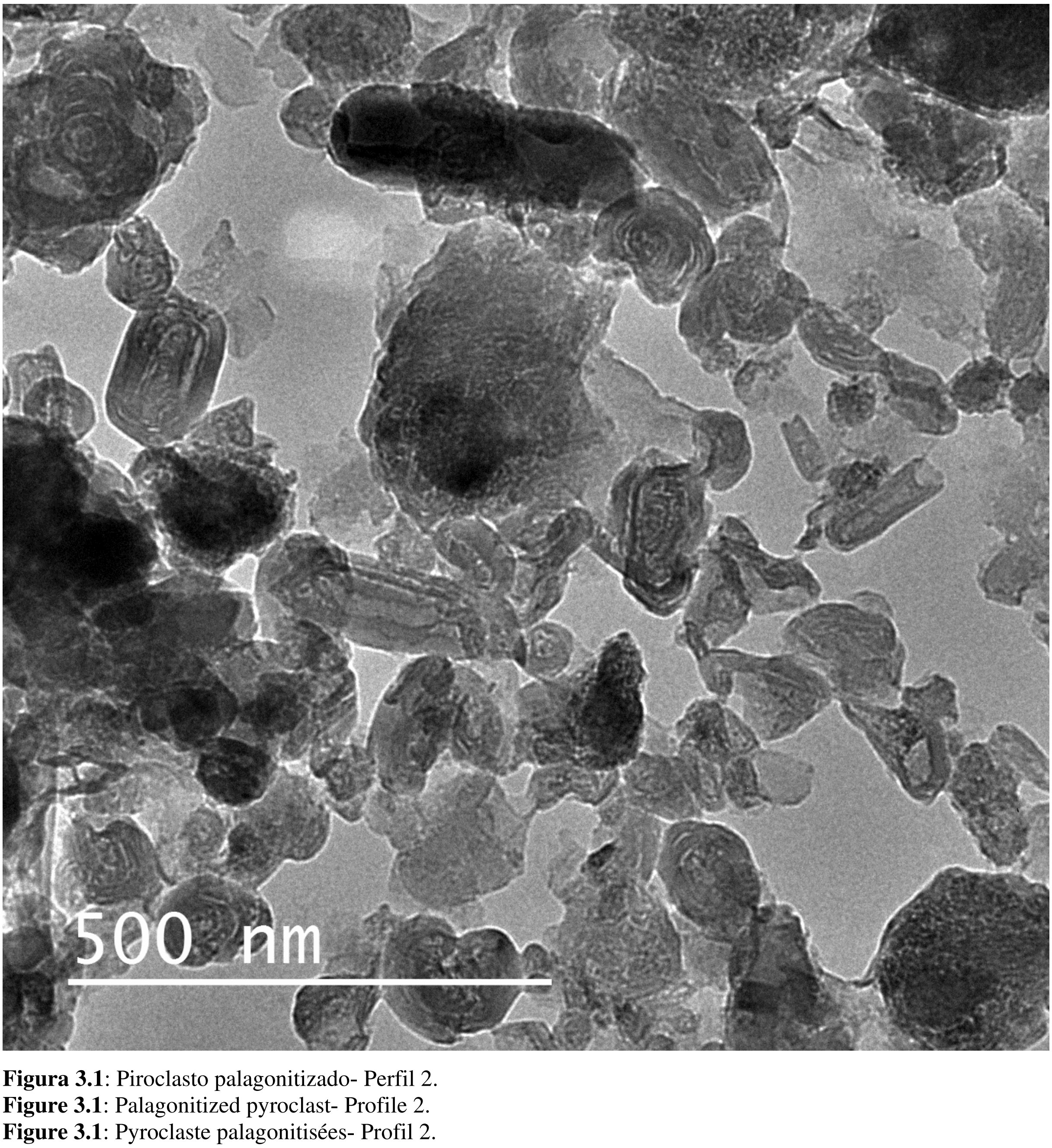

Figura 3.1: Piroclasto palagonitizado- Perfil 2.
Figure 3.1: Palagonitized pyroclast- Profile 2.
Figure 3.1: Pyroclaste palagonitisées- Profil 2.

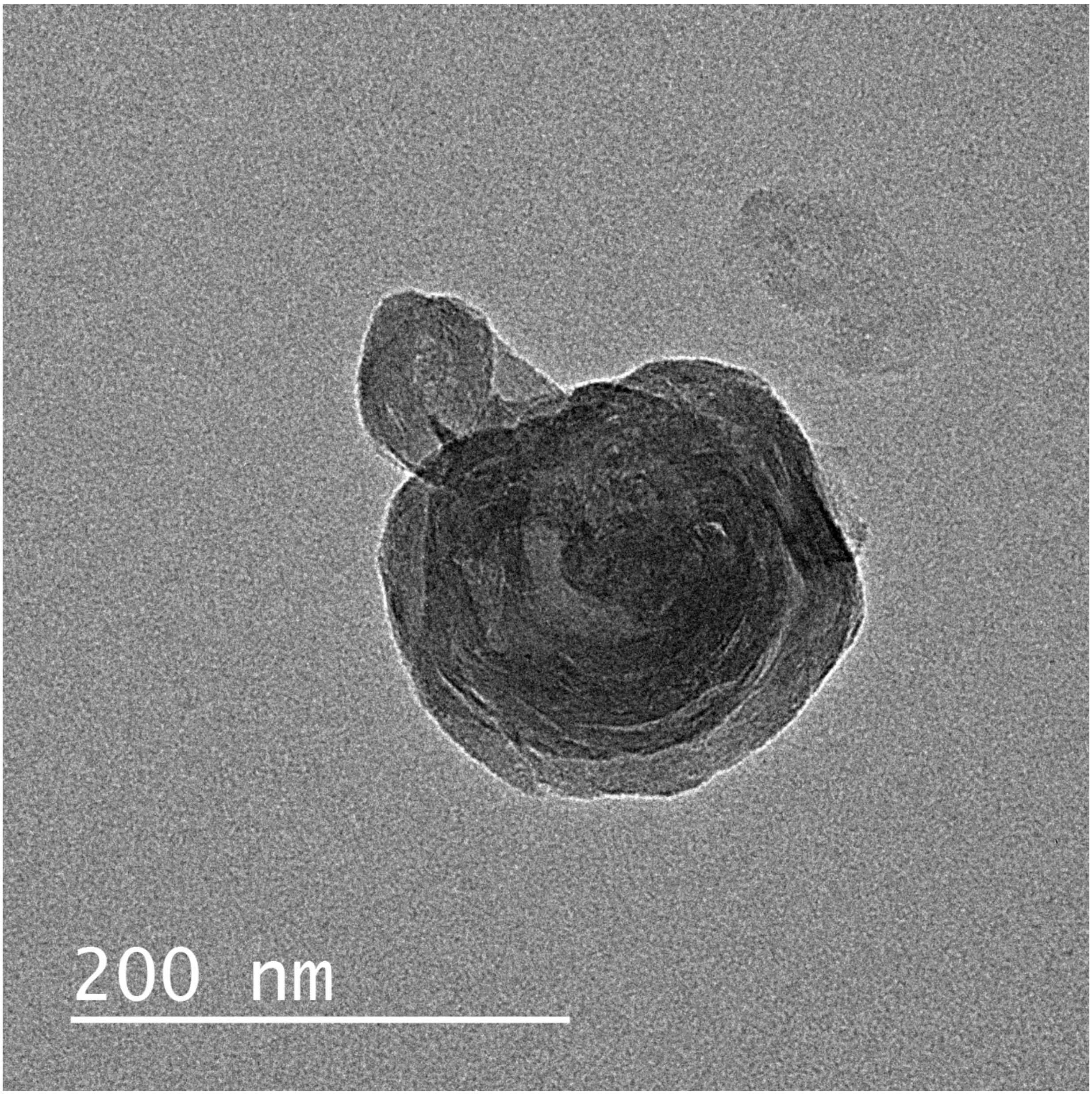

Figura 3.2: Horizonte C-Perfil 2.
Figure 3.2: C horizon – Profile 2.
Figure 3.2: Horizon C- Profil 2.

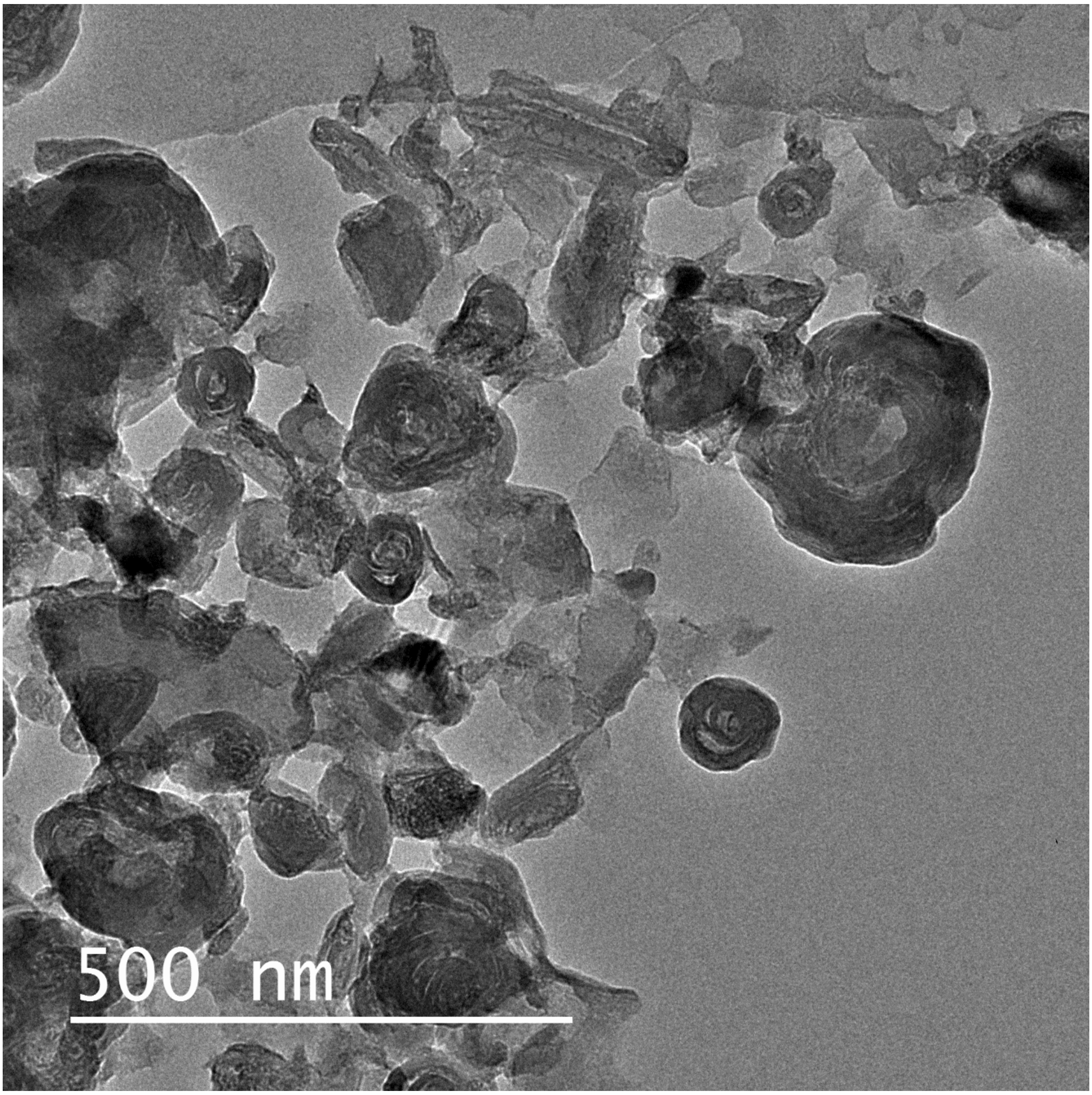

Figura 3.3: Piroclasto palagonitizado- Perfil 3.
Figure 3.3: Palagonitized pyroclast- Profile 3.
Figure 3.3: Pyroclaste palagonitisées- Profil 3.

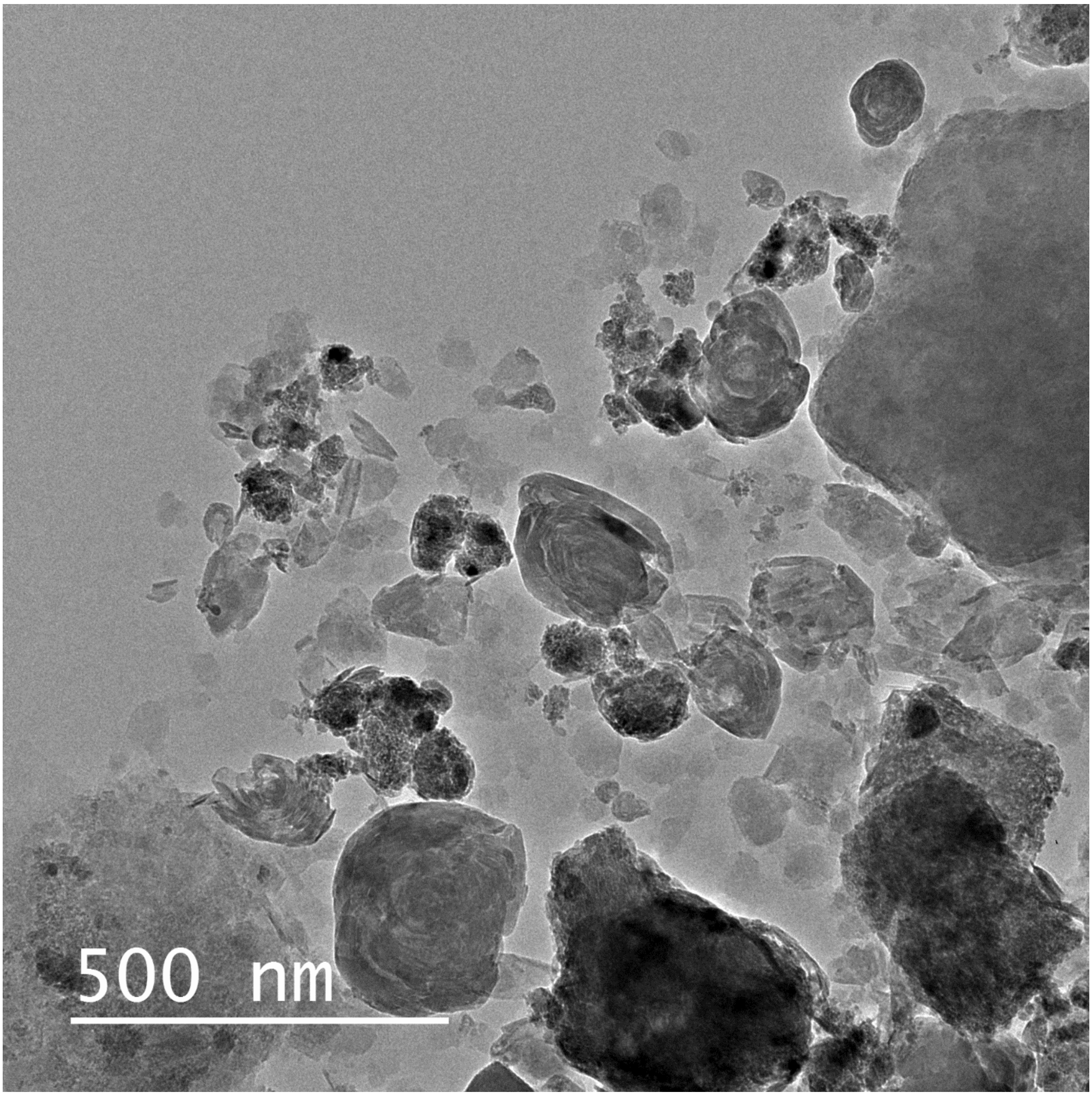

Figura 3.4: Horizonte C2-Perfil 3.
Figure 3.4: C2 horizon- Profile 3.
Figure 3.4: Horizon C2- Profil 3.

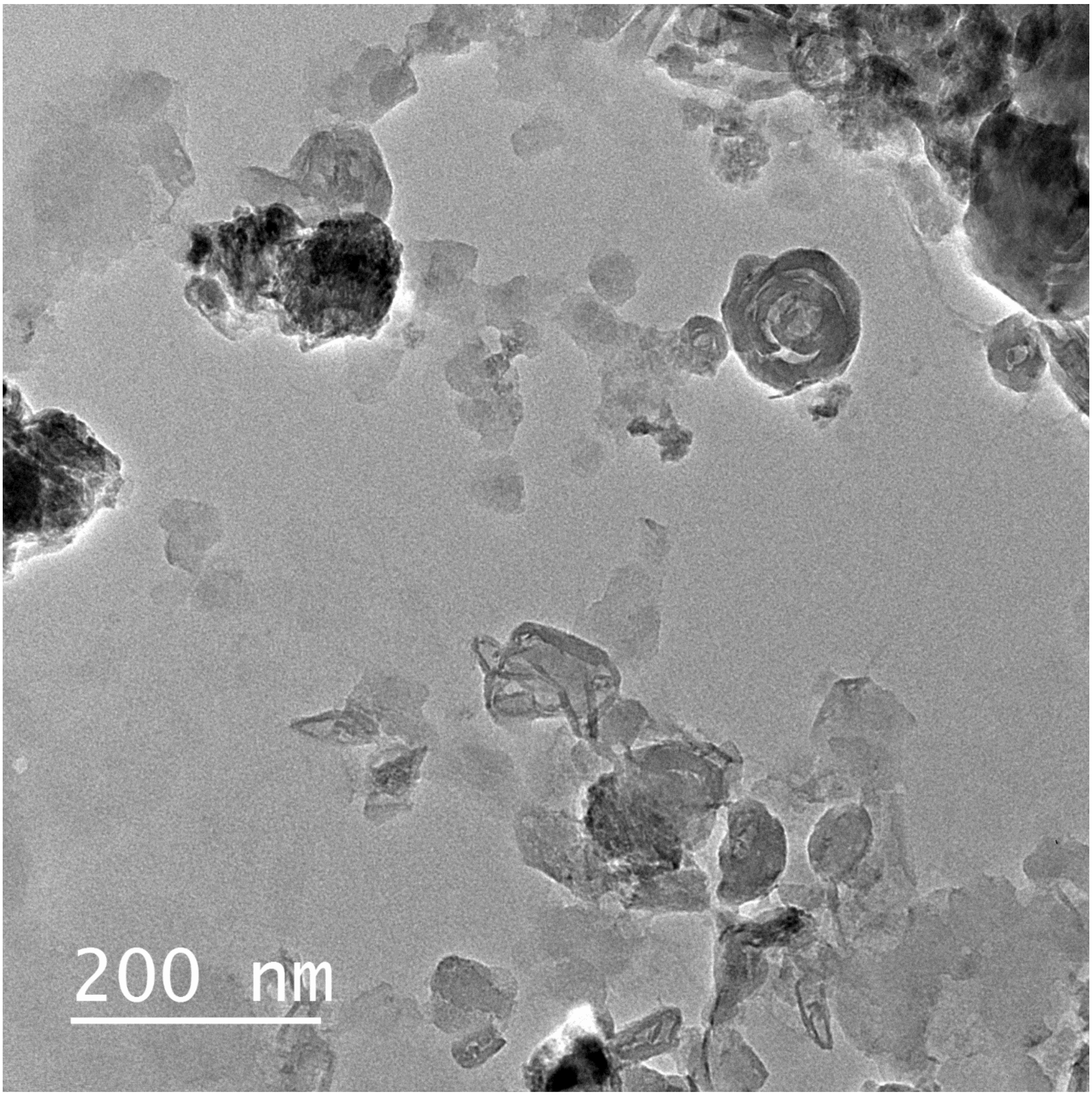

Figure 3.5: Horizonte A- Perfil 3.
Figure 3.5: A horizon- Profile 3.
Figure 3.5: A horizon- Profile 3.

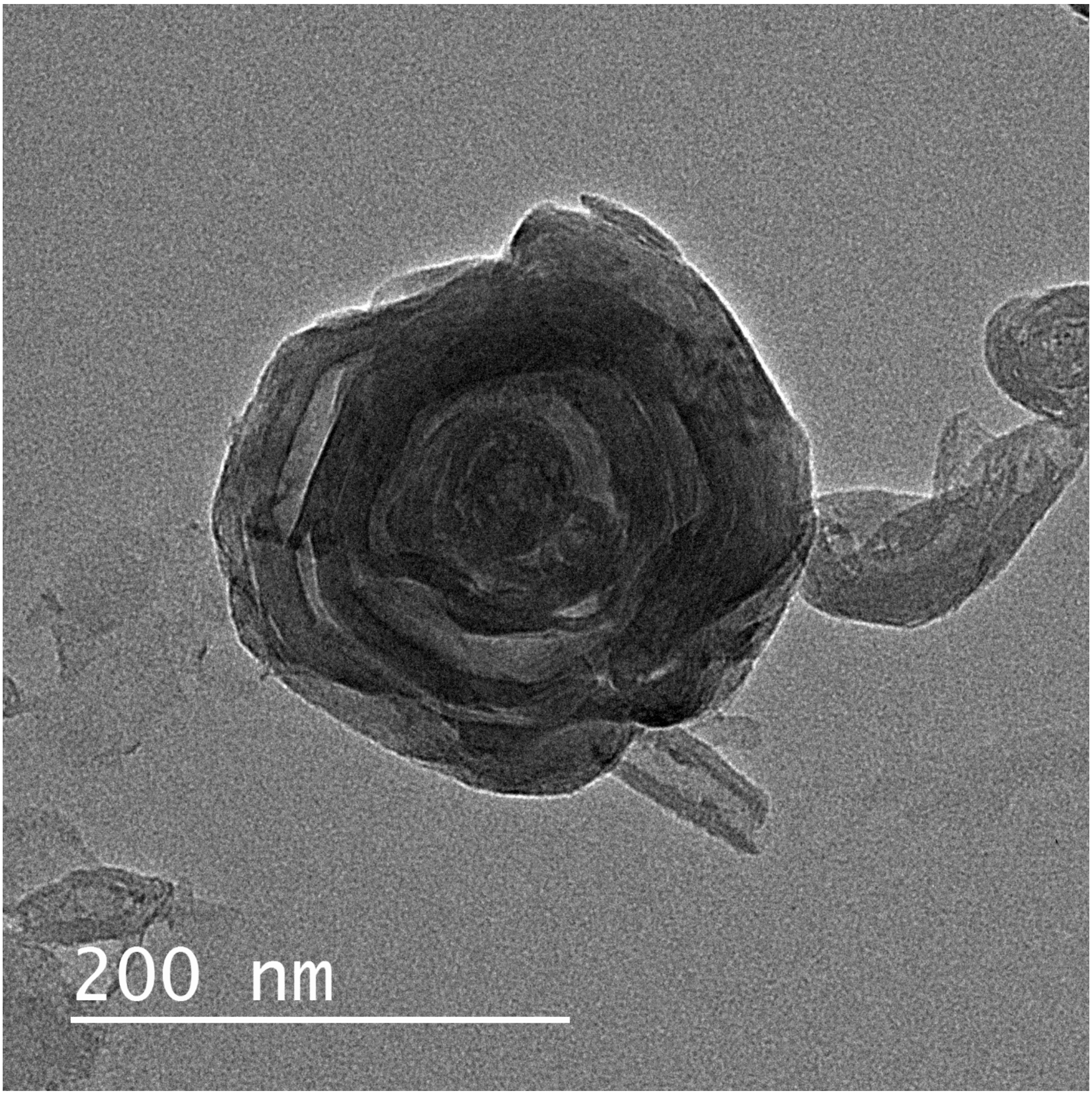

Figura 3.6: Horizonte C2-Perfil 4.
Figura 3.6: C2 horizon- Profile 4.
Figura 3.6: Horizon C2- Profil 4.

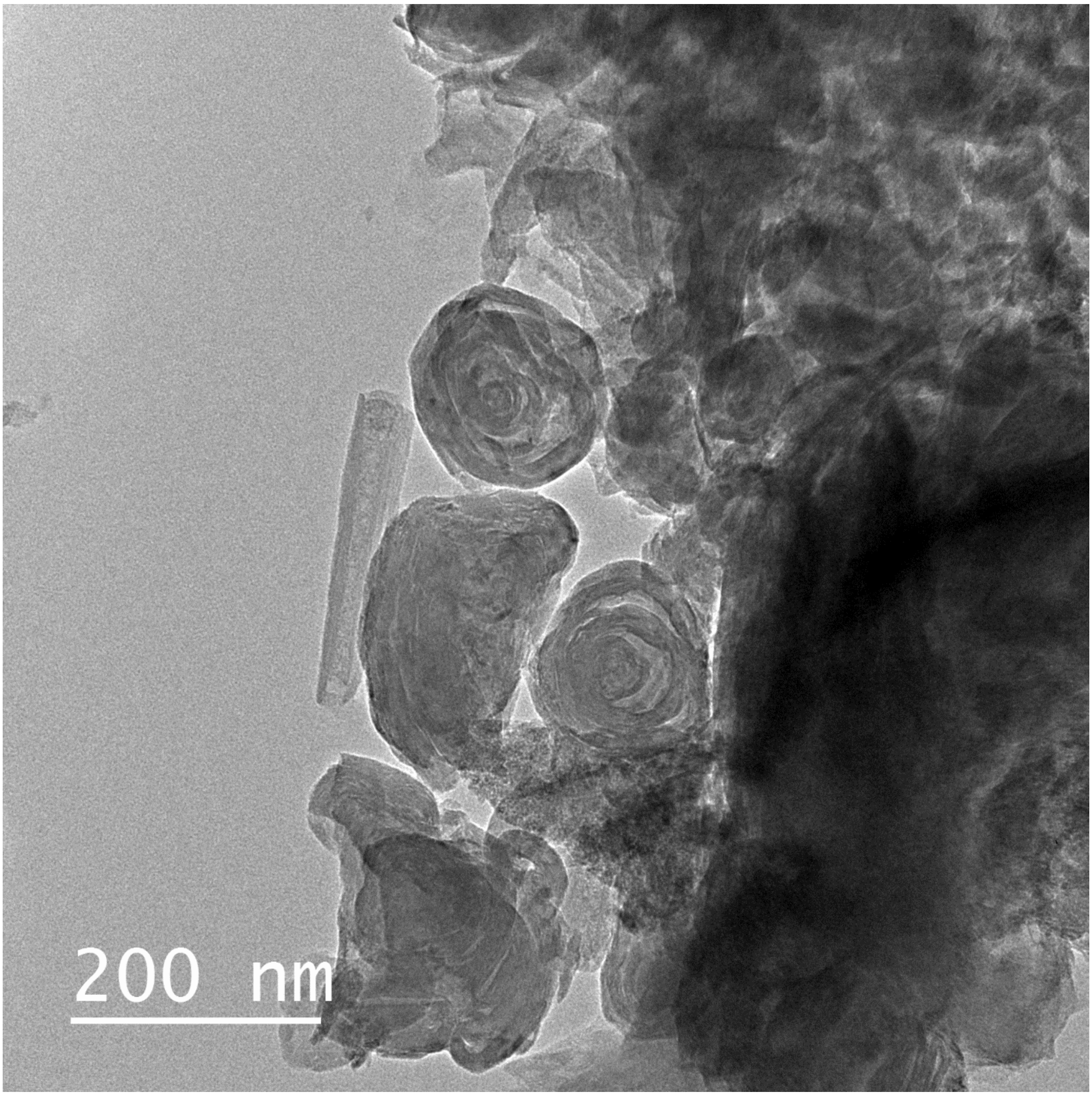

Figura 3.7: Horizonte A-Perfil 4.
Figure 3.7: A horizon- Profile 4.
Figure 3.7: Horizon A- Profil 4.